An aerial photograph showing a coastal town with significant flooding and debris. The water is murky and brown, covering large areas of the town. In the foreground, there are several large, multi-story houses, some of which appear to be partially submerged or surrounded by debris. The background shows more houses and trees, all under a grey, overcast sky. The overall scene depicts the aftermath of a major disaster, likely a hurricane or storm surge.

EXPLAINING EXTREME EVENTS OF 2012 FROM A CLIMATE PERSPECTIVE

Special Supplement to the
Bulletin of the American Meteorological Society
Vol. 94, No. 9, September 2013

EXPLAINING EXTREME EVENTS OF 2012 FROM A CLIMATE PERSPECTIVE

Editors

Thomas C. Peterson, Martin P. Hoerling, Peter A. Stott, and Stephanie C. Herring

Special Supplement to the

Bulletin of the American Meteorological Society

Vol. 94, No. 9, September 2013

AMERICAN METEOROLOGICAL SOCIETY

CORRESPONDING EDITOR:

Thomas C. Peterson
NOAA National Climatic Data Center
151 Patton Avenue, Asheville, NC 28801
E-mail: Thomas.C.Peterson@noaa.gov

COVER CREDITS:

FRONT: Breezy Point, New York, November 14, 2012, in the wake of Hurricane Sandy.
U.S. Navy photo by Chief Mass communication Specialist Ryan J. Courtade/Released

BACK: Herder moving cattle through a barren landscape in eastern Africa.
U.S. Geological Survey, Department of the Interior/USGS, U.S. Geological Survey/photo by Michael Budde

HOW TO CITE THIS DOCUMENT

Citing the complete report:

Peterson, T. C., M. P. Hoerling, P. A. Stott and S. Herring, Eds., 2013: Explaining Extreme Events of 2012 from a Climate Perspective. *Bull. Amer. Meteor. Soc.*, **94** (9), S1–S74.

Citing a section (example):

Diffenbaugh, N. S., and M. Scherer, 2013: Likelihood of July 2012 U.S. temperatures in pre-industrial and current forcing regimes [in “Explaining Extreme Events of 2012 from a Climate Perspective”]. *Bull. Amer. Meteor. Soc.*, **94** (9), S6–S9.

EDITORIAL AND PRODUCTION TEAM

Love-Brotak, S. Elizabeth, Graphics Support, NOAA/NESDIS
National Climatic Data Center, Asheville, NC

Misch, Deborah J., Graphics Support, LMI, Inc., NOAA/NESDIS
National Climatic Data Center, Asheville, NC

Osborne, Susan, Copy Editor, LMI, Inc., NOAA/NESDIS National
Climatic Data Center, Asheville, NC

Riddle, Deborah, Graphics Support, NOAA/NESDIS National
Climatic Data Center, Asheville, NC

Sprain, Mara, Technical Editor, LMI, Inc., NOAA/NESDIS
National Climatic Data Center, Asheville, NC

Veasey, Sara W., Lead Graphics Production, NOAA/NESDIS
National Climatic Data Center, Asheville, NC

Young, Teresa, Graphics Support, ERT/STG, Inc., NOAA/
NESDIS National Climatic Data Center, Asheville, NC

EDITOR & AUTHOR AFFILIATIONS (ALPHABETICAL BY NAME)

- Alexander, Lisa V.**, ARC Centre of Excellence for Climate System Science and Climate Change Research Centre, University of New South Wales, Sydney, Australia
- Allen, Myles R.**, School of Geography and the Environment and Department of Physics, University of Oxford, Oxford, United Kingdom
- Añel, Juan A.**, Smith School of Enterprise and the Environment, University of Oxford, Oxford, United Kingdom and EPhysLab, Faculty of Sciences, Universidade de Vigo, Ourense, Spain
- Barriopedro, David**, Dto. Física de la Tierra II, Facultad de Físicas, Universidad Complutense, Madrid, Spain and Instituto de Geociencias, IGEO (CSIC, UCM), Madrid, Spain
- Black, Mitchell T.**, ARC Centre of Excellence for Climate System Science and School of Earth Sciences, University of Melbourne, Melbourne, Australia
- Carey-Smith, Trevor**, National Institute of Water and Atmospheric Research (NIWA), Wellington, New Zealand
- Castillo, Rodrigo**, EPhysLab, Faculty of Sciences, Universidade de Vigo, Ourense, Spain
- Cattiaux, Julien**, Centre National de Recherches Météorologiques - Groupe d'Etude de l'Atmosphère Météorologique, Météo-France/CNRS, UMR3589, Toulouse, France
- Chen, Xianyan**, National Climate Center, China Meteorological Administration, Beijing, China
- Chen, Xiaolong**, LASG, Institute of Atmospheric Physics, Chinese Academy of Sciences, Beijing, China
- Chevallier, Matthieu**, Centre National de Recherches Météorologiques - Groupe d'Etude de l'Atmosphère Météorologique, Météo-France/CNRS, UMR3589, Toulouse, France
- Christidis, Nikolaos**, Met Office Hadley Centre, Exeter, United Kingdom
- Ciavarella, Andrew**, Met Office Hadley Centre, Exeter, United Kingdom
- Dean, Sam M.**, NIWA, Wellington, New Zealand
- Deans, Kirsten**, School of Geosciences, University of Edinburgh, Kings Buildings, Edinburgh, United Kingdom
- Diffenbaugh, Noah S.**, Department of Environmental Earth System Science and Woods Institute for the Environment, Stanford University, Stanford, California
- Doblas-Reyes, Francisco**, Institut Català de Ciències del Clima, Barcelona, Spain, and Institutió Catalana de Recerca i Estudis Avançats, Barcelona, Spain
- Donat, Markus G.**, ARC Centre of Excellence for Climate System Science and Climate Change Research Centre, University of New South Wales, Sydney, Australia
- Dong, Buwen**, National Centre for Atmospheric Science, Department of Meteorology, University of Reading, Reading, United Kingdom
- Eilerts, Gary**, USAID, Washington, D.C.
- Funk, Chris**, U.S. Geological Survey, Earth Resources Observation and Science Center, Sioux Falls, South Dakota and the Climate Hazards Group, University of California, Santa Barbara, California
- Galu, Gideon**, Climate Hazards Group, FEWS NET, Nairobi, Kenya
- García-Herrera, Ricardo**, Dto. Física de la Tierra II, Facultad de Físicas, Universidad Complutense, Madrid, Spain, and Instituto de Geociencias, IGEO (CSIC, UCM), Madrid, Spain
- Germe, Agathe**, Centre National de Recherches Météorologiques - Groupe d'Etude de l'Atmosphère Météorologique, Météo-France/CNRS, UMR3589, Toulouse, France
- Gill, Stephen**, NOAA/National Ocean Service (NOS), Center for Operational Oceanographic Products and Service (COOPS), Silver Spring, Maryland
- Gimeno, Luis**, EPhysLab, Faculty of Sciences, Universidade de Vigo, Ourense, Spain
- Guemas, Virginie**, Institut Català de Ciències del Clima, Barcelona, Spain, and Centre National de Recherches Météorologiques - Groupe d'Etude de l'Atmosphère Météorologique, Météo-France/CNRS, UMR3589, Toulouse, France
- Herring, Stephanie C.**, NOAA National Climatic Data Center, Boulder, Colorado
- Hoell, Andrew**, Climate Hazards Group, University of California Santa Barbara, Santa Barbara, California
- Hoerling, Martin P.**, NOAA/Earth System Research Laboratory, Boulder, Colorado
- Huntingford, Chris**, Centre for Ecology and Hydrology, Wallingford, United Kingdom
- Husak, Greg**, Climate Hazards Group, University of California Santa Barbara, Santa Barbara, California
- Imada, Yukiko**, Atmosphere and Ocean Research Institute, the University of Tokyo, Chiba, Japan
- Ishii, Masayoshi**, Meteorological Research Institute, Japan Meteorological Agency, Ibaraki, Japan
- Karoly, David J.**, ARC Centre of Excellence for Climate System Science and School of Earth Sciences, University of Melbourne, Melbourne, Australia
- Kimoto, Masahide**, Atmosphere and Ocean Research Institute, the University of Tokyo, Chiba, Japan
- King, Andrew D.**, ARC Centre of Excellence for Climate System Science and Climate Change Research Centre, University of New South Wales, Sydney, Australia

- Knutson, Thomas R.**, NOAA Geophysical Fluid Dynamics Laboratory, Princeton, New Jersey
- Lewis, Sophie C.**, ARC Centre of Excellence for Climate System Science and School of Earth Sciences, University of Melbourne, Melbourne, Australia
- Lin, Renping**, LASG, Institute of Atmospheric Physics, Chinese Academy of Sciences, Beijing, China
- Lyon, Bradfield**, International Research Institute for Climate and Society, Palisades, New York
- Massey, Neil**, Atmospheric, Oceanic and Planetary Physics, Department of Physics, University of Oxford, Oxford, United Kingdom, and Smith School of Enterprise and the Environment (SSEE), University of Oxford, Oxford, United Kingdom
- Mazza, Edoardo**, School of Geosciences, University of Edinburgh, Kings Buildings, Edinburgh, United Kingdom
- Michaelsen, Joel**, Climate Hazards Group, University of California Santa Barbara, Santa Barbara, California
- Mollard, James**, School of Geosciences, University of Edinburgh, Kings Buildings, Edinburgh, United Kingdom
- Mori, Masato**, Atmosphere and Ocean Research Institute, the University of Tokyo, Chiba, Japan
- Mote, Philip W.**, Oregon Climate Change Research Institute, College of Earth, Ocean, and Atmospheric Sciences, Oregon State University, Corvallis, Oregon
- Nieto, Raquel**, EPhysLab, Faculty of Sciences, Universidade de Vigo, Ourense, Spain
- van Oldenborgh, Geert Jan**, KNMI, De Bilt, The Netherlands
- Otto, Friederike E. L.**, Environmental Change Institute, School of Geography and the Environment, University of Oxford, Oxford, United Kingdom
- Park, Joseph**, NOAA/National Ocean Service (NOS), Center for Operational Oceanographic Products and Service (COOPS), Silver Spring, Maryland
- Perkins, Sarah E.**, ARC Centre of Excellence for Climate System Science and Climate Change Research Centre, University of New South Wales, Sydney, Australia
- Peterson, Thomas C.**, NOAA National Climatic Data Center, Asheville, North Carolina
- Rosier, Suzanne**, NIWA, Wellington, New Zealand, and Atmospheric, Oceanic and Planetary Physics, Department of Physics, University of Oxford, Oxford, United Kingdom
- Rowland, James**, U.S. Geological Survey, Earth Resources Observation and Science Center, Sioux Fall, South Dakota
- Rupp, David E.**, Oregon Climate Change Research Institute, College of Earth, Ocean, and Atmospheric Sciences, Oregon State University, Corvallis, Oregon
- Salas y Méliá, David**, Centre National de Recherches Météorologiques - Groupe d'Etude de l'Atmosphère Météorologique, Météo-France/CNRS, UMR3589, Toulouse, France
- Scherer, Martin**, Department of Environmental Earth System Science and Woods Institute for the Environment, Stanford University, Stanford, California
- Shiogama, Hideo**, National Institute for Environmental Studies, Ibaraki, Japan
- Shukla, Shraddhanand**, Climate Hazards Group, University of California Santa Barbara, Santa Barbara, California
- Song, Fengfei**, LASG, Institute of Atmospheric Physics, Chinese Academy of Sciences, Beijing, China
- Sparrow, Sarah**, Atmospheric, Oceanic and Planetary Physics, University of Oxford, Oxford, United Kingdom
- Stott, Peter A.**, Met Office Hadley Centre, Exeter, United Kingdom
- Sutton, Rowan**, National Centre for Atmospheric Science, Department of Meteorology, University of Reading, Reading, United Kingdom
- Sweet, William**, NOAA/National Ocean Service (NOS), Center for Operational Oceanographic Products and Service (COOPS), Silver Spring, Maryland
- Tett, Simon F. B.**, School of Geosciences, University of Edinburgh, Kings Buildings, Edinburgh, United Kingdom
- Trigo, Ricardo Machado**, IDL, Faculdade de Ciências, Universidade de Lisboa, Lisbon, Portugal
- Verdin, James**, U.S. Geological Survey, Earth Resources Observation and Science Center, Boulder, Colorado
- de Vries, Hylke**, KNMI, De Bilt, The Netherlands
- Watanabe, Masahiro**, Atmosphere and Ocean Research Institute, the University of Tokyo, Chiba, Japan
- van Westrhenen, Rudolf**, KNMI, De Bilt, The Netherlands
- Wittenberg, Andrew T.**, NOAA Geophysical Fluid Dynamics Laboratory, Princeton, New Jersey
- Woollings, Tim**, Department of Meteorology, University of Reading, Reading, United Kingdom
- Yiou, Pascal**, Laboratoire des Sciences du Climat et de l'Environnement (UMR 8212 CEA-CNRS-UVSQ) and IPSL, Gif-sur-Yvette, France
- Zeng, Fanrong**, NOAA Geophysical Fluid Dynamics Laboratory, Princeton, New Jersey
- Zervas, Chris**, NOAA/National Ocean Service (NOS), Center for Operational Oceanographic Products and Service (COOPS), Silver Spring, Maryland
- Zhang, Rong**, NOAA Geophysical Fluid Dynamics Laboratory, Princeton, New Jersey
- Zhou, Tianjun**, LASG, Institute of Atmospheric Physics, Chinese Academy of Sciences, Beijing, China

TABLE OF CONTENTS

LIST OF AUTHORS AND AFFILIATIONS.....	i
ABSTRACT	iv
1. INTRODUCTION	1
2. HUMAN INFLUENCE ON THE PROBABILITY OF LOW PRECIPITATION IN THE CENTRAL UNITED STATES IN 2012.....	2
3. LIKELIHOOD OF JULY 2012 U.S. TEMPERATURES IN PREINDUSTRIAL AND CURRENT FORCING REGIMES.....	6
4. U.S. HEAT WAVES OF SPRING AND SUMMER 2012 FROM THE FLOW-ANALOGUE PERSPECTIVE	10
5. THE EXTREME MARCH–MAY 2012 WARM ANOMALY OVER THE EASTERN UNITED STATES: GLOBAL CONTEXT AND MULTIMODEL TREND ANALYSIS.....	13
6. HURRICANE SANDY INUNDATION PROBABILITIES <i>TODAY AND TOMORROW</i>	17
7. SEPTEMBER 2012 ARCTIC SEA ICE MINIMUM: DISCRIMINATING BETWEEN SEA ICE MEMORY, THE AUGUST 2012 EXTREME STORM, AND PREVAILING WARM CONDITIONS.....	20
8. THE ROLE OF GLOBAL CLIMATE CHANGE IN THE EXTREME LOW SUMMER ARCTIC SEA ICE EXTENT IN 2012.....	23
9. THE FEBRUARY 2012 EUROPEAN COLD SPELL THAT DIDN'T BRING THE DUTCH ANOTHER 11-CITY TOUR.....	26
10. THE EXTREME EUROPEAN SUMMER 2012.....	28
11. ARE RECENT WET NORTHWESTERN EUROPEAN SUMMERS A RESPONSE TO SEA ICE RETREAT?.....	32
12. THE USE OF A VERY LARGE ATMOSPHERIC MODEL ENSEMBLE TO ASSESS POTENTIAL ANTHROPOGENIC INFLUENCE ON THE UK SUMMER 2012 HIGH RAINFALL TOTALS.....	36
13. CONTRIBUTION OF ATMOSPHERIC CIRCULATION TO WET NORTH EUROPEAN SUMMER PRECIPITATION OF 2012.....	39
14. THE RECORD WINTER DROUGHT OF 2011–12 IN THE IBERIAN PENINSULA	41
15. ATTRIBUTION OF 2012 AND 2003–12 RAINFALL DEFICITS IN EASTERN KENYA AND SOUTHERN SOMALIA.....	45
16. THE 2012 NORTH CHINA FLOODS: EXPLAINING AN EXTREME RAINFALL EVENT IN THE CONTEXT OF A LONGER-TERM DRYING TENDENCY.....	49
17. CONTRIBUTION OF ATMOSPHERIC CIRCULATION CHANGE TO THE 2012 HEAVY RAINFALL IN SOUTHWESTERN JAPAN	52
18. LIMITED EVIDENCE OF ANTHROPOGENIC INFLUENCE ON THE 2011–12 EXTREME RAINFALL OVER SOUTHEAST AUSTRALIA	55
19. AN ATTRIBUTION STUDY OF THE HEAVY RAINFALL OVER EASTERN AUSTRALIA IN MARCH 2012.....	58
20. THE ROLE OF CLIMATE CHANGE IN THE TWO-DAY EXTREME RAINFALL IN GOLDEN BAY, NEW ZEALAND, DECEMBER 2011.....	61
21. CONCLUSIONS AND EPILOGUE.....	64
REFERENCES	66

Attribution of extreme events is a challenging science and one that is currently undergoing considerable evolution. In this paper are 19 analyses by 18 different research groups, often using quite different methodologies, of 12 extreme events that occurred in 2012. In addition to investigating the causes of these extreme events, the multiple analyses of four of the events, the high temperatures in the United States, the record low levels of Arctic sea ice, and the heavy rain in northern Europe and eastern Australia, provide an opportunity to compare and contrast the strengths and weaknesses of the various methodologies.

The differences also provide insights into the structural uncertainty of event attribution, that is, the uncertainty that arises directly from the differences in analysis methodology. In these cases, there was considerable agreement between the different assessments of the same event. However, different events had very different causes. Approximately half the analyses found some evidence that anthropogenically caused climate change was a contributing factor to the extreme event examined, though the effects of natural fluctuations of weather and climate on the evolution of many of the extreme events played key roles as well.

I. INTRODUCTION

THOMAS C. PETERSON, PETER A. STOTT, STEPHANIE C. HERRING, AND MARTIN P. HOERLING

One of us distinctly remembers in graduate school when a professor put the first ever satellite image of a tropical cyclone on the screen and explained various features of the storm. Then he proceeded to editorialize by pointing out that someone wrote his entire PhD dissertation based on this one image and how we started graduate school too late because all the easy projects have been done. Now with decades of definitely not easy scientific analyses under our collective belts, we can look back and realize how wrong the professor was. The “easy” science of decades ago only looks easy now because its results seem obvious. Their work was difficult then and our work is difficult now.

However, among the difficult work we have before us, a few grand challenges arise. These are challenges (i) that have specific barriers preventing progress, (ii) where targeted research efforts would have the likelihood of significant progress over the next 5–10 years, (iii) that have measurable performance metrics, (iv) that can be transformative, (v) that are capable of capturing the public’s imagination, and (vi) that can offer compelling storylines (WCRP 2013). The World Climate Research Programme (WCRP) has identified six grand challenges that meet these criteria. Prediction and attribution of extreme events is one of them. It is gratifying to see that scientists from across the world are taking on this grand challenge. This includes the scientists that contributed to this collection of analyses, which assess the causes for 12 specific extreme events that took place around the world in 2012 (Fig. 1.1).

Extreme climate-related events command attention, and these are increasingly demanding prompt and credible scientific explanations. Last year’s paper, “Explaining Extreme Events of 2011 from a Climate Perspective” (Peterson et al. 2012), which was published as an article in the July issue of *BAMS*, is, at the time of this writing, the “most read” article of the previous 12 months from any AMS journal (AMS 2013), attesting to a broad

interest not only in the wider audience of the public, policy makers, and stakeholders, but also within the scientific community itself. One of the more interesting questions in response to the article was, “If you can attribute an event to specific forcings, could the event have been anticipated?” The answer depends on whether the particular forcing is itself predictable and whether the forcing altered the odds of the event happening or altered its intensity. From the practical perspective of being able to foresee the event and perhaps thereby mitigate its effects, the specificity with which forcing can explain the precise timing and location for an event is critical. Prediction and attribution are thus seen as related challenges. “Attribution of 2012 and 2003–12 Rainfall Deficits in Kenya and Somalia” (in this report) explains a drought that was, indeed, predicted and thereby facilitated prepositioning of humanitarian assistance.

Another interesting question that arose in response to last year’s paper was, “Are you able to attribute extremes in terms of costs, both in money and in lives?” No attribution of costs or lives to climate variability and change was performed for last year’s or this year’s report. That work can come later and is quite complex involving both the domains of social scientists and atmospheric scientists. For example, it would require consideration of preparations before and during an extreme event and the extent to which such preparations were informed by the predictability of the event and the capability of the people affected to use such information. Additionally, the cost of past

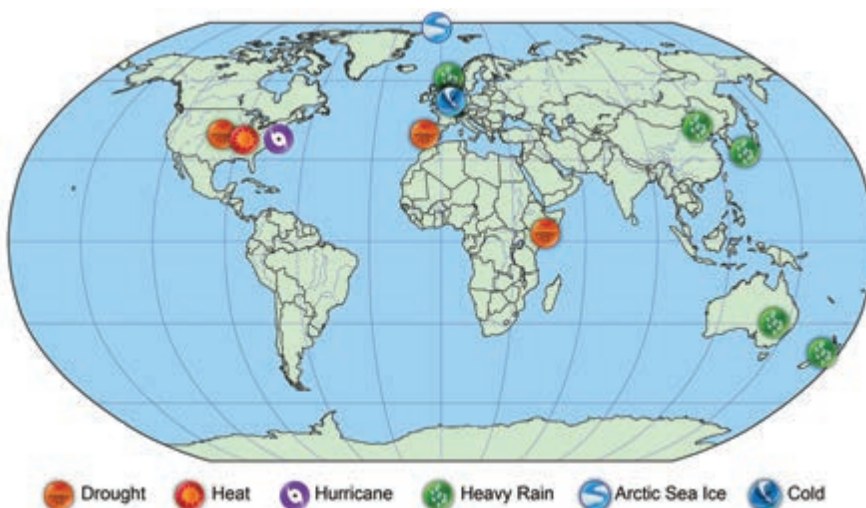


FIG. 1.1. Location and type of events analyzed in this paper.

adaptation that reduced the vulnerability to an extreme event might need to be factored in as well. The work in these pages, however, can guide such analyses as well as help determine what the appropriate responses are to the particular extremes examined.

Extreme events, by definition, can be both rare at any given location and common in a global sense. In any one place, the chance of a once in a 100-year heat extreme is so rare that, in principle, it only occurs, on average, once every 100-years. This also means that, on average and with a stationary climate, every year one percent of the world would be expected to experience a once in a 100-year heat extreme and one percent a cold extreme. On the other hand, a few extremes such as an EF-5 tornado are rare even in a global sense, while other extremes such as loss of sea ice are limited to specific regions. The fact that “The Extreme March–May 2012 Warm Anomaly over the Eastern United States: Global Context and Multimodel Trend Analysis” (in this report) found 15.3% of the world experiencing its first, second, or third warmest year, while no grid box experienced their first, second, or third coldest year implies that expectations based on the assumption of a stationary climate may no longer be fully applicable.

Hurricane Sandy is an example of an extreme event that required many different factors to come together to create the major impacts that it did (NOAA 2013a). Therefore, Sandy is probably one of the most difficult extreme events of 2012 to fully explain. One group, however, assessed how a storm like Sandy occurring in 2012 may have inflicted greater impacts this past year than it would have had the sea level been at the height it was a half century earlier (see “Hurricane Sandy Inundation Probabilities *Today and Tomorrow*” in this report). Hurricane Sandy, given its meteorological complexity and its great importance as a societal

watershed event in the United States, provides but one example of an extreme event from 2012 that will continue to require ongoing, careful, and detailed assessment.

Such work will be critical toward meeting the grand challenges outlined earlier, even if such studies do not appear in this issue owing to our tight space and time constraints. In order for papers in this report to be of interest to a wide variety of readers and not create an excessively long report, each submission was limited to 1500 words and two figures. Additionally, in order to go through peer-review and be published with the September issue of *BAMS*, while people are still interested in extreme events of the previous year, we had to submit our paper for peer-review by the middle of April. We moved the month of publication from July to September to help accommodate the research needs required for conducting thorough and rigorous assessments of events having occurred as recently as 2012. Yet, this timeline was still a considerable challenge for all the authors; as computers, software, and suddenly arising urgent demands on scientists’ time do not always pay attention to one’s plans. Despite these various constraining aspects, each paper has been subjected to critical peer-review.

In last year’s paper, six groups explained six different extremes. This year 18 different groups wrote 19 analyses explaining 12 different extreme events. Because four extreme events, high temperatures in the United States; record low levels of Arctic sea ice; and heavy rain in northern Europe, and eastern Australia, were each assessed by at least two different groups, this year we gain the added benefit of being able to compare and contrast the results of different types of analyses and from that improve our understanding of the potential error bars associated with the grand challenge of extreme event attribution.

2. HUMAN INFLUENCE ON THE PROBABILITY OF LOW PRECIPITATION IN THE CENTRAL UNITED STATES IN 2012

DAVID E. RUPP, PHILIP W. MOTE, NEIL MASSEY, FRIEDERIKE E. L. OTTO, AND MYLES R. ALLEN

Introduction. The contiguous United States experienced a severe drought in 2012, which by August of that year had become the most extensive since the 1950s, with more than half of all counties in the United States (spread among 32 states) listed as natural disaster areas by the U.S. Department of Agriculture ([\[drought-fast-track-designations-080812.pdf\]\(http://www.usda.gov/documents/usda-drought-fast-track-designations-080812.pdf\)\). For much of the central United States, such conditions of combined scarcity of precipitation and elevated temperature had not been experienced since the Dust Bowl years of 1934 and 1936 \(Fig. 2.1\).](http://www.usda.gov/documents/usda-</p></div><div data-bbox=)

A useful and general definition of drought is demand exceeding available water supply over a pro-

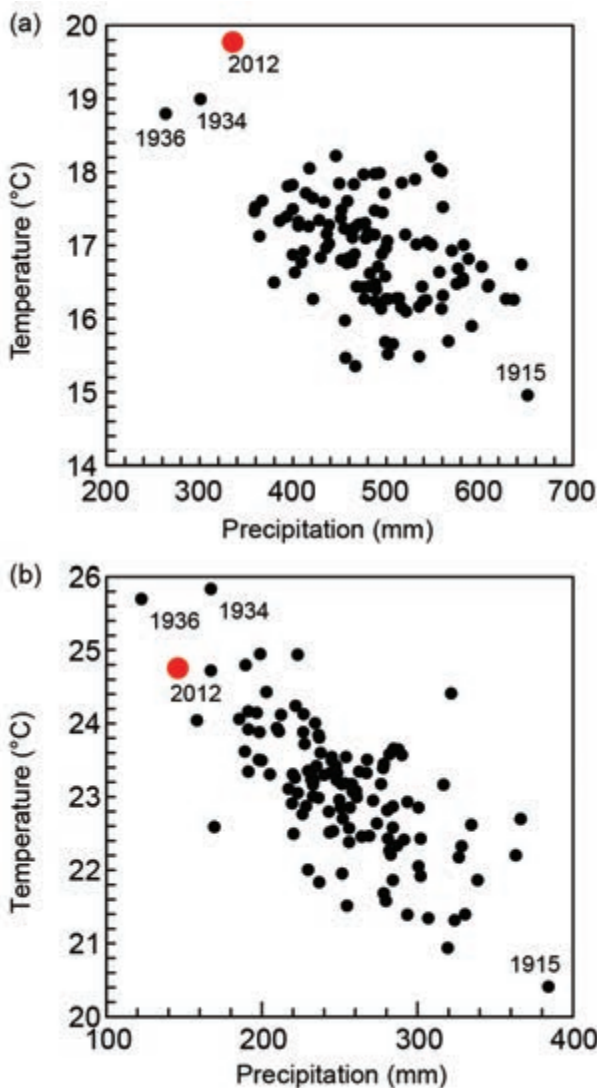


FIG. 2.1. Mean observed temperature against total observed precipitation for the central United States (CO, NE, KS, OK, IA, MO, AR, and IL) during the (a) growing season (MAMJJA) and (b) summer (JJA).

longed period (e.g., Redmond 2002). Increased surface heating due to increased greenhouse gas (GHG) concentrations directly affects the hydrological cycle, and thus, may alter both the demand and supply side of this equation. The recent Intergovernmental Panel on Climate Change (IPCC) report on climate extremes states that there is medium confidence that the central United States will experience an increase in duration and intensity of drought, driven in part by longer periods without precipitation (Seneviratne et al. 2012). The net anthropogenic effect on total precipitation, however, is unclear, as possible decreased frequency may be balanced by increased precipitation intensity (Trenberth et al. 2007), though projections from Coupled Model Intercomparison Project phases

3 and 5 (CMIP3 and CMIP5) simulations show a general trend into the 21st century toward slightly higher precipitation in spring and lower precipitation in summer for the central United States (Sheffield and Wood 2008; Scheff and Frierson 2012).

Here we focus solely on a dominant control of the supply side of this equation: precipitation. We explore, in particular, the effect of anthropogenic GHG emissions on the probability distributions of growing season and summer season precipitation in the year 2012. (For a discussion of the various factors contributing to the 2012 drought, see Hoerling et al. 2013, manuscript submitted to *Bull. Amer. Meteor. Soc.*) Our methodology is similar to Pall et al. (2011) in which very large ensembles of climate simulations from GCMs are generated under contrasting scenarios and where the generation of such large ensembles becomes feasible through the use of public-volunteered distributed computing (Allen 1999; Massey et al. 2006). Having such large ensembles permits the analysis of the distribution tails of climate variables and not simply the average response to anthropogenic activity. Here we analyze the return periods of low precipitation over the central United States for 2012 under two scenarios: actual forcing and natural-only forcing.

Data and methods. Values of observed monthly precipitation for the years 1895–2012 were obtained from the U.S. National Climatic Data Center (NCDC) Climate at a Glance dataset (<ftp://ftp.ncdc.noaa.gov/pub/data/cirs/>). The values were spatially averaged over eight states that were strongly afflicted by the drought: Colorado, Nebraska, Kansas, Oklahoma, Iowa, Missouri, Arkansas, and Illinois.

We used the UK Meteorological Office’s Had-AM3P atmospheric circulation model (Pope et al. 2000; Gordon et al. 2000; Jones et al. 2004; $1.875^\circ \times 1.25^\circ$, 19 levels, 15-minute time step) to simulate the atmospheric and land-surface climate from December 2011 through November 2012 under two distinct scenarios. In the first (which we refer to as “All Forcings”), atmospheric gas concentrations were set to actual concentrations during the period in question and the SST and sea ice boundary conditions were derived from the Operational Sea Surface Temperature and Sea Ice Analysis (OSTIA; Stark et al. 2007). In the second scenario (“Natural Forcings”), preindustrial era atmospheric gas concentrations were assumed, while the solar irradiance and volcanic aerosols were kept the same as for the “All Forcings” scenario. We also derived SSTs and sea ice fractions consistent with a “natural analog” of the world in 2012 absent increased

greenhouse gases in the following manner. A pattern of SST changes due to anthropogenic emissions was estimated by using members of the HadGEM2-ES ensemble submitted to CMIP5. The monthly SSTs in the modeled year 2012 for a single member from the “Natural” ensemble were subtracted from the corresponding SSTs in a single member from the “All Forcings” ensemble (e.g., see the second figure in “The Use of a Very Large Atmospheric Model Ensemble to Assess Potential Anthropogenic Influence on the United Kingdom Summer 2012 High Rainfall Totals” in this report). This resulting pattern of modeled SST changes was then subtracted from the observed OSTIA SST pattern. The net increase in SST from the “Natural” to the “All Forcings” scenarios was 0.5°C averaged over the period December 2011 to August 2012 and between 70°S and 70°N. Globally, the area covered by sea ice was decreased by 8.9% averaged over the same period.

Baseline initial conditions for each of the two scenarios were taken as the final conditions from simulations like those described above, but for the period, December 2010 through November 2011 and with “All Forcings” SSTs derived from the HadISST observational dataset (Rayner et al. 2003). To generate an ensemble of runs, the baseline initial conditions were subjected to random perturbations to generate an ensemble of initial conditions. (It is worth mentioning that for our study domain, temperature and precipitation show no memory, via correlation, of the December 2011 initial atmospheric conditions by February 2012). We used all ensemble members that were available by the time of this writing (183 and 428, for the “Natural” and “All Forcings” scenarios, respectively).

Precipitation was spatially averaged over the 66 GCM grid boxes that fell within the study domain (i.e., the eight states listed above), with weights proportional to the cosine of the latitude. The return period for growing (MAMJJA), spring (MAM), and summer (JJA) season precipitation from each ensemble member was calculated, and bootstrapping was used to estimate the 2.5% and 97.5% confidence limits. Regional HadAM3P biases (e.g., Rupp et al. 2012) preclude direct estimation of the return period of the actual 2012 precipitation in a nonstationary setting. We attempted no model bias correction because our objective at this stage was simply to examine relative changes in the entire modeled probability distribution due to anthropogenic forcing; biases, being approximately equivalent in each scenario, should thus, cancel each other in the difference.

Results and discussion. We found no statistically significant differences in the dry tail (> five-year return period) of the distributions of spring or summer precipitation between the “Natural” and “All Forcings” scenarios (Figs. 2.2a-c). However, there was a detectable shift in the center of the distributions. For example, the “All Forcings” scenario gave decreased median precipitation by 6% and 11% in spring and summer, respectively. This decrease occurred with a concomitant positive shift of 1.7°C or 1.6°C across the distributions of spring and summer temperature, respectively, between the “Natural” and “All Forcings” scenarios (results not show). The absence of a detectable signal in the tail of the precipitation distribution may in part be associated with the sample size. However, it is not merely a matter of the 95% confidence intervals from each scenario overlapping; the empirical distributions from the “Natural” and “All Forcings” runs converge at return periods greater than about 10 years. Consequently, weakening the significance criteria (e.g., decreasing the confidence intervals from 95% to 67%) would not lead to a separation of the confidence intervals in the tail between 10- and 50-year return periods. Beyond 50 years, inferences cannot be made with confidence due to the sample size of the “Natural Forcings” dataset.

The implication is that human alteration of the atmospheric composition may have had little effect on the frequency of low-precipitation periods. This leads us to hypothesize that if there are consequential changes to the hydrological cycle driving extreme dryness at seasonal scales, they will not be to rates of input, but to rates of output, via evaporative demand with increased surface warming. However, a recent GCM-based study using improved land surface representation suggests the effects of warming on drought in the central United States will be modest (Hoerling et al. 2012a).

Our findings are generally consistent with two studies of the severe drought/heat wave that occurred in the region of Texas and Oklahoma in 2011 (Hoerling et al. 2013a; Rupp et al. 2012). Using methods different from those used in this study, both found little or no change in precipitation likelihood due to anthropogenic GHGs. It is also worth pointing out that observational records indicate long-term trends of slight increases in annual precipitation over the central United States since the beginning of the 20th century (McRoberts and Nielson-Gammon 2011).

The lack of a detectable anthropogenic signal argues that the unconditional return period of the 2012 precipitation total could be estimated simply

by traditional means of fitting theoretical probability distributions to the observed data. For the purposes of discussion only, we fitted, as an example, a generalized extreme value (GEV) distribution to the observations, which resulted in return periods of approximately 40 years and 100 years for precipitation totals as low as those experienced in 2012 for the growing season and summer, respectively (Figs. 2.2d,f).

It merits mention that though the simulated (“All Forcings”) and observed tails of the distributions were

similar in spring (Figs. 2.2b,e), they differed notably in summer (Figs. 2.2c,f). For example, in summer the 10-year return period anomaly was about -40% and -25% in the simulations and observations, respectively. While we would not expect the distributions to be identical given the modeled distributions are conditional on the SST patterns in 2011–12 only, the bias could indicate a deficiency in the model that may, possibly to an important extent, affect the model’s regional response to greenhouse forcing.

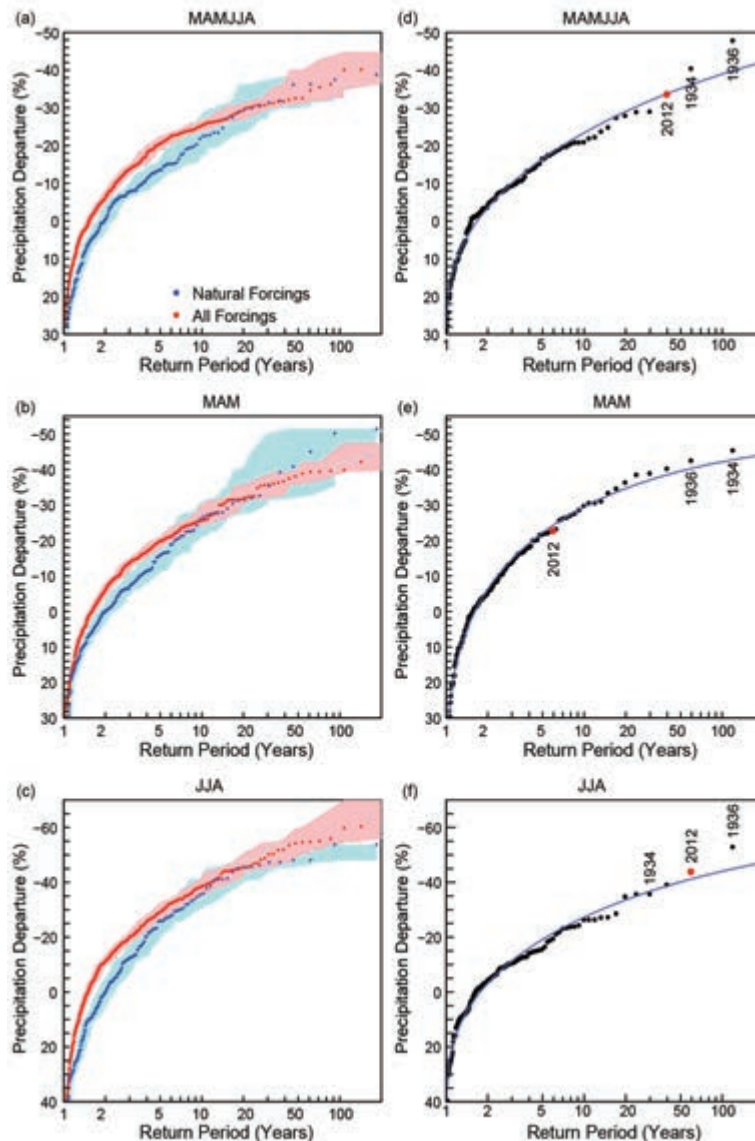


FIG. 2.2. Return period of simulated (a) MAMJJA, (c) MAM, and (b) JJA precipitation for the year 2012 over the central United States with 95% confidence intervals (shaded). Simulations were from Had-AM3P with “Natural Forcings” and “All Forcings.” Return period of observed (d) MAMJJA, (e) MAM, and (f) JJA precipitation. The blue line shows a fitted GEV distribution. For the simulations, precipitation departure is calculated as the departure from the ensemble mean of the “Natural Forcings” scenario. For the observations, it is the departure from the 1895–2012 average.

Lastly, we emphasize that these conclusions are based on a single pattern of SST changes that were developed from a GCM to create the “Natural” scenario. It is possible, for example, that while overall global warming could increase the likelihood of periods of very low precipitation in the region, the lack of change in precipitation between the two scenarios may have

arisen because of the particular spatial pattern of differential warming/cooling of SSTs that was imposed. We expect to test this hypothesis through an ensemble of SST changes derived from various CMIP5 ensemble members. In conclusion, these results should not stand alone but form one step towards a comprehensive analysis of the causes of the 2012 U.S. drought.

3. LIKELIHOOD OF JULY 2012 U.S. TEMPERATURES IN PREINDUSTRIAL AND CURRENT FORCING REGIMES

NOAH S. DIFFENBAUGH AND MARTIN SCHERER

“The Event”: July 2012 heat in the United States. The year 2012 was the warmest on record in the United States (NOAA 2013b), due in part to extremely high temperatures over much of the central and eastern United States during spring and summer. The summer heat was associated with one of the most severe droughts on record (Hoerling et al. 2013, manuscript submitted to *Bull. Amer. Meteor. Soc.*; Hoerling et al. 2013b). A suite of impacts has been ascribed to the drought and associated summer heat, including low (or even zero) crop yields (USDA 2013a), low livestock inventory (USDA 2013b), sharp increases in commodity prices (USDA 2013c), and at least 123 direct human deaths (with the number of additional deaths from heat stress not yet quantified) (NOAA 2013c). While much of the United States experienced severe heat during various periods of the summer, the month of July was the warmest on record for the contiguous United States, while June was the eighth warmest and August the thirteenth (NOAA 2013b).

The likely proximal causes of the summer 2012 severe heat were changes in the surface energy balance caused by severe rainfall deficits and the large-scale atmospheric conditions that contributed to those rainfall deficits (Hoerling et al. 2013, manuscript submitted to *Bull. Amer. Meteor. Soc.*; Hoerling et al. 2013b). Midlatitude severe heat events often co-occur with rainfall deficits (Madden and Williams 1978; Namias 1982; Hoerling et al. 2013a) and the associated atmospheric conditions and changes in surface energy balance that act to reinforce dry, hot conditions at the surface. These include positive geopotential height anomalies in the mid-troposphere (e.g., Chang and Wallace 1987; Meehl and Tebaldi 2004; Pal et al. 2004; Fischer et al. 2007a), which result in anticyclonic circulation anomalies and a relatively stable atmosphere, leading to decreased cloudiness and decreased

precipitation along with decreased input of moisture and increased input of solar radiation at the surface. Such events are also often associated with negative soil moisture anomalies (e.g., Hong and Kalnay 2000; Schubert et al. 2004; Fischer et al. 2007b; Seneviratne et al. 2010; Hirschi et al. 2011; Quesada et al. 2012), which result in decreased surface evapotranspiration, leading to decreased latent cooling and increased surface air temperature. In addition, because surface moisture and temperature are influenced by precipitation and solar radiation, and because geopotential height is influenced by surface temperature, land-atmosphere coupling can amplify the severity of hot events (e.g., Fischer et al. 2007a,b). We, therefore, analyze the July 2012 circulation and soil moisture anomalies along with the surface temperature anomalies.

Quantifying the likelihood of a 2012-magnitude event.

We use the Coupled Model Intercomparison Project Phase 5 (CMIP5) GCM experiments (Taylor et al. 2012) to quantify the likelihood of a 2012-magnitude event in the current and preindustrial forcing regimes. We define “a 2012-magnitude event” as the July 2012 anomaly from the 1979–2011 July mean. We use reanalysis to define the event, which allows us to quantify the frequency of anomalies in surface air temperature, 500-hPa geopotential height, and 0 cm–200 cm soil moisture within a framework that is physically consistent between the three variables and with the GCM calculation for the 1979–2011 (“20C”) and preindustrial (“PI”) forcing regimes. [The July 2012 temperature event is similar in National Centers for Environmental Prediction (NCEP), ERA-Interim, and observations; Supplementary Fig. S3.3 and S3.4.] In order to normalize across CMIP5 realizations of different lengths (Supplementary Table S3.1), we divide the CMIP5 20C and PI time series into 33-year

subperiods, yielding an ensemble of 24 20C periods and 134 PI periods. This subperiod length is chosen arbitrarily to be the length of the period from 1979 (the start of the satellite era, when we have higher confidence in the reanalysis) through 2011 (the year prior to the 2012 event). Before subdividing the CMIP5 time series, we bias-correct the mean and variability of the CMIP5 time series using the reanalysis values. (See Supplementary material for further details.)

How rare was July 2012 in the current forcing regime? The July 2012 temperature anomalies exceeded 1.6°C over much of the northern United States, with peak anomalies exceeding 4.0°C over the central United States (Fig. 3.1a). The temperature anomalies were outside the bounds of the 1979–2011 reanalysis over much of the northern Great Plains, Midwest, and Northeast (Fig. 3.1d and Supplementary Figs. S3.1, and S3.4) and outside the bounds of the last century

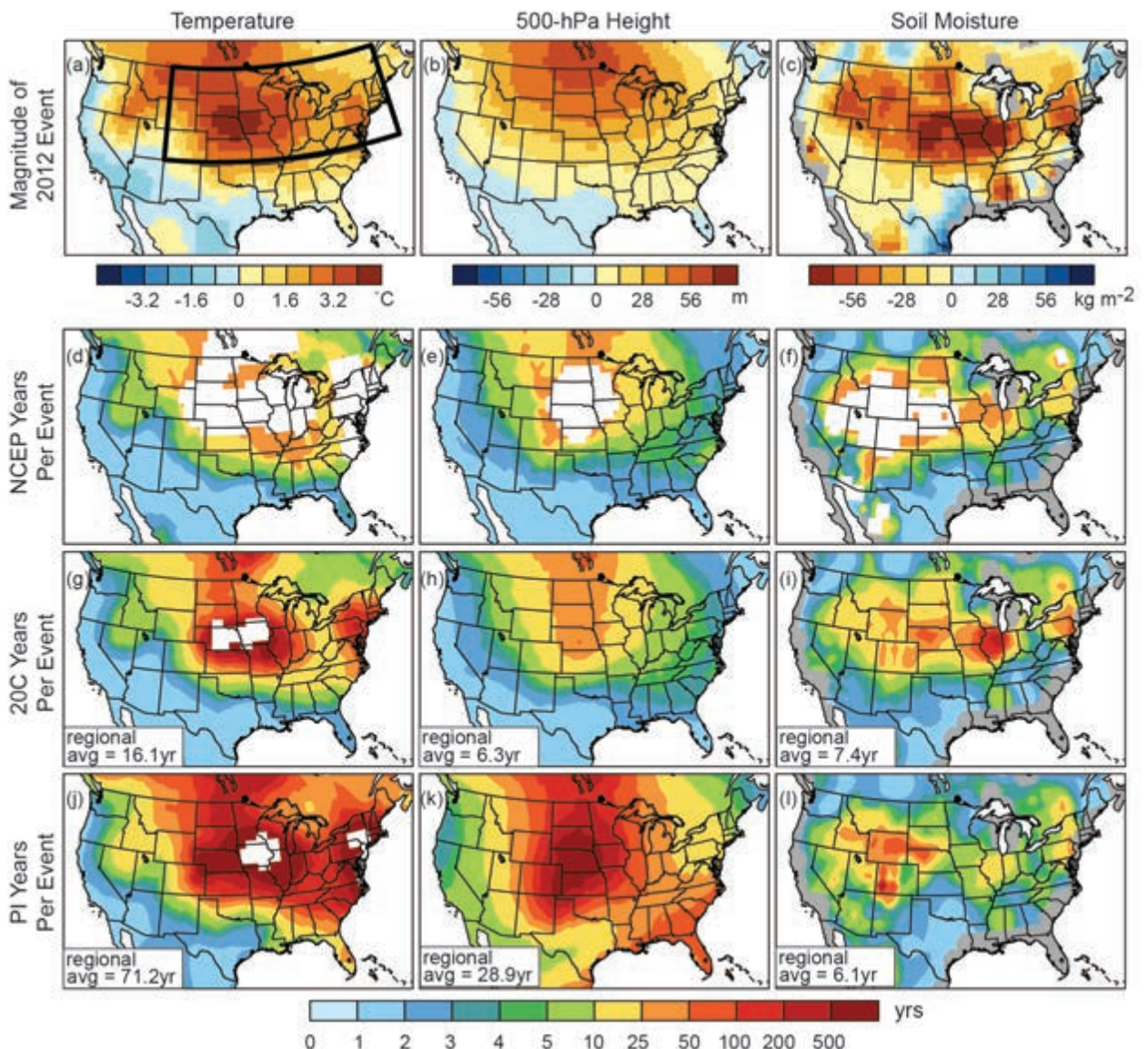


FIG. 3.1. The likelihood of a 2012-magnitude event. Top row shows the magnitude of the Jul 2012 event as an anomaly from the 1979–2011 mean. Other rows show the mean number of years required to achieve an event of the Jul 2012 magnitude in the 1979–2011 period of NCEP (second row), the 1979–2011 period (20C) of CMIP5 (third row), and the preindustrial period (PI) of CMIP5 (bottom row). White areas show where no event occurred in any 33-year period in any realization. Box in the upper left panel shows the region that is used in Fig. 3.2. The “regional avg” in (g)–(l) indicates the mean number of years required to achieve a 2012-magnitude event for the grid points within the regional box. White areas are ignored in the regional calculations in (g)–(l). See Online Supplemental material for details of the ensemble analysis.

of observations over much of the Midwest and Northeast (Supplementary Fig. S3.3). Likewise, the 500-hPa height anomalies were outside the bounds of the 1979–2011 reanalysis over much of the northern Great Plains (Fig. 3.1e and Supplementary Figs. S3.1, and S3.4) as were the soil moisture anomalies over areas of the Great Plains and Mountain West (Fig. 3.1f and Supplementary Figs. S3.1, and S3.4).

In contrast, the July 2012 temperature, 500-hPa geopotential height, and soil moisture anomalies were not outside the bounds of the 1979–2011 forcing regime over most of the United States (Figs. 3.1g, 3.1h, and 3.1i), suggesting that climate variability within the current forcing played an important role in the event. However, the temperature anomalies were a century-scale event over much of the north-central and northeastern United States (Figs. 3.1g, 3.1h, and 3.1i) and were far more rare (regional mean of 16.1 years per event) than either the geopotential height anomalies (6.3 years per event) or soil moisture anomalies (7.4 years per event). [The relative rarity of the July 2012 temperatures is also clearly revealed in the probability density functions (PDFs) of grid-point anomalies; Fig. 3.2.]

Is the likelihood of a 2012-magnitude event different in the current and preindustrial forcing regimes? Comparison of the CMIP5 20C and PI experiments reveals that a 2012-magnitude temperature event occurs more frequently in the current forcing than in the preindustrial forcing over almost all areas of the United States (Figs. 3.1g and 3.1j). The mean occurrence is more than four times as frequent in the 20C period over

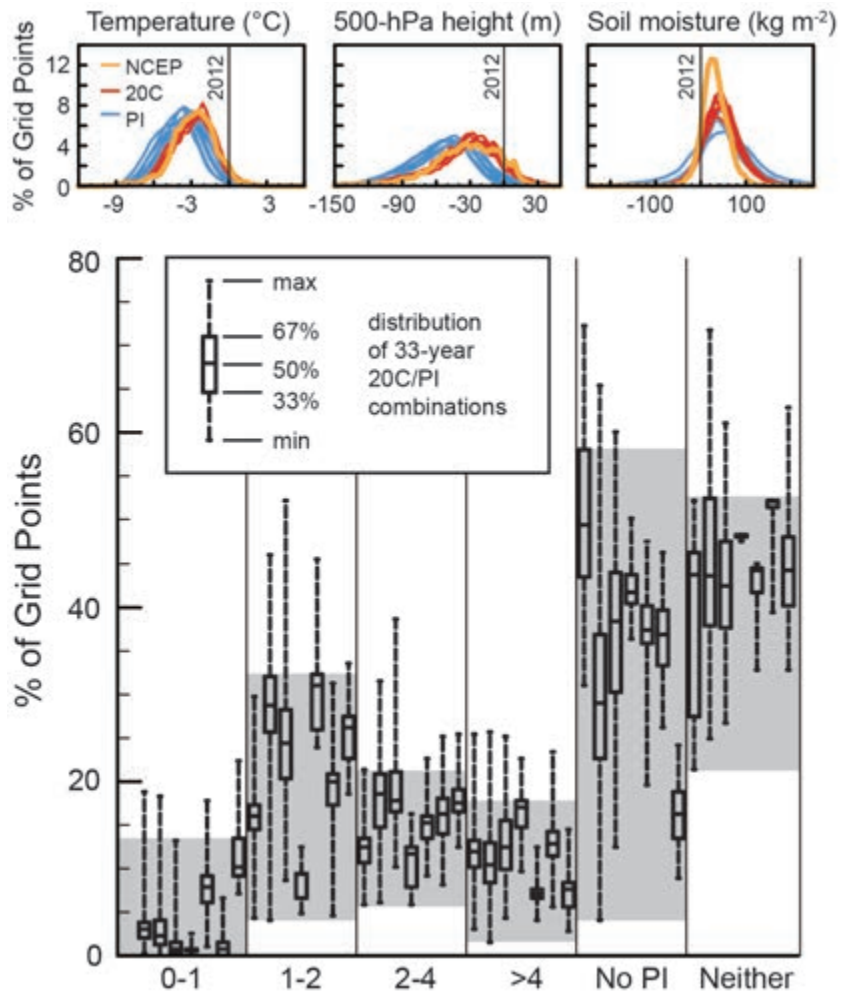


FIG. 3.2. (Top) Anomalies from the Jul 2012 mean in the 1979–2011 period of NCEP, the 1979–2011 period of CMIP5 (20C), and the preindustrial period of CMIP5 (PI), calculated over the north-central and northeastern United States (37°N–49°N, 251°E–290°E). (Bottom) The difference in the frequency of occurrence of a Jul 2012 temperature event over the north-central and northeastern United States between the PI and 20C forcings. The difference is calculated by comparing the occurrence at each grid point in all possible combinations of 33-year 20C and PI periods from each CMIP5 model, enabling probabilistic quantification of the likelihood that a 33-year period in the 20C forcing yields a different frequency of occurrence than a 33-year period in the PI forcing. The percentage of grid points are binned by magnitude of difference, calculated as the number of occurrences in the 20C period divided by the number of occurrences in the PI period for which there was at least one occurrence in the PI period. The “No PI” bin includes grid points where there was at least one event in the 1979–2011 period but no event in the preindustrial period. The “Neither” bin includes grid points where there was no event in either the 1979–2011 or PI period. Each box-and-whisker shows the distribution of grid point values in a given CMIP5 model in a given magnitude bin. The gray field in each bin encompasses the lowest 67% of values in 100% of the CMIP5 models. For example, between 4% and 33% of grid points exhibit a 2012-magnitude temperature event one to two times as frequently in the 20C forcing in at least 67% of the 33-year period combinations of 100% of the CMIP5 models.

the north-central and northeastern United States (Figs. 3.1g and 3.1j), with large areas requiring a mean of greater than ten 33-year PI periods to achieve a 2012-magnitude temperature event but a mean of less than five 33-year 20C periods (Supplementary Fig. S3.2). The mean occurrence of the 2012-magnitude geopotential height is also more than four times as frequent in the current forcing than the preindustrial forcing (Figs. 3.1h and 3.1k), with large areas of the central United States requiring a mean of greater than ten PI periods but less than two 20C periods (Supplementary Fig. S3.2). In contrast, most areas of the north-central and northeastern United States exhibit greater frequency of a 2012-magnitude soil moisture event in the preindustrial forcing (Fig. 3.1i) than in the current forcing (Fig. 3.1l). However, the soil moisture anomalies should be viewed with caution, as different reanalysis datasets exhibit different patterns and magnitudes of anomalies across the United States (Fig. 3.1, and Supplementary Fig. S3.4), and there is greater discrepancy between the reanalysis and 20C simulations for soil moisture than for temperature or geopotential height (Fig. 3.2, and Supplementary Fig. S3.4). (We note that a 2012-magnitude soil moisture event occurs more often in the 20C simulations than in the PI simulations over much of the western United States in both reanalysis datasets that we evaluate; Fig. 3.1, and Supplementary Fig. S3.4.)

Like the regional mean (Figs. 3.1g and 3.2), the PDF of grid-point anomalies reveals a shift towards more frequent occurrence of 2012-magnitude temperatures over the north-central and northeastern United States in the 20C simulations (Fig. 3.2). To quantify the difference in likelihood of a 2012-magnitude temperature event over this region, we compare the fractional difference in occurrence between all possible combinations of 33-year periods in the CMIP5 PI and 20C simulations (Fig. 3.2). Following the Intergovernmental Panel on Climate Change (IPCC) uncertainty guidance (Mastrandrea et al. 2011), we frame this analysis around a likelihood threshold of 67%. This probabilistic analysis reveals >67% likelihood that a 2012-magnitude temperature event is more frequent in the PI forcing over less than 14% of the grid points. In addition, there is >67% likelihood that a 2012-magnitude temperature event is one to two times as frequent in the 20C forcing over 4%–33% of the grid points, two to four times as frequent in the 20C forcing over 6%–21% of the grid points, and more than four times as frequent in the 20C forcing over

2%–18% of the grid points. Further, there is >67% likelihood that 4%–58% of the grid points would experience a 2012-magnitude temperature event in a 33-year period of the current forcing but not in a 33-year period of the preindustrial forcing. However, there is also >67% likelihood that 21%–52% of the grid points would not experience a 2012-magnitude event in a given 33-year period of the current forcing.

Conclusions. Our analyses of the CMIP5 global climate model ensemble suggest that the likelihood of extreme July temperature anomalies is greater in the current forcing than in the preindustrial forcing. In particular, the mean occurrence of 2012-magnitude temperatures is more than four times as frequent over the north-central and northeastern United States in the current forcing. The mean occurrence of 2012-magnitude geopotential height anomalies is also more than four times as frequent, suggesting increased likelihood of the atmospheric conditions that often occur in conjunction with severe heat at the surface. Further, although there are important uncertainties in the soil moisture conditions, the July 2012 soil moisture anomalies were substantial within the context of the past three decades, and the May–July precipitation was “much below normal” over much of the central United States (NOAA 2013b), suggesting that surface drying could have amplified the temperature event (as in Fischer et al. 2007b; Quesada et al. 2012). The role of changes in ocean conditions (e.g., Supplementary Fig. S3.5) requires further investigation.

The CMIP5 simulations also suggest that the July 2012 temperatures remain a century-scale event over large areas even in the current forcing regime. Indeed, it is very likely (Mastrandrea et al. 2011) that more than a fifth of the north-central and northeastern United States would not experience a 2012-magnitude event in a given 33-year period of the current forcing. The continued rarity of the July 2012 temperatures in the current forcing regime likely arises from the fact that record rainfall deficits played a critical role in shaping the 2012 severe heat. Given the considerably lower signal-to-noise ratio of the summer precipitation response to global warming over the central and eastern United States (relative to the summer temperature response; e.g., Diffenbaugh et al. 2011), occurrence of the most severe heat events is likely to continue to be strongly regulated by rainfall variability.

4. U.S. HEAT WAVES OF SPRING AND SUMMER 2012 FROM THE FLOW-ANALOGUE PERSPECTIVE

JULIEN CATTIAUX AND PASCAL YIOU

Introduction. The contiguous United States experienced extremely high temperature anomalies during the year 2012, especially during spring and summer east of the Rocky Mountains (Fig. 4.1, top). This exceptional heat wave, causing important socio-environmental damages due to the heat stress, was associated with a severe drought, additionally accounting for the spreading of wildfires over broad regions. We aim to put such an episode in the context of

longer-term climate variability and change. However, this piece should be viewed as a “process-attribution” analysis rather than a formal attribution study (e.g., an evaluation of the anthropogenic fingerprint). Our focus is on the contribution of atmospheric circulation to the U.S. heat wave of spring-summer 2012, which we evaluate through a flow-analogue approach similar to the analysis of 2011 European temperatures by Cattiaux and Yiou (2012; hereafter CY12).

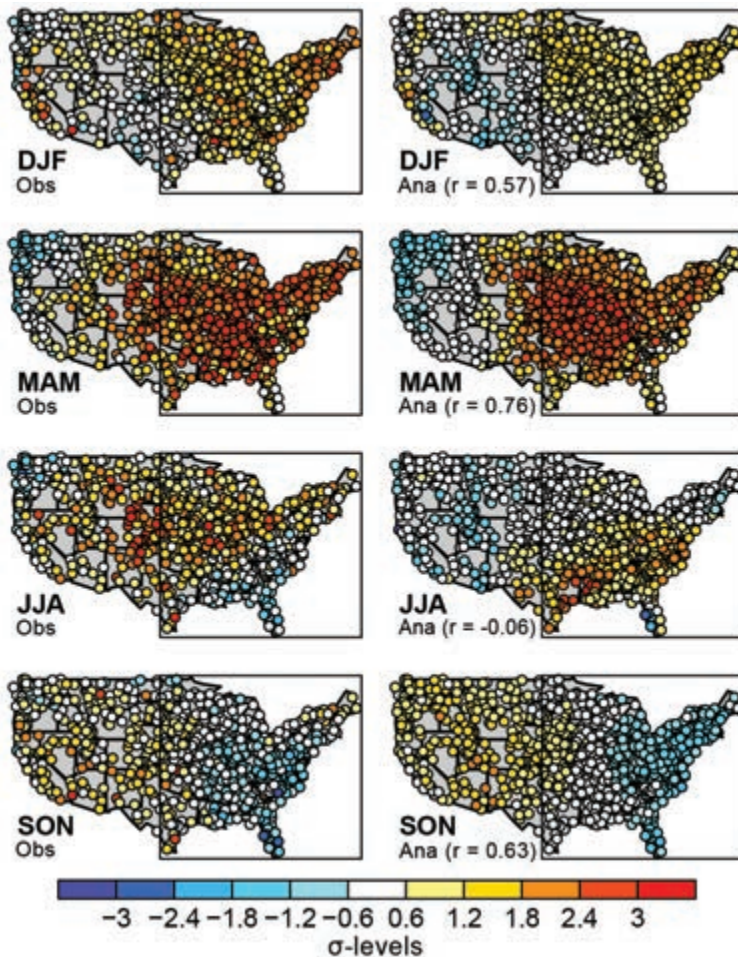


FIG. 4.1. (Left column) Observed temperatures of winter (DJF months), spring (MAM), summer (JJA), and autumn (SON) 2012, represented as normalized anomalies (σ -levels) relative to 1971–2000 climatological standards at each station. The box over the eastern United States encompasses the area retained for regionally averaged statistics throughout the paper (171 stations over 306). (Right column) The same for analog temperatures. Correlations with observed patterns are indicated in parentheses.

Data and methods. As the flow-analogue approach requires daily data, we use daily temperature observations from the Global Historical Climatology Network (GHCN Version 3.01; <http://www.ncdc.noaa.gov/oa/climate/ghcn-daily/>) over more than 1218 U.S. stations, together with daily reanalyses of sea level pressure (SLP) provided by NCEP/NCAR (<http://www.esrl.noaa.gov/psd/data/gridded/data.ncep.reanalysis.html>) over the period 1948–2012. Although GHCN daily data are not adjusted to account for inhomogeneities (Caussinus and Mestre 2004), we only consider values having passed all quality checks so that their monthly averages closely fit monthly temperatures homogenized over the United States by Menne et al. (2009; USHCN Version 2.5; <http://www.ncdc.noaa.gov/oa/climate/research/uschn>), albeit slightly underestimating the recent warming (not shown). Unless otherwise specified, the following monthly or seasonal temperature statistics are, therefore, not altered by the need of using daily data for analogues. We retain 801 USHCN stations on the basis of (i) an altitude lower than 2000 m, (ii) the availability of more than 90% of daily values over the period 1948–2012, and (iii) only one station per $0.5^\circ \times 0.5^\circ$ box for spatial homogeneity (the one with the more data for 2012). These criteria are similar to those of CY12 for European stations and do not materially impact

our results. Finally, we compute anomalies relative to 1971–2000 climatological standards [mean and standard deviation (σ)]. Albeit similar results were obtained from daily minimum temperatures (not shown), we focus our analysis on daily maximum temperature, generally occurring in daytime.

How exceptional was 2012 in the United States? Over the United States, the year 2012 was characterized by anomalously high maximum temperatures persisting from the beginning of winter (including December 2011) to the end of summer over the major part of the country, followed by a slightly colder than normal autumn (Fig. 4.1, left). The amplitude of these anomalies was stronger over the eastern part of the country (box in Fig. 4.1), where, on average over all stations, all monthly temperatures were above normal with the exception of October 2012. Hence, 2012 constitutes the hottest calendar year on record over our period of study (1948–2012), while October 2011–September 2012 establishes the absolute warm

record for a 12-month period. In particular, two monthly records were broken in March and July 2012, with exceptional widespread departures of 3.7σ and 2.5σ , respectively. These were associated with two extreme heat waves in late March and early July, both marked by ten consecutive days with anomalies exceeding 2σ and breaking daily records (Fig. 4.2a). Particularly high temperatures were also observed in January and May 2012 over the eastern United States, with these two months ranking as fifth and third warmest January and May over the period of study with monthly departures of 1.5σ and 1.6σ , respectively. Overall, the spring 2012 departure (3σ) broke the previous spring record (Fig. 4.2b), while the summer 2012 departure (1.5σ) ranked eighth warmest summer since 1948, but the second warmest of the last two decades behind 2011 (Fig. 4.2c). These rankings are even higher when using USHCN adjusted monthly data, with summer 2012 getting up to the fourth position (not shown). Overall, with 49 days out of 184 presenting an anomaly of maximum

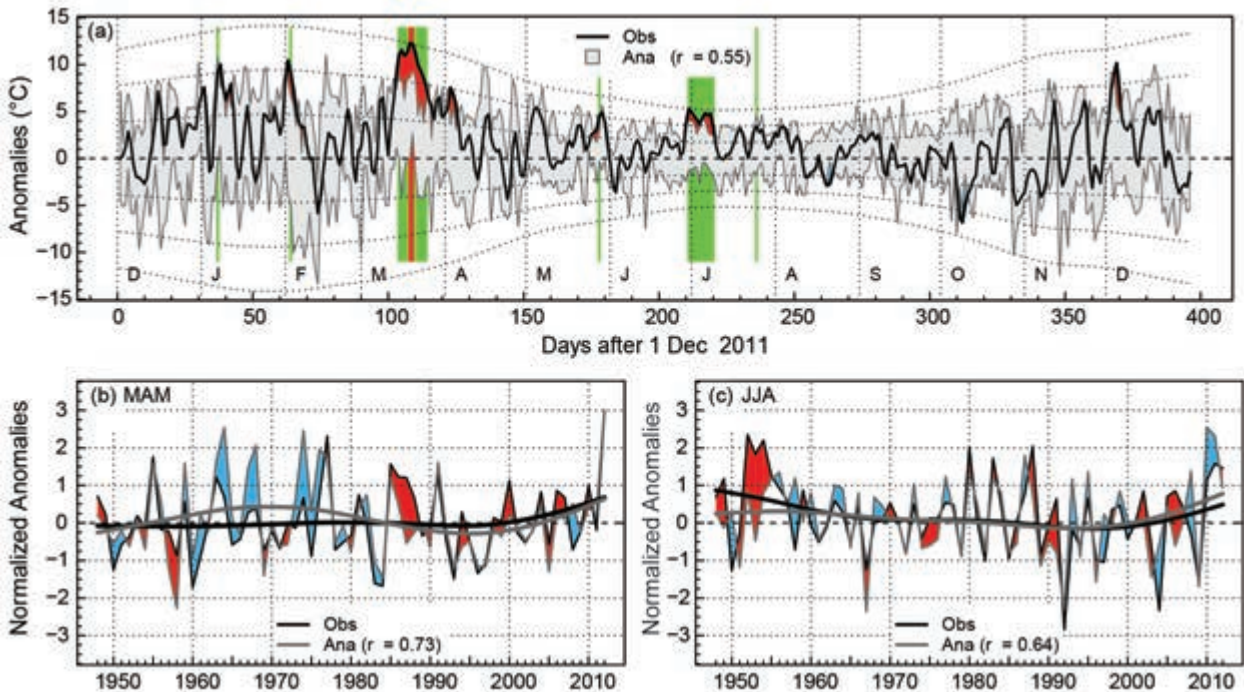


FIG. 4.2. (a) Daily anomalies ($^{\circ}\text{C}$) of observed (black line) and analog (gray spread encompassing the 10 values) eastern U.S. temperatures from Dec 2011 to Dec 2012, exhibiting exceptional heat waves in Mar and Jul. Dashed lines indicate climatological σ -levels (higher variability in winter than summer), and red (blue) indicates days with observed temperatures above (below) the 10 analog values. On average over the eastern United States, 25 daily records were broken in 2012 (green background shading), with two days (18–19 Mar) breaking a record for the 31-day window in which analogues are sampled (red background shading). (b) Spring (MAM) observed (black) and analog (gray) temperatures averaged over the eastern United States, represented as normalized anomalies (σ -levels) relative to the period 1971–2000, with 2012 breaking both observed and analog records. Smoothing by splines with four degrees of freedom is added, and red (blue) indicates years with observed temperatures above (below) analog ones. (c) Same as (b) for summer (JJA), with 2012 ranking as the eighth (fifteenth) warmest summer in observations (analogues).

temperature above the climatological level of 1.5σ , the persisting heat wave of spring-summer 2012 is unprecedented over the eastern United States in our observational record.

The flow-analogue methodology. The contribution of the large-scale atmospheric circulation to temperature anomalies of 1948–2012 is estimated from the same flow-analogue approach as used in CY12 (derived from Lorenz 1969). For each day, we select the 10 days with the closest atmospheric circulation among days of other years but within a moving window of 31 calendar days. This provides a range of 10 daily “analog” temperatures, which we compare to the actual observed temperature of the given day. Circulations are derived from SLP anomalies relative to a 1971–2000 climatology and are considered over a large area encompassing the U.S. domain (130°W – 60°W , 20°N – 50°N). While this method has been applied to both European temperatures and precipitation by many recent studies (Cattiaux et al. 2010; Vautard and Yiou 2009; Yiou et al. 2007), including in this collection (“Contribution of Atmospheric Circulation to Wet North European Summer Precipitation of 2012,” this issue), it has not been applied to U.S. surface variables. A prior step, therefore, consisted in (i) verifying whether atmospheric circulations explain a sizable fraction of the intra-seasonal to interannual variability of U.S. temperatures, and (ii) checking the quality of flow-analogues over the United States. We first verified that the discriminatory power of flow-analogues on U.S. daily and seasonal temperatures is similar to that found over Europe and larger in winter than in summer, which is consistent with correlation values found in the following paragraphs. On average, observed and analog SLP patterns are better correlated for the United States than for Europe ($r = 0.77$ instead of 0.68 in CY12’s Table 1), and the quality of 2012 analogues is close to the 1948–2011 mean. These elements support the relevance of applying the flow-analogue method to the United States. In addition, we verified that our results are insensitive to both the number of selected analogues (here we use ten, but we tested five and twenty) and the metrics used for assessing analogy (here we use the root mean square difference, and we tested the rank correlation and the Mahalanobis distance).

Large-scale circulations explain the hot record of spring 2012....For all seasons of 2012 except summer, mean analog temperatures (i.e., averaged over the 10 analog days for each day and then seasonally) reproduce both

the amplitudes and the geographical distributions of observed anomalies reasonably well (Fig. 4.1, right). In particular, flow-analogues fairly capture the extremely warm spring of 2012, with a rather high spatial correlation compared to springs of other years ($r = 0.76$ over U.S. stations, while the 1948–2012 median is $r = 0.49$). On average over the eastern United States, observed and analog spring temperature anomalies appear highly correlated at an interannual timescale ($r = 0.73$), and we find that atmospheric circulations fully explain the amplitude (3σ) of the 2012 record in maximum temperature (Fig. 4.2b). Interestingly, this is not the case for minimum temperatures, the observed anomaly of 3.3σ being larger than the analog one (2.3σ , not shown). Additionally, for daily timescales, extremely hot days of late March 2012 lie outside the analog range (Fig. 4.2a), suggesting that local processes, such as drought-related decreased evaporative cooling, may have amplified this particular heat wave in addition to the effects of the atmospheric dynamics. However, here we reach the limits of the flow-analogue methodology, since two days in March 2012 (18th and 19th) were hotter than all days of the 31-day window in which analogues are sampled (see red shading in Fig. 4.2a).

...but not the spatial pattern of the following warm summer. Conversely to spring, flow-analogues fail to capture the spatial pattern of the observed temperature anomaly of the summer 2012 ($r = -0.06$ over U.S. stations), even showing an opposite meridional gradient east of the Rockies (Fig. 4.1). However, summer anomalies of other years are generally better reproduced (the 1948–2012 median being $r = 0.37$), suggesting a particularly strong influence of regional processes during summer 2012, possibly linking with dry soils caused by the preceding spring heat wave (Mueller and Seneviratne 2012). Despite this geographical discrepancy, on average over the eastern United States, atmospheric circulations explain a large fraction of both the interannual variability of summer temperatures ($r = 0.64$) and the summer 2012 anomaly (1σ out of 1.5σ ; Fig. 4.2c). As for the March heat wave, extremely hot days of early July are found to be significantly warmer than their analogues (Fig. 4.2a). Overall, during both the spring and summer seasons, 22% of days were warmer than the maximum of the 10 analogues and 71% were warmer than the median, while expected statistical values would be respectively $1/11 = 9\%$ [0%–25%] and $1/2 = 50\%$ [30%–70%]. Brackets for 95% confidence intervals were derived from binomial quantiles assuming 20

independent days among the 184, i.e., a de-correlation time of about 10 days, which might, however, be a strong hypothesis in the case of persisting hot events involving long-memory processes such as soil moisture deficit.

Conclusions. In conclusion, the record hot spring of 2012 over the eastern United States can be mainly explained by atmospheric dynamics. Conversely, while large-scale circulations were favorable to anomalously high temperatures over this region in summer, other local factors, possibly linked to the exceptionally hot spring and the persisting drought throughout summer, shaped the spatial pattern of the following summer heat wave. In a long-term climate perspective, Fig. 4.2b reveals a positive trend over the last 20 years (1993–2012) in spring maximum temperatures

over the eastern United States, which is found to be statistically significant at the 5% level and consistent with the flow-analogue temperature reconstruction. By contrast, no significant trend is found in summer for maximum temperatures (Fig. 4.2c), albeit additional observations show a significant increase of 0.5σ per decade over the past 40 years (1973–2012) for minimum temperatures, partially explained by flow-analogues (not shown). This trend analysis, nevertheless, reaches the limits of daily unadjusted GHCN temperatures, since homogenized USHCN monthly temperatures exhibit a one-to-two times larger warming over recent years (but still not significant for summer maximum temperatures). The contribution of potential changes in circulation to the recent long-term warming in the United States, therefore, requires further research.

5. THE EXTREME MARCH–MAY 2012 WARM ANOMALY OVER THE EASTERN UNITED STATES: GLOBAL CONTEXT AND MULTIMODEL TREND ANALYSIS

THOMAS R. KNUTSON, FANRONG ZENG, AND ANDREW T. WITTENBERG

Introduction. We survey the globe for seasonal and annual mean surface temperature extremes that occurred during 2012. We define an extreme seasonal mean anomaly as one that ranks first, second, or third in the period of record, using the HadCRUT4 observations (Morice et al. 2012). Anomalous warmth over the eastern United States during March–May (MAM) is found to be particularly extreme and spatially extensive. To place this seasonal extreme warmth in the context of long-term climate change, we analyze the time series for this region, comparing observed trends with model simulations of internal climate variability and modeled responses to both anthropogenic and natural forcings using 23 Coupled Model Intercomparison Project phase 5 (CMIP5) models (Taylor et al. 2012).

Where did record or near-record seasonal mean surface temperatures occur in 2012? Global maps of the seasonal- and annual-mean temperature anomalies for 2012 are shown in Fig. 5.1 (left column). Maps in the right column depict where the anomalies were the first, second, or third most extreme in the record—either warm (red colors) or cold (blue colors). The results show a predominance of warm versus cold

extreme occurrences. For extreme annual means, the percent of global analyzed area with first, second, or third warmest in the record, starting as early as 1851, was 15.3% compared with zero cold extremes. The ratios of warm-extreme-to-cold-extreme percent areas were 6.2% : 0.1% for December–February (DJF); 7.7% : 0.2% for MAM; 11.4% : 0.7% for June–August (JJA); and 12.5% : 0.1% for September–November (SON).

A pronounced broader-scale feature in the extremes maps is the record MAM warmth over the eastern continental United States, which was also highly anomalous for the annual means. Much of the Mediterranean region experienced record or near-record JJA and SON warm anomalies. The SON map also shows near-record Atlantic Ocean warmth off the east coast of the United States, which spanned the time of occurrence and extratropical transition of Hurricane Sandy in this region. Other extreme seasonal warmth occurred near the Somali current (western Indian Ocean) during SON and other scattered locations around the globe.

How much did anthropogenic forcing contribute to the extreme eastern U.S. warm anomalies during MAM 2012? Having established where extreme seasonal

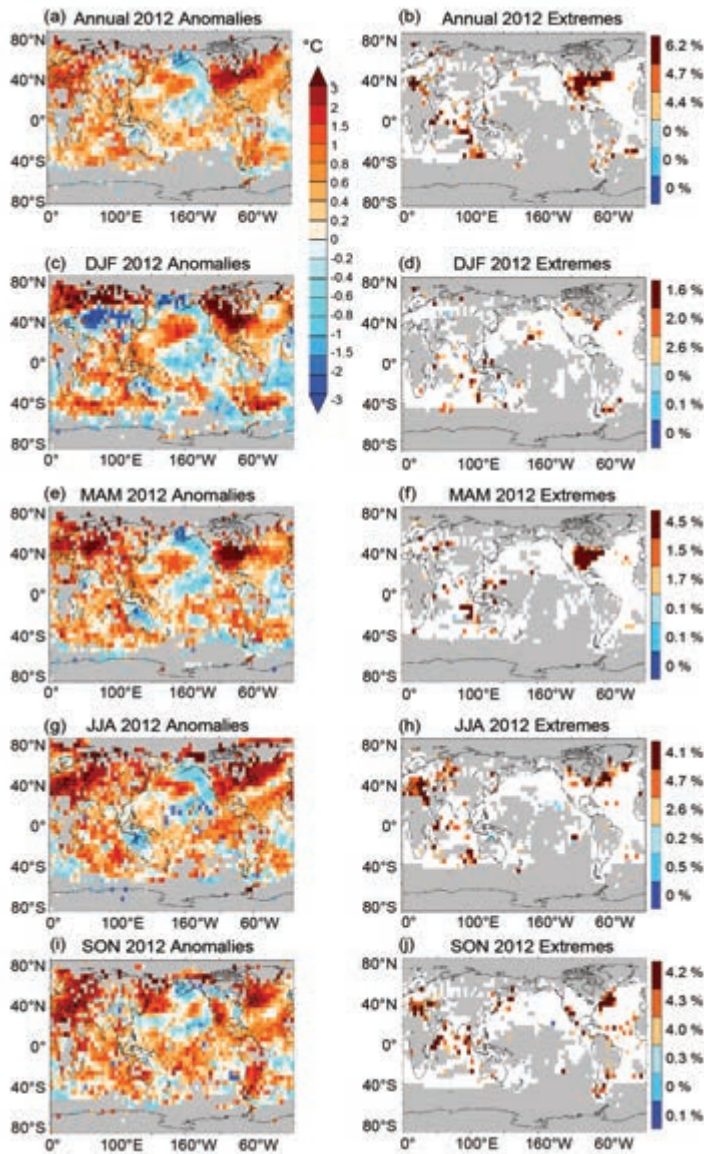


FIG. 5.1. (Left column) Annual (a) or seasonal (c), (e), (g), (i) mean surface air temperature anomalies (°C) for 2012 (1961–90 base period) from the HadCRUT4 dataset. The seasons are DJF (Dec 2011–Feb 2012), MAM (Mar–May), JJA (Jun–Aug), and SON (Sep–Nov). (Right column) Colors identify grid boxes with annual (b) or seasonal (d), (f), (h), (j) mean warm anomalies that rank first (dark red), second (orange-red), or third (yellow-orange) warmest in the available observed record, with blue colors for cold extremes. Gray areas did not have sufficiently long records, defined here as containing at least 100 available annual or seasonal means, with an annual mean requiring at least four available months and a seasonal mean requiring at least two of three months to be available.

and annual mean temperatures occurred in 2012, we now examine the extensive warm anomalies over the eastern United States during MAM in more detail.

Using the Hegerl et al. (2009) guidance paper on detection and attribution methods, we first explore

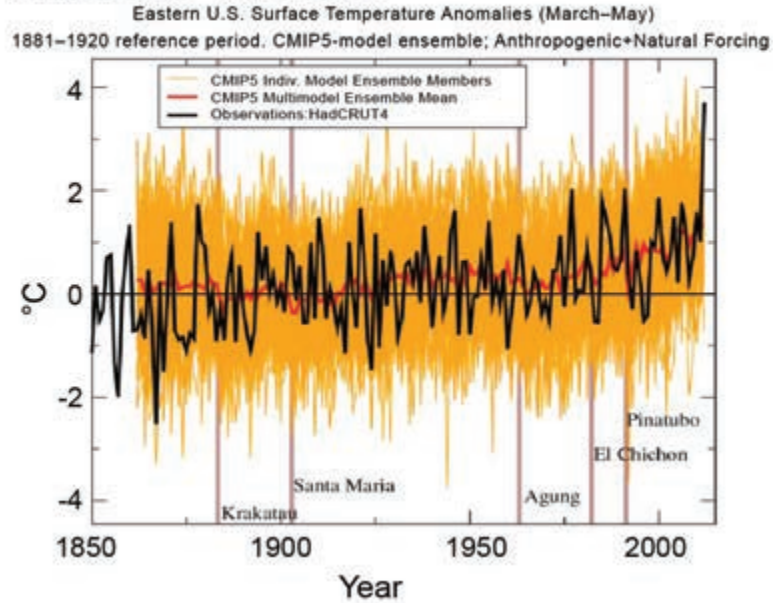
a “multistep attribution” approach. This involves, in general, assessments that attribute an observed change in a variable of interest (in this case, seasonal mean temperature extremes) to a change in climate and/or environmental conditions (in this case, century-long trends in seasonal mean temperatures), plus separate assessments that attribute the change in climate and/or environmental conditions to external drivers and external forcings. We first posit that it is likely that increases in seasonal mean temperatures caused by anthropogenic warming will eventually lead to increases in the extremes (e.g., record or near-record values) of seasonal mean temperatures, but that it may take a substantial record length for this signal to be apparent in the data.

The next step is to assess whether there is detectable warming that is attributable to anthropogenic forcing in the MAM mean temperatures for the eastern U.S. region. For this, we rely on a more extensive trend assessment study that provides further details on our methods and evaluation of model internal variability (Knutson et al. 2013).

Figure 5.2a shows the MAM time series averaged over the region of the eastern United States and southern Canada where the MAM 2012 anomalies were warmest in the record (dark red colors in Fig. 5.1f). The HadCRUT4 observations show a gradual rising trend, with a distinct positive anomaly in 2012 that was nearly twice as warm as the previous record season. The observations lay within the range of the CMIP5 ensemble members, although 2012 is near the upper edge of this range.

Figure 5.2b summarizes a trend analysis for the MAM eastern U.S. time series in Fig. 5.2a, comparing models and observations. Each of the models contributes equally to the multimodel distribution from which the percentiles are derived. The distribution of trends broadens for later start dates, because these represent shorter randomly sampled trends in the control runs, and models can produce larger trend rates by chance for smaller trend lengths. The spread of the All-Forcing (anthropogenic and natural combined) multimodel ensemble (pink) is slightly wider than that of the control run ensemble

(a) Temperature Time Series



(b) Trend Assessment

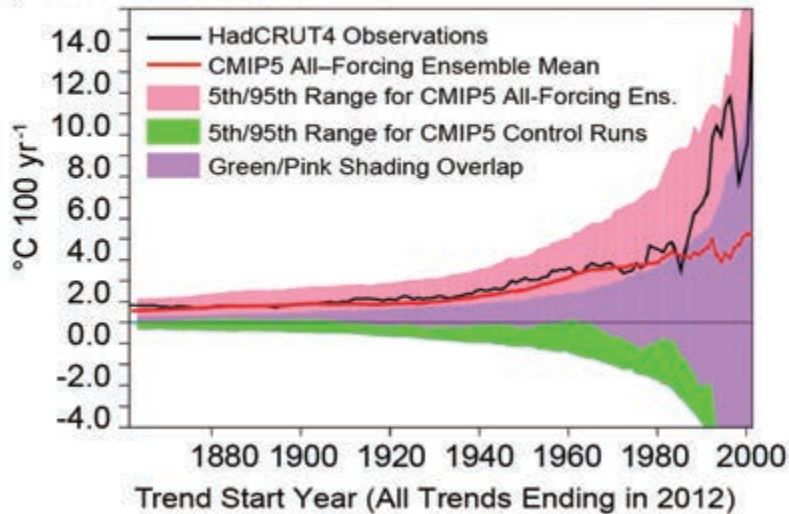


FIG. 5.2. (a) Time series of Mar–May (MAM) averaged surface air temperature anomalies ($^{\circ}\text{C}$) averaged over the region in Fig. 5.1f of record MAM warmth in the eastern United States and southern Canada during 2012. The black line depicts the observed (HadCRUT4) anomalies; the dark red line depicts the multimodel ensemble anomalies from the CMIP5 All-Forcing runs, with each of the 23 models weighted equally; and the orange lines are individual ensemble members making up the CMIP5 multimodel ensemble. The All-Forcing simulations for this region included both anthropogenic and natural forcings from about 1860 to the present, with data from RCP4.5 runs used to extend the time series through 2012 where necessary. All time series shown are adjusted to have zero mean over the period 1881–1920. (b) Trends ($^{\circ}\text{C } 100 \text{ yr}^{-1}$) in the area-averaged MAM mean surface temperature series in (a) as a function of starting year, with all trends ending in 2012. The black curve shows trends from observations (HadCRUT4). The thick red curve shows the ensemble mean trends from the 23-member CMIP5 All-Forcing ensemble. The pink shading shows the 5th–95th percentile range of the distribution of trends obtained by combining random samples from each of the 23 CMIP5 model control runs together with the corresponding model’s ensemble-mean forced trend (All-Forcing runs) to create a multimodel distribution of total trends that reflects uncertainty in both the forced response and the influence of internal climate variability. The green-shaded region shows the 5th–95th percentile range of the trends from the 23 model control runs. Purple shading indicates where the pink- and green-shaded regions overlap.

(green) because it also includes the uncertainty due to the different ensemble mean responses of the individual models. See Knutson et al. (2013) for more discussion and details.

The observed trends in Fig. 5.2b (black line) generally lie outside of the control run 5th–95th percentile range, indicating that (according to the model-generated variability) the observed trends are inconsistent with internal climate variability alone. The observed trend also lies within the pink- or purple-shaded region for all start dates, indicating that the observed MAM trends for the region are consistent with the CMIP5 All-Forcing multimodel ensemble. Using the control run internal variability as a surrogate for natural variability (generally a good assumption for relatively long trend lengths; see Knutson et al. 2013), we conclude that the observed trend is both inconsistent with natural variability and consistent with anthropogenic plus natural forcing runs, meaning that the warming in the observations is very likely attributable in part to anthropogenic forcing.

Since the anomalous warmth of MAM 2012 occurred in a region with detectable long-term anthropogenic warming, we conclude that anthropogenic forcing also likely contributed significantly to the observed anomalies of MAM 2012 over the eastern United States. A rough estimate of the anthropogenic contribution based on Fig. 5.2a would be about 35% (based on the modeled value of $\sim 1.3^{\circ}\text{C}$ near 2012 and the 2012 observed anomaly of $\sim 3.7^{\circ}\text{C}$). Under the assumption that the real-world uncertainty is well represented by the multimodel ensemble mean plus aggregated control-run distribution (i.e., that there is no change in the variability about the mean) and interpreting the difference between the All-Forcing and control-run distributions as the anthropogenic influence, we can conclude the following regarding the 2012 MAM eastern U.S. anomaly. This 3.7°C event was 2.8 times stronger than the expected ensemble-mean contribution of 1.3°C due to anthropogenic forcing in 2012—so, internal variability almost certainly played a substantial role. Based on the model ensemble, an event this warm or warmer would occur with probability 0.07% (unforced) or 0.85% (forced)—a factor of 12 increase in risk. Under the forced scenario, the fraction of risk of such an extreme warm event that is attributable to the forcing is $(0.0085 - 0.0007) / 0.0085 = 92\%$. These estimates of change in risk are sensitive to the baseline period assumed. Here we use the period 1881–1920 as the baseline; if we use 1861–2012 as the baseline period, the risk of the event increases by about a factor of 5

rather than 12, and the fraction of attributable risk is estimated as 78%. As a further sensitivity test, we examined the occurrence of anomalies larger than an alternative threshold equivalent to the second warmest MAM anomaly in the observed series (2.04°C in 1991). Anomalies exceeding this level occur about 11 times more often in the forced simulations than in the unforced runs.

Discussion and conclusions. From the viewpoint of seasonal or annual mean extreme temperatures, 2012 was characterized by a much greater occurrence globally of warm extremes than cold extremes. Notable large-scale regions with extreme seasonal warmth included the United States east of the Rocky Mountains during MAM and much of the Mediterranean region during July–November. The extreme warmth over the eastern United States occurred in a region where there has also been longer-term warming that our model-based assessment attributes at least in part to anthropogenic forcing.

Although the long-term warming during MAM over the eastern U.S. region of record 2012 warmth in Fig. 5.1f was assessed as detectable, a number of caveats apply. For example, when we tested the warming trends since 1901 for individual grid points around the globe, a number of grid points in the eastern U.S. region did not have significant trends (Supplementary Fig. S5.1i). Previous studies have suggested a lack of statistically significant long-term warming over the eastern United States; in particular, Portmann et al. (2009) discussed possible physical explanations for this feature and showed that there is a statistical relationship between the trends in daily maximum temperatures across the United States and the climatological mean precipitation. However, our results illustrate the potential effects of spatial averaging for this type of detection/attribution analysis. After averaging over the entire region of anomalous record warmth in the eastern United States, we *do* find a detectable trend-to-2012 across a wide range of possible start dates. Differences between our results and previous studies may also be due to the averaging area or season chosen and the inclusion of the very warm 2012 anomalies. Our region definition tends to enhance the influence of the very warm anomalies occurring in MAM 2012.

Other caveats to our analysis include remaining uncertainties in estimates of internal variability of the climate system, in climate forcing agents, and in model sensitivity to the forcings. We have found that the models' low-frequency (>10 yr) internal

climate variability in this region is larger than our current best estimate of the real climate system's low frequency internal variability (e.g., Fig. 2 of Knutson et al. 2013). If internal climate variability were in fact overestimated by the models, this would make it overly difficult for a climate signal to be detected above internal variability noise in our analysis, so the detection result would be robust to such a bias. Such a bias would also widen the envelope of the forced simulations, possibly obscuring an underestimate of the warming by the forced models.

The anthropogenic contribution to the extreme seasonal (MAM) warmth over the eastern United States can be estimated as about 35%, or in terms of risk, anthropogenic forcing leads to a factor of 12

increase in the risk of such an event according to our calculations. An important issue for future studies is to explore potential changes in the shape of the temperature distributions under climate change and its effect on the risk estimates for extreme events in the tails of the distribution.

The much larger fraction of global analyzed area with extreme warm seasonal-mean anomalies in Fig. 5.1 (right column), compared to the fraction of area with extreme cold seasonal-mean anomalies, suggests another future approach to multistep attribution. For example, we plan to further explore the rates of occurrence of seasonal warm and cold extremes in the observations and compare the observed changes with those simulated in the All-Forcing runs.

6. HURRICANE SANDY INUNDATION PROBABILITIES TODAY AND TOMORROW

WILLIAM SWEET, CHRIS ZERVAS, STEPHEN GILL, AND JOSEPH PARK

Introduction. Hurricane Sandy slammed into the U.S. mid-Atlantic seaboard on 29–30 October 2012 causing widespread damage and functional disruption to critical infrastructure resulting in repair and mitigation expenditures funded at \$60.2 billion U.S. dollars (GPO 2013). Sandy's impacts exposed many unrealized sector-specific thresholds and general-public vulnerabilities across a region generally accustomed to Nor'easters (Hirsch et al. 2001; Colle et al. 2010; Sweet and Zervas 2011), but not hurricane strikes. As rebuilding occurs, concerns remain as to how sea level rise (SLR) will change probabilities of future events leading to recurring economic losses within an increasingly crowded coastal zone (<http://stateofthecoast.noaa.gov/population>). Here, we summarize tide gauge water level statistics from Sandy and discuss how the probabilities of exceeding its peak impact elevations (relative to *today's* reference frame) have changed since the mid-20th century from relative SLR (SLR_{rel}) and provide future estimates based upon SLR_{rel} scenarios.

Data and methods. Peak water level measurements during Sandy were recorded by National Oceanic and Atmospheric Administration (NOAA) tide gauges (Fig. 6.1; <http://tidesandcurrents.noaa.gov>). In the case of the Sandy Hook gauge, which was destroyed before reaching its peak, an average of two high-water marks at the adjacent U.S. Coast Guard base

(McCallum et al. 2012) were used instead of the last value recorded. Exceedance probabilities are quantified by a generalized extreme value (GEV) model of annual maxima whose cumulative distribution is described by location (centering), scale (dispersion), and shape (distribution tail) parameters (Coles 2001).

We provide time-dependent return intervals (expected time between recurring events and the inverse of the exceedance probability) associated with peak Sandy storm tide levels (tide + surge; referred to as impact levels) based upon GEV models shown with 95% confidence intervals at <http://tidesandcurrents.noaa.gov/est>. The return curves are based upon records through 2010 (Fig. 6.1a), except for the Battery, Bridgeport, and Sandy Hook where impacts from Sandy warranted a recomputation of the stations' probability models through 2012 since GEV models are sensitive to outlier influences (Fig. 6.1a). The GEV models are also sensitive to record length, implying that if Sandy Hook's record was as long as the Battery's, its return interval for Sandy would be longer (Fig. 6.2a). All levels are relative to 1983–2001 epoch mean higher high-water (MHHW; http://tidesandcurrents.noaa.gov/datum_options) tidal datum to normalize for varying tidal ranges.

Current (2012) and historical (1950) return intervals for Sandy's impact levels are obtained by raising or lowering, respectively, a station's GEV model by its long-term relative mean sea level (MSL) trend ([AMERICAN METEOROLOGICAL SOCIETY](http://</p></div><div data-bbox=)

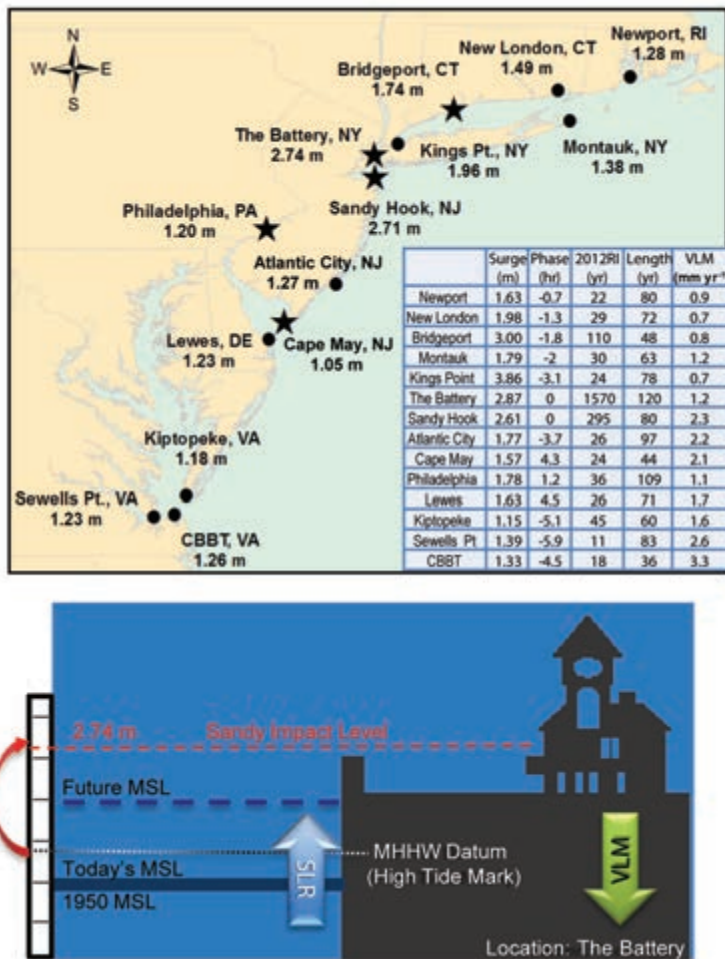


FIG. 6.1. (a) Hurricane Sandy's impact levels (above MHHW) at NOAA tide gauges (shown as dots or stars, with stars signifying highest-ever storm tide) with the table showing maximum storm surge recorded, phase of maximum surge relative to peak storm tide level near high tide (± 6.4 hr near low tide), 2012 return interval (RI) of Sandy's impact levels, length of record used for RI computation, and sinking vertical land motion (VLM) rates. (b) Schematic (not to scale) describing the reference frame for measuring Sandy's impact levels at the Battery and how SLR and VLM contribute to SLR_{rel} changes.

tidesandcurrents.noaa.gov/sltrends), except for Philadelphia where the mean high-water (MHW) trend is applied (discussed below). Future (2050 and 2100) return intervals associated with Sandy's impact levels are formulated by applying four SLR_{rel} scenarios, which incorporate a global mean SLR component estimated for 2100 by the U.S. Global Climate Research Program 2013 National Climatic Assessment (Parris et al. 2012, below):

- Low (0.2 m)
- Intermediate Low (0.5 m)
- Intermediate High (1.2 m)
- High (2 m)

Philadelphia from 20th century channel deepening (Zervas 2003).

How have the return intervals for Sandy's impact levels changed since 1950? Hurricane Sandy broke 16 historical storm-tide levels along the East Coast (Fanelli et al. 2013). Though Sandy's magnitude on the Saffir-Simpson hurricane wind scale was not particularly large, its westward strike heading was very abnormal (Hall and Sobel 2013). Since 1851, nine other hurricanes (Category 1 and 2) have made landfall with similar proximities but all were heading north-northeastward (<http://csc.noaa.gov/hurricanes>). Also important

The Low SLR_{rel} scenario assumes a continuation of global mean SLR estimates for the 20th century (1.7 mm yr^{-1} ; Church and White 2011) and site-specific (sinking) vertical land motion (VLM; Zervas et al. 2013) rates shown in Fig. 6.1a, whereas the other scenarios that incorporate a range of warming and ice-melt projections also include a quadratic parameter. SLR_{rel} amounts by 2050 and 2100 under each scenario (Fig. 6.2b) initiate in 2013 following USACE (2011) guidelines:

$SLR_{rel}(t) = 0.0017(t_2 - t_1) + b(t_2^2 - t_1^2) + VLM$ where t_1 (t_2) is the time between the beginning (ending) year of interest and 1992 and b is a constant ($1.56E-04$ High, $8.71E-05$ Intermediate High, and $2.71E-05$ Intermediate Low).

Future extremes are expected to track the projected SLR_{rel} scenarios and their distribution is modeled using a time-dependent GEV location parameter. Changes to annual maximum variance and outlier occurrences relative to their historical distributions (affecting GEV scale and shape parameters, respectively) from storminess variability/change (Menendez and Woodworth 2010; Grinsted et al. 2012) is a current topic of future climate research (Lin et al. 2012; Grinsted et al. 2013) and not considered here from lack of incorporation guidance (Hunter 2010; Tebaldi et al. 2012). Nor are changes to storm-surge or tide-range characteristics from MSL-changing feedbacks, although the latter has increased significantly ($\sim 1.5 \text{ mm yr}^{-1}$) relative to its MSL trend in

was that Sandy's massive storm surge within New York harbor coincided with peak high tide at Sandy Hook and the Battery contributing to their ~2.7 m storm tide (above MHHW). A couple stations experienced larger storm surges (Kings Point and Bridgeport) but were at lower tide stages (Fig. 6.1a) and not at peak storm tide levels.

Throughout the mid-Atlantic coast, SLR_{rel} has decreased return intervals (i.e., increased probabilities) of Sandy-level inundation events (Fig. 6.2c). For instance, Sandy had a probability equivalent to an occurrence every 295 and 1570 years at Sandy Hook and the Battery, respectively. However, in 1950, MSL was lower and required a larger storm tide to reach Sandy's impact levels. A storm with Sandy's impact level of inundation then would have had to return intervals of 435 and 2330 years, respectively. This represents a one-third decrease in return intervals over this period at these locations. This model also suggests that from Atlantic City southward, a once-in-a-century event or beyond in 1950 can now be expected to recur every couple of decades (approximately two-thirds decrease in return intervals) due to SLR_{rel} .

How might return intervals for Sandy's impact levels change in the future? Results for 2050 and 2100 (Fig. 6.2c) illustrate how the return intervals matching Sandy's impact levels (Fig. 6.1) will decrease in all four SLR_{rel} scenarios. By 2050, return intervals under the Low scenario are slightly more frequent than in 2012. High-scenario forcing suggests Sandy-level events recurring ~annually (red disappears) south of Atlantic City, whereas by 2100, they become \leq annual events under the Intermediate High and Intermediate Low scenarios (yellow and green disappear). Northward between Newport and Kings Point, though Sandy's impact levels (Fig. 6.1a) were generally higher, the cor-

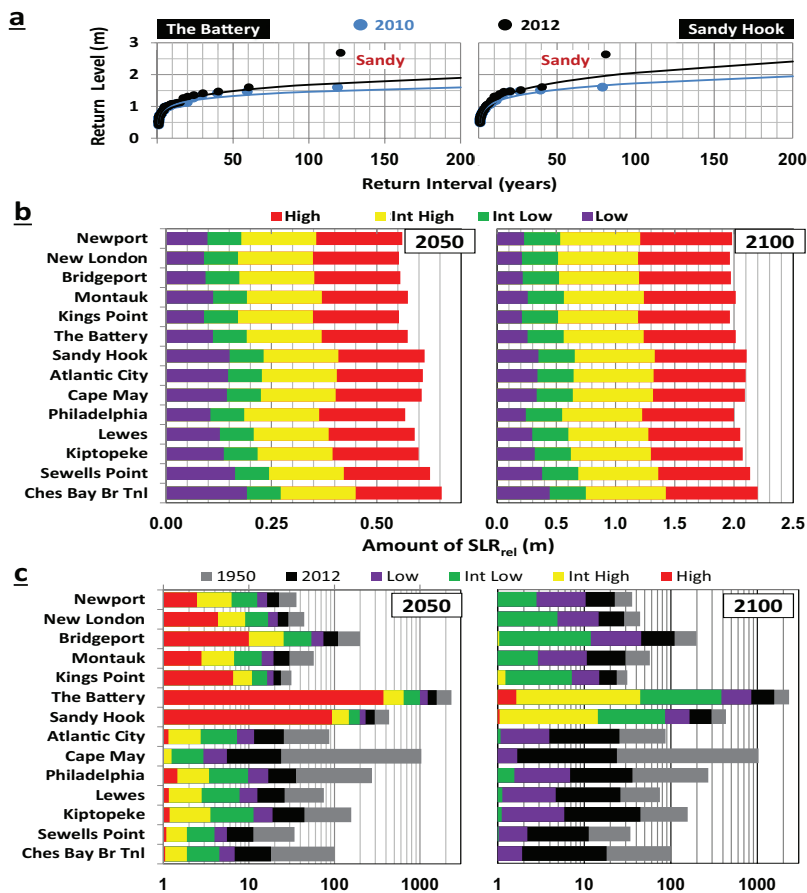


FIG. 6.2. (a) Generalized extreme value (GEV) return curves for the Battery and Sandy Hook with annual maximum storm tide levels (dot) through 2010 (blue) and recomputed for data through 2012 (black) that include Hurricane Sandy; Sandy's return interval is the x-axis value when the black line intersects the Sandy value on the y-axis (not shown). (b) The amount of SLR_{rel} by 2050 and 2100 under each scenario utilized in (c), which shows the time-dependent comparisons of return intervals associated with Hurricane Sandy-impact levels between 1950 (gray) and 2012 (black) by application of each station's long-term relative mean sea level (MSL) trend and in the future (2050 and 2100) by application of four SLR_{rel} scenarios.

responding 2012 return intervals were similar (Fig. 6.2c). However, the decay of the return interval in this region by 2050 and 2100 is slower, i.e., ≤ 10 years in 2050 for High and in 2100 for Intermediate Low scenarios. This is consistent with frequent exposure to powerful Nor'easters captured in the GEV models as well as higher VLM rates southward (Fig. 6.1a). At the Battery and Sandy Hook, the return intervals become approximately 50- and 20-year events in 2100, respectively, under the Intermediate High scenario and ≤ 2 years under the High scenario.

Concluding remarks. Impacts of Hurricane Sandy were record setting, largely attributable to its westward strike heading (~1-in-700 year probability; Hall and

Sobell 2013), massive storm surge, and damaging inundation. Peak storm-tide levels, which occurred near local high tide, had staggering recurrence probabilities (e.g., 1570 years at the Battery, Fig. 6.1a). Though the data records do not always span such long intervals, Sandy was phenomenal based on historical data. Our model aspects (e.g., flatter GEV return curve at the Battery than at Sandy Hook, Fig. 6.2a) are sensitive to tide gauge record length, which miss a relevant 1821 hurricane strike (Scileppi and Donnelly 2007). This may explain why our direct statistical recurrence estimates for Sandy at the Battery are longer than the ~1000-year estimate (MHHW adjusted) simulated under historical climatic conditions by circulation-hurricane models (Lin et al. 2012).

Another important but less-salient factor attributable to Sandy impacts is the effect of SLR. Climate change-related SLR exacerbates extreme-event inundation relative to fixed elevations (Hunter 2010; Tebaldi et al. 2012, Obeysekera and Park 2012). Accordingly, we estimate that SLR_{rel} over 1950–2012 from global SLR (thermal expansion and ice melt), VLM (subsidence), and ocean circulation variability

has contributed to a one- to two-thirds decrease in Sandy-level event recurrences. Our future scenarios of Sandy-level return intervals are concerning, as they imply that events of less and less severity (from less powerful storms) will produce similar impacts (Field et al. 2012). Further aggravating, the frequency and intensity of major storms/surges are likely to increase in a warming climate (Lin et al. 2012; Grinstead et al. 2013). Our scenarios scale similarly with future-climate/circulation/hurricane models (Lin et al. 2012) and show that present (Boon 2012) and future SLR accelerations will nonlinearly compress the time-dependent recurrence intervals in a nonuniform fashion across the region. Lastly, the scenarios do not include regional SLR contributions from ocean freshening and circulation slowdown (Sallenger et al. 2012; Ezer et al. 2013), which affect regional coastal flooding (Sweet et al. 2009) and may add ≥ 0.25 m to overall mid-Atlantic SLR_{rel} (Yin et al. 2009). Coastal communities are facing a looming SLR_{rel} crisis, one that will manifest itself as increased frequency of Sandy-like inundation disasters in the coming decades along the mid-Atlantic and elsewhere.

7. SEPTEMBER 2012 ARCTIC SEA ICE MINIMUM: DISCRIMINATING BETWEEN SEA ICE MEMORY, THE AUGUST 2012 EXTREME STORM, AND PREVAILING WARM CONDITIONS

VIRGINIE GUEMAS, FRANCISCO DOBLAS-REYES, AGATHE GERME, MATTHIEU CHEVALLIER,
AND DAVID SALAS Y MÉLIA

Introduction. On 18 September 2012, the Arctic sea ice extent hit a new record low of 3.41 million km² as reported by the National Snow and Ice Data Center (NSIDC), i.e., about half of the 1979–2000 September mean. From 6 August to 8 August 2012, an extreme storm (Simmonds and Rudeva 2012) also transited over the Arctic. Such an intense storm had the potential to accelerate the sea ice loss through increased ice breaking and transport toward warmer regions (Parkinson and Comiso 2013) and through increased ocean mixing (Zhang et al. 2013). None of the forecast systems participating in the Study of Environmental Arctic CHange (SEARCH) program were able to predict the extreme 2012 summer sea ice melting at lead times greater than one month. Was this record low extent preconditioned by the sea ice loss from previ-

ous years but missed by the climate models because they underestimate the rate of radiatively forced sea ice loss (Stroeve et al. 2012)? Was this record largely driven by the extreme storm?

Reproducing the Arctic sea ice minimum. We performed an experiment, called CTRL, with the Louvan-la-Neuve 2 (LIM2) sea ice model (Fichefet and Maqueda 1997; Goosse and Fichefet 1999) embedded into the Nucleus for European Modelling of the Ocean 3.2 (NEMO3.2) ocean model (Madec et al. 2008) forced with ERA-Interim (Dee et al. 2011) atmospheric surface fields through the Large and Yeager's (2004) bulk formulae. Five members were initialized every 1 June from 2000 to 2012 from a five-member sea ice reconstruction described and validated extensively

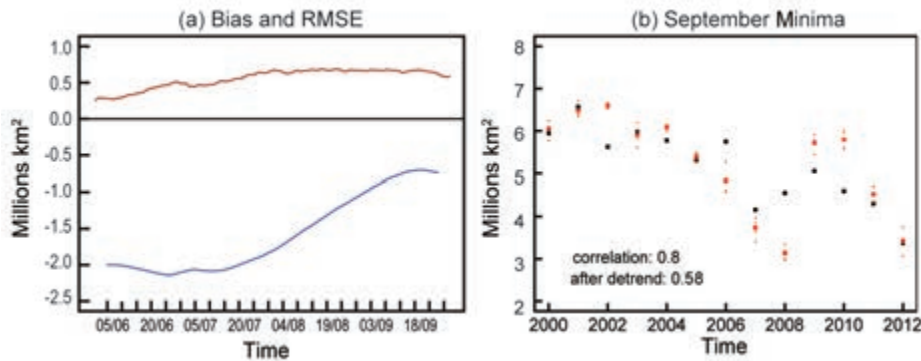


FIG. 7.1. CTRL performance in capturing the Arctic sea ice extent ($\times 10^6$ km²). (a) Mean 2000–12 bias as compared to the NSIDC daily observations (http://nsidc.org/data/seaice_index/archives.html) in blue and RMSE of the anomalies after bias correction (Kharin et al. 2012) in brown as a function of the simulation day. (b) Sep minima in the NSIDC daily observations in black and in CTRL after bias correction (Kharin et al. 2012) in red as a function of the year. A big square is shown for the ensemble mean, small dots for the ensemble members. The method from Kharin et al. (2012) consists in correcting, not only the mean bias shown in panel (a), but also the differences in the long-term trend between the model and the observations, both obtained by a least square linear regression as a function of the calendar day.

in Guemas et al. (2013; HistEraNudg simulation) and described briefly in the Supplemental materials.

The mean bias in CTRL daily sea ice extent, computed over the 2000–12 period, as a function of the boreal summer day (Fig. 7.1a, blue curve) shows an underestimation as compared to the NSIDC estimates (Fetterer et al. 2009). After bias correction following the Kharin et al. (2012) method, which accounts for the influence of the long-term trend on the model bias, the RMSE of the anomalies (Fig. 7.1a, brown curve) shows an error of about 0.25 million km² at the beginning of the summer that increases to about 0.75 million km² at the end of the summer. The September minima in sea ice extent (Fig. 7.1b) are captured with a correlation of 0.80, reduced to 0.58 after linear detrending, both significant at the 95% level. The observed 2012 September minimum is 2.01 million km² lower than the 2000–11 average September minimum. This excess sea ice loss is underestimated by 0.05 million km² (2.5%) by our ensemble mean 2012 CTRL minimum when using the Kharin et al. (2012) method for bias correction (Fig. 7.1b) while it is overestimated by 0.43 million km² (21%) if we bias correct by subtracting the climatology shown in Fig. 7.1a, indicating that our climate model overestimates the long-term trend in sea ice extent. We aim here at attributing the observed 2.01 million km² excess loss to either the extreme August cyclone, the warmer than usual atmospheric conditions, or the persistence of 1 June 2012 sea ice initial conditions.

Attribution through sensitivity experiments. We performed a first sensitivity experiment, called STORM, (Fig. 7.2; blue) in which we replaced all the global atmospheric forcing fields during 5 August–8 August 2012, when the extreme storm occurred, by the global atmospheric forcing fields from the 5 August–8 August 2011. The simulated excess sea ice loss relative to the 2000–11 average is reduced by 0.02 million km² (1%; blue-red in Fig. 7.2) only in STORM as compared to CTRL. We, therefore, conclude to a negligible contribution of the extreme 2012 summer cyclone to the Arctic sea ice extent minimum, which is consistent with the results of Zhang et al. (2013). However, sea ice fracturation processes and melt ponds are not represented in our model, which can be responsible for an underestimated response to the extreme storm, through an underestimation of the shortwave radiation absorption (Screen and Simmonds 2012) and of

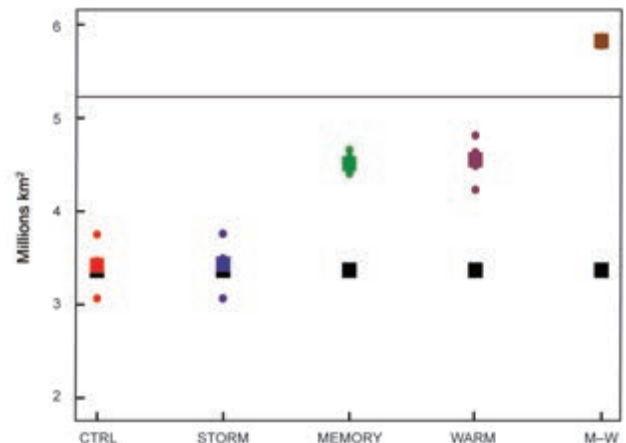


FIG. 7.2. Sensitivity experiments of 2012. Black squares indicate the observed 2012 minimum ($\times 10^6$ km²). The black line indicates the 2000–11 average minimum. Red is the same 2012 CTRL minimum as in Fig. 7.1b. Blue, green, purple, and brown are the September minima from the STORM, MEMORY, WARM, and M-W sensitivity experiments, respectively. A square indicates the ensemble mean, small dots the ensemble members.

the heat exchanges between the sea ice and ocean components. Indeed, the study by Parkinson and Comiso (2013) suggests a larger contribution from the extreme storm. Hence, the robustness of those conclusions should be assessed with more sea ice models.

We performed a second sensitivity experiment, called MEMORY, (Fig. 7.2; green) in which we replaced the observed sea ice initial conditions for 1 June 2012 with the climatology of 1 June 2000–11. The simulated excess sea ice loss relative to the 2000–11 average is reduced by 1.09 million km² (54%; green-red in Fig. 7.2) in MEMORY as compared to CTRL. We, therefore, conclude that about half of the excess sea ice loss during the 2012 summer was preconditioned by the previous history of the sea ice cover. However, the 1 June 2012 sea ice extent is underestimated in CTRL, which might lead to an overestimated role of the sea ice memory.

A third sensitivity experiment, called WARM, (Fig. 7.2; purple) was performed in which we introduced an offset in the near-surface atmospheric temperature and humidity computed as the difference at the grid-point level between the average over the 2000–11 melting season and the 2012 melting season. The simulated sea ice loss relative to the 2000–11 average is reduced by 1.14 million km² (56%; purple-red in Fig. 7.2) in WARM as compared to CTRL. We, therefore, conclude that about half of the excess sea ice loss during the 2012 summer was induced by the warmer-than-usual atmospheric conditions. Those warmer atmospheric conditions over the Arctic might have been, however, themselves partly forced by the feedback of the sea ice loss into the atmosphere.

We, therefore, performed a last sensitivity experiment, called M-W (Fig. 7.2, brown) which combines both the characteristics of the MEMORY and WARM experiments to assess the contribution of the interaction between the sea ice memory and the warmer atmospheric conditions. We replaced, in this M-W experiment, the observed sea ice initial conditions for 1 June 2012 with the climatology of 1 June 2000–11, and we introduced an offset in the near-surface atmospheric temperature and humidity computed as the difference at the grid-point level between the average over the 2000–11 melting season and the 2012 melting season. The simulated sea ice loss is reduced by 2.41 million km² in M-W as compared to CTRL, i.e., 0.17 million km² (8%) in excess compared to the sum of the individual contributions from the preconditioning by

the previous history of the sea ice cover (1.09 million km²) and from the 2012 warmer atmospheric conditions (1.14 million km²). We, therefore, conclude that the positive retroaction between the sea ice memory and the warm atmospheric conditions explain a few percentage of the excess sea ice loss during the 2012 summer.

The 2012 sea ice loss we attributed to the storm, to the sea ice memory, to the atmospheric warming, and to the interaction between sea ice memory and atmospheric warming amount respectively to 0.02 million km², 1.09 million km², 1.14 million km², and 0.17 million km². This makes a total of 2.42 million km², which overestimates the 2012 observed sea ice loss by 0.41 million km². This amount of 0.41 million km² corresponds approximately to the bias corrected by the Kharin et al. (2012) method to account for the overestimated long-term trend in sea ice extent in CTRL. This overestimation by 0.41 million km², therefore, corresponds most probably to an overestimation of the contribution from the sea ice memory and the warm atmospheric conditions (and their positive retroaction).

Conclusions. The Arctic sea ice extent experienced an extreme low on 18 September 2012, 2.01 million km² below the 2000–11 mean September minimum. This study aimed at estimating the contributions from three different factors to this 2.01 million km² excess sea ice loss: (i) the extreme August summer storm that transited over the Arctic, fracturing sea ice, transporting it toward warmer regions, and increasing the ocean mixing; (ii) the preconditioning by the history of the sea ice cover prior to the beginning of the melt season (among which the sea ice thinning related to the long-term warming); and (iii) the warmer-than-usual surface atmospheric conditions (also partly related to the long-term warming). Our modeling results indicate that the exceptional 2012 sea ice loss was primarily due to the sea ice memory and to the positive feedback of the warm atmospheric conditions, both contributing approximately equally. Our results also point at a negligible contribution of the extreme 2012 summer storm. However, our model fails to reproduce the abrupt fall in daily sea ice extent observed by satellite at the storm passage (not shown), which suggests that we underestimate its contribution in this study.

8. THE ROLE OF GLOBAL CLIMATE CHANGE IN THE EXTREME LOW SUMMER ARCTIC SEA ICE EXTENT IN 2012

RONG ZHANG AND THOMAS R. KNUTSON

Introduction. Satellite observations reveal a record-breaking low September Arctic sea ice extent (ASIE) of 3.61 million km² in 2012. Over the satellite period (1979–2012), September ASIE declined 49% compared to the 1979–2000 climatology of 7.04 million km². The extreme low summer ASIE in 2012 continued the rapid downward trend seen in the early 21st century. The observed decline in ASIE has been attributed in large part to greenhouse gas forcing (Hegerl et al. 2007), and some climate models project that the Arctic Ocean will be ice free in summer within a few decades (Stroeve et al. 2012; Massonnet et al. 2012). Extrapolations of recent trends in ice volume would predict a nearly ice-free summer in less than a decade (e.g., Overland and Wang 2013). In this study, we compare both the observed September 2012 ASIE anomaly and the 2001–12 trend with model-simulated internal variability and response to climate forcings. We use Coupled Model Intercomparison Project Phase 5 (CMIP5) simulations (Taylor et al. 2012) to explore whether the observed summer 2012 ASIE anomaly and the 2001–12 trend can be explained as a response to anthropogenic and natural forcing and how they relate to the observed increase in global mean surface air temperature (SAT_{gm}).

Data and methods. Our observed September ASIE analysis for the satellite period 1979–2012 uses the National Snow and Ice Data Center (NSIDC) sea ice index (Fetterer et al. 2009) and observed September SAT_{gm} data is from the NCEP/NCAR Reanalysis (Kalnay et al. 1996). The model outputs from the CMIP5 archive combine 20th century All-Forcing (anthropogenic and natural combined) simulations with the representative concentration pathway (RCP) 4.5 future emission scenario experiments for years beyond 2005. We selected 19 CMIP5 models, with 88 All-Forcing ensemble members, requiring each model have at least three RCP4.5 ensemble members and 100 years of preindustrial control run. For observations and models, ASIE is defined as total Northern Hemisphere marine area with sea ice concentrations of at least 15%.

Both observed and modeled ASIE and SAT_{gm} anomalies are referenced to means for 1979–2000, a relatively stable period for ASIE and the same period

used by NSIDC. Long-term drifts in the preindustrial control runs of each model were subtracted from all experiments. To derive the range of internal variability for each model, we drew 1000 random samples of 34-year segments from the detrended preindustrial control simulation and derived the anomalies using the first 22-year average as the climatology, as was done with observations. We then calculated the 5th to 95th percentile ranges (PR₅₋₉₅) of the anomalies and trends from the 1000 random samples. The PR₅₋₉₅ of the multimodel distribution was constructed using 19000 samples—1000 from each of the 19 control simulations. The PR₅₋₉₅ of the multimodel distribution of forced response was constructed by adding random samples from each model's control simulation to that model's ensemble mean from the forced (All-Forcing historical/RCP4.5) experiments. This methodology is similar to that in Knutson et al. (2013) for surface temperature. Thus, the total distribution represents the uncertainties due to both the difference in the models' ensemble-mean forced response and the internal variability of each model.

If the observed anomaly or trend (for either ASIE or SAT_{gm}) lies below the PR₅₋₉₅ of the multimodel distribution of internal (control run) variability alone, we classify the observed trend/anomaly as “detectable”; if it is both detectable and within the PR₅₋₉₅ of the multimodel distribution of the forced response, we interpret it as “detectable and consistent with All-Forcing runs”; if the trend/anomaly is detectable but below the PR₅₋₉₅ of the All-Forcing runs, we interpret it as “detectable and significantly stronger than the models' ensemble All-Forcing response.”

Results. The observed September ASIE in 2012 (Fig. 8.1a,c) was an extreme low anomaly (-3.41 million km²) for the 34-year record. This anomaly was much lower than the simulated multimodel ensemble mean anomaly for 2012 of -1.5 million km² and even lies below the PR₅₋₉₅ of the multimodel distribution of both internal variability (-1.0 million km²) and forced response (-2.9 million km²). Hence the ASIE anomaly is detectable and significantly stronger than the ensemble All-Forcing response. Meanwhile the observed September SAT_{gm} anomaly of 0.55 K in 2012

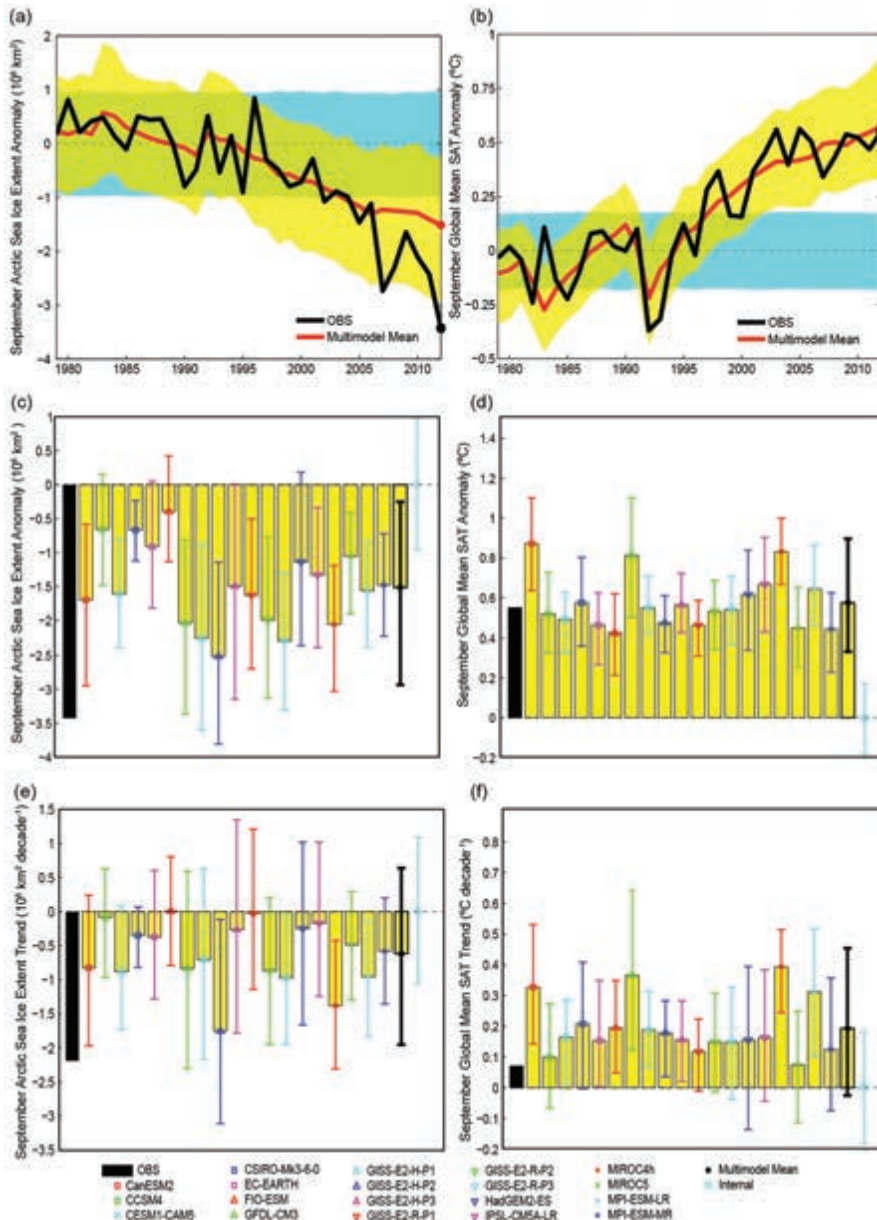


FIG. 8.1. (a) September Arctic sea ice extent (ASIE) anomalies. (b) September global mean surface air temperature (SAT_{gm}) anomalies. In (a) and (b) the thick black lines are observations, and the thick red lines are multimodel ensemble mean from 19 CMIP5 models (All-Forcing historical simulations through 2005 combined with RCP4.5 projections for the period after 2005). The yellow shading is the 5th to 95th percentile range ($\text{PR}_{5,95}$) of the multimodel distribution of forced response. The cyan shading is the $\text{PR}_{5,95}$ of internal variability constructed from the detrended multimodel control simulations. (c) September ASIE anomaly for the year 2012. (d) September SAT_{gm} anomaly for the year 2012. (e) September ASIE trend for the period 2001–12. (f) September SAT_{gm} trend for the period 2001–12. In (c)–(f), the black bars are the observations. The yellow bars with color error bars are ensemble means from 19 CMIP5 models and the $\text{PR}_{5,95}$ of internal variability constructed from each model’s control simulation. The yellow bars with the thick black error bars are the multimodel ensemble means and the $\text{PR}_{5,95}$ of the multimodel distributions of forced response. The stand-alone cyan error bars without yellow data bars depict the $\text{PR}_{5,95}$ of internal variability constructed from multimodel control simulations. All anomalies are relative to the climatology for 1979–2000.

(relative to 1979–2000) is not warmer than the peaks in 2003 and 2005 but matches well with the CMIP5 multimodel ensemble mean and is detectable and consistent with the models’ All-Forcing response (Fig. 8.1b,d).

The observed summer ASIE declined precipitously and diverged from the simulated multimodel ensemble mean in the early 21st century (Fig. 8.1a). The observed decline trend of September ASIE over the period 2001–12 (-2.2 million $\text{km}^2 \text{ decade}^{-1}$), is detectable but significantly more rapid than the CMIP5 All-Forcing ensemble-mean trend of -0.6 million $\text{km}^2 \text{ decade}^{-1}$ (Fig. 8.1e). Meanwhile, the observed warming trend of September SAT_{gm} over the same period ($0.07 \text{ K} \text{ decade}^{-1}$) is much less than the CMIP5 ensemble-mean trend ($0.19 \text{ K} \text{ decade}^{-1}$), and is not detectable compared to internal variability; however, it is not significantly different from the All-Forcing response (Fig. 8.1f). The observed September ASIE decline trend for 2001–12 is more rapid than the ensemble mean trend in any of the 19 CMIP5 models, while the observed September SAT_{gm} warming trend over the same period is less than the ensemble mean trend in any of the same 19 models (Fig. 8.1e,f). The $\text{PR}_{5,95}$ for the All-Forcing responses (Fig. 8.1c–f) do not include the uncertainty in each model’s ensemble mean caused by the model’s limited number of available ensemble members—an issue discussed in more detail in Knutson et al. (2013).

Figure 8.2 shows the joint plots of September ASIE and SAT_{gm} for the 2012 anomalies and the 2001–12 trends. For 2012, the observed September ASIE anomaly lies outside the multimodel PR_{5-95} for the All-Forcing experiments, although the observed September SAT_{gm} anomaly is consistent with All-Forcing experiments (Fig. 8.2a). The observed September ASIE decline trend for 2001–12 is so rapid that it lies outside the multimodel PR_{5-95} of the All-Forcing runs, but the observed September SAT_{gm} warming trend for the same period is so small that it is not detectable (Fig. 8.2b). The above findings raise the question as to why such a rapid decline in the summer ASIE occurred at the same time as the relatively “flat” trend in the SAT_{gm} .

The discrepancy between observations and multimodel simulations of both 2012 and the early 21st century trend (Fig. 8.2a,b) suggests several possibilities: (i) most CMIP5 models may underestimate the polar amplification of temperature change and the decrease of summer ASIE in the response to a given forcing; (ii) internal variability of summer ASIE may be underestimated by the models; (iii) there may be important errors/omissions in forcings used in the models that can directly or indirectly affect summer ASIE; or (iv) the observations represent an extreme, rare scenario, i.e., outside the PR_{5-95} . Concerning the second possibility, a previous study (Winton 2011) suggested that substantial natural variability is necessary to reconcile models with observations. For example, if the amplitude of the internal variability in all 19 control simulations is increased by 25%, then the observed September ASIE decline trend for 2001–12 will fall within the multimodel PR_{5-95} of the All-Forcing runs. If the internal variability of ASIE is increasing due to the lower base state values (e.g., Goosse et al. 2009), our use of preindustrial control runs may lead to a systematic underestimation of the present levels of internal variability. Concerning the fourth possibility, we plotted all 19 000 random samples of summer ASIE trends, including those outside the models’ PR_{5-95} of either internal variability or forced response, as dots in Fig. 8.2. The observed summer ASIE trend in the early 21st century is not outside of this model range, indicating that it can possibly be explained as an extreme, rare scenario in either the “pure internal variability” case (cyan dots) or the “forced plus internal variability” case (orange dots; Fig. 8.2b). ASIE anomalies for 2012 remain outside the complete (19 000-member) sample of internal variability.

Among the 19 CMIP5 models, the GISS-E2-H-P2 model simulated the largest 2012 summer ASIE reduction and the largest decreasing trend for 2001–12 (Fig. 8.1c,e). However, this model has unrealistically low climatological summer ASIE (4.0

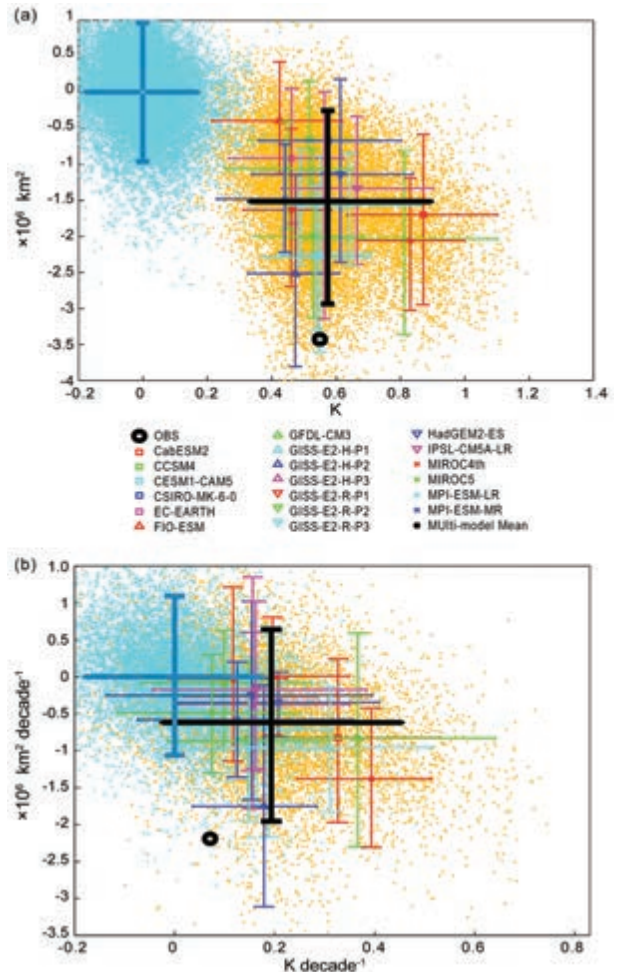


FIG. 8.2. (a) Anomalies of September sea ice extent (ASIE) versus September global mean surface air temperature (SAT_{gm}) for the year 2012 and (b) trends of September ASIE versus September SAT_{gm} for the period 2001–12 in observation (OBS) and 19 CMIP5 models. The thin color error bars are the PR_{5-95} in ASIE and SAT_{gm} , respectively, for each CMIP5 model. The thick black cross and error bars are multimodel ensemble mean and the PR_{5-95} of multimodel distributions of forced response. The thick blue error bars are the PR_{5-95} of multimodel distributions of internal variability. The orange scatter dots are 19 000 random samples of multimodel distributions of forced response in both ASIE and SAT_{gm} , sampled together. The cyan scatter dots are 19 000 random samples of internal variability in both ASIE and SAT_{gm} constructed from multimodel control simulations, sampled together. All anomalies are relative to the climatology of 1979–2000.

million km²) for the reference period 1979–2000, compared to observations (~7.0 million km²).

Conclusions. Comparisons between observations and 19 CMIP5 models reveal that the 2012 ASIE anomaly and the rapid decline of ASIE in the early 21st century are very rare occurrences in the context of these models and their responses to anthropogenic and natural forcing combined. The observed 2012 record low in ASIE is extremely unlikely to have occurred due to internal climate variability alone, according

to the models, i.e., and has a much greater likelihood of occurrence in the “forced plus internal variability” scenario. The 2012 anomaly is significantly stronger than the multimodel’s mean response to both anthropogenic and natural forcing combined. In addition, the observed September ASIE decline trend for 2001–12 is much more rapid than in the previous decades and even lies outside of the PR_{5,95} of the multimodel distribution of forced responses, despite the observed September SAT_{gm} warming trend for the same period being smaller than in the previous two decades.

9. THE FEBRUARY 2012 EUROPEAN COLD SPELL THAT DIDN'T BRING THE DUTCH ANOTHER 11-CITY TOUR

HYLKE DE VRIES, RUDOLF VAN WESTRHENEN, AND GEERT JAN VAN OLDENBORGH

Introduction. Western European winters are characterized by strong temperature variability. While on average, westerly winds transport relatively mild, moist oceanic air towards the continent, occasionally the circulation reverses, leading to cold conditions with northeasterly flow from Siberia and sometimes snowfall (van Ulden and van Oldenborgh 2006). To the Dutch, these cold spells come as a great relief, as they ignite hope that the 11-City Tour of Friesland can be held, a classic ice-skating marathon over 200 km [a few hundred professional competitors, 16 000 recreational skaters, and more than a million spectators along the route (http://nl.wikipedia.org/wiki/Vijftiende_Elfstedentocht)]. Because of the great number of people, strict safety regulations are nowadays imposed:

at least 15 cm of ice thickness is demanded along the entire route. In the previous century, the 11-City Tour had been held only 15 times, the last one in January 1997 (Fig. 9.1).

After a mild start of the winter [December 2011 was the fifth warmest on record (van der Schrier et al. 2011)], an extensive high-pressure area built over Russia near the end of January 2012 and migrated slowly westward. With strong easterly to northeasterly winds, bitterly cold air was advected straight from the Arctic and northeastern Siberia in the direction of western and central Europe and even northern Africa. Many regions were exposed for more than two weeks to temperatures more than 10°C below average. The ice-skating community had high expectations since the cold spell had been forecast very well by the meteorological institutes due to its large spatial scale. Nevertheless, also in 2012 the 11-City Tour could not be organized due to lack of sufficient ice thickness on many lakes and canals. “What prevented the ice from growing?” and “Could climate change be responsible for the insufficient ice thickness?” were among the most frequently asked ques-

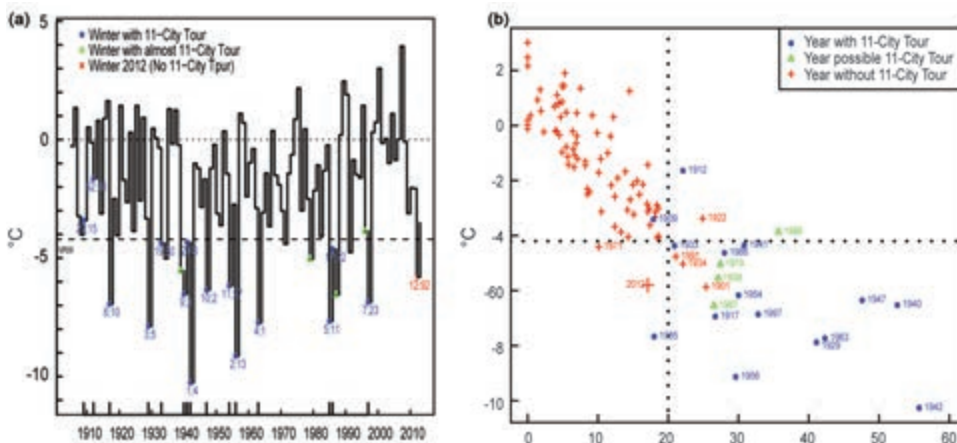


FIG. 9.1. (a) Yearly minimum of 15-day average temperature (°C) for De Bilt, Netherlands. The filled dots indicate years in which an 11-City Tour was organized. The two numbers below the dots indicate the rank of the cold spell and DJF respectively (1905–2013). (b) Scatterplot of maximal simulated ice thickness (cm) and minimal 15-day average temperature (°C) in Friesland. (Source: KNMI.)

community had high expectations since the cold spell had been forecast very well by the meteorological institutes due to its large spatial scale. Nevertheless, also in 2012 the 11-City Tour could not be organized due to lack of sufficient ice thickness on many lakes and canals. “What prevented the ice from growing?” and “Could climate change be responsible for the insufficient ice thickness?” were among the most frequently asked ques-

tions in the aftermath of the cold spell. In this contribution, we seek answers to these two questions¹.

Ice growth. Theoretically, water turns into ice if the water temperature gets below freezing. It is obvious that at least a number of “ice days” (a day with maximum temperature below freezing) are required to produce 15 cm ice thickness along the entire 11-City route. In a recent study, Visser and Petersen (2009) quantify the constraint by showing that the observed ice thickness in the northern parts of the Netherlands is usually sufficient for the 11-City Tour to be held if the 15-day observed average temperature in De Bilt falls below -4.2°C (Fig. 9.1). With the observed -5.8°C for the 15-day average temperature in De Bilt, this criterion was obviously satisfied in February 2012. We give a short overview of factors influencing ice growth on lakes and canals.

Because the cooling occurs at the surface due to heat loss with the air aloft and because water reaches its highest density at 4°C , turbulent vertical mixing will occur as long as the average water temperature exceeds 4°C . Only after the entire water column has been cooled to 4°C , the top-layer can start to freeze. For this reason, deeper water freezes later than shallow water. Wind provides nonlinear feedback; it speeds up the initial cooling of the water but prevents the incipient ice formation. However, once a continuous ice cover has formed, wind may enhance the ice growth again. Because the essential heat-loss to the atmosphere occurs at the surface, an existing ice layer frustrates its own growth. In much the same way, a layer of snow on top of the ice works as an insulating cover, especially if the snow is fresh and has fallen under cold conditions. Finally, we mention the role of radiation. Ice melt during sunny days can provide a serious threat to the ice-growing process, especially later in winter when the days lengthen. Clouds reduce daytime melting, but they also limit cooling at night. Moreover, on cloudy days the humidity is often higher, reducing the ice-growing process again.

Results. In this section, we analyze the role of the different contributions to the ice growth in the case of the 2012 cold spell. We make use of the Royal Netherlands Meteorological Institute (KNMI) ice-growth model (de Bruin and Wessels 1988). This model estimates the water temperature and ice thickness for calm water of 2-m depth, on the base of observed

meteorological parameters such as air temperature and snow cover, taking all factors discussed above into account. Historical simulations show that an 11-City Tour was organized or could have been organized when this model computes an ice thickness of 20 cm. The 5 cm difference takes into account the differences between the idealized 2-m deep water in the model and the real route with deeper water, trees, towns, and bridges.

Figure 9.2 displays the observed 12-hourly air temperature (black) and snow cover (green) as well as the simulated water temperature (blue) and ice thickness (red). As already discussed, the 2012 winter had a mild start. Until the start of the cold spell, the Hellmann number (negative integral of daily mean temperature below zero) was zero. During an average winter this number reaches about 30–40 at the end of January. The week before the cold spell, temperatures were about 5°C above normal (purple) with strong winds. Therefore, the lakes were also less cold than normal and it took more than two ice days before ice formation could start. The ice initially thickened rapidly, but then an unwelcome snowfall event occurred, putting 6 cm of very fluffy snow with maximal insulating capacity on top of the thin ice. The ice growth responded immediately and reduced strongly. Even though some of the snow disappeared in the following days due to the abundant sunshine, the ice thickness did not reach the threshold of Visser and Petersen (2009). During this entire period, the temperatures remained very low. (These low temperatures were in turn enhanced by the rapid nighttime cooling above the snow). Unfortunately for the ice-skaters, the high-pressure system eventually migrated southwestward before the ice was thick enough, leading to westerly winds and milder temperatures.

Using the KNMI ice model, two artificial scenarios were constructed. In the first scenario, all meteorological conditions were kept identical except for snowfall, which was removed. In this situation, the ice growth (red dotted line) continues to increase, leading to a thickness above the 20-cm threshold of Visser and Petersen (2009). Thus, in the case without snow, an 11-City Tour had likely been possible (in a historic “no-snow” case with similar cold-spell intensity, the 11-City Tour was organized in 1997). It should be noted that the warmer temperatures that would have been associated with the lack of snow cover are not taken into account.

In the second scenario, we retained the snow but artificially lowered the air temperature by 1.5°C , to simulate the ice growth in a colder (historic) cli-

¹ Part of this study has appeared in Dutch as de Vries and van Westrhenen (2012)

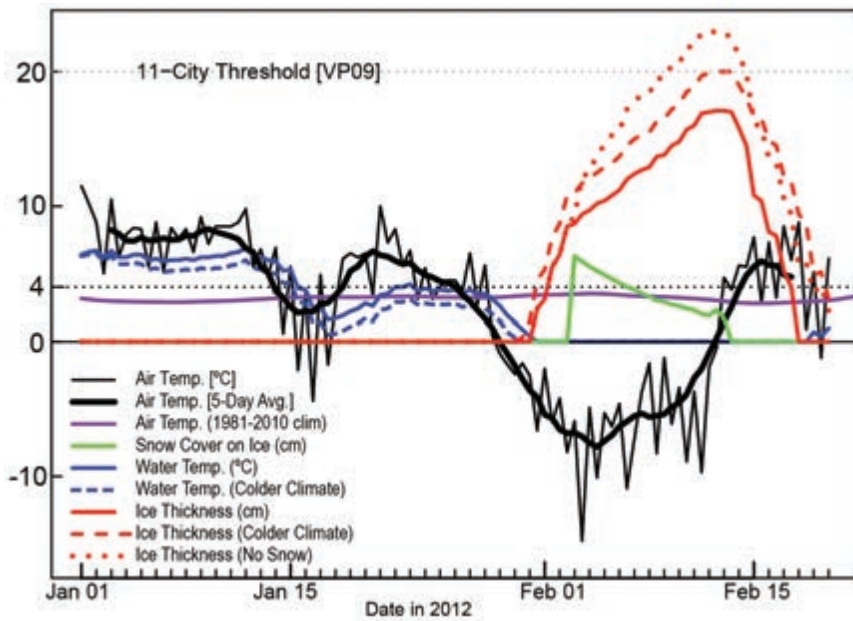


FIG. 9.2. The cold spell 2012 as simulated by the KNMI ice model (de Bruin and Wessels 1988), showing observed snow depth (green), 12-hourly temperature (thin black), five-day average (thick black), 1981–2010 climatology (purple), simulated water temperature (blue), and ice thickness (red). The dashed lines indicate a simulation in a colder climate, while the dotted line indicates the ice growth without snow. (Source: KNMI.)

mate. The Netherlands has warmed by about 1.5°C since 1950 (Kattenberg et al. 2008). This is actually a conservative estimate as the cold spells warm more strongly because of the stronger warming of Siberia (de Vries et al. 2012a). The resulting ice growth curve leads to a marginal situation where the ice thickness would have been almost equal to the historic threshold.

natural variability in these events is large, leading to low signal-to-noise ratios. A remaining question is whether future cold spells will be accompanied by increasingly frequent snowfall events. There are indications from both observations and global climate models that the opposite is the case (de Vries et al. 2012b), but this has to be verified in more detail using regional climate models.

Conclusions. We have analyzed the February 2012 cold spell from the perspective of its ability to generate sufficient ice thickness to organize the classic 200-km ice-skating 11-City Tour in the Netherlands. Despite very low temperatures, the ice was too thin in many locations. We investigated whether global warming could be responsible for this. A simulation with the KNMI ice-growth model, however, points to another more important cause. Snowfall on the thin ice that had just formed is shown to limit the ice growth more strongly than the effect of warming. This study emphasizes that interpreting the role of global warming in the cases of extreme winter European cold spells has to be carried out with care, as the

10. THE EXTREME EUROPEAN SUMMER 2012

BUWEN DONG, ROWAN SUTTON, AND TIM WOOLLINGS

Introduction. The summer of 2012 was marked by strongly contrasting precipitation anomalies across Europe. For example, the United Kingdom experienced its wettest summer (JJA) since 1912, which led to widespread flooding. Spain, in contrast, suffered drought and wildfires associated with the second lowest summer rainfall in the last 60 years (see “The Record Winter Drought of 2011–12 in the Iberian Peninsula” in this report). These extremes were associated with a clear dipole in precipitation anomalies, indicating a northward concentration of European precipitation (Fig 10.1b). Here we show

that the precipitation anomalies can be understood as consequences of anomalies in the large-scale atmospheric circulation. We also present preliminary investigations into the potential role of anomalous SSTs in forcing the atmospheric circulation.

Large-scale circulation. The JJA 2012 anomalies in European precipitation were related to a large-scale dipole pattern in sea level pressure (SLP) over the North Atlantic (Fig 10.1a), with low-pressure anomalies stretching from the Atlantic across the British Isles and Scandinavia (tracking the region of high

precipitation) and high pressure over Greenland. This pattern projects strongly onto the negative phase of the summer North Atlantic Oscillation (SNAO; Folland et al. 2009).

As in winter, this dominant pattern of variability describes meridional shifts of the storm track and the associated eddy-driven jet. However, the seasonal migration of the storm tracks means that over

Europe, the precipitation response is opposite to that in winter, so that a northward shift of European precipitation is associated with a negative SNAO and a southward shift of the Atlantic storm track and jet (Dong et al. 2013, manuscript submitted to *Environ. Res. Lett.*). These features are illustrated for JJA 2012 in Figs. 10.1e–h. Compared to climatology, the jet in summer 2012 was displaced south over the eastern

North Atlantic and extended into central Europe. The climatology of cyclone track density (Fig. 10.1g) shows a split into two preferred cyclone paths, one passing to the south of Iceland and into the Nordic Seas and the other across the British Isles and into southern Scandinavia. In the summer of 2012, almost all cyclones took the southern path, following the northern flank of the jet across the British Isles (Fig. 10.1h). The European precipitation anomalies are, therefore, consistent with the modulation of preferred cyclone paths and the large-scale circulation.

Summer 2012 in the context of recent variability. The Atlantic/European summer of 2012 should not be viewed in isolation but as the latest in a succession of very similar summers. A dipole in precipitation anomalies resembling that in Fig. 10.1b was very clear in all of the summers from 2007 to 2011, with the exception of summer 2010 (Supplementary Fig. S10.1). Similarly, the SNAO has been negative for all of the last six summers (e.g., Allan and Folland 2012). Taking JJA means of the daily SNAO index from NOAA's Climate Prediction Center gives values of -0.8, -1.9, -1.6, -1.1, -2.0, and -2.2

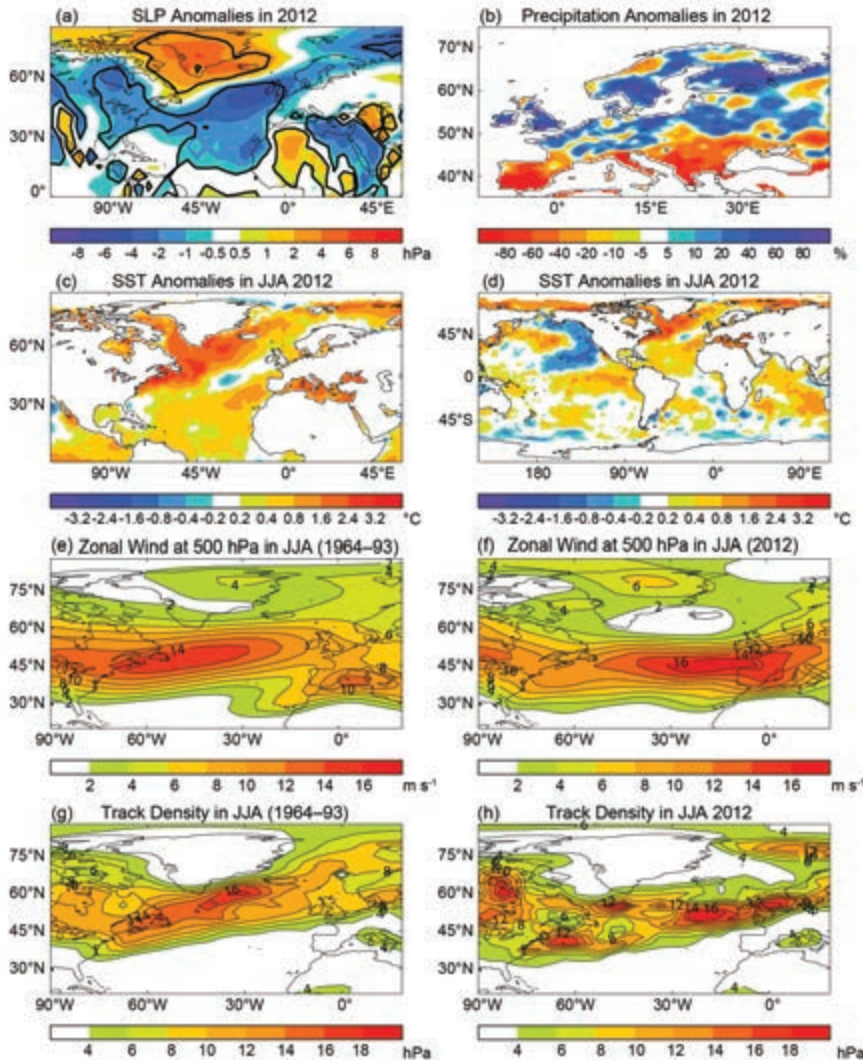


FIG. 10.1. Anomalies for JJA 2012 from the climatological period 1964–93 for (a) SLP (hPa) from HadSLP2, and (b) percentage precipitation change (%) from the daily gridded E-OBS precipitation (version 7.0) over Europe (Haylock et al. 2008). (c), (d) SSTs (°C) from HadISST (Rayner et al. 2003). 500-hPa zonal wind (m s⁻¹) from the NCEP reanalysis for (e) the climatological period 1964–93 and (f) 2012. Cyclone track density as in Hoskins and Hodges (2002) for (g) the climatological period and (h) 2012. Track density is in unit of numbers per month per unit area, where the unit area is equivalent to a 5° spherical cap (about 10⁶ km²). Note that this climatological period is dominated by cold AMO conditions and is the period used for the climatological model simulations. Thick lines in (a) highlight regions where the differences are statistically significant at the 90% confidence level using a two-tailed Student's *t* test.

standard deviations for the summers from 2007 to 2012. These summers contain four out of the five in the record since 1950 that have an index with less than -1.5 standard deviations. Similarly, in the England and Wales precipitation record (Alexander and Jones 2001), 2012 was the wettest summer since 1912, and the average anomaly of the last six summers is 1.15 standard deviations (with respect to the last 100 years, 1913–2012). This string of recent European summers is consistent with the high importance of decadal variability in shaping European summer climate. Sutton and Dong (2012) demonstrated clear variations on decadal timescales in SLP and precipitation patterns across Europe, which are very similar to those seen in summer 2012. This is consistent with the low-frequency variability of the SNAO (Folland et al. 2009), which suggests the influence of some factor external to the atmosphere.

These decadal variations in large-scale circulation are well correlated with basin-wide fluctuations in Atlantic Ocean SSTs, known as the Atlantic Multidecadal Oscillation (AMO). The recent summers occurred during a period of warm SSTs not seen since the 1950s, and it is likely that these Atlantic temperatures have played a role in influencing the SNAO (Knight et al. 2006; Folland et al. 2009; Sutton and Dong 2012). The North Atlantic SST anomalies for JJA 2012 (Fig. 10.1c) show a similar structure to that associated with the AMO and with interannual variations of the summer storm track (Dong et al. 2013, manuscript submitted to *Environ. Res. Lett.*). Warm SSTs are evident across the subtropics but especially in the subpolar North Atlantic, where anomalies exceed 2°C. This anomaly pattern reflects the superposition of the mixed layer ocean response to the atmospheric anomalies and the low-frequency warming associated with the AMO (Dong et al. 2013, manuscript submitted to *Environ. Res. Lett.*).

Global SST anomalies for the same season are given in Fig. 10.1d, showing close to neutral ENSO conditions in the tropical Pacific. Outside of the North Atlantic, the strongest anomalies are in the subtropical/midlatitude

North Pacific. Warm anomalies are evident in the Arctic, consistent with the continuing decline of sea ice. The rate of this decline might have been enhanced by recent atmospheric circulation anomalies related to the SNAO (Overland et al. 2012), and these sea ice extent anomalies may have had an influence on the atmospheric circulation (Balmaseda et al. 2010).

Investigating the potential role of external forcing. We now briefly report on preliminary numerical model experiments to assess the importance of the SST and sea ice anomalies seen in summer 2012. We use the atmosphere configuration of the UK Met Office Hadley Centre Global Environment Model version 3 (HadGEM3-A), similar to the version used by Hewitt et al. (2011), with a resolution of 1.875° longitude by 1.25° latitude and 85 levels in the vertical. The experiments performed are summarized in Table 10.1; the last 25 years of each experiment are used for analysis. The CONTROL experiment reproduces the observed SLP and precipitation patterns very realistically for JJA (Supplementary Fig. S10.2).

The SLP changes in the GLOBAL simulation show a significant low-pressure response around 30°N over North America, the Atlantic Ocean, and North Africa, also extending into Southern Europe (Fig.

TABLE 10.1. Summary of Numerical Experiments

Experiments	Boundary Conditions	Length of Run
CONTROL	Forced with monthly climatological SST and sea ice averaged over the period 1964–93 using HadISST (Rayner et al. 2003)	32 years
GLOBAL	Forced with monthly SST and sea ice from Dec 2011 to Nov 2012	27 years
ATLANTIC	Forced with SST and sea ice from Dec 2011 to Nov 2012 over the Atlantic sector (including the southern Atlantic Ocean) in the longitude range 32.5°W–17.5°E and climatological SST and sea ice outside the Atlantic	27 years
NORTH ATLANTIC	Forced with SST and sea ice extent from Dec 2011 to Nov 2012 over the North Atlantic (north of 35°N with SST linearly smoothed southward to the climatology at 30°N) but climatological SST and sea ice outside the North Atlantic	27 years

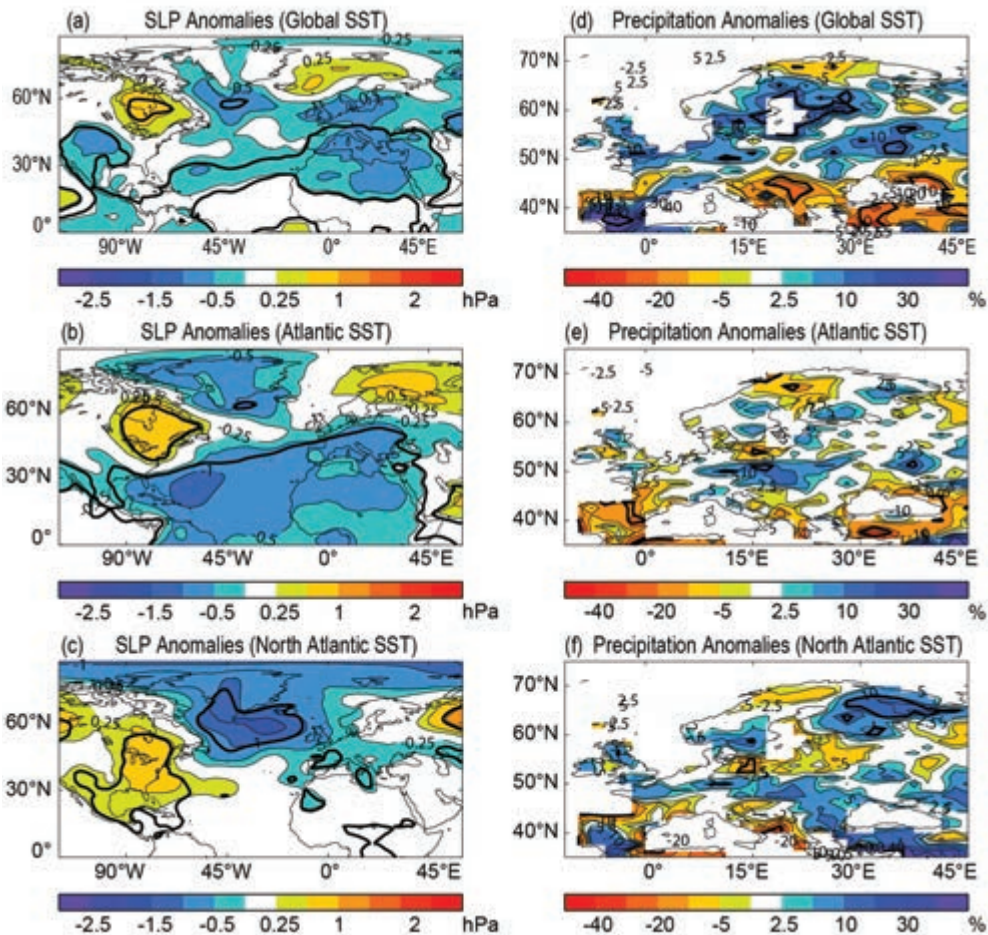


FIG. 10.2. (a)–(c) SLP anomalies (hPa) and (d)–(f) precipitation changes (%) in the model simulations forced by different configurations of SST and sea ice in 2012 relative to the control simulation forced by climatological SST and sea ice (1964–93 mean). (a) and (d) Forced by global SST and sea ice in 2012; (b) and (e) forced by SST and sea ice in 2012 over the Atlantic sector but with climatological SST outside the Atlantic; and (c) and (f) forced by North Atlantic (northward of 35°N) SST and sea ice in 2012, with climatological SST and sea ice outside the North Atlantic. Thick lines highlight regions where the differences are statistically significant at the 90% confidence level using a two-tailed Student’s *t* test.

10.2a). Over Northern Europe, a pattern resembling the negative phase of the SNAO is simulated, but the anomaly is much weaker than that observed (Fig. 10.1a) and is not significant. The pattern of simulated European precipitation anomalies (Fig. 10.2d) is consistent with the negative phase of the SNAO, and is, therefore, very similar to the observations (Fig. 10.1b), but the magnitudes are again much weaker.

The ATLANTIC experiment shows a much stronger SLP response in the tropical North Atlantic (Fig. 10.2b). This is part of a baroclinic response (vertical structure not shown) that is not consistent with the observations and suggests that the influence of SST anomalies outside the Atlantic damps the direct response to Atlantic SSTs in this region. Negative precipitation anomalies are again simulated in southern

Europe, but the pattern further north is very noisy (Fig. 10.2e).

In the NORTH ATLANTIC experiment, the model simulates a substantial low-pressure anomaly over the midlatitude North Atlantic, with a weak extension into western Europe (Fig. 10.2c). This is similar to the response found (using a different model) by Sutton and Hodson (2005) and suggests a significant response to the warm SST anomalies in the northwest Atlantic (Fig. 10.1c), but one which is sensitive to the influence of lower latitude Atlantic SST anomalies (implied by comparison Figs. 10.2b and 10.2c). The response is equivalent barotropic (not shown), which indicates a significant role for eddy-mediated processes (e.g., Kushnir et al. 2002; Feldstein 2007). Consistent with the observations (Fig. 10.1a), the

simulated SLP response implies enhanced westerly winds to the southwest of the United Kingdom, but the response is weaker than the observed anomalies and is displaced northwards.

Overall, the model results suggest that the atmospheric circulation over the North Atlantic and European region in summer 2012 (negative phase of the SNAO), which was largely responsible for the observed extreme anomalies in European precipitation, was influenced by global SST and sea ice extent anomalies, and that it is likely that SST anomalies in the North Atlantic played a particularly important role (consistent with Dong et al. 2013, manuscript submitted to *Environ. Res. Lett.*; Sutton and Hodson 2005). Differences between the simulated responses and observed anomalies—in terms of both spatial patterns and the much weaker magnitude of the simulated anomalies—require some explanation. The simplest explanation would be internal variability. However, the fact that 2012 is only the latest in a series of negative SNAO European summers makes this possibility unlikely. Furthermore, the level of internal variability in the model simulations is insufficient to account, with significant likelihood, for the magnitude of the observed anomalies (not shown). Other possible factors include an important role for coupled ocean-atmosphere interactions in shaping

the response (Sutton and Mathieu 2002; Dong et al. 2013, manuscript submitted to *Environ. Res. Lett.*) and the direct impact of changes in radiative forcings from greenhouse gases and aerosols, which were not considered in the experiments discussed here. Model biases may also be a factor. Investigating these possibilities is the subject of ongoing research.

Conclusions. The European summer of 2012 was marked by strongly contrasting rainfall anomalies, which led to flooding in northern Europe and droughts and wildfires in southern Europe. This season was not an isolated event, rather the latest in a string of summers characterized by a southward shifted Atlantic storm track as described by the negative phase of the SNAO. The degree of decadal variability in these features suggests a role for forcing from outside the dynamical atmosphere, and preliminary numerical experiments suggest that the global SST and low Arctic sea ice extent anomalies are likely to have played a role and that warm North Atlantic SSTs were a particular contributing factor. The direct effects of changes in radiative forcing from greenhouse gas and aerosol forcing are not included in these experiments, but both anthropogenic forcing and natural variability may have influenced the SST and sea ice changes.

II. ARE RECENT WET NORTHWESTERN EUROPEAN SUMMERS A RESPONSE TO SEA ICE RETREAT?

SIMON F. B. TETT, KIRSTEN DEANS, EDOARDO MAZZA, AND JAMES MOLLARD

Introduction. Since 2007, UK and northwestern (NW) European summers have been anomalously wet, with summer 2007 being notable for significant flooding in southern England. Arctic sea ice extent had record low values in September 2007 and 2012 (Parkinson & Comiso, 2013). To explore the potential impact of these changes in sea ice on precipitation, we carried out a set of numerical simulations of the high-resolution version of HadAM3 (Pope et al. 2000) driven with different sea surface temperature and sea ice boundary conditions.

Observational data and experimental design. We focus on percentage of 1961–90 precipitation from the Global Precipitation Climatology Centre GPCP reanalysis V5 $1^\circ \times 1^\circ$ product for which we use 1950–2006. From 2007 to 2012, we use the GPCP monitoring product

(Schneider et al. 2011) to give a homogeneous dataset from 2007 and allow consideration of 2011 and 2012 in near-real time. We processed the GPCP datasets so that in each $1^\circ \times 1^\circ$ grid box where there are no stations the data was set as 'missing'. Precipitation was conservatively regridded to the $1.25^\circ \times 1.875^\circ$ grid of the model and converted to percentage of the 1961–90 seasonal average. We then area-averaged the percentage of normal precipitation for the northwest European region—the western half (48°N – 75°N , 10°E – 15°W) of the northern European region of Giorgi and Francisco (2000). We find that the GPCP monitoring dataset is biased with respect to the reanalysis dataset, so we correct the monitoring product by the difference between it and the reanalysis product for the 2007–10 period of overlap. These biases are generally between -10% and 10%, though larger in dry regions. For NW

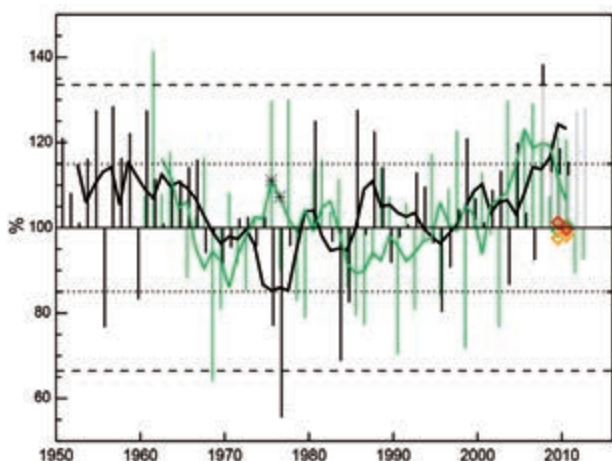


FIG. 11.1. Mean JJA percentage of normal (1961–90) precipitation in northwest Europe for GPCP reanalysis precipitation (black bars), 1960–2012 HadAM3P simulation (green bars), and GPCP monitoring data (gray bars). Observed precipitation is displaced rightwards from simulated precipitation. Also shown are the five-year running average values for combined GPCP data (thick black); Historical simulation (thick green); and from 12-member Historical ensemble (green diamonds), Ice85_89 ensemble (orange diamonds), and Ice85_90-NH ensemble (red diamonds). Dashed (dotted) lines show 2- σ range from five-year smoothed (unsmoothed) intra-ensemble variability. Black line outside that range indicates observed or simulated values significantly different from normal. Asterisk values on the simulated smoothed time series show where model and observations are significantly different.

Europe the area-average bias is about 4% (Fig. 11.1), though with some year-to-year variability. In addition to the precipitation record, we also use the variance reduced HadSLP2r record (Allan and Ansell 2006).

The observed precipitation time series shows considerable year-to-year variability ranging from 55% to 140% of the 1961–90 normals (Fig. 11.1). The five-year running mean time series has a smaller range of 85%–125% of normal and has its largest values for the 2007–11 average. The six-year average for June–August (JJA) 2007–12 has anomalously high precipitation across most of northern Europe (Fig. 11.2a) with the exception of northern Norway. Parts of western Scotland, Iceland, Greenland, Svalbard, and southern Europe are also anomalously dry. This is consistent with the mean sea level pressure (MSLP) anomalies with a low centered on Britain and a high over Greenland with only small changes in MSLP in the Mediterranean region. As suggested by others (e.g., “The Extreme European Summer 2012” in this report), this is consistent with a southwards shift of the summer storm track. While

NW Europe is anomalously wet, southern Europe has about 50%–75% of normal precipitation.

We explore three hypotheses for the recent NW European rainfall anomaly: (i) internal atmospheric variability, (ii) forced by recent changes in *both* SST and sea ice, and (iii) forced only by changes in SST.

To explore these hypotheses we used the HadAM3P Atmosphere General Circulation Model (Rowell 2005), which is a N96 ($1.25^\circ \times 1.875^\circ$) resolution version of HadAM3 (Pope et al. 2000) with some other changes. We drove it with the HadISST dataset (Rayner et al. 2003) with both SSTs and sea ice area-averaged to N96 resolution. HadISST uses SSM/I (Special Sensor Microwave Imager) data to estimate sea-ice. SSMI degraded in early 2009 and was replaced with data from AMSR-E (Advanced Microwave Scanning Radiometer - Earth Observing System). Screen (2011) investigated the impact of this and found it had a large impact in the southern hemisphere but found no apparent step-changes in Arctic sea-ice extent. Nevertheless, there remains the possibility of time-varying biases in the HadISST record.

The model was also driven with historical concentrations of greenhouse gases, and both the direct and indirect effect on cloud brightness (Jones et al. 2001) were included with SO_2 emissions using the historical IPCC emissions. Land-surface values were set to standard climatological values, and ozone values used the ozone forcing dataset of Tett et al. (2007). A single simulation driven with these boundary conditions was run from December 1959 to August 2012 (“Historical”). A further 11 simulations were started from the December 2006 state with small random perturbations. In addition to this “factual” ensemble, we carry out two “counterfactual” ensembles in which sea ice was set to monthly average conditions for 1985–89. Both ensembles start with December 2005 conditions from the Historical simulation and run for seven years (Table 11.1).

In the first ensemble (“Ice85_89”), we set all sea ice fractions to the 1985–89 seasonal-average. In the second ensemble (“Ice85_89-NH”) we only do this in the Northern Hemisphere. In all cases sea ice fractions below 0.1 were set to zero. Where sea ice fractions were set to their 1985–89 average, we also set SST to the 1985–89 value. A few times and locations had sea ice but no sea ice in the 1985–89 average. For those locations, we set the sea ice to zero and SST values to the 1985–89 average. Locations and times where

TABLE 11.1. Summary of numerical experiments and experiment IDs.

Experiment	Historical: Dec 1959–Aug 2012	Historical: 11-member ensemble Dec 2006–Aug 2012	Ice85_89: 12-member ensemble Dec 2005–Nov 2012	Ice85_90-NH:12-member ensemble Dec 2005–Nov 2012
Boundary Conditions	HadISST SST and sea ice + forcings	HadISST SST and sea ice + forcings	Mean 1985–89 sea ice, HadISST SST + forcings	Mean 1985–89 NH sea ice, HadISST SST and sea ice + forcings
Experiment ID	xhod#g/xhsw#a	xhsw#n-#w	xija#a-#l	xijj#a-#l

there was no sea ice and none in the 1985–89 average were unmodified.

Results. Before using a model to evaluate recent changes we need to have some confidence in its ability to simulate observed means and variability. The climatological JJA MSLP from the Historical simulation is broadly consistent with the observed climatology (Fig. 11.2b,c) though missing the arc of low pressure in northern Europe. Both simulations and observations show the least precipitation in the Mediterranean and the most in the West. The simulation is generally drier than the observations so further analysis focuses on the percentages of normal.

For our study we assume that both the simulations and observations consist of deterministic and unpredictable components with the latter arising from internal climate variability. We estimate the unpredictable component from the pooled intra-ensemble variances of the three 12-member ensembles for 2007–12. This is about 70% of the Historical simulation’s variance. Cautiously assuming that simulated and smoothed intra-ensemble variability for the 2007–12 period is representative of the entire 1960–2012 period, then SST variability contributes about 30% of the variance in NW European precipitation.

The results from the single Historical simulation are largely consistent at the two-sigma level with observations for 1960–2012 (Fig. 11.1). However, there is one period around 1975 when the difference between the two-filtered time series is significant. In a time series, we would expect differences to arise solely by chance, and to test for this possibility, we use a Kolmogorov-Smirnov test on the two datasets and an F-test on the sum-of-squares of the differences weighted by twice the intra-ensemble variance. We applied both these tests on the summer averages and on five-year smoothed summer averages (sampling every fifth point) and found no significant differences. We also compared the simulated and observed

standard deviations and found simulated values were larger, though not significantly so, than the observed values. The simulated and observed lag-1 autocorrelations are also not significantly different from one another. Overall, this suggests that we can use the variability in HadAM3P to evaluate the observed changes.

Among recent summers, only 2007 is outside 2σ of the 1961–90 climatology (Fig. 11.1). This illustrates the difficulty in analyzing individual events when there is a great deal of internal variability and so we focus on longer timescales. On five-year timescales, the recent run of wet summers is extremely unusual with observed values at about 120% of normal, corresponding to a deviation of more than 2.5 standard deviations. For each of the factual, counterfactual, and counterfactual-NH ensembles the average NW Europe precipitation for 2007–12 is close to 100% (Fig.11.1). These are all inconsistent with observations. The maximum percentage of normal precipitation from any single simulation in the three ensembles is 112%. This suggests that the recent changes cannot be explained by sea ice changes or internal variability, as simulated by HadAM3P.

Where the observations have anomalously low pressures (Fig. 11.2a), the differences between them and the 2007–12 Historical ensemble average (Fig. 11.2d) are significant at the 2σ level. MSLP differences are also significant over Greenland and Russia. Precipitation percentage differences are significant over Ireland, Wales, much of Scotland, and around the Baltic. Interestingly, in the Mediterranean region, the differences are less significantly different suggesting that HadAM3P is capturing the observed drying there.

In HadAM3P during 2003–07, the NW European precipitation is more than 120% of normal and so is comparable with the recent observed extreme values. The percentage precipitation and MSLP patterns for this period (not shown) are different from the observed

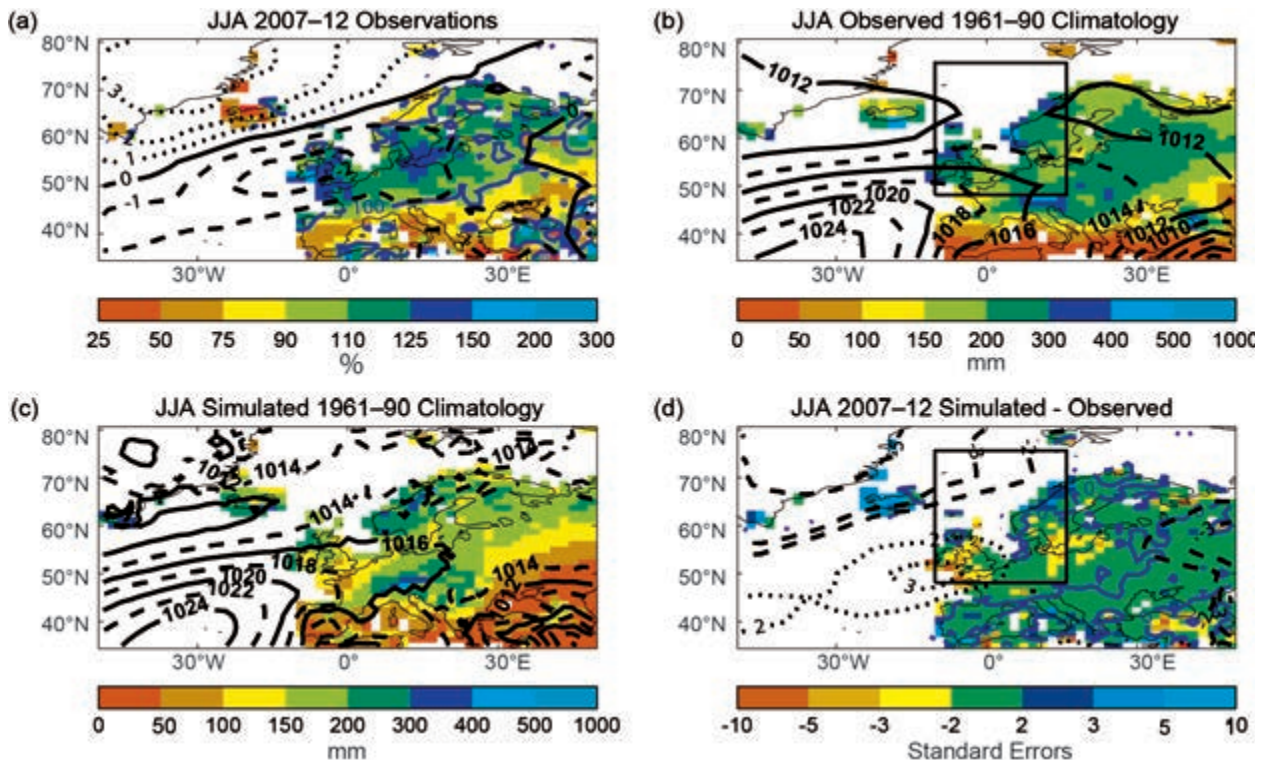


FIG. 11.2. (a) Percent of 1961–90 precipitation (color scale) and difference from 1961–90 mean sea level pressure (contours every hPa). Blue contour line shows 100% precipitation. (b) Summer total land precipitation (mm) from GPCP reanalysis (color scale) and HadCRUT2r MSLP (contours every 2 hPa) for 1961–90. (c) Same as (b) but for HadAM3P simulation. MSLP pressure has been adjusted by difference (about 2 hPa) between global average JJA climatological and simulated MSLP. (d) Difference in standard errors (see main text) between adjusted GPCP monitoring product and 12-member historical ensemble for precipitation (color) and MSLP (contour lines). Blue line shows zero difference. Values are at -10, -5, -3, -2, 2, 3, 5, and 10 standard errors. The black box in plots (b) and (d) show the NW Europe region.

pattern in 2007–12. The observations are characterized by a southwards shift of the storm track, while the model has an east/west dipole suggesting a westward shift of the storm track. This suggests that the earlier extreme precipitation event in the model is not comparable with the recent observed precipitation anomalies.

Conclusions. Recent summers in NW Europe have been unusually wet with the 2007–11 average having the largest percentage of normal precipitation for 1950–2012 and are, based on model variability, significantly different from the 1961–90 normal. The circulation anomaly associated with this event is consistent with a southward shift in the summer storm track. We find no evidence that declines in sea ice can explain these recent wet summers, with the expected response to changes in sea ice since the late 1980s being small. Our results support the findings of Screen et al. (2013)

who found (their Fig. 7) no significant precipitation response in summer to sea ice decline over NW Europe.

HadAM3P did not, in any of 36 simulations, produce a precipitation anomaly for 2007–2011 or 2008–2012 similar to that observed. The simulated 5-year average from 2003–2007 had average NW Europe percentage precipitation comparable to the observed values for 2007–2011. In this case the mechanism appears different with a westward shift of low pressure over Europe rather than a southwards shift as observed. Thus we conclude that the recent precipitation anomalies over North Western Europe likely represent an unusual event not well represented in HadAM3P. Given that HadAM3P is not capable of simulating the recent heavy precipitation, the possibility remains that recent European summer precipitation anomalies are due to other drivers in the climate system rather than chance.

12. THE USE OF A VERY LARGE ATMOSPHERIC MODEL ENSEMBLE TO ASSESS POTENTIAL ANTHROPOGENIC INFLUENCE ON THE UK SUMMER 2012 HIGH RAINFALL TOTALS

SARAH SPARROW, CHRIS HUNTINGFORD, NEIL MASSEY, AND MYLES R. ALLEN

Introduction. In 2012, the United Kingdom experienced a drier than average first three months followed by an exceptionally wet period lasting well in to the summer months. Overall, 2012 was the wettest on record since 1910 (CEH 2012), except for 2000 (Met Office 2013). The high rainfall amounts experienced were brought in to focus given the international attention placed on the United Kingdom in the months leading up to the Olympics. The contrasting rainfall features are particularly noteworthy given that towards the end of March 2012, many water utility companies were warning of potential drought conditions ahead, including predictions such as summer hosepipe bans. At the end of March, reservoir levels were becoming exceptionally low in water levels (CEH 2012). However, by the end of year 2012, flooding was causing repeated problems, affecting homes and the ability to travel (JBA Risk Management and Met Office 2012). The aim of this study is to assess whether there was an attributable anthropogenic contribution to the high rainfall totals experienced over the United Kingdom in summer 2012.

Experimental configuration. Existing studies with single simulations by a “nested” version of the Hadley Centre Regional Climate Model (RCM) suggest that for many parts of the United Kingdom and as atmospheric greenhouse gas concentrations rise, extreme rainfall return periods might reduce in the future (Huntingford et al. 2003). Here we use very large ensembles of the atmospheric component of version 3 of the Hadley Centre GCM; (Pope et al. 2000), HadAM3P, combined with the same model in a nested regional configuration over Europe. These simulations have been undertaken by “citizen scientists,” through performing calculations by their screensavers and on otherwise idle computers, and in each instance with slightly altered initial conditions (Allen 1999). This system, called ClimatePrediction.Net (CPDN), has already been utilized to analyze the floods of 2000 (Pall et al. 2011).

The advantage of large ensembles is that they can generate well-sampled distributions of predicted quantities of interest (in this case, precipitation) and account for chaotic aspects of the weather system, where predictions can diverge significantly even if initialized with almost identical starting conditions. Such distributions can be derived for present day and simultaneously for an estimate of preindustrial conditions by running the same model setup with two different climate scenarios and associated forcing conditions.

Hence, we make two ensembles, one representing 2012 and the other representing an imagined analogous year in the preindustrial period. This involves the prescription of differences in three sets of driving conditions between these scenarios: (i) changes of atmospheric gas constituents (most notably raised levels of carbon dioxide), (ii) different SSTs, and (iii) different sea ice fractions. SST and sea ice fraction values for 2012 are taken from the Operational Sea Surface Temperature and Sea Ice Analysis (OSTIA) dataset (Stark et al. 2007; Donlon et al. 2012). To estimate preindustrial conditions for SSTs, we calculate SST differences between nonindustrial and present day simulations of the HadGEM2-ES model and subtract them from the OSTIA SST data for 2012. For nonindustrial sea ice, we adopt conditions that correspond to the year of maximum sea ice extent in each hemisphere of the OSTIA record. The ensemble modeling structure then provides two probability distributions of seasonal rainfall for each UK grid box: for 2012 (called “All Forcings” and with prescribed CO₂ concentration of 385 ppm) and for an estimate of nonindustrial conditions (called “Natural,” CO₂ concentration of 296 ppm), available from the nested RCM.

Modeling summer 2012 UK precipitation. We present our findings in Fig. 12.1, where we concentrate on the summer period of June, July, and August (JJA). In panel (a), we show the actual seasonal mean

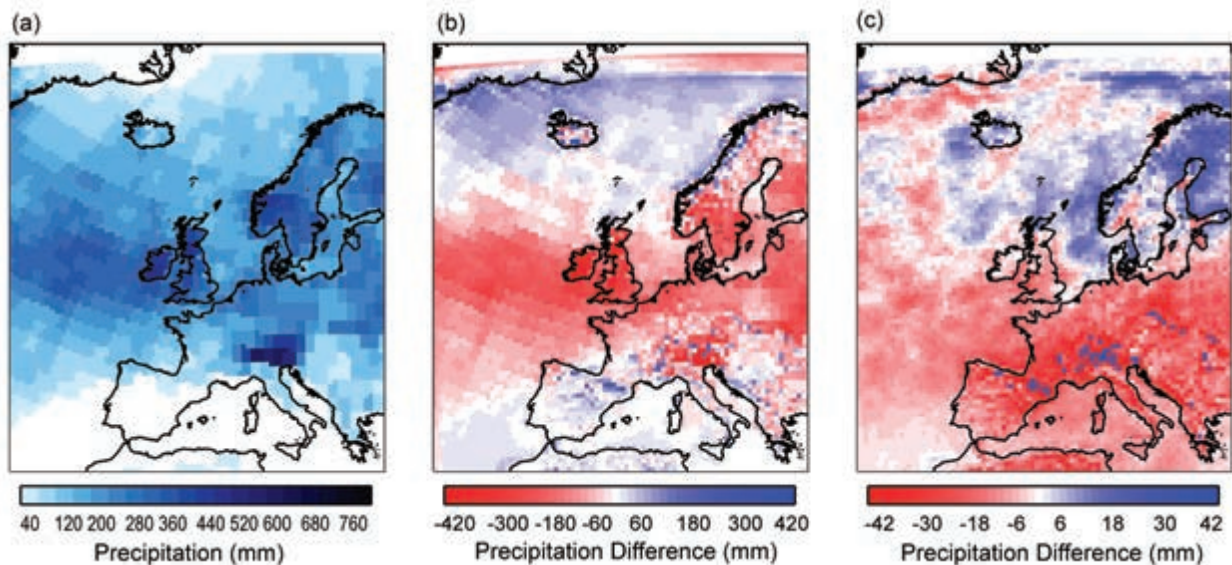


FIG. 12.1. (a) ECMWF ERA-Interim estimates of Jun–Aug 2012 total rainfall (mm) mapped onto part of the nested European RCM grid of the CPDN simulations with HadAM3P. (b) The difference in total seasonal rainfall between the 50th percentile of the All Forcings simulation (representative of 2012) and the ERA-Interim data. (c) The difference at the 50th percentile between the All Forcing and Natural (latter representative of preindustrial conditions).

rainfall amounts based on the European Center for Medium Range Weather Forecasting (ECMWF) Interim reanalysis product (Dee et al. 2011). In panel (b), we show the difference between the ECMWF values of panel (a) and the 50th percentile from the All Forcings ensemble. The differences in this plot are large, especially for the United Kingdom. In fact, the rainfall amounts from the ECMWF reanalysis dataset are greater than the 99th percentile for the All Forcings ensemble distribution for most locations in the United Kingdom. This implies one of two possibilities: either (1) our findings are correct for the prescribed atmospheric CO₂ concentrations, SST, and sea ice fractions appropriate to 2012, then the chances of the observed summer UK rainfall patterns occurring are in fact incredibly small, or (2) there are systematic biases in our atmospheric modeling structure. These biases possibly correspond to raised rainfall amounts falling incorrectly over the seas more to the north of the United Kingdom, rather than over the United Kingdom as seen in the observations. Problems in capturing heavy precipitation with this model have also been noted in "Are Recent Wet North Western European Summers a Response to Sea-Ice Retreat?" in this report. Figure 12.1c shows the precipitation difference between the 50th percentile All Forcings simulation minus that of Natural. There is a distinct geographical feature where, in general, northerly regions experience higher

JJA rainfall amounts, whereas for southern Europe the opposite is true. The United Kingdom lies close to the nodal line of this pattern.

In Fig. 12.2a, we present the SST changes prescribed to our modeling system, which are based on HadGEM2-ES GCM. When compared to the differences in the observationally based HadISST dataset (Rayner et al. 2003) of seasonal decadal averages between the 1880s and the 2000s [shown in panel (b) and as 2000s minus 1880s], our model-based changes, although of a similar magnitude on a global scale, show different patterns locally. The largest discrepancies in the SST differences occur in the North Atlantic and North Pacific, the former of which could impact modeled storm tracks and European weather patterns (Brayshaw et al. 2011; Woollings et al. 2012).

How was summer 2012 UK precipitation influenced by climate change? If we regard the rainfall experienced as an extreme event for the given year, 2012, CO₂ concentrations and SST and sea ice conditions (i.e., possibility "i" above), produced by the natural variability of the climate system, then we may still wish to understand how anthropogenic forcings may have altered its probability of occurrence. Our calculations of the FAR statistic (Fractional Attributable Risk; methodology e.g., Otto et al. 2012), not shown but based on comparing the two ensembles' distributions at the known precipitation levels, sug-

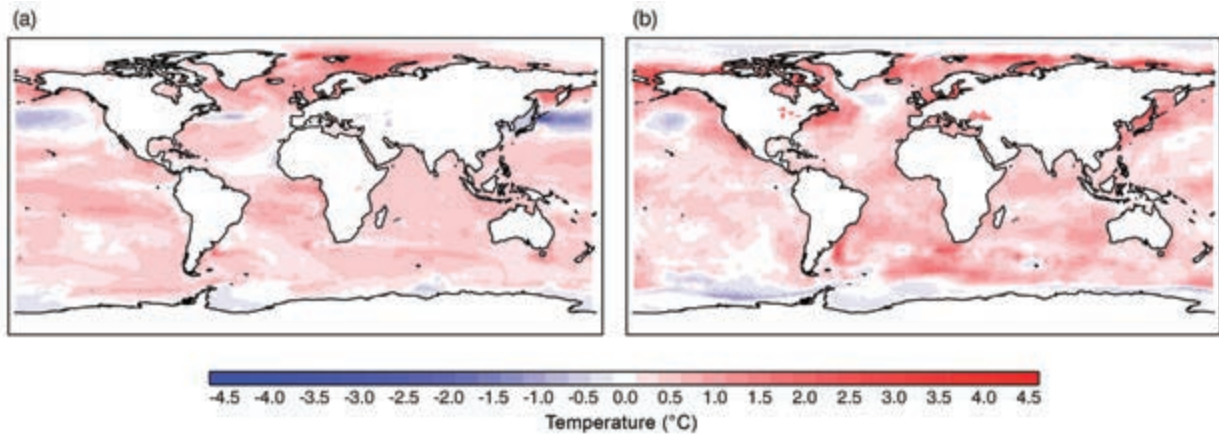


FIG. 12.2. (a) The temperature differences between the HadGEM2ES-based SSTs prescribed to the CPDN simulations, here as All Forcings minus Natural. Panel (b) shows the change in SSTs based directly on the HadISST dataset and presented as the 2000s minus the 1880s.

gests there was almost no anthropogenic influence on the rainfall patterns over the United Kingdom for summer 2012. However, in this instance, we suggest caution in providing this as a headline result. This is because, as noted above, the event occurs beyond the 99th percentile of the All Forcings model ensemble distribution. Instead, we suspect that there remain deficiencies in our atmospheric model that require resolution before making any such definitive statements regarding human influence on changed probabilities of rainfall events. The major differences in modeled and measured forcing SSTs also require consideration. Our initial argument was that until recently (and certainly before satellite retrievals), the number of measurements contributing to SST climatologies is relatively small (Rayner et al. 2003) and model derived differences may be more trustworthy. However, we now plan to make a new set of simulations using both the longer HadISST dataset directly and SST warming patterns based on other GCMs that have contributed to the CMIP5 database. A recently submitted paper (Haynes et al. 2013, manuscript submitted to *PLOS ONE*) using a similar methodology, but an observed pattern of SST warming, shows detectable changes to UK precipitation between the 1960s and 2000s. This study reinforces our conjecture that UK precipitation is sensitive to the pattern of warming in SSTs and not just the magnitude of the changes.

We believe very large ensembles and the associated capability to generate FAR-type statistics is a powerful method to quantify any anthropogenic influence in the event of more extreme weather occurrences. This avoids any polarized views, where statements over

extremes can sometimes reduce to either being completely the fault of human-induced climate change or the opposite. However, this study also reiterates that there are likely still issues of model development and refinement of forcing conditions that need to be undertaken simultaneously. This study shows that taking a purely thermodynamic argument, as in Pall et al. 2011 (their supplementary information), can give potentially misleading results; therefore, it is important to continue building physically based ensembles and within these ensembles, explore the implications of uncertainty in boundary conditions and model physics.

Conclusions. Although the summer UK rainfall in 2012 was unusually large, the model distributions studied suggest that any anthropogenic influence on these patterns was minimal. However, a note of caution must be expressed with regard to this result. Firstly, the summer UK rainfall totals fall beyond the 99th-percentile range of our All Forcings distribution. So, whilst the rainfall experienced may simply have been extreme for the given driving conditions, there may also remain deficiencies in the atmospheric model that need to be resolved. Secondly, large differences exist between the pattern and the amount of observed and model derived SST differences under climate change. We feel it is necessary to establish the impact of such differences before making a formal statement on the size of any human influence to 2012 UK precipitation, based on any probability distributions from GCM ensembles. Further experiments are planned to address these issues.

13. CONTRIBUTION OF ATMOSPHERIC CIRCULATION TO WET NORTH EUROPEAN SUMMER PRECIPITATION OF 2012

PASCAL YIOU AND JULIEN CATTIAUX

Introduction. Northern Europe witnessed anomalously high precipitation rates during the year 2012, especially during summer. The goal of this paper is to put those regional events into the context of long-term variability. In Europe, studies have highlighted that recent temperatures have been systematically warmer than expected due to the North-Atlantic dynamics, which control their intra-seasonal to interannual variability (e.g., Cattiaux et al. 2010; Vautard and Yiou 2009). Here we investigate the contribution of large-scale circulations to the precipitation anomalies of 2012 using the same flow-analogue approach as in the analysis of 2011 temperatures done by Cattiaux and Yiou (2012).

Data. We used in situ measurements provided by the European Climate Assessment dataset at more than 4500 stations over the period 1948–2012 (Klein-Tank et al. 2002). We computed anomalies relative to a 1971–2000 climatology. The daily climatology is obtained by averaging over each calendar day in 1971–2000, then smoothing by splines. We selected 351 stations on the basis of (i) an altitude lower than 800 m, longitudes between 8°W and 40°E and lati-

tudes between 30°N and 72°N, (ii) the availability of more than 70% of daily values between 1 January 1971 and 31 December 2000 for a reliable estimate of the climatology, and (iii) more than 90% of daily values between 1 January 2012 and 31 December 2012 for a reliable estimate of the 2012 anomalies. We averaged precipitation values over Northern Europe (50°N–72°N, 8°W–35°E) after selecting (iv) only one station per $0.5^\circ \times 0.5^\circ$ latitude/longitude box for spatial homogeneity, leaving 142 stations in that region. Although we mainly focus on cumulated precipitation, we also computed the precipitation frequency (or fraction of wet days) for each month, as in Vautard et al. (2007) and Vautard and Yiou (2009). The precipitation frequency is the empirical probability in a given month of observing a daily precipitation rate larger than 0.5 mm. It provides an indicator of the temporal continuity of precipitation.

Observed rainfall anomaly. Anomalously high precipitation rates were observed in Northern Europe (France, Scandinavia, Netherlands, Germany, UK) in June–July 2012 (Fig. 13.1, upper panels). The high precipitation rates extended to August and September in Scandinavia and the United Kingdom, although with a smaller spatial extent. Those wet conditions contrast with drier than usual conditions in Southern Europe (Spain, Balkans, Eastern Europe). The precipitation frequency during summer 2012 also had positive anomalies in Northern Europe, indicating that the rain episodes lasted for prolonged periods of time (Supplementary Fig. S13.1). Therefore, the generally wet conditions mainly concerned the northern part of Europe for summer 2012, with variable conditions (from wet to dry) in France and on the northern coast of Norway.

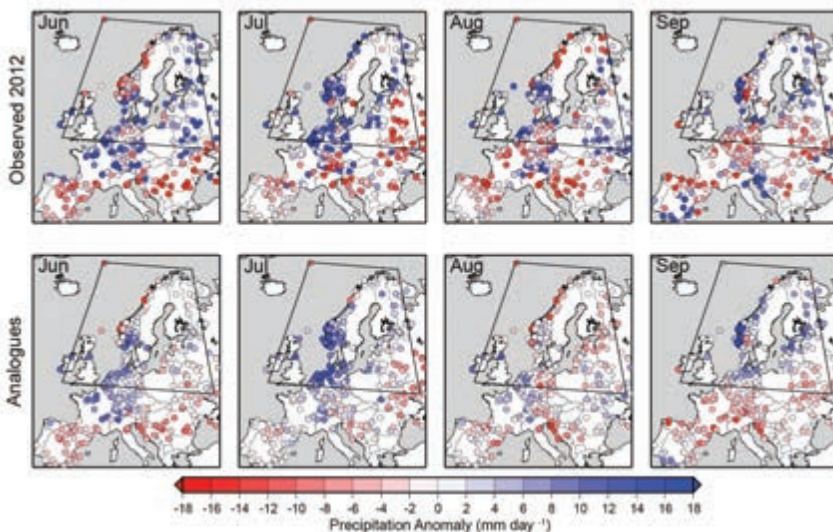


FIG. 13.1. Anomalies of precipitation over Europe (in mm day^{-1}) for the summer months in 2012 (Jun–Sep). The colored points represent the 351 ECA&D stations we retained. The polygon outlines the region over which the averages are computed (50°N – 70°N , 8°W – 35°E). The upper panels represent observed precipitation anomalies; the lower panels represent the mean precipitation obtained from 20 analogues of circulation.

The highest daily precipitation rates in northern Europe occurred in January and October, although high precipitation rates were also observed in June and July (Fig. 13.2a). The longest spell of precipitation in summer was in July.

The time series of seasonal cumulated precipitation for averages of stations north of 50°N and between 8°W and 35°E are shown in Fig. 13.2b. Although the average precipitation anomaly was positive in summer 2012, it was not exceptional over the 1948–2012 period. The records of summer average precipitations occurred in 2011 and 1988, and the 2012 summer is the 13th wettest summer since 1948.

Contribution of the atmospheric circulation. The contribution of the large-scale dynamics to the temperature anomalies of 1948–2012 was estimated from the same flow-analogue approach as used in Cattiaux and Yiou (2012). For each day, we selected the 20 days with the most correlated atmospheric circulation among days of other years but within a moving window of 60 calendar days to account for seasonality (for details, see Yiou et al. 2007). Circulations are derived from sea level pressure (SLP) anomalies of NCEP/NCAR reanalyses (Kistler et al. 2001) and considered over the period 1948–2012 and the area 22.5°N–70°N, 80°W–20°E.

For each station and each day, we computed the mean of the 20 analogue composites. Mean analogue precipitations (averaged over 20 analogue days) are higher than usual in northern Europe, both in terms of precipitation amount (Fig. 13.1) and frequency (Supplementary Fig. S13.1). Spatial

patterns of analogue precipitation follow the observed ones, albeit with lower amplitudes (Fig. 13.1). The spatial correlations are 0.61, 0.56, 0.32, and 0.44 in June to September, respectively. On a daily time scale

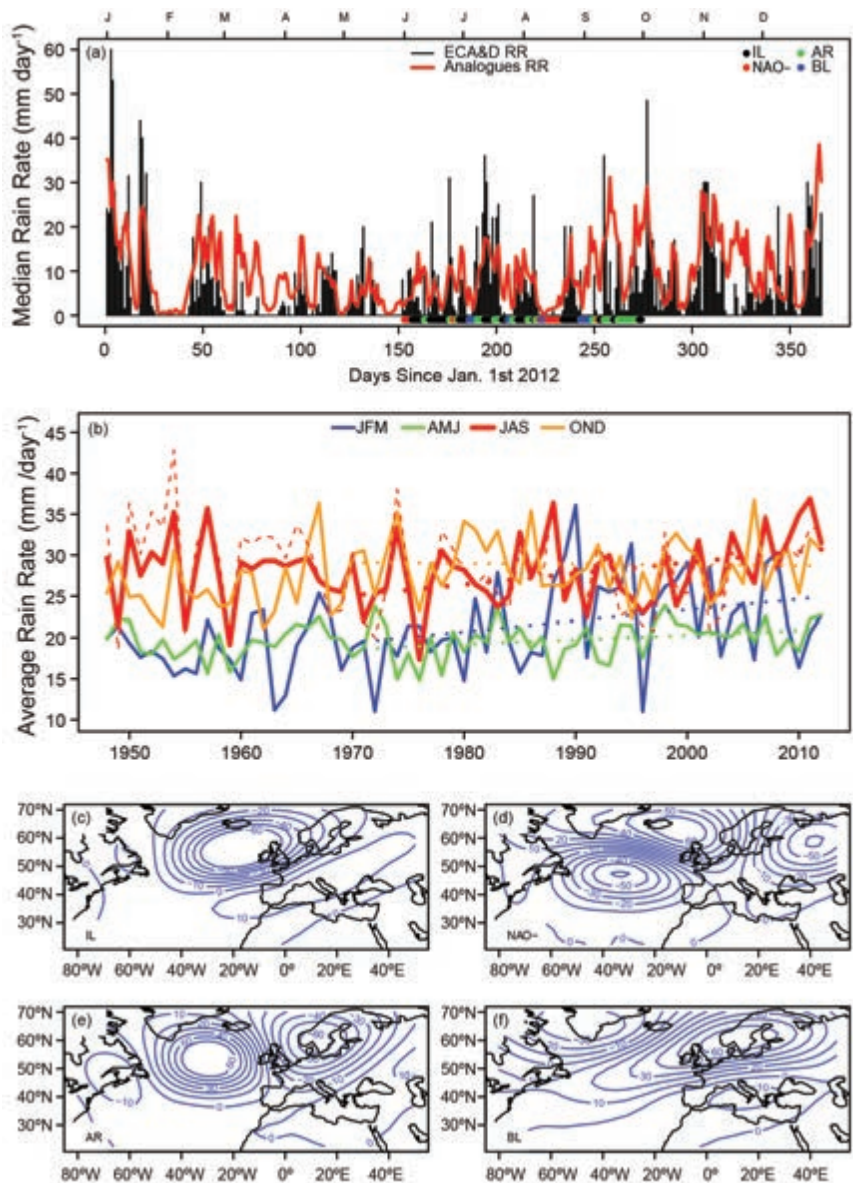


FIG. 13.2. Temporal evolution of precipitation in the outlined northern Europe region and summer weather regimes. (a) Temporal evolution of precipitation in 2012 (black vertical lines). The thick red line represents the median of analogue composites across stations and the 20 analogues. The colored points at the bottom of the panel indicate the daily weather regime. (b) Time series of average precipitation for winter (JFM, black), spring (AMJ, green), summer (JAS, red), and fall (OND, blue) between 1948 and 2012. Dotted lines are the linear trends between 1971 and 2012. The red dashed line represents the mean over northern Europe stations of the upper 75th quantile of analogues. (c)–(f) Summer weather regimes computed from a classification of NCEP sea level pressure data. We use the terminology of Cassou et al. (2005): Icelandic Low (IL), negative North Atlantic Oscillation (NAO), Atlantic Ridge (AR), and Scandinavian Blocking (BL). The isolines (contour intervals every 10 hPa) represent anomalies with respect to a 1971–2000 climatology.

over the northern Europe region, the precipitation analogues follow the observed averages closely (Fig. 13.2a; $r = 0.62$; $p\text{-value} < 10^{-15}$). This shows that the precipitation rates are influenced by the large-scale atmospheric circulation.

In order to describe the circulation patterns of summer 2012, we used the clustering approach of Yiou et al. (2008) to derive the four preferential summer weather regimes over the North Atlantic region and the period 1948–2012. The rationale for this analysis is to visualize the atmospheric circulation temporal variability and associate episodes of high precipitation with circulation patterns (Fig. 13.2a). This complements the analysis of flow analogues. The weather regimes are computed from SLP anomalies during 1948–2012. These four weather regimes correspond to modifications in the flow and affect the advection of temperature and humidity (Fig. 13.2c–f). We find that the wet spells over Northern Europe correspond with episodes of the Icelandic Low and Atlantic Ridge [following the terminology of Cassou et al. (2005)], which both yield low pressure centers near Scandinavia (Fig. 13.2a). When the circulation reverts to anticyclonic patterns over Scandinavia (Blocking or NAO-), precipitation rates fall to low values.

Trends of precipitation. We computed the linear trends of the seasonal average precipitation over the outline region (Fig. 13.2b) for the period between 1971 and 2012. A significant increasing trend is found for summer and winter precipitation ($p\text{-value} < 2 \cdot 10^{-3}$). The trends for other seasons are not statistically significant ($p\text{-values} > 0.1$). The mean analogue precipitation for summer is well correlated ($r = 0.86$, $p\text{-value} < 10^{-15}$) with the observed average (Fig. 13.2b), and the

analogue also yields a positive summer trend found in the observations, although it is not statistically significant ($p\text{-value} = 0.14$).

Conclusions. Our analysis suggests that the high precipitation rates were caused by the cyclonic conditions that prevailed during the early summer (June and July) over Scandinavia. Such conditions brought moist air over northern Europe. This conclusion is drawn from the significant correlations over Europe between the observed and the analogue precipitation, deduced from the north Atlantic atmospheric circulation.

The trend in summer precipitation over northern Europe is significantly positive but is marginally reproduced by analogues of circulation (with no statistical significance), although the precipitation analogues are correlated with the observations on daily to seasonal timescales. The frequency of cyclonic regimes over Scandinavia (Icelandic Low and Atlantic Ridge) has also increased, albeit not significantly (not shown).

Hence, we cannot attribute this upward summer precipitation trend since 1971 to changes in the atmospheric patterns themselves, because the frequency of cyclonic patterns has not significantly increased nor have the analogue reconstructions of precipitation. This suggests a contribution of climate change to precipitation rate in northern Europe. We conjecture that such a trend could be due to precipitation rates within the cyclonic patterns, which convey more moisture because of increased temperatures. This is consistent with recent process studies of convective precipitations (Berg et al. 2013), although this requires more studies on fine-scale precipitation processes.

14. THE RECORD WINTER DROUGHT OF 2011–12 IN THE IBERIAN PENINSULA

RICARDO MACHADO TRIGO, JUAN A. AÑEL, DAVID BARRIOPEDRO, RICARDO GARCÍA-HERRERA,
LUIS GIMENO, RAQUEL NIETO, RODRIGO CASTILLO, MYLES R. ALLEN, AND NEIL MASSEY

Introduction. The Iberian Peninsula (IP) was hit in 2011–12 by one of the most severe droughts ever recorded in this increasingly dry region of the world. This drought event had major socioeconomic impacts due to the decline in agricultural and hydroelectric power production. There are hints of an increase in the frequency of drought events in the Mediterranean basin (Sousa et al. 2011; Hoerling et al. 2012b;

Seneviratne et al. 2012) and over the IP in particular (Xoplaki et al. 2012). Despite some contradictory results with state-of-the-art models (Scaife et al. 2012), this drying trend fits into an expected tendency towards more frequent dry periods in a future warmer climate in that region (Seneviratne et al. 2012). The IP precipitation regime is characterized by a strong interannual (and decadal) variability but is also shaped

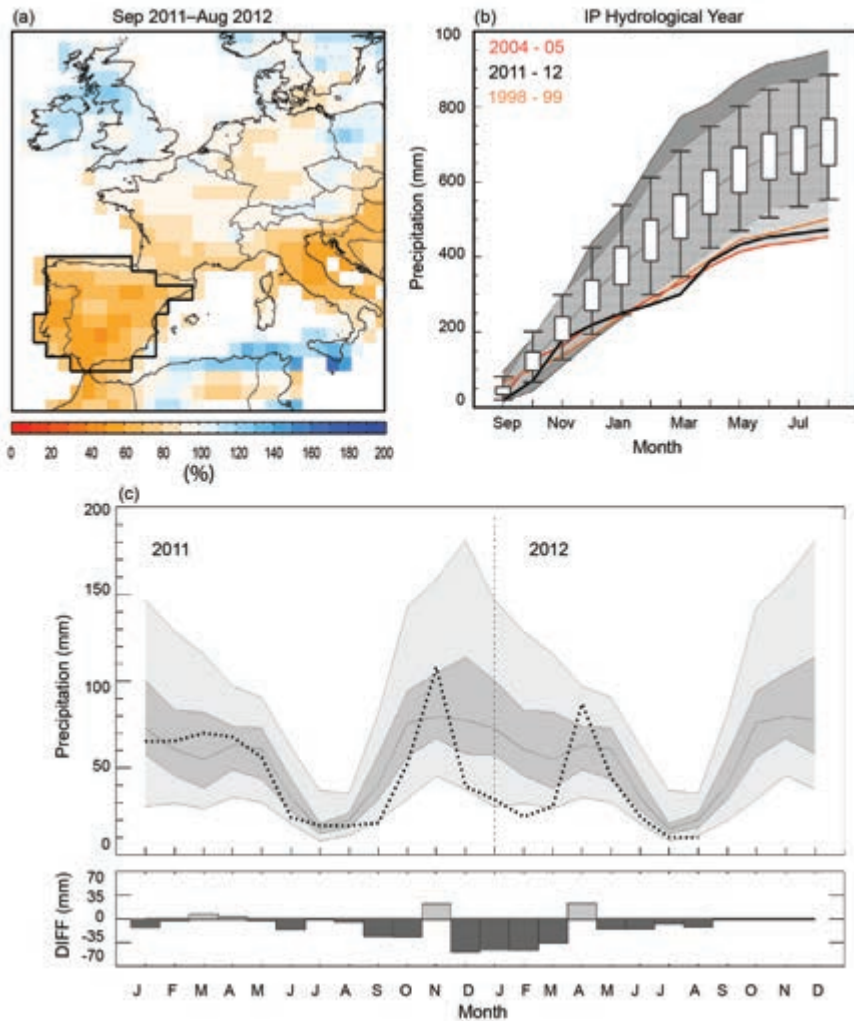


FIG. 14.1. (a) Accumulated monthly precipitation (in percentage of the 1951–2010 normals) during the hydrological year 2011–12. Black box delimits the region considered IP. (b) Accumulated monthly precipitation averaged over the IP during the hydrological year 2011–12 (black line) and during the other two most severe drought events in the period 1950–2012 (colored lines). Light, dark, and medium gray shaded areas show the ensemble spread from the corresponding evolutions of all hydrological years between 2002–03 and 2011–12, 1950–51 and 1959–60, and the overlapping between them, respectively. The gray thick line indicates the 1950–2010 mean evolution, with boxes and whiskers representing the ± 0.5 sigma level and the 10th–90th percentile interval, respectively. (c) Climatological (1950–2010) annual cycle of monthly precipitation averaged over the IP box, with the light (dark) shaded areas comprising the 10th–90th (30th–70th) percentiles, and the median in between. The dashed line shows the time series for 2011 and 2012, with the corresponding monthly departure from the climatological mean represented in the bottom graphic.

by great spatial variability. This spatial complexity has been characterized through comprehensive drought analysis (Vicente-Serrano 2006). Thus, most drought events have not affected the entire IP territory, being often restricted to 20% or 30% of the IP area, while less frequent extreme events have reached

more than 50% of the territory, including the 2004–05 episode (García-Herrera et al. 2007) and the more recent 2011–12 event. Here we intend to assess how extraordinary this last extreme drought was and analyze some of the main factors contributing to it.

Spatial and temporal assessment of the drought episode. Monthly precipitation data based on in situ rain gauges at 1.0° by 1.0° resolution were provided by the Global Precipitation Climatology Centre (GPCC; Rudolf and Schneider 2005). Since the number of stations over Iberia experiences a pronounced decrease before the 1950s in this dataset, the period of analysis has been limited to 1950–2012. Precipitation for the period 1950–2010 was obtained from the so-called full data product (1901–2010). For 2011–12, data were derived from the monitoring product (2007–present) that only uses a network of near-real-time stations. Previous work on Mediterranean drought events (e.g., García-Herrera et al. 2007; Trigo et al. 2010) has shown a high consistency between these two GPCC products during their overlapping period.

Droughts in partially semi-arid regions, such as the IP, can evolve with some complexity in both spatial and temporal domains. It is highly advisable to avoid use of the calendar year and instead evaluate the anomalous hydrological year, which extends from September of year $n-1$ through August of year n . The accumulated precipitation over the IP between September 2011 and August 2012 dropped to roughly 50% of the 1950–2000 climatological average over the southwestern IP (Fig. 14.1a). The evolution of

TABLE 14.1. Monthly values (standardized units) of NAO and EA indices (from CPC/NOAA). The fourth column shows the expected value of the IP for the given month of the drought as inferred from the observed values of NAO and EA patterns. For comparison, columns five and six show the observed IP value and the climatological mean IP value for 1950–2012, respectively.

	NAO	EA	Regressed IP with NAO & EA (mm)	Observed IP (mm)	Climatological IP mean (mm)
DEC 2011	2.25	0.11	19.2	39.6	89.0
JAN 2012	0.86	-1.76	37.1	31.8	78.0
FEB 2012	0.03	-1.73	38.2	21.9	68.6
MAR 2012	0.93	-0.64	37.9	27.8	62.8

the accumulated monthly IP-averaged precipitation between September 2011 and August 2012 is also shown in Fig. 14.1b, together with the corresponding evolution of the climatological accumulated monthly precipitation distribution (whiskers plot). At the end of the considered period, the accumulated precipitation average over the IP (~470 mm) was ~67% of the long-term mean value (~700 mm), corresponding to the second lowest accumulated value in any hydrological year since 1950, only second to the 2004–05 drought (evaluated in García-Herrera et al. 2007).

Most of the precipitation over the IP falls between October and March, thus major droughts are always characterized by lower-than-usual rainfall during these months (García-Herrera et al. 2007). To better assess the months that specifically contributed to this drought, we show in Fig. 14.1c the evolution of monthly precipitation. The entire hydrological year of 2011–12 is characterized by lower-than-average values with two exceptions (November 2011 and April 2012). Nevertheless, the peak period of rainfall during the winter (December to March; DJFM) is characterized by an outstanding sequence of dry months, often close or even below the 10th percentile of its climatological distribution. Next we analyze these four months more in depth.

Main physical mechanisms. The most important large-scale teleconnection pattern of the Euro Atlantic region corresponds to the North Atlantic Oscillation (NAO) that has a significant influence on the precipitation regime of the IP (Trigo et al. 2004). The NAO modulates the westerly atmospheric flow in such a way that positive values of the NAO index are usually

associated with below-average precipitation in the IP. Additionally, the Eastern Atlantic (EA) pattern also plays an important role (Trigo et al. 2008), with positive values of the EA index associated with above normal precipitation in the IP. Values of these two indices were obtained from NOAA's Climate Prediction Center or DJFM of 2011–12. The values are shown in Table 14.1 and confirm a total predominance of positive NAO, while the EA was characterized by negative values (with the exception of December). Note that extreme values in one or another index were observed through the entire winter season. The fourth column shows the expected value of the IP for the given month of the drought as inferred from the observed values of NAO and EA patterns. The expected value of the IP for that month and year was derived from a regression analysis of the IP with monthly NAO & EA series, after removing that year from the series. As expected, the regressed value is considerably lower than the climatological average (last column) and closer to the low IP values observed.

The IP winter precipitation is influenced not only by the preferred path of synoptic disturbances (storm tracks), and associated atmospheric instability that forces air masses to rise, but also by the supply of moisture from the major moisture source regions (MSR) in the North Atlantic (Gimeno et al. 2010a). The most important MSR affecting the winter precipitation in the IP corresponds to a large tropical-subtropical North Atlantic corridor stretching from the Gulf of Mexico to the Caribbean Islands (Gimeno et al. 2010b, 2013). Herein, we use the MSRs identified by Gimeno et al. (2010b) over the Atlantic: North Atlantic (NATL) and Mexico Caribbean (MEXCAR; Fig. 14.2, top panel).

We quantify how much less moisture from these MSR regions was received in the IP during the winter of 2011–12 compared with a long-term climatology (1979–80 to 1999–2000). For that purpose, a Lagrangian analysis was used, which in summary, consists of identifying all trajectories originating from MSR regions and coming to the IP. By quantifying the net rate of change of water vapor along each trajectory and adding this for all the trajectories over the 10 days of transport (averaged atmospheric moisture residence time), it is possible to quantify moisture received by the IP from each MSR in terms of E-P (see method section in Gimeno et al. 2010a,b for details). The resulting climatology is shown in the middle panels of Fig. 14.2 (shading), together with the percentage of reduction of (E-P) for the 2011–12 winter (calculated from ERA-Interim reanalysis data) with respect to the period 1979–80 to 1999–2000 (contour lines). The generalized reduction of moisture supply is clear for 2011–12, particularly in the southern (up to 80%), western, and northern regions (higher than 60%) and is in agreement with a steering of storm tracks away from Iberia due to extreme values of NAO and EA. Over the center of the IP, the reduction is limited to less than 20% for both sources.

Changing probabilities of an event such as the 2012 Iberian drought. Figure 14.2 (bottom panel) shows the comparison of return periods of averaged cumulative precipitation for the same area as that shown in Figure 14.1a, but using an ensemble of climate simulations of at least 2300 members per decade. The simulations are exactly

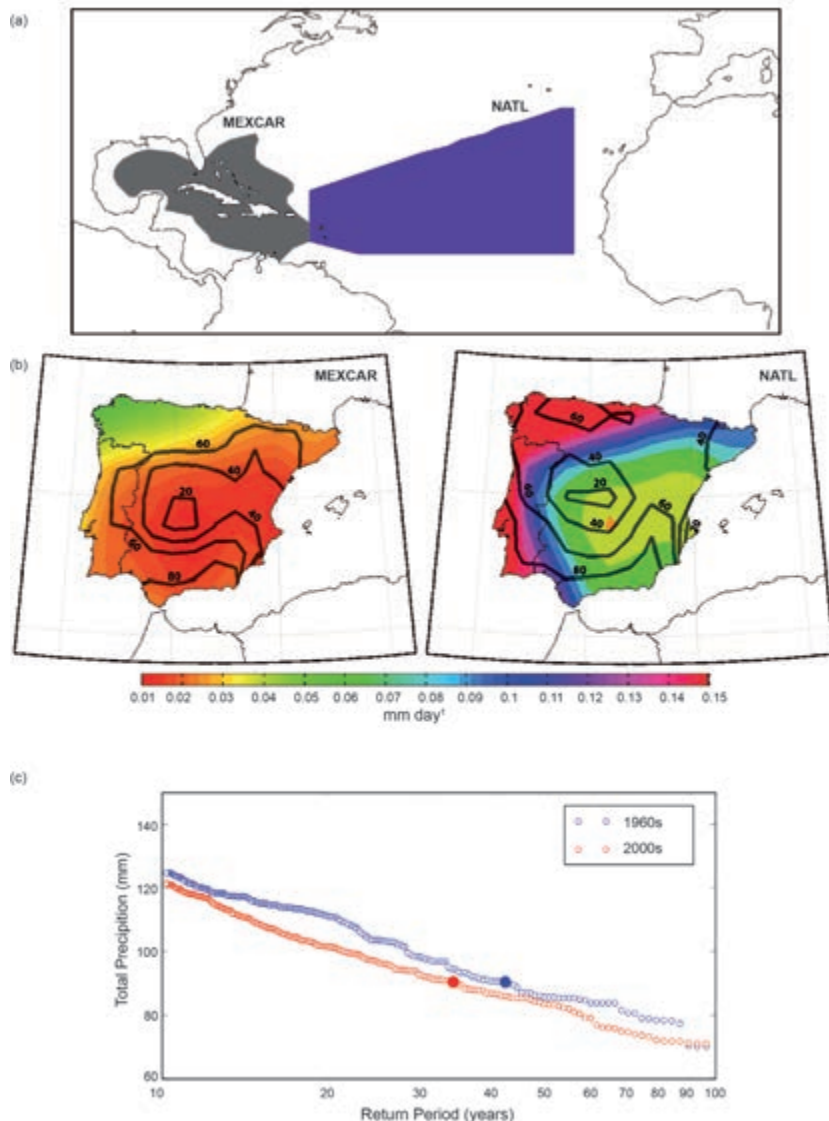


FIG. 14.2. Main moisture sources associated with winter precipitation over the IP and changes in return of winter accumulated precipitation. (a) Winter moisture source regions for the IP, defined based on the threshold of 750 mm yr⁻¹ of the annual vertically integrated moisture flux calculated for the period 1958–2001 using data from ERA-40 [see Fig. 1 of Gimeno et al. (2010a)], NATL, and MEXCAR. (b) Climatological (1979–80 to 1999–2000) values of E-P (mm day⁻¹) integrated over 10-day winter periods from the ERA-40 reanalysis (color shading) coming from MEXCAR and NATL respectively. Only values below -0.01 mm day⁻¹ are plotted. Black contours indicate percentage of reduction of E-P during the 2011–12 winter with respect to the period 1979–80 to 1999–2000. (c) Return periods of winter (DJFM) accumulated precipitation (mm) averaged over the IP for 1960–69 (blue curve) and 2000–09 (red curve). The observed value for the 2011–12 winter drought (121 mm) corresponds to a value of 91 mm in the ensemble, shown on both curves as a filled circle.

the same as those used by Massey et al. (2012) (the same configurations for sea surface temperature, sea ice fraction, atmospheric gas concentrations, volcanic emissions, solar forcing, and topography), simply studying a different region (the IP). They were performed embedding the regional climate model

HadRM3P with $0.44^\circ \times 0.44^\circ$ grid size in the global climate model HadAM3P. The DJFM cumulative precipitation in the ensemble for this area is 223 mm. That is 25% less than the observed mean and agrees with previous results of an existing dry bias in the model (Haynes et al. 2013, manuscript submitted to *PLOS ONE*). To compensate for model bias, we calculate the percentage below the observed mean of the 2011–12 drought over the IP and then apply this percentage to the model data. The resulting value in the ensemble that corresponds to the recorded precipitation of 121 mm is 91 mm. The return period of this value (computed from the total number of occurrences for each decade) has been reduced by ~8 years, i.e., from 41.7 years in the 1960s to 33.6 years in the 2000s. That is, assuming that the model bias can be linearly corrected for, currently we can expect 3.0 winter IP droughts per century like the one observed in 2011–12, compared with 2.4 in the 1960s.

Summary and conclusions. The 2011–12 winter drought over the IP was extreme in its magnitude and spatial extent. The season was dominated by a positive NAO and negative EA, thus both large-scale

circulation patterns acted in such a way that did not favor the steering of low-pressure systems over Iberia and, therefore, promoted the very dry winter period. We believe that these two mechanisms are not independent, although the predominant mechanism is related to the steering of storm tracks by the large-scale patterns mentioned, particularly the NAO. Further work is currently being undertaken to evaluate possible changes of conversion efficiency of moisture to precipitation during dry and wet years. Finally, we have quantified significant reductions of moisture advection from the two main Atlantic sources that usually supply the IP. Using a relatively large ensemble of climate simulations based on the regional model HadRM3P, it was shown that the return period of such an extreme drought has decreased between the 1960s and 2000s decades. Overall these results agree with previous ones by Hoerling et al. (2012b), who found a tendency toward a drier Mediterranean for the period 1970–2010 in comparison with 1901–70, and that such a trend has been partially driven by the anthropogenic emissions of greenhouse gases and aerosols, although modulated by the NAO phase.

15. ATTRIBUTION OF 2012 AND 2003–12 RAINFALL DEFICITS IN EASTERN KENYA AND SOUTHERN SOMALIA

CHRIS FUNK, GREG HUSAK, JOEL MICHAELSEN, SHRADDHANAND SHUKLA, ANDREW HOELL, BRADFIELD LYON, MARTIN P. HOERLING, BRANT LIEBMANN, TAO ZHANG, JAMES VERDIN, GIDEON GALU, GARY EILERTS, AND JAMES ROWLAND

Introduction. Over the past 14 years, eastern East Africa (EA) has experienced more frequent boreal spring dry events (Funk et al. 2008; Williams and Funk 2011; Lyon and DeWitt 2012; Funk 2012). In the spring of 2012, below-average March–May rains across parts of eastern Kenya and Southern Somalia (a region bounded by 4°S – 4°N , 37°E – 43°E , green polygon, Fig. 15.1a) once again contributed to crisis and emergency levels of food insecurity (FEWS NET 2012a). In some regions, rainfall deficits of more than 30% led to crop failures and poor pasture conditions, causing families in Kenya to move in search of work or take children out of school, and inhibiting Somalia’s recovery from the acute malnutrition and famine caused by the 2010–11 drought. While not particularly severe, the poor March–May 2012 rains added to climatic stresses associated with a series of March–May dry events occurring in 2007, 2008, 2009, and 2011. Figure

15.1b shows March–May (three month) Standardized Precipitation Index (SPI; McKee et al. 1993) values, based on 1981–2012 Famine Early Warning Systems Network (FEWS NET) precipitation data (see Supplemental Material for a brief description). Dry events, defined as March–May seasons with SPI values of less than -0.5 , are shown in orange. In fragile food economies, these repetitive dry events can lower resilience, disrupt development, and require large infusions of emergency assistance. It is not the climate alone that creates these outcomes, but rather the climate’s interaction with extreme poverty, high endemic rates of malnutrition, limited or nonexistent governmental safety nets, and poor governance. In 2011, for example, the worst drought in 60 years combined with chronic food insecurity, high global food prices, and the actions of Somali terrorists to produce an estimated 258 000 deaths in Somalia (FEWS NET 2013).

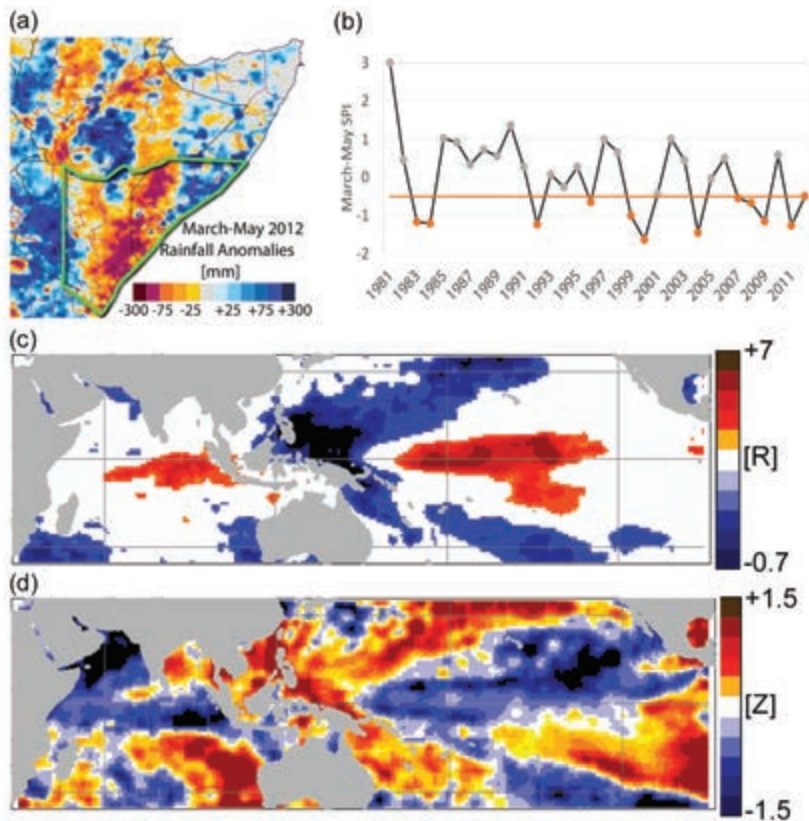


FIG. 15.1. (a) Mar–May rainfall anomalies (mm) from the Climate Prediction Center’s RFE2 dataset. (b) 1981–2012 time series of EA rainfall (mm) based on blended infrared observations, the CFS reanalysis, and station data. (c) 1999–2012 correlations between EA SPI and Mar SSTS. (d) Observed (NOAA AVHRR OI) Mar SST anomalies.

In this study, we examine the question of whether SSTs caused the poor 2012 March–May eastern East African rains and increased the frequency of dry events over the past decade (2003–12), using two new Global Forecast System (Environmental Modeling Center 2003) version 2 (GFS) ensembles to estimate fractions of attributable risk (FAR; Allen 2003) associated with 30 full-ocean simulations and 30 simulations driven only with de-trended ENSO-only SSTs.

The approach taken here is somewhat similar to the attribution study of Lott et al. (2013), which focused on the 2010 and 2011 East African droughts, except that where Lott et al. (2013) contrast full-ocean and “natural” SST influences, we examine the differences between full-ocean and ENSO-only SST effects. Lott et al. (2013) drove a state-of-the-art atmosphere model with observed (full-ocean) and “natural” SSTs. “Natural” SSTs were observed SSTs with estimates of anthropogenic warming removed. Ensembles of full and natural precipitation ensembles were compared, and the fraction of attributable drought risk (Allen 2003) estimated ($FAR = 1.0 - \text{PROB}_{\text{nat}}/\text{PROB}_{\text{full}}$). Lott

et al. (2013) found that the risk of the 2011 spring drought, but not the 2010 ENSO-related fall drought, increased substantially; a result consistent with a recent regional modeling study by Cook and Vizy (2013), which found that during the 21st century, anomalous dry anticyclonic flow from the Arabian peninsula reduced boreal spring rains, while boreal winter rains are lengthened by a northeastward shift of the South Indian convergence zone.

Rather than comparing “natural” and full-ocean results, here we present an analysis contrasting full-ocean and ENSO-only simulations. We examine FAR values based on the full-ocean and ENSO-only simulations: $FAR = 1.0 - \text{PROB}_{\text{ENSO}}/\text{PROB}_{\text{full}}$. Full-ocean GFS simulations were driven with observed SSTs and atmospheric carbon dioxide variability. ENSO-only simulations were driven with de-trended SST variations associated with the first principal component of

Pacific SSTs and atmospheric carbon dioxide variability. Comparisons of these simulations allow us to examine whether recent dry events have likely been due to La Niña-like anomalies (Ogallo 1988) or other SST changes, potentially related to warming in the Indo-Pacific. The full-ocean and ENSO-only ensembles are based on T126 spectral resolution GFS precipitation simulations.

2012 SST conditions. Our understanding of the sea surface and climate conditions underpinning recent East African (EA) dry events is growing rapidly. The most recent (21st century) increase in March–May EA dry event frequency appears related to Indo-Pacific warming (Funk et al. 2008; Williams and Funk 2011; Funk 2012), a stronger western-to-central Pacific SST gradient (Lyon and DeWitt 2012), and an intensification of the Walker circulation (Hoerling et al. 2010; Williams and Funk 2011; Merrifield and Maltrud 2011; Meng et al. 2011; L’Heureux et al. 2013). When the Central Pacific is cool and the Western Pacific warm, a vigorous circulation response (Hoerling and

Kumar 2002, 2003) increases rainfall over the eastern Indian and western Pacific oceans but can reduce rainfall over eastern Africa and other teleconnected regions, such as southwest Asia (Hoell and Funk 2013, manuscript submitted to *J. Climate*). Standardized equatorial Indo-Pacific SST transects for dry events (Supplementary Fig. S15.1a) associate below-normal EA rainfall with stronger western-to-eastern Pacific SST gradients.

Correlations between 1993–2012 March–May EA SPI and March SSTs (Fig. 15.1c) indicate fairly strong teleconnections. Warm SSTs in the Western Pacific combined with cool SSTs in the central Indian Ocean and central Pacific tend to produce drier-than-normal rainfall in eastern East Africa.

In March of 2012, the East African food security was tenuous, and the March SST anomalies (Fig. 15.1d) exhibited anomalies congruent with below-normal rains. Indices based on teleconnected regions were used to define analogs to the observed 2012 March SSTs, and below-normal rainfall was anticipated by FEWS NET (2012a). These results were similar to forecast outlooks produced by African experts at the 30th Greater Horn of Africa Climate Outlook Forum (GHACOF) and bias corrected ECHAM4.5 rainfall forecasts provided by the International Research Institute (IRI). The FEWS NET, GHACOF, and IRI outlooks all indicated below-normal rains. On 3 April, FEWS NET (2012b) released a forecast of below-normal precipitation. On 5 April, the State Department announced an increase in humanitarian assistance (State Department 2012). In June, prepositioned resources and contingency planning helped mitigate crisis-level food insecurity conditions (FEWS NET 2012b).

Attribution of the 2012 East African dry event. In the results presented here, we use a simple regression (see Supplemental Material for more details) between 1993–2012 EA SPI values and GFS precipitation over the western Pacific (0°–20°N, 120°E–160°E) to estimate EA precipitation conditions. This approach was taken because (i) the correlation between local EA SPI and the EA GFS precipitation was low ($r = 0.34$, $df. 18$, $p = 0.08$), while the anti-correlation to western Pacific precipitation was fairly strong (-0.71), and (ii) the intensity of convection in the equatorial western Pacific has been linked to recent EA dry events (Lyon and DeWitt 2012; Williams and Funk 2011).

The results presented here indicate that both ENSO and non-ENSO SST variations played some role in forcing the 1993–2012 EA SPI, but that non-ENSO forcing dominated during the 2012 boreal spring. The scatterplot shown in Fig. 15.2a shows the ensemble mean full-ocean and ENSO-only estimate, indicated respectively with * and Δ . Between 1993 and 2012,

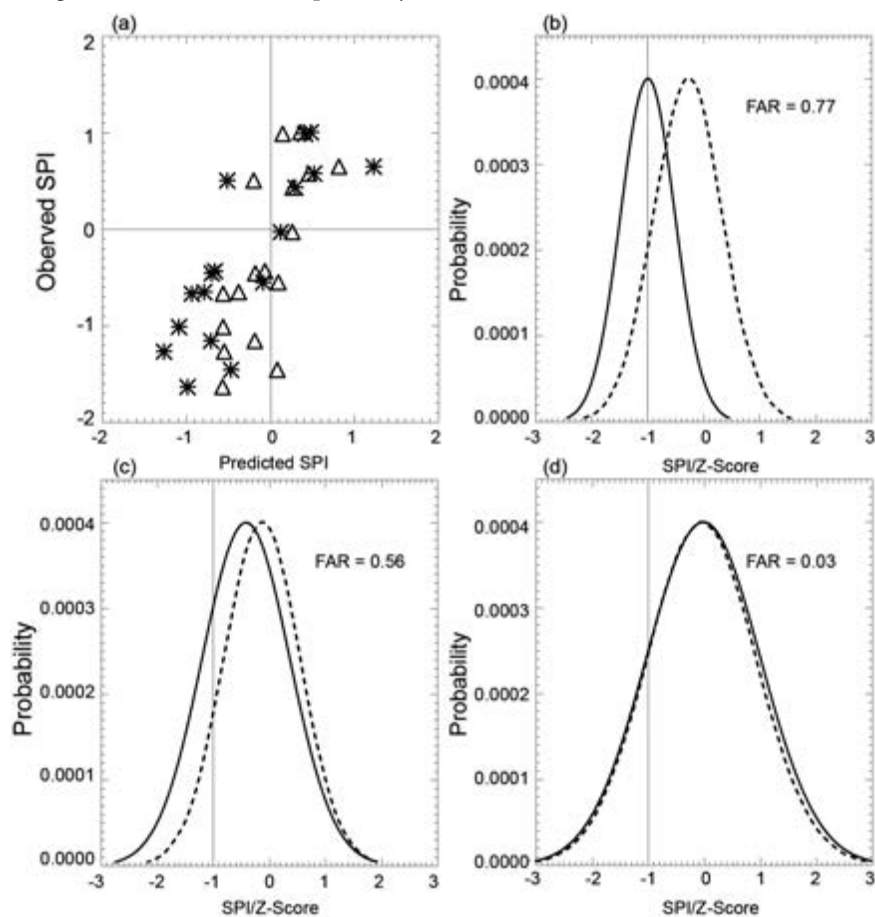


FIG. 15.2. (a) Predicted and observed EA SPI values for the full-ocean GFS (*) and ENSO-only GFS (Δ). (b) 2012 EA SPI probability distributions for the full-ocean GFS predictions (solid line) and ENSO-only predictions (dashed line). (c) Same as (b) but calculated over 2003–12. (d) Same as (b) but calculated over 1993–2002.

the cross-validated full-ocean estimates explained 50% of the variance of the observed rainfall and captured many of the recent dry events. The ENSO-only estimates, however, failed to recreate the observed dry event intensities. The ENSO-only estimates also missed dry events in 2004 and 2012 that were captured in the full-ocean simulations. The full-ocean and ENSO estimates are correlated at 0.74, but the standard deviation of the full-ocean estimates is 25% greater. During years with suppressed western Pacific precipitation and normal-to-above-normal EA SPI estimates, the two ensembles track closely. In seasons with above-normal western Pacific precipitation and below-normal EA SPI estimates, the agreement is weaker, and the full-ocean estimates of EA SPI are lower. This may indicate substantial forcing by non-ENSO sources.

Ensembles of downscaled full-ocean and ENSO-only SPI estimates can be used to calculate the 2012 dry event FAR (Allen 2003). FAR measures how much more likely an event is, given a change in the climate system. The two sets of ensembles define two probability distributions, and FAR is calculated based on their differences. Figure 15.2b shows the distributions of the 2012 full-ocean and ENSO-only estimated SPI ensembles. The full-ocean (ENSO-only) predictions had a mean and standard deviation of -1.0 and 0.6 (-0.1 and 0.4). Defining a dry event as having an SPI value of -0.5 or less, we find that dry events were much more likely (85% probability) in the full-ocean than in the ENSO-only simulations (18% probability) yielding a $F_{AR} = 1.0 - P_{ENSO}/P_{FULL} = 0.77$. Non-ENSO SSTs appear to have substantially increased the risk of a dry event in 2012.

Attribution of the 2003–12 and 1993–2002 East African dry events. We can apply the same FAR analysis technique to all GFS estimates for the past 10 years (2003–12). The mean and standard deviation of the 300 full-ocean simulations (10 seasons with 30 simulations) was -0.3 and 0.7. The corresponding mean and standard deviation for the 300 ENSO-only simulations was -0.1 and 0.6. Over this decade, the full-ocean simulations indicated a 42% chance of dry events (SPI < -0.5), while the ENSO-only simulations indicated a 27% chance. These frequencies correspond to a dry event every 2.4 and 3.7 years. The corresponding FAR value is 0.33 (Fig. 15.2c), signify-

ing that non-ENSO SST variations have made dry events more likely. A similar analysis is also shown for the 1993–2002 period (Fig. 15.2d). In this decade, the probability of dry events was similar in the full-ocean and ENSO-only ensembles (~30%). Together, the 1993–2002 and 2003–12 results suggest the recent emergence of a non-ENSO driven dry event forcing.

Conclusions. The results indicate that non-ENSO SST variations substantially increased the risk of a dry event in 2012, and over the 2003–12 period. ENSO SST conditions cannot fully account for the recent increase in eastern East African dry event frequencies. It seems likely that other factors, such as warming in the western Pacific (Williams and Funk 2011; Lyon and DeWitt 2012; Funk 2012), a recent transition in Pacific decadal variability (Gu and Adler 2013), and stronger western-to-central Pacific SST gradients (Hoell and Funk 2013, manuscript submitted to *J. Climate*) may be contributing to the recent dryness. On the other hand, it is also important to recognize that the results indicate that ENSO has had substantial links to recent EA precipitation variations.

It is worth noting, however, that the procedure used here does not necessarily indicate an anthropogenic attribution since we are comparing the full SST results with ENSO-only SSTs, rather than estimates of “natural” SSTs as in Lott et al. (2013). Observed western Pacific and eastern Indian Ocean SSTs do, however, track very closely with historical simulations from coupled ocean-atmosphere climate change models (Funk 2012), and this region has been warming substantially faster than the eastern Pacific (Cane et al. 1997; Compo and Sardeshmukh 2010; Lott et al. 2013; Solomon and Newman 2012) in a manner that may be consistent with a stronger radiative control of the western versus eastern Pacific (Clement et al. 1996). Recent studies using paleoclimate data associate such warming with East African drying (Tierney et al. 2013), and more trend analyses are identifying recent rainfall declines (Viste et al. 2012). On the other hand, coupled ocean-atmosphere climate change models tend to indicate a tendency for wetter conditions in eastern Africa. Finally, Pacific decadal variations have also likely played an important role, triggering a post-1998 climate shift (Gu and Adler 2013) that enhanced tropical Pacific precipitation and SST gradients.

16. THE 2012 NORTH CHINA FLOODS: EXPLAINING AN EXTREME RAINFALL EVENT IN THE CONTEXT OF A LONGER-TERM DRYING TENDENCY

TIANJUN ZHOU, FENGFEI SONG, RENPING LIN, XIAOLONG CHEN, AND XIANYAN CHEN

Introduction. North China, including Beijing (~39°52'N, 116°28'E), Tianjin (~39°10'N, 117°10'E), and part of Hebei Province, experienced severe flooding in the summer of 2012. During 21–22 July, Beijing received a regionally averaged total precipitation of 190.3 mm, and the center of the rainfall event received 460.0 mm; the observations of 11 stations broke the historical records (CMA 2013). The flood-affected area in Beijing was about 16 000 km², and the damage-suffering population was estimated at 1.9 million with 77 people dead. The direct economic loss is more than 10 billion Chinese renminbi.

Flooding events are not unusual in China, but have been uncommon in North China in recent decades. The East Asian summer monsoon (EASM) circulation has been weakening since the end of the 1970s, which led to a drying tendency in North China (see Zhou et al. 2009 for a review). The occurrence of the 2012 flood in the context of a multidecadal drying tendency has received great attention. In this study, we analyze the 2012 North China flood in the context of summer monsoon changes in the past 62 years (1951–2012). We examine whether climate change may have played a role in either the 2012 extreme rainfall or the recent multidecadal trend of decreased precipitation in North China.

Observed heavy rainfall in North China. A heavy rainfall occurred on 21–22 July 2012 where the major rain belt extended from Southwest China to North China and was centered in Beijing (Fig. 16.1a). The Beijing area received a regionally averaged rainfall of 190.3 mm, as measured by 20 stations in the area. The Hebei Town station of Fangshan District in the western mountain area of Beijing received the largest amount of rainfall and recorded 460.0 mm within 24 hours (CMA 2013). The 24-hour precipitation accumulation in the western mountain area was nearly equal to the area's

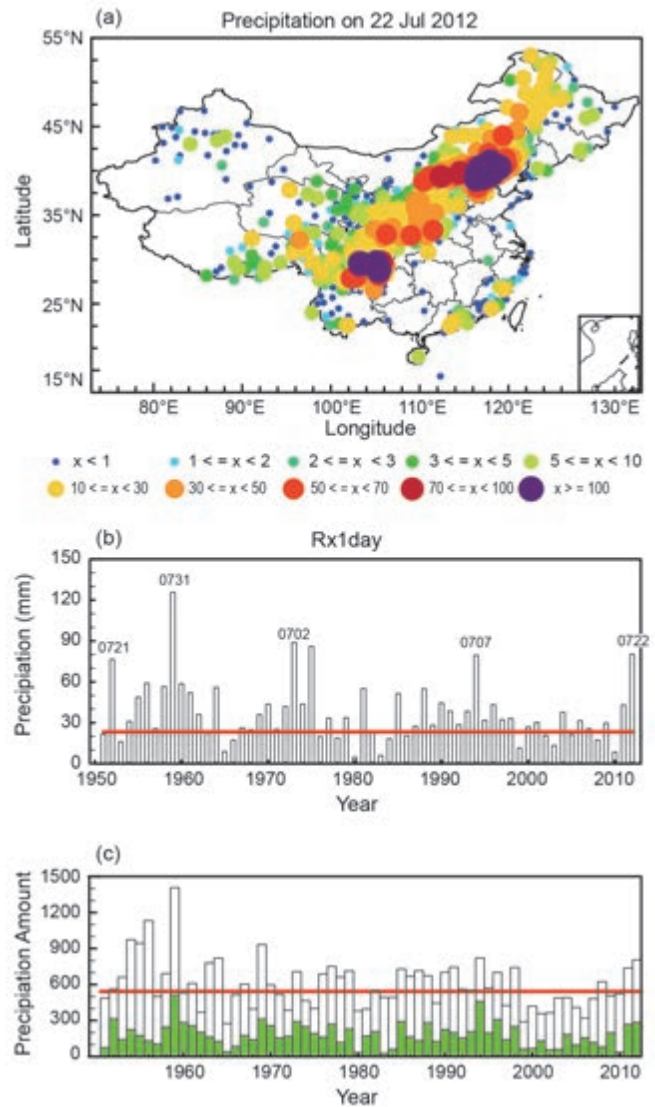


FIG. 16.1. (a) The accumulated precipitation (mm) from 21 July 2012 08:00 China Standard Time (CST) to 22 July 2012 08:00 CST. (b) Time series of the July maximum one-day precipitation (RX1DAY) index in Beijing station (station number: 54511). The red solid line is the climatological mean (1981–2000) threshold of the 95th percentile of all precipitation days in July (mm day⁻¹). The text denotes the date when the RX1DAY value appeared, e.g., "0721" means the RX1DAY occurred on 21 July. (c) July (green) and annual total (white) precipitation (mm) in Beijing station, the red solid line denotes the mean total annual precipitation during 1981–2010.

annual precipitation and far more than the area's average for a single rainfall event. Note, the mean July precipitation for the period 1981–2010 is 160.5 mm, and the mean total annual precipitation is 541.8 mm at *Beijing station* (station number 54511; Fig. 16.1c). The average 24-hour rainfall in the Tianjin area was 98.6 mm, with 294.7 mm of total precipitation at the rainfall center on 21–22. Flooding was observed in part of the Haihe River valley in Hebei province (CMA 2013).

The maximum one-day precipitation (RX1DAY) index of July during 1951–2012 at Beijing is examined in Fig. 16.1b. Since the original daily precipitation amount is defined as the accumulation of precipitation starting at 20:00 China Standard Time (CST) one day and ending at 20:00 CST the next day, to catch the heavy rainfall that occurred starting 21 July 08:00 CST, a two-day running mean is applied to the original daily data. The RX1DAY of 2012 was

the strongest since 1995, but not unprecedented in the past 62 years. RX1DAY indices stronger than the 2012 case are seen in the historical record (Fig. 16.1b). The total July precipitation was more than 30% of the annual precipitation at the Beijing station (Fig. 16.1c).

Was the extreme rainfall of July 2012 due to climate change? Precipitation in North China is known to be directly linked to the strength of the EASM circulation, which is measured by a commonly used index (Guo 1983) and has been weakening since the end of the 1970s (Fig. 16.2a), as reported in previous studies (e.g., Yu et al. 2004; Yu and Zhou 2007; Zhou et al. 2009). The declining trend can also be regarded as an inter-decadal variation due to the short data length. The EASM circulation of 2012 is greater than most years following 1980, but still weaker than the period 1951–79 (Fig. 16.2a,b). Following the decreasing trend of the EASM circulation, the July precipitation in

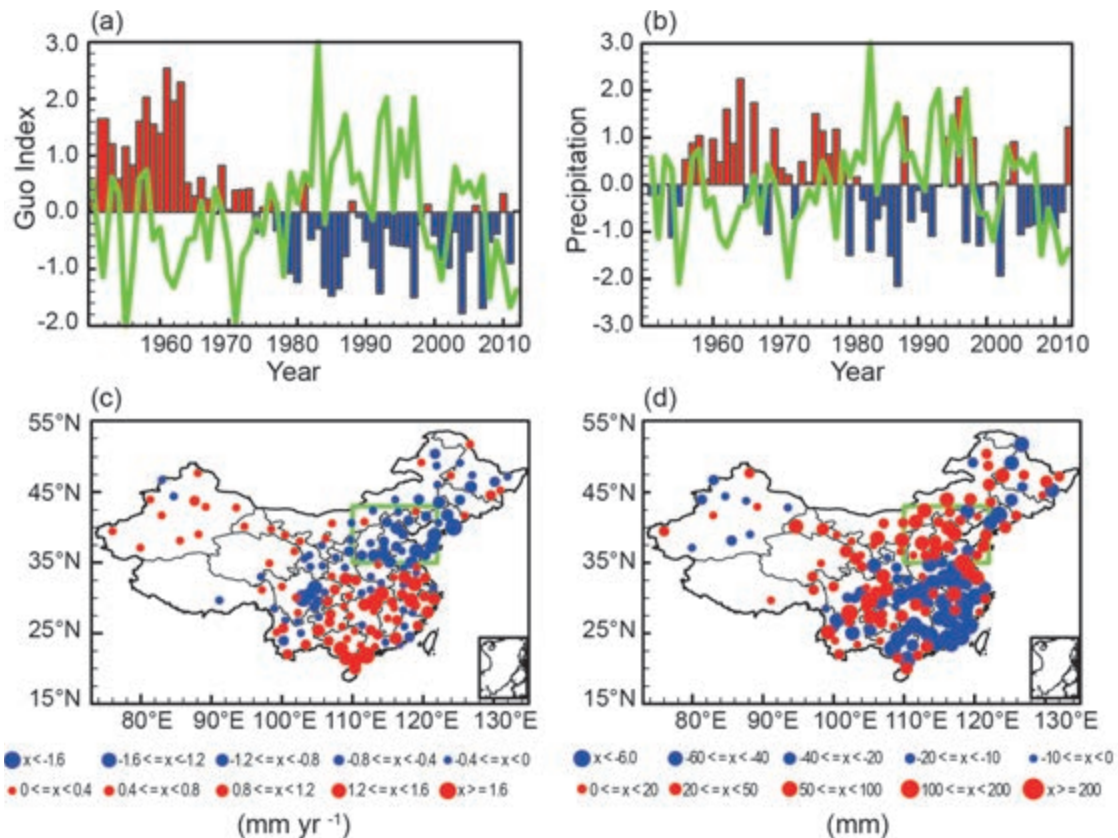


FIG. 16.2. (a) Normalized Jul EASM index derived from NCEP/NCAR reanalysis based on Guo (1983). The green line indicates the PDO index derived from <http://jisao.washington.edu/pdo/PDO.latest>. (b) Normalized Jul precipitation amount averaged over North China (35°N–43°N, 110°E–122°E; 23 stations included; dimensionless). The green line indicates the PDO. (c) Linear trends of July precipitation during 1951–2011 (mm yr⁻¹; the absolute values of anomalies larger than 0.4 are statically significant at the 5% level), the green box indicates the North China region (35°N–43°N, 110°E–122°E). (d) Anomalies of Jul precipitation in 2012 relative to 1981–2010.

North China has also been decreasing since the end of 1970s. However, as with only five other Julies in the last 30 years, July 2012 was above normal. More importantly, July 2012 was the strongest event in the last 15 years (Fig. 16.2b).

While North China precipitation and the EASM circulation index are directly correlated, they are inversely correlated with the phase of the Pacific Decadal Oscillation (PDO), or “Inter-decadal Pacific Oscillation” (IPO; Power et al. 1999). A negative phase of the PDO corresponds to a stronger EASM circulation (Fig. 16.2a) and more precipitation in North China (Fig. 16.2b). The PDO affects the EASM circulation through changing land-sea thermal contrast (Li et al. 2010). The recent transition of the PDO from a positive to a negative phase (Zhu et al. 2011; Liu et al. 2012) provides a large-scale background for the stronger summer monsoon in 2012.

The precipitation anomaly of July 2012 is compared to the long-term trend in Fig. 16.2c. Following the weakening tendency of the EASM circulation (Fig. 16.2a), decreasing precipitation trends are seen in most stations of North China (Fig. 16.2c). The extreme precipitation of July 2012 is in contrast to the long-term trend, and most stations in North China witnessed a positive July 2012 precipitation anomaly (Fig. 16.2d). There is insufficient data to conclude whether this indicates a recovery of the EASM after experiencing a weakening stage since the end of the 1970s (Liu et al. 2012).

Following the declining trend of the EASM circulation, the average rainfall amount and frequency have significantly decreased but the rainfall intensity has increased in North China (Yu et al. 2010). July 2012 is in contrast to the long-term trend in rainfall amount but consistent with rainfall intensity trends.

To understand the relationship of the July North China rainfall event with climate change, the July precipitation averaged in North China derived from the historical simulation and Representative Concentration Pathway (RCP) projection of 39 Coupled Model Intercomparison Project Phase 5 (CMIP5) models are analyzed (Supplementary Fig. S16.1). The models show an increasing trend from 1950–2000, in contrast to the decreasing trend observed during this period. The inability of CMIP5 models to replicate the observations is partly due to the inconsistency of PDO phase transition, since the CMIP5 models were not initialized with contemporary observations and, therefore, would not reproduce the observed phase transition of the PDO event. Under RCP4.5

and RCP8.5 scenarios, the July precipitation in North China is projected to increase in the future by CMIP5 models. However, the credibility of the projection is reduced due to the weakness of historical simulation. Due to the inability of climate models to reproduce the observed trend, it is difficult to make any conclusions about the role of climate change in the trend of decreasing (increasing) precipitation amount (intensity) observed in North China over the last three decades. In addition, the performance of global models in reproducing regional precipitation changes in North China may be limited by their low resolutions. Whether a dynamical downscaling using a higher resolution regional model can improve the simulation deserves further study

Concluding remarks. Although the damage caused by the 2012 floods in North China was large, the amount of precipitation was not unprecedented in the past 62 years. The flood occurred in the background of a longer-term drying tendency. Since the late 1970s, the total summer rainfall amounts have significantly decreased, but the rainfall intensity of single events has increased in North China associated with the weakening tendency of the EASM circulation partly due to the phase transition of the PDO. We are unable to confirm or reject the role of climate change in the 21–22 July 2012 rainfall event due to the inability of the CMIP5 models to accurately replicate observations in this region of China. The CMIP5 models show an increasing trend from 1950 to 2000, in contrast to the decreasing trend observed during this period. Both the mean and extreme precipitation in North China are projected to increase in the future, but the credibility of the projection is limited by the weakness of models to simulate the climatology of EASM and the design of CMIP5 projection experiments, which were not initialized with contemporary ocean observations and would not be able to reproduce the observed phase transition of the PDO.

In addition, we should note that the inability of CMIP5 models to replicate the observations is not due entirely to the unmodelled phase transition of the PDO. The trend of the PDO during 1971–2012 is nearly zero, but the precipitation trend in North China is nonzero, which is $-1.44 \text{ mm day}^{-1}$ and statistically significant at the 5% level. This suggests an underlying trend caused by processes other than the PDO. Further studies are needed to understand the underlying processes.

17. CONTRIBUTION OF ATMOSPHERIC CIRCULATION CHANGE TO THE 2012 HEAVY RAINFALL IN SOUTHWESTERN JAPAN

YUKIKO IMADA, MASAHIRO WATANABE, MASATO MORI, MASAHIDE KIMOTO, HIDEO SHIOGAMA, AND MASAYOSHI ISHII

Introduction. From 11 July to 14 July 2012, during the late Japanese “Baiu” rainy season, the southwestern part of Japan experienced an extraordinary heavy rainfall. This event was record breaking at many sites (detailed rainfall analysis is shown in Supplementary Fig. S17.1), and caused devastating damage with 31 deaths, 3 missing persons, floods, mudslides, and damaged homes in the southwestern part of the mainland of Japan.

In a normal rainy season from June to July, a persistent rain band called the “Baiu front” supplies a large amount of water to southwestern Japan and some parts of East Asia (Fig. 17.1a). The Baiu front is associated with the large-scale Asian summer monsoon circulation and a development of the northwestern Pacific subtropical high (PASH). In 2012, water vapor supply to Kyushu, the southernmost part of Japan, was extremely large (Fig. 17.1b). The intense convergence over these areas was forced by the anomalously strong PASH and an anomalous cyclonic circulation over the South China Sea, both inducing southerly

convergence flows, which transported a large amount of water vapor into southwestern Japan (Fig. 17.1b).

The stronger PASH during the 2012 rainy season was characterized by a dominant teleconnection pattern over East Asia called the Pacific-Japan (PJ) pattern (Nitta 1987). The PJ pattern consists of a meridional dipole of circulation between the tropical and midlatitude northwestern Pacific (highlighted in Fig. 17.2b by red plus and cross symbols), and is an important teleconnection pattern affecting the East Asian summer climate. Contours in Fig. 17.2a show that convection was more active than normal in the tropics [negative outgoing longwave radiation (OLR)] to the east of the Philippines and Indonesia, associated with a descending high-pressure anomaly over the subtropical area (corresponding to the PASH region) and a low-pressure anomaly to the north of the PASH region. This pressure pattern in 2012 was located to the east of the typical PJ pattern, which tends to intensify heavy rainfall especially in southwestern Japan (Fig. 17.2b, as described hereinafter in detail). In

addition, the emergence of another teleconnection pattern called the circumglobal teleconnection (CGT; Ding and Wang 2005; Yasui and Watanabe 2010), which is characterized by a dominant wave train along the Asian Jet located around 30°N–40°N, amplified the PASH in the rainy season of 2012 (the observed wave train can be found in Supplementary Fig. S17.2). These two independent teleconnection patterns both have barotropic structure and affect the PASH activity and Japanese rainfall.

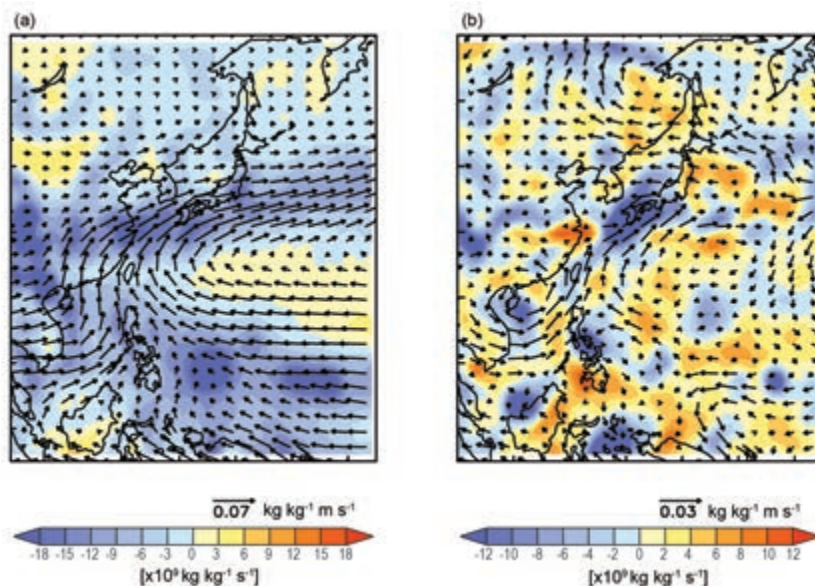


FIG. 17.1. (a) A climatology of the Japanese rainy season (15 Jun–15 Jul) from the JRA-25 reanalysis (1979–2011) column-averaged water vapor flux ($\text{kg kg}^{-1} \text{m s}^{-1}$, arrows) and its divergence ($\times 10^9 \text{kg kg}^{-1} \text{s}^{-1}$, shading). (b) Same as (a) but for anomalies in 2012.

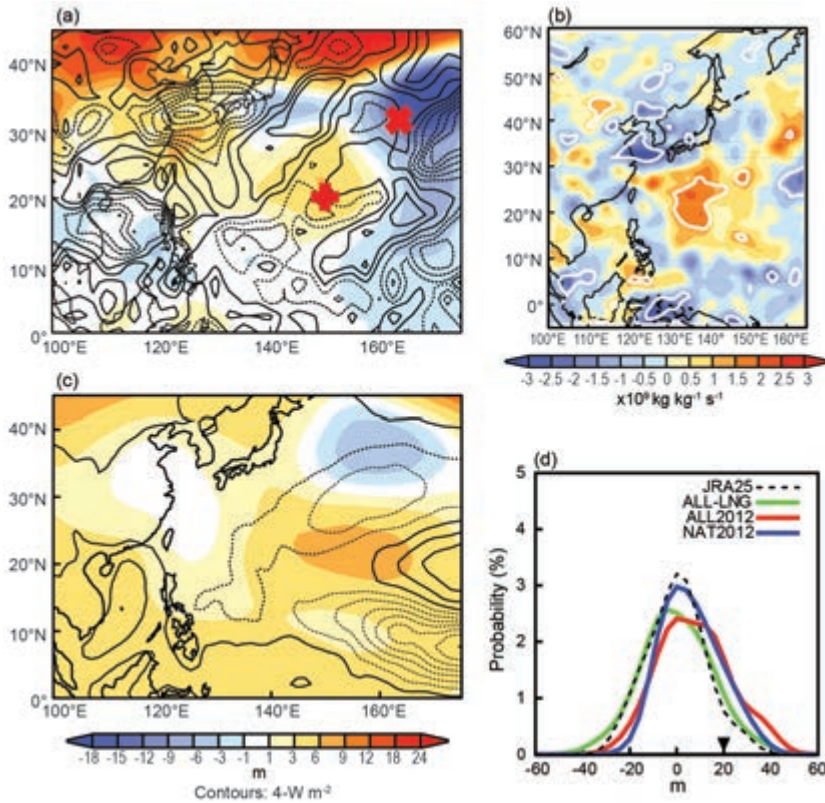


FIG. 17.2. (a) Same as Fig. 17.1b but for Z500 (m, shading) and OLR (contour, 4- W m^{-2} interval). (b) Regression coefficient of column-averaged water vapor divergence onto the observed PJ index from 1979 to 2012 ($\times 10^9$ $kg\ kg^{-1}\ s^{-1}$). White lines denote a 90% significance level. (c) Same as (a) but for a 100-member ensemble-mean of ALL run for the 2012 rainy season. (d) Histogram (bars) and PDF (curve) estimated by the kernel method (Silverman 1986; Kimoto and Ghil 1993) of the PJ index; 1979–2011 climatology based on the JRA-25 (dashed) and 10-member ensemble of ALL-LNG (green), 100-member ALL (red), and NAT (blue) runs for 2012. Triangle indicates an observed anomaly in the 2012 rainy season.

The importance of evaluating the extent to which anthropogenic global warming affects specific extreme weather events has been increasing. In this context, Pall et al. (2011) conducted huge ensemble experiments with an atmospheric general circulation model (AGCM) under two specific boundary conditions corresponding to the period of an extreme event, the observed forcing and a counterfactual forcing without anthropogenic climate change, and evaluated the probabilistic difference in event occurrence rates as the contribution of anthropogenic effect by analyzing the huge pool of AGCM ensemble experiments.

We basically adopted the methodology of Pall et al. (2011). In the case of rainfall events over Japan, most AGCMs do not have the ability to reproduce such regional phenomena but may possibly represent large-scale circulations such as the PJ pattern and the CGT.

In general, CGT is said to be atmospheric internal variability that cannot be attributed to SST forcing (Kosaka et al. 2009). On the other hand, the PJ pattern is a teleconnection from the tropics and has the potential to respond to SST variability, although the PJ pattern is also affected by the stochastic CGT. In terms of global warming, Kusunoki et al. (2006) demonstrated an increase in Baiu rainfall due to the El Niño-like tropical SST changes associated with the intensification of the PASH using time-slice experiments of future projections with a high-resolution AGCM. Therefore, in this study, we focused on the extent to which the anthropogenic SST change raises the level of the PJ occurrence in 2012 relative to natural variability.

Method. We conducted a 100-member AGCM ensemble experiment (factual run, called the ALL run) by an atmospheric component model of the Model for Interdisciplinary Research on Climate version 5 (MIROC5, T85L40, Watanabe et al. 2010). The model was integrated over the recent four years (2009–12), with observed SST and sea ice under the anthropogenic external conditions during the period. In order to assess the influence of possible anthropogenic effects, another 100-member ensemble was generated under anthropogenic forcing fixed at conditions from the year 1850, with modified boundary conditions (SST and sea ice) in which possible human-induced components were removed (counterfactual run under the natural external conditions, called the NAT run, see Shiogama et al. 2013 for details). The difference in the SST boundary conditions between the ALL and NAT runs is characterized by the El Niño-like warming trend pattern in the tropical Pacific, as is the case for most 20th century experiments with coupled GCMs. To validate the model reproducibility of the

primary Research on Climate version 5 (MIROC5, T85L40, Watanabe et al. 2010). The model was integrated over the recent four years (2009–12), with observed SST and sea ice under the anthropogenic external conditions during the period. In order to assess the influence of possible anthropogenic effects, another 100-member ensemble was generated under anthropogenic forcing fixed at conditions from the year 1850, with modified boundary conditions (SST and sea ice) in which possible human-induced components were removed (counterfactual run under the natural external conditions, called the NAT run, see Shiogama et al. 2013 for details). The difference in the SST boundary conditions between the ALL and NAT runs is characterized by the El Niño-like warming trend pattern in the tropical Pacific, as is the case for most 20th century experiments with coupled GCMs. To validate the model reproducibility of the

interannual variability, the ALL run for 1946–2011 was replicated with a reduced ensemble size of 10 (ALL-LNG run).

Validation. Most AGCMs generally have difficulty in reproducing local rainfall variability associated with the Baiu front but have the potential to represent the background circulation. Anomaly correlation maps of rainfall and pressure patterns (500-hPa geopotential height; Z500) between the ALL-LNG and observed anomalies are shown in Supplementary Fig. S17.3a, b, respectively, and they indicate that high correlation is distributed only over a limited area in the equatorial oceans for precipitation, while a significant correlation for Z500 extends to midlatitudes. Therefore, we focused on the specific PJ pattern in 2012. Figure 17.2c shows simulated anomalies of OLR and Z500 in an ensemble mean of the ALL run as in Fig. 17.2a. The ensemble captured the observed PJ pattern responding to active convection in the tropics. We defined a PJ index as the difference of Z500 anomalies between 20°N, 150°E and 32°N, 163°E (plus and cross symbols, respectively, in Fig. 17.2a; the index is defined as the former minus the latter and a positive value corresponds stronger PASH). This index represents the 2012 extreme rainfall well because an observed water vapor supply regressed onto the PJ index shows an enhanced Baiu rainfall over southwestern Japan (Fig. 17.2b). The PJ index for 2012 is the third highest since 1979 (the time series can be found in Supplementary Fig. S17.3c), where the other two extreme cases (1995 and 2006) also involved disastrous heavy Baiu rainfall. The model ensemble average of this index from the ALL-LNG run is positively correlated with the index calculated from observations ($r = 0.35$, exceeding the 90% significant level), indicating that the "PJ pattern responds to the SST forcing to a degree through a convection change in the tropical western Pacific and that there is a potential to detect human influences through our method using the

AGCM. The smallness of the correlation suggests that atmospheric natural variability that is independent from the SST variability also plays an important role in this region. Because the top/bottom 15 cases of the ALL-LNG run diagnosed by the PJ index clearly show the CGT pattern, which intensifies/depresses the PJ pattern (the pattern for the top 15 cases can be seen in Supplementary Fig. S17.2b), our AGCM also has the ability to capture this stochastic atmospheric internal variability. The shape of the probability density function (PDF) of the PJ index based on the model (green curve in Fig. 17.2d) and that derived from observations (dashed curve) are sufficiently similar that we consider our model suitable for the purpose of this study.

Results. We showed the PDFs for the PJ index from ALL and NAT runs with red and blue curves, respectively, in Fig. 17.2d to evaluate the anthropogenic effect to an occurrence rate of the 2012 circulation pattern. The PDFs of both ALL and NAT runs are shifted to the positive PJ pattern relative to the climatological distribution (green). On the other hand, the difference between the ALL and NAT runs is subtle and an ensemble mean of the ALL run is slightly larger than that of the NAT run; it implies that human-induced El Niño-like SST change slightly intensifies the "PJ pattern through the enhanced PASH. These results suggest that our results support the indication of Kusunoki et al. (2006), but in the case of the 2012 event, the effect of anthropogenic global warming is too small to be detected compared with the variability due to the natural variability of the SST.

Conclusions. The extremeness of the Japanese heavy rainfall of 2012 was mainly caused by the oceanic natural variability and probabilistic atmospheric natural variability rather than by anthropogenic climate change.

18. LIMITED EVIDENCE OF ANTHROPOGENIC INFLUENCE ON THE 2011–12 EXTREME RAINFALL OVER SOUTHEAST AUSTRALIA

ANDREW D. KING, SOPHIE C. LEWIS, SARAH E. PERKINS, LISA V. ALEXANDER, MARKUS G. DONAT, DAVID J. KAROLY, AND MITCHELL T. BLACK

Introduction. The 2010–12 period was characterized by well-above-average rainfall over much of Australia. The wetter conditions brought an end to the 13-year drought in southeastern (SE) Australia, although they also led to severe flooding across large areas of New South Wales and Victoria in early 2012. Both total and extreme rainfall were above average in the austral warm seasons (October–March) of 2010–11 and 2011–12 across SE Australia [2011–12 spatial anomalies are shown in Figs. 18.1a and 18.1b for rain-

fall totals and maximum consecutive five-day rainfall (Rx5day; Zhang et al. 2011) respectively]. Many stations across this region broke daily and multiday rainfall records as well as monthly records during February and March 2012 (Bureau of Meteorology 2012; Ganter and Tobin 2013).

ENSO is the primary driver of climate variability in eastern Australia (Nicholls et al. 1997) with greater rainfall totals during La Niña seasons than El Niño seasons in SE Australia (Fig. 18.1c). There is an asym-

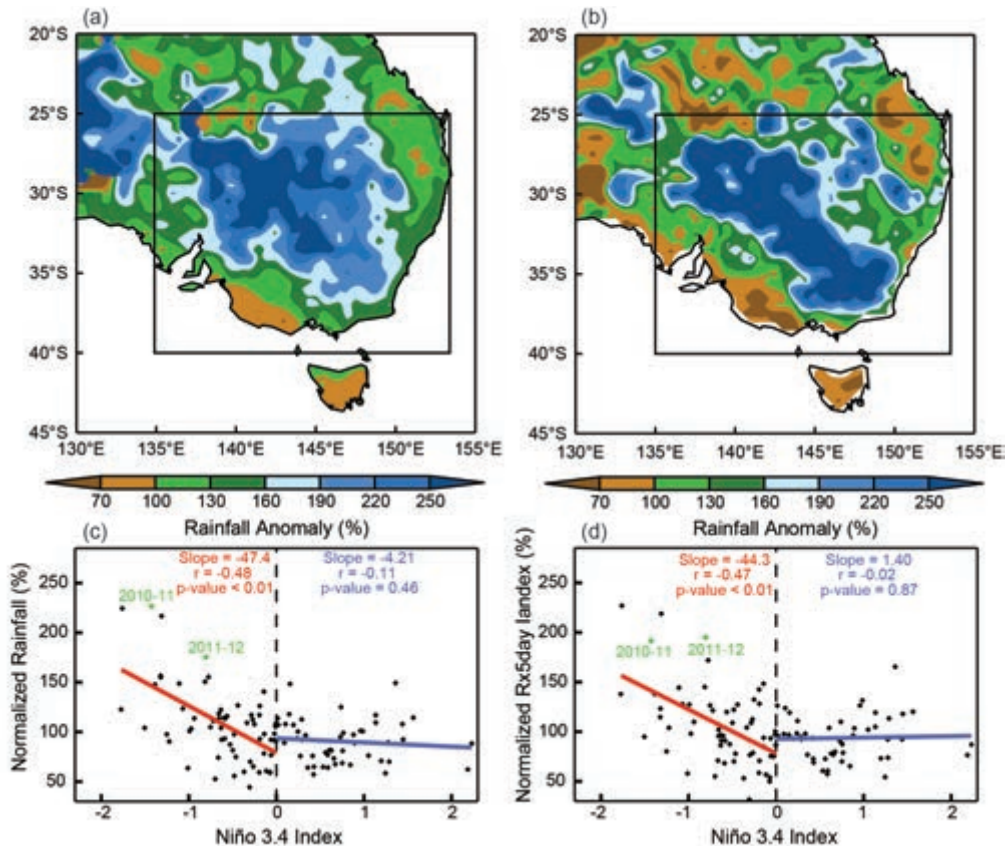


FIG. 18.1. Maps of Oct 2011–Mar 2012 (a) total rainfall and (b) Rx5day anomalies as a percentage of the Oct–Mar mean seasonal rainfall and Rx5day, respectively, for the period 1900–2012. The boxed region represents our area of study. Scatter plots of Oct–Mar Niño-3.4 SSTAs against area-averaged Oct–Mar (c) total rainfall and (d) Rx5day values for southeast Australia. Lines of best fit, calculated using ordinary least squares regression, are shown for warm SSTA (red) and cool SSTA (blue) seasons with corresponding slope values. The correlation (Spearman's Rank, r) and the significance of the fit (p -value) are also shown. The recent 2010–11 and 2011–12 seasons are marked in green.

metry whereby negative SST anomalies have a greater effect than positive SST anomalies on rainfall totals. Similar asymmetric relationships were reported by Power et al. (2006) for the Australian continent as a whole and by Cai et al. (2010) for SE Queensland.

A strong asymmetric ENSO-extreme rainfall teleconnection also exists for the SE Australia region (Fig. 18.1d) for area-averaged values of Rx5day. King et al. (2013) observed an asymmetric ENSO-extreme rainfall relationship for eastern Australia. The 2010–11 and 2011–12 seasons are two of the four largest Rx5day totals in the 1900–2012 series. This begs the question whether anthropogenic effects on the climate have affected the ENSO-extreme rainfall relationship, thus altering the probability of extreme rainfall in this area.

Data and methods. Observed monthly total rainfall and Rx5day amounts were calculated from the Australian Water Availability Project (AWAP) gridded dataset of daily rainfall (Jones et al. 2009) interpolated onto a regular 0.5° grid. Anomalies from the 1900–2012 means of total rainfall and Rx5day were calculated for each grid box separately. SSTs in the Niño-3.4 region (5°N–5°S, 170°W–120°W) were used as an index for ENSO from the HadISST dataset (Rayner et al. 2003). Observed total and Rx5day anomalies were averaged across the SE Australia region as defined by the boxed area (25°S–40°S, 135°E–154°E) in Fig. 18.1a,b and plotted against Niño-3.4 SSTs (Fig. 18.1c,d). As Rx5day anomalies at individual gridboxes were calculated relative to the gridbox mean values, the area-average Rx5day values are not biased towards wetter areas of SE Australia. The boxed region includes Australia's largest cities (i.e., Sydney, Melbourne, and Brisbane), with more than three-quarters of the country's population, and the entire Murray-Darling Basin, an area accounting for over 40% of Australia's agricultural production in terms of gross value (Nicholls 2004).

To make inferences about potential anthropogenic impacts, historical runs from models in the Coupled Model Intercomparison Project phase 5 (CMIP5) archive (Taylor et al. 2012) were analyzed and compared with observations. Ten models were selected based on the availability of data in the Australian node of the CMIP5 data repository and on their ability to capture variability in ENSO (see Supplementary Table S18.1). As ENSO strongly drives Australian rainfall variability, models that do not capture ENSO variability cannot replicate the observed teleconnection. These ten models adequately capture the amplitude

of variability in Niño-3.4 region surface air temperatures seen in the observational HadCRUT4 dataset (Morice et al. 2012). The absolute SE Australia Rx5day amounts were taken from data downloaded from Environment Canada's CLIMDEX website (<http://www.cccma.ec.gc.ca/data/climdex/>; Sillmann et al. 2013). Rx5day anomalies were first calculated for each grid box in each model run and then averaged over the SE Australia domain. The anomalies were calculated in the same way as for the observations, so the area-averaged Rx5day anomaly values are not biased towards wetter areas. Sea surface temperature anomalies (SSTAs) in the Niño-3.4 region and Rx5day anomaly values for SE Australia were calculated for each individual model run and examined against each other per model. All models had greater Rx5day values in La Niña seasons than El Niño seasons. Models that did not have a stronger relationship between Niño-3.4 SSTAs and Rx5day when SSTAs are negative than when they are positive were removed leaving five models to be analyzed in more detail (models in bold in Supplementary Table S18.1). The area-averaged Rx5day anomaly values for each model were normalized against the model mean values over the historical period. Niño-3.4 SSTAs and normalized values of Rx5day could then be plotted together for the five models studied.

To examine for possible changes in extreme rainfall and in the ENSO-extreme rainfall teleconnection, the relationships in the modeled 1861–90 and 1976–2005 periods were compared. The earlier period (1861–90) was used to represent a time of much lower anthropogenic influence on the climate than the later period. Values of Rx5day in La Niña seasons only (defined as October–March seasons with SSTAs less than -0.5°C) were used to plot probability distribution functions (PDFs) in the two 30-year periods and these were examined for anthropogenic signals. Any low-frequency variability in the model runs would be unlikely to influence our results as multiple model runs were considered together. To examine the effect of ENSO variability, PDFs of La Niña Rx5day values and all other seasons' values through the entire historical period were also analyzed.

A Kolmogorov-Smirnov (KS) test was used to quantify differences between the respective sets of PDFs. Each PDF was bootstrapped 1000 times based on sub-samples of 50% of the smaller data sample being examined. Fractional Attributable Risk (FAR; Allen 2003) was calculated to examine change in risk of extreme rainfall events associated with anthropogenic influences and ENSO variability. FAR was

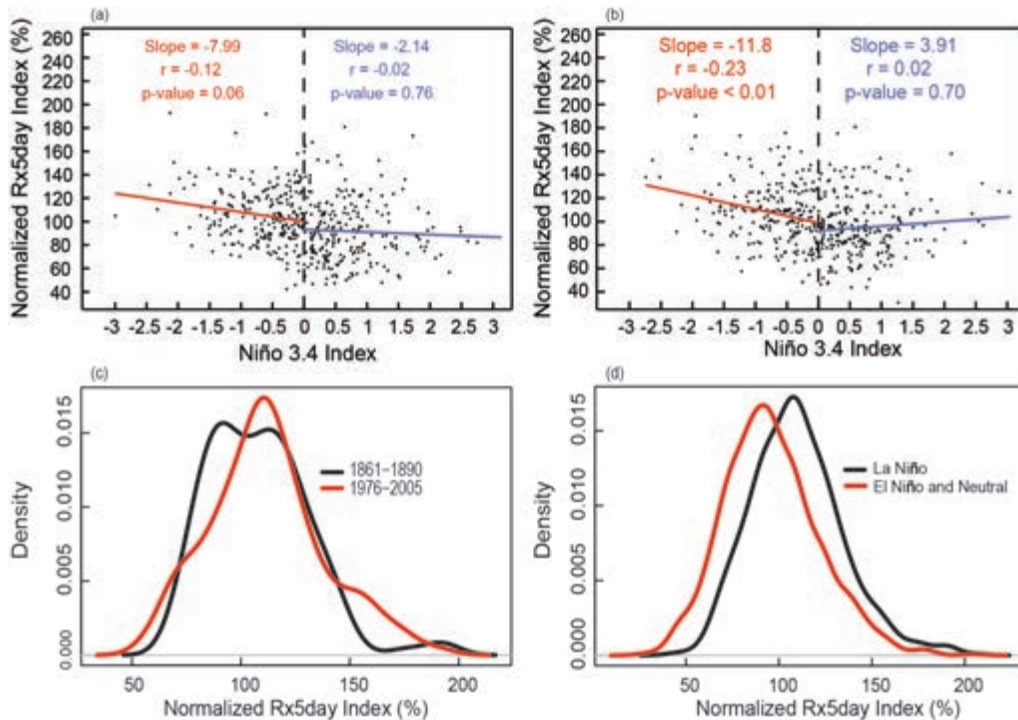


FIG. 18.2. (a) and (b) Scatter plots of Oct–Mar Niño-3.4 SSTAs against area-averaged Oct–Mar Rx5day values for southeast Australia for five CMIP5 models. Lines of best fit, calculated using ordinary least squares regression, are shown for warm SSTA (red) and cool SSTA (blue) seasons with corresponding slope values. The correlation (Spearman's Rank, r) and the significance of the fit (p -value) are also shown. These scatter plots are for the (a) 1861–90 and (b) 1976–2005 periods. PDFs of (c) La Niña-only normalized Rx5day values in the 1861–90 (black line) and 1976–2005 (red line) periods from the five CMIP5 models and of (d) La Niña-only (black line) and El Niño and Neutral (red line) normalized Rx5day values for the entire historical period from the five CMIP5 models.

calculated using Rx5day values above 150% of the mean Rx5day over the entire period to compare the frequency of extreme events between the early and late periods, and La Niña and all other events. The 150% threshold permitted the inclusion of only extreme rainfall events and provided a reasonable sample size for the FAR calculation.

All analysis involving both observations and models was done over October–March periods, coinciding with the peak in the annual ENSO cycle and the warm season in SE Australia when more of the extreme rainfall events occur.

Results. The analysis was conducted using the subselection of five CMIP5 models (those in bold in Supplementary Table S18.1), as the relationship in La Niña seasons is reproduced to some degree. The ENSO-extreme rainfall relationship is plotted for all five models combined, for the 1861–90 and 1976–2005 periods (Figs. 18.2a,b). There is little obvious change in the relationship between the two periods. On average, Rx5day values are 1.9% greater in the latter period

than the earlier one. The increase is slightly weaker in La Niña seasons (1.3%) than El Niño (October–March with SSTAs greater than 0.5°C) seasons (3.4%).

The normalized Rx5day values in La Niña seasons only were selected to form PDFs for each of the 30-year periods (Fig. 18.2c). These PDFs are based on 124 samples for the 1861–90 period and a sample size of 119 for 1976–2005. There is some difference between the two PDFs in terms of their shape, but a KS-test suggests the two PDFs are not significantly different (at the 5% level). Examining values above a 150% threshold in the two periods gives a FAR value of +64% (with a standard deviation of $\pm 22\%$ calculated through bootstrapping) for extreme Rx5day values due to anthropogenic climate change in the recent period. It is worth noting that the FAR value is strongly sensitive to choice of threshold, selection of models, and region of study. Therefore, a robust anthropogenic influence cannot be detected.

Taking all normalized Rx5day values across the historical period in La Niña seasons and comparing with those values from neutral and El Niño seasons,

the PDFs shown in Fig. 18.2d were plotted. These PDFs are formed from 637 samples representing La Niña Rx5day values and 1523 samples representing El Niño and neutral Rx5day values. These PDFs are significantly different. FAR values show an increase in the likelihood of Rx5day values above a 150% threshold of 58% (with a standard deviation of $\pm 15\%$ across the 1000 estimates) in La Niña seasons compared with El Niño and neutral seasons combined. This FAR value is robust to the choice of threshold used.

Conclusions. We examined SE Australia extreme rainfall and its teleconnection with ENSO in observations and a selection of CMIP5 models. In observations, the magnitude of anomalously cool SSTs in the Niño-3.4 region has a far greater effect on Rx5day in SE Australia compared to the magnitude of anomalously warm SSTs. Five CMIP5 models were selected as the focus for our study as they possess aspects of ENSO variability and an asymmetric ENSO-extreme

rainfall relationship. Using these models, we found little evidence of significant change in the ENSO-extreme rainfall relationship between 1861–90 and 1976–2005. The PDFs of Rx5day values in La Niña seasons also show nonsignificant differences between the same periods. There is little robust change in the risk of extreme rainfall events between 1861–90 and 1976–2005. Interannual variability related to ENSO has played a greater role than any long-term trend on the magnitude of extreme rainfall events in southeast Australia over the period 1861–2005. In summary, we detect limited evidence of a change in the relationship between ENSO and SE Australia extreme rainfall, or of a change in extreme rainfall itself, that may be attributed to anthropogenic climate change. Similar analysis of the austral summer mean rainfall anomalies in 2010–11 and 2011–12 also show some influence from La Niña with no apparent influence from anthropogenic climate change in the observed rainfall anomalies.

19. AN ATTRIBUTION STUDY OF THE HEAVY RAINFALL OVER EASTERN AUSTRALIA IN MARCH 2012

NIKOLAOS CHRISTIDIS, PETER A. STOTT, DAVID J. KAROLY, AND ANDREW CIAVARELLA

Introduction. Heavy rains at the end of summer 2012 across eastern Australia (Bureau of Meteorology 2012) led to swollen rivers and widespread flooding that swamped agricultural land, caused loss of life, and forced tens of thousands of people to evacuate their homes. The event came only a year after the catastrophic floods in Queensland, when the largest part of the north-eastern state was declared a disaster zone. In the aftermath of two major floods in consecutive years, the question arises whether the odds of heavy rain in eastern Australia are set to increase under the synergy between internal climate variability and externally forced climate change. Here we investigate the possible contributions of the ENSO and the long-term effect of human influences on the climate to the heavy rainfall in March 2012 over eastern Australia (10°S–45°S, 140°E–160°E). The anthropogenic contribution is estimated with a new state-of-the-art system for Attribution of extreme weather and Climate Events (ACE; Christidis et al. 2013), built on HadGEM3-A, the latest atmospheric model from the Hadley Centre. We concentrate on March, as the main flooding occurred in the beginning of that month and the total rainfall in the region was exceptionally high

in comparison with the summer months (Fig. 19.1a). In fact, March 2012 ranks as the third wettest after 2011 and 1956 in the Global Historical Climatology Network (GHCN) dataset used to provide rainfall observations for this study (Peterson and Vose 1997). Although the heavy rainfall event examined here is not unprecedented, the adverse impacts associated with two consecutive wet years in the region make it an interesting case to study.

The influence of ENSO. A correlation between the phase of ENSO and rainfall in Australia has long been identified (McBride and Nicholls 1983). La Niña episodes, characterized by warm SST anomalies over the West Pacific are associated with wetter-than-normal conditions over eastern Australia. While La Niña conditions prevailed at the end of 2011 and beginning of 2012, they had considerably weakened by March, and ENSO changed phase in April. Figure 19.1b illustrates the relationship between March precipitation in the region and the Southern Oscillation Index (SOI) from summer to early autumn. An increase in rainfall with the SOI is evident, and the slope of the least-square fit is found to be significantly different

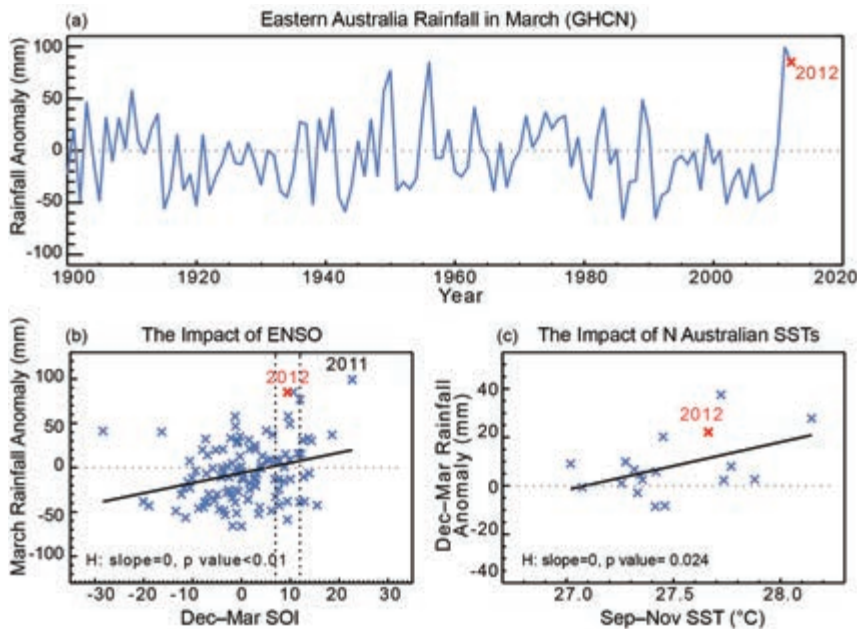


FIG. 19.1. GHCN observations of rainfall anomalies relative to 1961–1990 over eastern Australia. (a) 1900–2012 Mar rainfall time series; (b) the relationship between Mar rainfall and the Dec–Mar mean value of the Southern Oscillation Index (from <http://www.bom.gov.au/climate/current/soi2.shtml>); (c) the relationship between Dec–Mar rainfall and spring north Australian SST anomalies (from HadISST) for years with $7 < \text{SOI} < 12$ (marked by the vertical dotted lines in panel b). The year 2012 is highlighted in red. The p-values (panels b and c) refer to testing of the hypothesis that the least square fit (plotted in black) has a zero trend.

from zero. While the La Niña episode early in the year is likely to increase the chances of a wet March, the extremely high rainfall amount (marked with a red cross in Fig. 19.1b) is unlikely to be attributable solely to ENSO.

SST warming to the north of Australia. Australian rainfall is also influenced by the SSTs to the north of the country, and it is found that warm anomalies during spring are associated with heavy summer rainfall across eastern Australia (Nicholls 1984; Evans and Boyer-Souchet 2012). Figure 19.1c depicts the relationship between summer-to-early-autumn rainfall and the spring SSTs around northern Australia (0° – 22°S , 94°E – 174°E) taken from the HadISST dataset (Rayner et al. 2003). Both external forcings and variability may contribute to warm SSTs. In order to minimize the effect of variability due to ENSO (Catto et al. 2012) we examine only years with SOI between 7 and 12 (marked by the vertical dotted lines in Fig. 19.1b), i.e., similar conditions to the event we consider here. We find a significant increase in rainfall with SST, which could explain wetter conditions in December–March 2012 given the warm ocean temperature. The observations suggest an increase in the SSTs north of

Australia by 0.1 K decade^{-1} over the last 50 years, consistent with the multidecadal anthropogenic global ocean warming (Glecker et al. 2012; Pierce et al. 2006). While the SST warming is indicative of more wet summers over eastern Australia, which could also be exacerbated by La Niña conditions, it is important to assess whether the occurrence of extreme rainfall also becomes more frequent. So far, we have only assumed that long-term externally forced climate change might have contributed to the heavy rainfall in 2012 through the warming of the ocean. We next attempt to investigate the overall contribution of human influences in more detail and examine how they may have changed the odds of above average and extreme rainfall in March 2012.

Anthropogenic influence. The new Hadley Centre ACE system has already been employed to study several high-impact extreme events in recent years (Christidis and Stott 2012; Christidis et al. 2013; Lott et al. 2013). We carried out a new experiment that comprises ensembles of 600 simulations with HadGEM3-A over the period September 2011–August 2012. We have one ensemble that represents the actual climate where the effect of all external forcings is accounted for and two ensembles that provide two possible representations of a hypothetical “natural” climate without the effect of human influences. In simulations of the natural climate, an estimate of the anthropogenic change in the SSTs has been subtracted from the prescribed observations and the sea ice has been adjusted accordingly. The estimate of the change in the SST comes from two Earth System models, HadGEM2-ES (Jones et al. 2011) and CanESM2 (Gillett et al. 2012), hence, we have two different representations of the natural climate without human influences. Details on the ACE experimental setup are given in Christidis et al. (2013). We assessed the model skill in reproducing high rainfall during March over eastern Australia on the basis of reliability diagrams, as in previous work. Using GHCN observations and a five-member

ensemble of multidecadal simulations of the actual climate, we find that the forecast probability is consistent with the observed frequency of heavy rainfall in the reference region, which suggests the model can represent well drivers of high rainfall events and is therefore a reliable tool for our analysis.

Figure 19.2 illustrates the regional rainfall distributions for March 2012 with and without anthropogenic effects as well as the change in the odds of above average, heavy, and extreme precipitation (defined in the figure caption) due to human influences. Note that the observed rainfall in March 2012 was three standard deviations above the climatological average, i.e., well above the extreme threshold. Our results (Figs. 19.2a and 19.2c) indicate a small but statistically significant (as inferred from a Kolmogorov-Smirnov test) shift in the rainfall distribution towards wetter conditions under the effect of anthropogenic forcings. For the calculation of the change in the odds, the probabilities of exceeding a threshold are computed using the generalized Pareto distribution if the threshold lies at the tails, and a Monte Carlo bootstrap procedure is employed to estimate the sampling uncertainty (Christidis et al. 2013). Figures 19.2b and 19.2d show that the uncertainty in our estimate of the change in the odds increases as the threshold becomes more extreme, which implies that larger samples would be required to estimate small probabilities with greater precision. Our analysis provides evidence for increasing odds of above average rainfall relative to the natural climate. Therefore, although there is no evident trend in rainfall observations (Fig. 19.1a), once we constrain the SSTs and thus minimize the effect of natural variability, we begin to see an emerging signal of wetter months under the influence of anthropogenic forcings, as also indicated in Fig. 19.1c. The odds of heavy and extreme precipitation also seem to increase, as the largest part

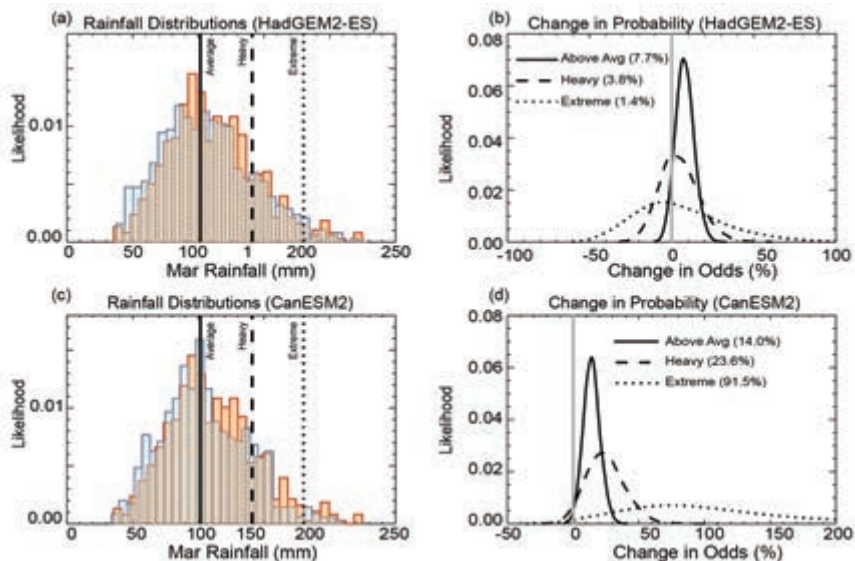


FIG. 19.2. Normalized distributions of the rainfall over eastern Australia in Mar 2012 (panels a and c) constructed with the ACE ensembles with (red histograms) and without (blue histograms) the effect of human influences. Simulations of the natural climate use estimates of the change in the SST and sea ice due to anthropogenic forcings from HadGEM2-ES and CanESM2 (blue histograms in panels a and c respectively). The normalized distributions of the change in the odds of above average, heavy, and extreme rainfall in the region in Mar 2012 due to anthropogenic forcings are shown in panels (b) and (d) for the two versions of the natural climate. The thresholds for average, heavy, and extreme rainfall correspond to the 1960–2010 climatological mean and the rainfall levels of one and two standard deviations above the mean. The best estimate of the change in the odds, approximated by the median of the distribution, is also noted in panels (b) and (d).

of the corresponding distributions in Figs. 19.2b and 19.2d lies over positive values, but the uncertainty in these cases is much larger. The results for these higher thresholds are also more sensitive to the SSTs prescribed in the simulations of the natural climate with the CanESM2 version providing a much stronger indication of an increase in heavy and extreme rainfall. It should be noted that the anthropogenic warming in north Australian SSTs computed with CanESM2 is 0.54 K higher than the HadGEM2-ES estimate, indicative of a greater separation between the rainfall distributions with and without the effect of human influences.

Conclusions. The La Niña episode in early 2012 is unlikely to entirely explain why March 2012 was the third wettest in the observational record in eastern Australia. Warm north Australian SSTs, however, are expected to result in wetter conditions and given the continuing warming trend of the ocean, increased rainfall over the eastern part of the country could become more common. Using the ACE methodology we find that the overall long-term effect of human

influences on the climate increases the chances of above-average rainfall by 5%–15% (best estimate), although the impact on extreme precipitation is much more uncertain. Even when all climatic forcings are accounted for, the observed rainfall in March 2012

lies in the far tail of the expected rainfall distribution from the ACE ensembles. Therefore, despite the potential contribution of all factors examined here, the extreme magnitude of the event appears to arise mainly from unforced internal climatic variations.

20. THE ROLE OF CLIMATE CHANGE IN THE TWO-DAY EXTREME RAINFALL IN GOLDEN BAY, NEW ZEALAND, DECEMBER 2011

SAM M. DEAN, SUZANNE ROSIER, TREVOR CAREY-SMITH, AND PETER A. STOTT

Introduction. In December 2011, a torrent of water fell from the sky in Golden Bay and Nelson, overwhelming local streams and inundating the landscape with mud and debris. Barren scars of earth littered the hillsides of the region, a testimony to the power of the event (see Supplementary figures). The culprit was a low-pressure weather system that transported moist air directly from the subtropics to New Zealand (Fig. 20.1a and Supplementary animation). When this “atmospheric river” collided with the coastal hills of Golden Bay and Nelson, the rainfall amounts were staggering—in the township of Takaka 453 mm was recorded in just 24 hours and 674 mm in 48 hours. This greatly exceeds any previous record at this site, and from the available observations, it has been estimated that the 48-hour total is a one in 500-year event. The event was also the largest 48-hour accumulation ever recorded in an urban area in New Zealand.

Strikingly, the rain fell predominantly on coastal hills within 2 km–5 km of the coast (all <500 m elevation), such that none of the major rivers with headwaters in the mountains reached extreme flood lev-

els. Such high rainfall in coastal areas is damaging, predominantly because of higher population density. The event was unusual due to its rare combination of high humidity in the lower atmosphere accompanied by only moderate winds (Doyle and Harvey 2012). A stationary high east of New Zealand also played a key role in slowing the progress of the deep low.

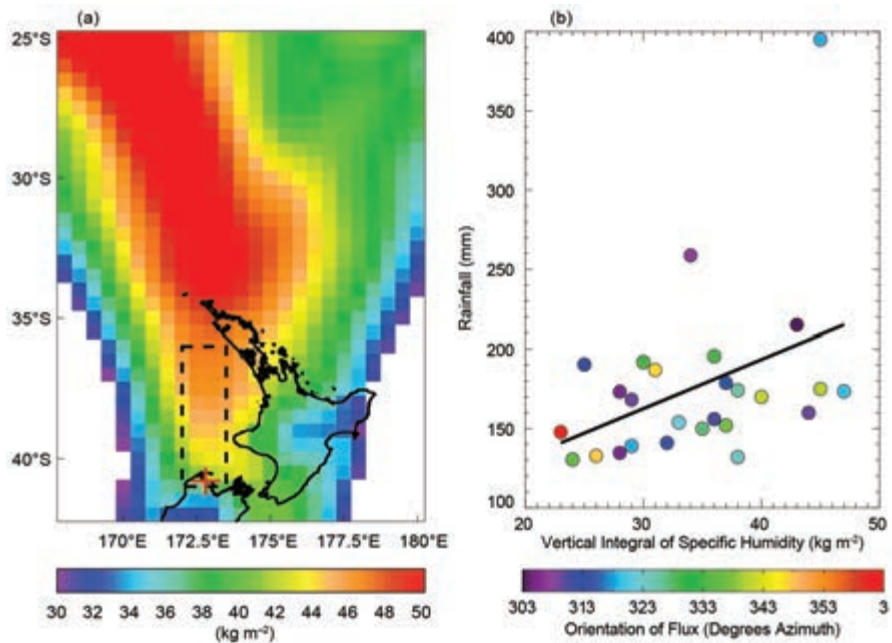


FIG. 20.1. Observations of the Dec 2011 Golden Bay and Nelson extreme rainfall event. (a) Vertical integral of the specific humidity (kg m^{-2}) for 14 Dec 2011 from the ERA-Interim reanalysis. The location of the Takaka rain gauge is indicated by the red cross, while the dashed lines indicate the box over which the large-scale fields were averaged. (b) Vertical integral of the specific humidity (kg m^{-2}) from ERA-Interim averaged for the box in (a) plotted against all daily rainfall amounts (09:00 to 09:00 NZST) measured at Takaka that exceeded 130 mm for the period 1979–2012. Colors indicate the orientation of the vertical integral of the moisture flux. Note that the Dec 2011 event lies in the top right of the figure.

Was this event influenced by climate change? Pall et al. (2011) have recently demonstrated how the risk of a monthly scale flooding event in England and Wales changed due to the emission of anthropogenic greenhouse gases (GHGs). However, it is difficult to apply their techniques to the short duration rainfall events that are typical of flooding in New Zealand, largely because of the higher spatial and temporal variability involved.

Here it is suggested that progress might be made on this question by using a methodology that is capable of identifying all occurrences of the synoptic situation matching the Golden Bay/Nelson event within large ensembles of climate-model simulations that alternatively exclude and include the impact of GHGs. If the observed precipitation distribution for these events is well simulated by the model for the past climate, then any change in the rainfall distribution due to GHGs can be considered.

A formal attribution based on precipitation requires a large ensemble from a regional climate model capable of resolving the fine structure of atmospheric rivers, and this is an objective of the Australia/New Zealand “weatherathome” experiment (<http://www.weatherathome.net>). As a first step, this paper tests the proposed methodology in a simplified manner by considering the daily data available from the Coupled Model Intercomparison Project 5 (CMIP5) archive of global climate models (Taylor et al. 2012). Our analysis relies on the relationship between rainfall extremes at midlatitudes and the large-scale moisture fluxes associated with atmospheric rivers (Junker et al. 2008; Ralph and Dettinger 2012). Here we derive the relationship between the large-scale circulation and Golden Bay extreme rainfall events using station observations and moisture fluxes from the ERA-Interim reanalyses (Dee et al. 2011). We then apply these constraints to the CMIP5 models and consider the impact on the humidity available for precipitation.

Observations of rainfall and moisture. In Fig. 20.1b, all observations are 09:00 New Zealand Standard Time (NZST) 24-hour rainfall accumulations, which have exceeded 130 mm in Takaka (1979–2012). This corresponds to all observations at or above the 99.8th percentile of the rainfall distribution, an arbitrary threshold for an extreme. For each of these 26 events, the vertical integral of the meridional and zonal moisture fluxes from ERA-Interim were used to calculate an orientation and magnitude for the integrated moisture flux averaged over the dashed box shown in Fig. 20.1a. The direction of origin for the moisture

fluxes (Fig. 20.1b, colors) lies in a narrow range of angles between north and northwest. This is a direct consequence of the topography that surrounds this location.

The vertical integral of specific humidity derived from ERA-Interim, and averaged over the same area, is plotted against the extreme precipitation amounts in Fig. 20.1b. Rainfall extremes are hypothesized to increase with the availability of moisture (Allen and Ingram 2002; Trenberth et al. 2003), and the moderate positive correlation in this very small sample of observations suggests some support for this conclusion. The observations also suggest that high moisture flux magnitudes are a prerequisite for extreme precipitation (not shown), but there is no similar linear relationship between moisture fluxes and extreme precipitation (not shown).

Altogether, this analysis suggests that an angle constraint on moisture flux direction, combined with a minimum magnitude of moisture flux and specific humidity, may be used to define large-scale synoptic conditions that are a prerequisite for rainfall extremes at this location. Thresholds used for the integrated specific humidity and moisture flux are the minimum values observed for Takaka extreme events, 23 kg m⁻² and 400 kg m⁻¹ s⁻¹ respectively. However, these basic criteria overpredict extreme precipitation: for 1979–2012 ERA-Interim has 315 events that match the criteria while only 26 extreme events (>130 mm day⁻¹) are observed at Takaka.

Is there evidence from global climate models that the total moisture available for this event has changed as a result of GHG emissions? Daily pressure, humidity, and wind fields were acquired from the CMIP5 archive for climate models providing historical simulations (1950–2005) that included all natural and anthropogenic forcings (ALL) as well as matching simulations that included only natural forcings (NAT). The only four climate models that met these criteria were BNU-ESM, GFDL-ESM2M, IPSL-CM5A-LR, and IPSL-CM5A-MR (see PCMDI 2013 and links therein for model descriptions). From these, the vertical integrals of moisture flux and specific humidity were calculated for the dashed box in Fig. 20.1a. Potential extreme rainfall events were identified using the constraints for moisture flux and humidity described previously. The number of events that match these synoptic criteria for a Takaka rainfall extreme in the ALL simulations range from 469 to 738, which can be compared to an estimate of 525 from ERA-Interim for a period of 55 years. This suggests the models do a

reasonable job of reproducing the frequency of these synoptic conditions. All four models show an increase in the number of events for the ALL simulations compared to the NAT, with a range of 8% to 32%. In all cases, this is dominated by an increase in the number of events that exceed the moisture thresholds, rather than because of changes in the occurrence of synoptic lows. This gives confidence that these increases in the ALL simulations are a thermodynamic response to the emission of GHGs.

Figure 20.2 shows the percentage change in the vertically integrated specific humidity for these events for ALL relative to NAT. The plot is created by calculating the quantiles for the smaller number of events in the NAT simulations (a percentile for every value) and then interpolating the events in the ALL simulations onto these percentiles. While all four model distributions are noisy at this scale, there is a consistent trend for the models to increase the specific humidity, particularly in the high tail of the distribution. To calculate the change at the actual value of the Takaka event, we reduce this noise by averaging over the 16 quantile values centered on 45 kg m^{-2} . All four models increase the integrated specific humidity in

the ALL simulations relative to the NAT, with a range of 1.3%–5.4% and an average of 3.6%.

It is hypothesized that rainfall extremes should increase with global warming, primarily as the availability of moisture in the atmosphere increases by about 7% per degree of warming following the Clausius-Clapeyron constraint. For this particular event, the integrated specific humidity increases from NAT to ALL by an average 6% per degree of warming (range of 2%–10%), where the change in temperature is calculated over a region covering both Golden Bay and the moisture source region for the event. For midlatitudes, the increase in precipitation expected to have occurred may be somewhat more or less than these changes in moisture due to the way vertical winds and the vertical temperature structure change locally (O’Gorman and Schneider 2009; Pall et al. 2007).

Conclusions. This analysis indicates that the total moisture available for precipitation in the Golden Bay/Nelson extreme rainfall event of December 2011 was 1%–5% higher as a result of the emission of anthropogenic greenhouse gases. Theory and observations imply that this should have led to increased

precipitation for this location. This analysis also found that the number of synoptic events with enough moisture to cause extreme rainfall in Takaka has increased, which indicates there may have been an elevated risk of this type of event. In this study, no attempt has been made to adequately assess the uncertainty on these results. A much larger ensemble of a higher resolution model, such as in the “weatherathome” experiment, is required for formal attribution statements about precipitation extremes.

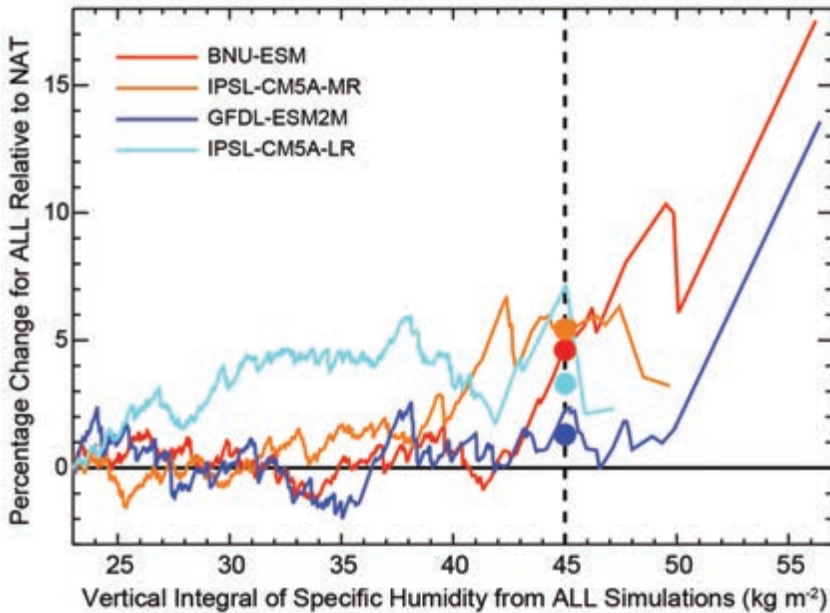


FIG. 20.2. Percentage change in the vertical integral of specific humidity for an ALL simulation relative to a NAT simulation for each of four CMIP5 models over the period 1950–2005. This is shown plotted against the values of the vertical integral of specific humidity for the ALL simulations, such that the value for the Golden Bay/Nelson event (45 kg m^{-2}) calculated from ERA-Interim can be shown by the dashed line. The colored dots are the respective values for the change in vertical integral of specific humidity when 16 quantile values are averaged about the value of the Golden Bay/Nelson event. In the case of IPSL-CM5A-LR, there are only two points above 45 kg m^{-2} available for the calculation.

21. CONCLUSIONS AND EPILOGUE

THOMAS C. PETERSON, PETER A. STOTT, STEPHANIE C. HERRING, AND MARTIN P. HOERLING

To help understand the difficulty of determining the anthropogenic contribution to specific extreme events, consider this driving analogy (UCAR 2012). “Adding just a little bit of speed to your highway commute each month can substantially raise the odds that you’ll get hurt some day. But if an accident does occur, the primary cause may not be your speed itself: it could be a wet road or a texting driver.” Similarly, while climate models may indicate a human effect is causing increases in the chances of having extremely high precipitation in a region (much like speeding increases the chances of having an accident), natural variability can still be the primary factor in any individual extreme event. The difficulty in determining the precise sensitivity of, according to our analogy, driving speed on risks of accidents in particular conditions (wet roads, texting drivers) can explain why somewhat different analyses of the same meteorological event can reach somewhat different conclusions about the extent to which human influence has altered the likelihood and magnitude of the event.

For example, one assessment of seasonal changes in heavy five-day precipitation events in Australia finds little modeled evidence of long-term changes in such events once ENSO is factored in, while another analysis that examined the human influence on total monthly precipitation for March in roughly the same area found that it increased the probability of above average rainfall by 5%–15% (“Limited Evidence of Anthropogenic Influence on the 2011–12 Extreme Rainfall over Southeast Australia” and “An Attribution Study of the Heavy Rainfall over Eastern Australia in March 2012” in this report). These differences arose despite the two analyses having an author in common. However, the bottom line of the event attribution was basically the same: that the heavy rain last year in eastern Australia was predominately due to natural variability. But for rare events, the results of these analyses of Australian rainfall illustrate how attribution studies that examine the effects of human influences on an extreme event can be dependent on both the methodology used in the assessment as well as the choice of metrics.

Among all the extreme events that occurred around the world in 2012, the subset of events analyzed in this paper was not chosen at random. While “The Extreme March–May 2012 Warm Anomaly over

the Eastern United States: Global Context and Multi-model Trend Analysis” (in this report) used objective criteria to search the globe to determine the event to analyze, other analysis topics were selected based on a variety of factors similar to what drives a great deal of scientific research, including the researchers’ interests and subjective estimation of what events present tractable problems. It is likely no accident that the majority of the submissions focus on events related to temperature and precipitation, given that these are two variables where the observational record is strong. We also see a natural bias towards addressing local events as scientists in Australia, China, France, Japan, the Netherlands, New Zealand, Spain, the United Kingdom, and the United States examined extreme events impacting themselves, their friends, and their neighbors. A few groups examined events in distant locations, including Arctic sea ice and drought in the Horn of Africa, which they deemed important. It is also noteworthy that only one group examined a cold event, which global warming might theoretically be expected to decrease in frequency or intensity. So, there is a danger in drawing too strong a conclusion from a small sample of 19 analyses of 12 events that were not chosen at random. That said, approximately half of the analyses found some evidence that anthropogenic climate change was a contributing factor to the extreme event examined, though the effects of natural fluctuations of weather and climate on the evolution of many of the extreme events played key roles as well.

In this second issue of the annual *BAMS* attribution report, an important innovation is that we have now included multiple analyses of a single event. The differences in the results also provide insights into the structural uncertainty of event attribution, that is, the uncertainty that arises directly from the differences in analysis methodology. For example, there are four different studies of the wet summer in northern Europe using different methodological approaches, observational datasets, and climate models. While these studies provide complementary perspectives into the possible roles of North Atlantic sea surface temperatures, Arctic sea ice reduction, atmospheric circulation, and an enhanced moisture carrying capacity of the atmosphere, these studies also highlight certain deficiencies of current models, observations, and methods. As a result, the attribution conclusions

for such relatively complex events remain somewhat equivocal. The results in general contained in this special issue are not necessarily the final word nor the definitive treatments on these cases. Other studies, using different and perhaps improved tools (e.g. new models) will undoubtedly come forth and will further test the efficacy of surmised and plausible causal factors. In the manner that has become common in our field to "re-analyze" historical data as new data, analysis methods and models come forward, so too we foresee a rich science enterprise of "re-attribution". A priority for further research is to develop modeling systems that have been shown to be sufficiently reliable with respect to the specific type of extreme being assessed to generate less equivocal and more robust results for such complex events.

With the increasing sophistication of event attribution studies comes a greater focus on assessing the capability of the various current approaches to provide robust answers to such difficult questions as whether there is a link between anthropogenic climate change and the extremely wet summer in northern Europe in 2012, which was not only an extreme event in itself but also the sixth summer in a row in which UK rainfall was higher than the 1981–2010 average.

Where does the work on event attribution go from here? At the September 2012 workshop on the Attribution of Climate and Weather Extremes: Assessing, Anticipating and Communicating Climate Risks, which was held at Oxford University, it became clear that there was a broad range of stakeholders interested in the results of this science. For example, the insurance and legal sectors are keenly interested in understanding how the risks associated with extreme events are changing (Stott and Walton 2013, manuscript submitted to *Weather*). Climate forecasting services are likewise keenly interested in knowing the causes of extreme events. The process

of clarifying the proximate and underlying causes is seen as key to providing a narrative of their origins, which advances predictive understanding. It is here where the dual challenges of improved prediction and improved explanation of causes intertwine.

This information is critical to preparing for future events, and the need to make this information accessible, timely, and relevant for the user is broadly recognized. For example, one of the key drivers of the Global Framework for Climate Services (GFCS) is to mainstream the provision of "information that governments, organizations, and individuals can use to manage climate risks and opportunities" (WMO 2012). One-fourth of the World Meteorological Organization (WMO) Commission for Climatology is dedicated to improving climate information for adaptation and risk management (WMO 2013). And, this is in addition to action being taken at the national and local scales by various governmental and nongovernmental groups. Extreme events are, of course, a key source of climate risk (Schiermeier 2011).

As the science underpinning the attribution of extreme events matures, it will nurture and make possible the creation of operational climate attribution systems (Stott et al. 2013). Then, as attribution of extreme events become part of routine climate services and part of the GFCS, scientists will need to continue outreach into our stakeholder communities. Climate risk reduction is a key driver of many climate adaptation activities (van Aalst et al. 2008). Therefore, many communities will need to better understand exactly what attribution of extreme event science can and cannot say. To return to the opening analogy, this means answering the question of how the change in the driver's speed was responsible for changing the odds of colliding with a texting driver on a wet road, which would be the extreme event we are trying to attribute.

REFERENCES

- Alexander, L. V., and P. D. Jones, 2001: Updated precipitation series for the U.K. and discussion of recent extremes. *Atmos. Sci. Lett.*, **1**, 142–150, doi:10.1006/asle.2001.0025.
- Allan, R. J., and T. J. Ansell, 2006: A new globally complete monthly historical mean sea level pressure data set (Had-SLP2): 1850–2004. *J. Climate*, **19**, 5816–5842.
- , and C. K. Folland, 2012: [Global climate] Atmospheric circulation: 1. Mean sea level pressure [in “State of the Climate in 2011”]. *Bull. Amer. Meteor. Soc.*, **93** (7), S35–S36.
- Allen, M. R., 1999: Do-it-yourself climate prediction. *Nature*, **401**, 642–642.
- , 2003: Liability for climate change. *Nature*, **421**, 891–892.
- , and W. J. Ingram, 2002: Constraints on future changes in climate and the hydrologic cycle. *Nature*, **419**, 224–232.
- AMS, cited 2013: Top 10 most read articles. Accessed July 18. [Available online at <http://journals.ametsoc.org/>.]
- Balmaseda, M. A., L. Ferranti, F. Molteni, and T. N. Palmer, 2010: Impact of 2007 and 2008 Arctic ice anomalies on the atmospheric circulation: Implications for long-range predictions. *Quart. J. Roy. Meteor. Soc.*, **136**, 1655–1664.
- Berg, P., C. Moseley, and J. O. Harter, 2013: Strong increase in convective precipitation in response to higher temperatures. *Nature Geosci.*, **6**, 181–185, doi:10.1038/NGEO1731.
- Boon, J. D., 2012: Evidence of sea level acceleration at U.S. and Canadian tide stations, Atlantic Coast, North America. *J. Coast. Res.*, **28**, 1437–1445.
- Brayshaw, D., B. Hoskins, and M. Blackburn, 2011: The basic ingredients of the North Atlantic storm track. Part II: Sea surface temperatures. *J. Atmos. Sci.*, **68**, 1784–1805.
- Bureau of Meteorology, 2012: Exceptionally heavy rainfall across southeast Australia. Special Climate Statement 39, 19 pp.
- Cai, W., P. van Rensch, T. Cowan, and A. Sullivan, 2010: Asymmetry in ENSO teleconnection with regional rainfall, its multidecadal variability and impact. *J. Climate*, **23**, 4944–4955.
- Cane, M. A., and Coauthors, 1997: Twentieth-century sea surface temperature trends. *Science*, **275**, 957–960.
- Cassou, C., L. Terray, and A. Phillips, 2005: Tropical Atlantic influence on European heat waves. *J. Climate*, **18**, 2805–2811.
- Cattiaux, J., and P. Yiou, 2012: Contribution of atmospheric circulation to remarkable European temperatures of 2011 [in “Explaining extreme events of 2011 from a climate perspective”]. *Bull. Amer. Meteor. Soc.*, **93**, 1054–1057.
- , R. Vautard, C. Cassou, P. Yiou, V. Masson-Delmotte, and F. Codron, 2010: Winter 2010 in Europe: A cold extreme in a warming climate. *Geophys. Res. Lett.*, **37**, L20704, doi:10.1029/2010GL044613.
- Catto, J., N. Nicholls, and C. Jakob, 2012: North Australian sea surface temperatures and the El Niño Southern Oscillation in observations and models. *J. Climate*, **25**, 5011–5029.
- Caussinus, H., and O. Mestre, 2004: Detection and correction of artificial shifts in climate series. *J. Roy. Stat. Soc. Ser. C Appl. Stat.*, **53**, 405–425.
- CEH, 2012: An overview of the 2010–12 drought and its dramatic termination. Centre for Ecology & Hydrology, 4 pp. [Available online at http://www.ceh.ac.uk/data/nrfa/nhmp/other_reports/2012_Drought_Transformation.pdf.]
- Chang, F.-C., and J. M. Wallace, 1987: Meteorological conditions during heat waves and droughts in the United States Great Plains. *Mon. Wea. Rev.*, **115**, 1253–1269.
- Christidis, N., and P. A. Stott, 2012: Lengthened odds of the cold UK winter of 2010/2011 attributable to human influence [in “Explaining extreme events of 2011 from a climate perspective”]. *Bull. Amer. Meteor. Soc.*, **93**, 1060–1062.
- , —, A. Scaife, A. Arribas, G. S. Jones, D. Copesey, J. R. Knight, and W. J. Tennant, 2013: A new HadGEM3-A based system for attribution of weather and climate-related extreme events. *J. Climate*, **26**, 2756–2783.
- Church, J. A., and N. J. White, 2011: Sea-level rise from the late 19th to the early 21st Century. *Surv. Geophys.*, **32**, 585–602, doi:10.1007/s10712-011-9119-1.
- Clement, A. C., R. Seager, M. A. Cane, and S. E. Zebiak, 1996: An ocean dynamical thermostat. *J. Climate*, **9**, 2190–2196.
- CMA, 2013: *China Climate Bulletin 2012*. China Meteorological Administration, 54 pp.
- Coles, S., 2001: *An Introduction to Statistical Modeling of Extreme Values*. Springer, 208 pp.
- Colle, B. A., K. Rojowsky, and F. Buonaito, 2010: New York City storm surges: Climatolgy and an analysis of the wind and cyclone evolution. *J. Appl. Meteor. Climatol.*, **49**, 85–100.
- Compo, G. P., and P. D. Sardeshmukh, 2010: Removing ENSO-related variations from the climate record. *J. Climate*, **23**, 1957–1978.
- Cook, K. H., and E. K. Vizy, 2013: Projected changes in East African rainy seasons. *J. Climate*, in press, doi:10.1175/JCLI-D-12-00455.1.
- de Bruin, H. A. R., and H. R. A. Wessels, 1988: A model for the formation and melting of ice on surface waters. *J. Appl. Meteor.*, **27**, 164–173.
- de Vries, H., and R. van Westrhenen, 2012: Weer (g)een Elfstedentocht. *Meteorologica*, **21**, 4–7.
- , R. J. Haarsma, and W. Hazeleger, 2012a: Western European cold spells in current and future climate. *Geophys. Res. Lett.*, **39**, L04706, doi:10.1029/2011GL050665.

- , —, and —, 2012b: On the future reduction of snowfall in western and central Europe. *Climate Dyn.*, in press, doi:10.1007/s00382-012-1583-x.
- Dee, D. P., and Coauthors, 2011: The ERA-interim reanalysis: Configuration and performance of the data assimilation system. *Quart. J. Roy. Meteor. Soc.*, **137**, 553–597.
- Diffenbaugh, N. S., M. Ashfaq, and M. Scherer, 2011: Transient regional climate change: Analysis of the summer climate response in a high-resolution, century-scale ensemble experiment over the continental United States. *J. Geophys. Res.*, **116**, D24111, doi:10.1029/2011JD016458.
- Ding, Q., and B. Wang, 2005: Circumglobal teleconnection in the Northern Hemisphere summer. *J. Climate*, **18**, 3483–3505.
- Donlon, C. J., M. Martin, J. D. Stark, J. Roberts-Jones, E. Fiedler, and W. Wimmer, 2012: The Operational Sea Surface Temperature and Sea Ice Analysis (OSTIA) system. *Remote Sens. Environ.*, **116**, 140–158.
- Doyle, M., and M. Harvey, 2012: A storm like no other. *Newsline: the mag*, Issue 267, 2–4. [Available online at <http://www.tasman.govt.nz/tasman/newsline-online/2012/newsline-267-27-january-2012/>]
- Environmental Modeling Center, 2003: The GFS Atmospheric Model. NCEP Office Note 442, Global Climate and Weather Modeling Branch, EMC, Camp Springs, MD. [Available online at <http://www.emc.ncep.noaa.gov/GFS/php/>]
- Evans, J. P., and I. Boyer-Souchet, 2012: Local sea surface temperatures add to extreme precipitation in northeast Australia during La Niña. *Geophys. Res. Lett.*, **39**, doi:10.1029/2012GL052014
- Ezer, T., L. P. Atkinson, W. B. Corlett, and J. L. Blanco, 2013: Gulf Stream's induced sea level rise and variability along the U.S. mid-Atlantic coast. *J. Geophys. Res.*, **118**, doi:10.1002/jgrc.20091.
- Fanelli, C., P. Fanelli, and D. Wolcott, 2013: Hurricane Sandy. NOAA Water Level and Meteorological Data Report, 60 pp. [Available online at http://tidesandcurrents.noaa.gov/publications/Hurricane_Sandy_2012_Water_Level_and_Meteorological_Data_Report.pdf]
- Feldstein, S. B., 2007: The dynamics of the North Atlantic Oscillation during the summer season. *Quart. J. Roy. Meteor. Soc.*, **133**, 1509–1518.
- Fetterer, F., K. Knowles, W. Meier, and M. Savoie, 2009: Sea ice index. Ice extent. National Snow and Ice Data Center, Boulder, CO, digital media. [Available online at <http://dx.doi.org/10.7265/N5QJ7F7W>]
- FEWS NET, 2012a: East Africa Food Security Alert: Poor forecast suggests that increased food insecurity is likely in the eastern Horn. 6 April 2012. [Available online at http://www.fews.net/docs/Publications/East%20Region_Alert_2012_04_06_final.pdf]
- , 2012b: East Africa Food Security Alert: Crisis levels of food insecurity will persist following below-average March to May rains. 14 June 2012. [Available online at http://www.fews.net/docs/Publications/East%20Region_Alert_2012_06_final.pdf]
- , 2013: Mortality among populations of southern and central Somalia affected by severe food insecurity and famine during 2010–2012. 1 May 2013. [Available online at http://www.fews.net/docs/Publications/Somalia_Mortality_Estimates_Final_Report_1May2013_upload.pdf]
- Fichefet, T., and M. A. M. Maqueda, 1997: Sensitivity of a global sea ice model to the treatment of ice thermodynamics and dynamics. *J. Geophys. Res.*, **102** (C6), 12 609–12 646.
- Field, C. B., and Coauthors, Eds., 2012: *Managing the Risks of Extreme Events and Disasters to Advance Climate Change Adaptation*. Cambridge University Press, 582 pp.
- Fischer, E. M., S. I. Seneviratne, D. Lüthi, and C. Schär, 2007a: Contribution of land-atmosphere coupling to recent European summer heat waves. *Geophys. Res. Lett.*, **34**, L06706, doi:10.1029/2006GL029068.
- , —, P. L. Vidale, D. Lüthi, and C. Schär, 2007b: Soil moisture–Atmosphere interactions during the 2003 European summer heat wave. *J. Climate*, **20**, 5081–5099.
- Folland, C. K., and Coauthors, 2009: The summer North Atlantic oscillation: Past, present, and future. *J. Climate*, **22**, 1082–1103.
- Funk, C., 2012: Exceptional warming in the western Pacific–Indian Ocean warm pool has contributed to more frequent droughts in eastern Africa [in "Explaining extreme events of 2011 from a climate perspective"]. *Bull. Amer. Meteor. Soc.*, **93**, 1049–1051.
- , M. D. Dettinger, J. C. Michaelsen, J. P. Verdin, M. E. Brown, M. Barlow, and A. Hoell, 2008: Warming of the Indian Ocean threatens eastern and southern African food security but could be mitigated by agricultural development. *Proc. Natl. Acad. Sci. USA*, **105**, 11 081–11 086.
- Ganter, C., and S. Tobin, 2013: [Regional climates] Australia [in "State of the Climate in 2012"]. *Bull. Amer. Meteor. Soc.*, **94** (8), S196–S198.
- García-Herrera, R., D. Paredes, R. M. Trigo, I. F. Trigo, H. Hernández, D. Barriopedro, and M. T. Mendes, 2007: The outstanding 2004–2005 drought in the Iberian Peninsula: The associated atmospheric circulation. *J. Hydrometeorol.*, **8**, 483–498.
- Gillett, N. P., V. K. Arora, G. M. Flato, J. F. Scinocca, and K. vonSalzen, 2012: Improved constraints on 21st-century warming derived using 160 years of temperature observations. *Geophys. Res. Lett.*, **39**, L01704, doi:10.1029/2011GL050226.

- Gimeno, L., R. Nieto, R. M. Trigo, S. M. Vicente-Serrano, and J. I. López-Moreno, 2010a: Where does the Iberian Peninsula moisture come from? An answer based on a Lagrangian approach. *J. Hydrometeorol.*, **11**, 421–436.
- , A. Drumond, R. Nieto, R. M. Trigo, and A. Stohl, 2010b: On the origin of continental precipitation. *Geophys. Res. Lett.*, **37**, L13804, doi:10.1029/2010GL04371.
- , R. Nieto, A. Drumond, R. Castillo, and R. Trigo, 2013: Influence of the intensification of the major oceanic moisture sources on continental precipitation. *Geophys. Res. Lett.*, **40**, 1443–1450, doi:10.1002/grl.50338.
- Giorgi, F., and R. Francisco, 2000: Uncertainties in regional climate change prediction: A regional analysis of ensemble simulations with the HADCM2 coupled AOGCM. *Climate Dyn.*, **16**, 169–182.
- Gleckler, P. J., and Coauthors, 2012: Human-induced global ocean warming on multidecadal timescales. *Nature Climate Change*, **2**, 524–529.
- Goosse, H., and T. Fichefet, 1999: Importance of ice-ocean interactions for the global ocean circulation: A model study. *J. Geophys. Res.*, **104** (C10), 23 337–23 355.
- , O. Arzel, C. M. Bitz, A. De Montety, and M. Vancoppenolle, 2009: Increased variability of the Arctic summer ice extent in a warmer climate. *Geophys. Res. Lett.*, **36**, L23702, doi:10.1029/2009GL040546.
- Gordon, C., C. Cooper, C. A. Senior, H. Banks, J. M. Gregory, T. C. Johns, J. F. B. Mitchell, and R. A. Wood, 2000: The simulation of SST, sea ice extents and ocean heat transports in a version of the Hadley Centre coupled model without flux adjustments. *Climate Dyn.*, **16**, 147–168.
- GPO, 2013: Disaster Relief Appropriations Act for 2013 (HR 152) and An Act To Temporarily Increase the Borrowing Authority of the Federal Emergency Management Agency for Carrying Out the National Flood Insurance Program (HR 41).
- Grinstead, A., J. C. Moore, and S. Jevrejeva, 2012: A homogeneous record of Atlantic hurricane surge threat since 1923. *Proc. Natl. Acad. Sci. USA*, **109**, 19 601–19 605.
- , —, and —, 2013: Projected Atlantic hurricane surge threat from rising temperatures. *Proc. Natl. Acad. Sci. USA*, **110**, 5369–5373, doi:10.1073/pnas.1209980110.
- Gu, G., and R. F. Adler, 2013: Interdecadal variability/long-term changes in global precipitation patterns during the past three decades: Global warming and/or Pacific decadal variability? *Climate Dyn.*, **40**, 3009–3022.
- Guemas, V., F. J. Doblas-Reyes, K. Mogensen, Y. Tang, and S. Keeley, 2013: Ensemble of sea ice initial conditions for interannual climate predictions. *Climate Dyn.*, submitted, CLIDY-D-13-00147.
- Guo, Q. Y., 1983: The summer monsoon intensity index in East Asia and its variation (in Chinese). *Acta Geograph. Sin.*, **38**, 207–217.
- Hall, T. M., and A. H. Sobel, 2013: On the impact angle of Hurricane Sandy's New Jersey landfall. *Geophys. Res. Lett.*, **40**, doi:10.1002/grl.50395.
- Haylock, M. R., and Coauthors, 2008: A European daily high-resolution gridded dataset of surface temperature and precipitation. *J. Geophys. Res.*, **113**, D20119, doi:10.1029/2008JD10201.
- Hegerl, G. C., and Coauthors, 2007: Understanding and attributing climate change. *Climate Change 2007: The Physical Science Basis*. S. Solomon, et al., Eds., Cambridge University Press, 663–745.
- , O. Hoegh-Guldberg, G. Casassa, M. P. Hoerling, R. S. Kovats, C. Parmesan, D. W. Pierce, and P. A. Stott, 2009: Good practice guidance paper on detection and attribution related to anthropogenic climate change. *Meeting Report of the Intergovernmental Panel on Climate Change Expert Meeting on Detection and Attribution of Anthropogenic Climate Change*, T. F. Stocker, et al., Eds., University of Bern, Switzerland, 1–8. [Available online at https://www.ipcc-wg1.unibe.ch/guidancepaper/IPCC_D&A_GoodPracticeGuidancePaper.pdf.]
- Hewitt, H. T., D. Copesey, I. D. Culverwell, C. M. Harris, R. S. R. Hill, A. B. Keen, A. J. McLaren, and E. C. Hunke, 2011: Design and implementation of the infrastructure of HadGEM3: The next-generation Met Office climate modelling system. *Geosci. Model Dev.*, **4**, 223–253.
- Hirsch, M. E., A. T. DeGaetano, and S. J. Colucci, 2001: An East Coast winter storm climatology. *J. Climate*, **14**, 882–899.
- Hirschi, M., and Coauthors, 2011: Observational evidence for soil-moisture impact on hot extremes in southeastern Europe. *Nature Geosci.*, **4**, 17–21.
- Hoerling, M. P., and A. Kumar, 2002: Atmospheric response patterns associated with tropical forcing. *J. Climate*, **15**, 2184–2203.
- , and —, 2003: The perfect ocean for drought. *Science*, **299**, 691–694.
- , J. Eischeid, and J. Perlwitz, 2010: Regional precipitation trends: Distinguishing natural variability from anthropogenic forcing. *J. Climate*, **23**, 2131–2145.
- , —, X.-W. Quan, H. F. Diaz, R. S. Webb, R. M. Dole, D. R. Easterling, 2012a: Is a transition to semipermanent drought conditions imminent in the U.S. Great Plains? *J. Climate*, **25**, 8380–8386.
- , —, J. Perlwitz, X. Quan, T. Zhang, and P. Pegion, 2012b: On the increased frequency of Mediterranean Drought. *J. Climate*, **25**, 2146–2161.
- , and Coauthors, 2013a: Anatomy of an extreme event. *J. Climate*, **26**, 2811–2832.
- , and Coauthors, 2013b: An interpretation of the origins of the 2012 central Great Plains drought. NOAA Drought Task Force/National Integrated Drought Information System (NIDIS), 44 pp. [Available online at <http://cpo>.

- noaa.gov/ClimatePrograms/ModelingAnalysisPredictionsandProjections/MAPPTaskForces/DroughtTaskForce/2012CentralGreatPlainsDrought.aspx.]
- Hong, S. Y., and E. Kalnay, 2000: Role of sea surface temperature and soil-moisture feedback in the 1998 Oklahoma-Texas drought. *Nature*, **408**, 842–844.
- Hoskins, B. J., and K. I. Hodges, 2002: New perspectives on the Northern Hemisphere winter storm tracks. *J. Atmos. Sci.*, **59**, 1041–1061.
- Hunter, J., 2010: Estimating sea-level extremes under conditions of uncertain sea-level rise. *Climatic Change*, **99**, 331–350, doi:10.1007/s10584-009-9671-6.
- Huntingford, C., R. G. Jones, C. Prudhomme, R. Lamb, J. H. C. Gash, and D. A. Jones, 2003: Regional climate-model predictions of extreme rainfall for a changing climate. *Quart. J. Roy. Meteor. Soc.*, **129**, 1607–1621.
- JBA Risk Management and Met Office, 2012: UK Flooding April to July 2012. JBA Risk Management and Met Office, [4 pp.] [Available online at http://www.metoffice.gov.uk/media/pdf/e/s/JBA_and_Met_Office_Bulletin_UK_Flooding_April_July_2012.pdf.]
- Jones, A., D. L. Roberts, M. J. Woodage, and C. E. Johnson, 2001: Indirect sulphate aerosol forcing in a climate model with an interactive sulphur cycle. *J. Geophys. Res.*, **106** (D17), 20 293–20 310, doi:10.1029/2000JD000089.
- Jones, C. D., and Coauthors, 2011: The HadGEM2-ES implementation of CMIP5 centennial simulations. *Geosci. Model Dev.*, **4**, 1–28.
- Jones, D. A., W. Wang, and R. Fawcett, 2009: High-quality spatial climate data-sets for Australia. *Aust. Meteor. Ocean. J.*, **58**, 233–248.
- Jones, R. G., M. Noguera, D. C. Hassell, D. Hudson, S. S. Wilson, G. J. Jenkins, and J. F. B. Mitchell, 2004: *Generating High Resolution Climate Change Scenarios Using PRECIS*. Met Office Hadley Centre, 40 pp.
- Junker, N. W., R. H. Grumm, R. Hart, L. F. Bosart, K. M. Bell, and F. J. Pereira, 2008: Use of normalized anomaly fields to anticipate extreme rainfall in the mountains of northern California. *Wea. Forecasting*, **23**, 336–356.
- Kalnay, E., and Coauthors, 1996: The NCEP/NCAR 40-year reanalysis project. *Bull. Amer. Meteor. Soc.*, **77**, 437–471.
- Kattenberg, A., and Coauthors, 2008: *De Toestand van het Klimaat in Nederland 2008*. KNMI, 47 pp. [Available online at <http://www.knmi.nl/cms/mmbase/attachments/67092/Toestand2008geheel.pdf>.]
- Kharin, V. V., G. J. Boer, W. J. Merryfield, J. F. Scinocca, and W.-S. Lee, 2012: Statistical adjustment of decadal predictions in a changing climate. *Geophys. Res. Lett.*, **39**, L19705, doi:10.1029/2012GL052647.
- Kimoto, M., and M. Ghil, 1993: Multiple flow regimes in the northern hemisphere winter. Part I: methodology and hemispheric regimes. *J. Atmos. Sci.*, **50**, 2625–2643.
- King, A. D., L. V. Alexander, and M. G. Donat, 2013: Asymmetry in the response of Eastern Australia extreme rainfall to low-frequency Pacific variability. *Geophys. Res. Lett.*, **40**, 2271–2277, doi:10.1002/grl.50427.
- Kistler, R., and Coauthors, 2001: The NCEP-NCAR 50-year reanalysis: Monthly means CD-ROM and documentation. *Bull. Amer. Meteor. Soc.*, **82**, 247–267.
- Klein-Tank, A., and Coauthors, 2002: Daily dataset of 20th-century surface air temperature and precipitation series for the European Climate Assessment. *Int. J. Climatol.*, **22**, 1441–1453.
- Knight, J. R., C. K. Folland, and A. A. Scaife, 2006: Climate impacts of the Atlantic Multidecadal Oscillation. *Geophys. Res. Lett.*, **33**, L17706, doi:10.1029/2006GL026242.
- Knutson, T. R., F. Zeng, and A. T. Wittenberg, 2013: Multi-model assessment of regional surface temperature trends: CMIP3 and CMIP5 20th century simulations. *J. Climate*, in press, doi:10.1175/JCLI-D-12-00567.1.
- Kosaka, Y., H. Nakamura, M. Watanabe, and M. Kimoto, 2009: Analysis on the dynamics of a wave-like teleconnection pattern along the summertime Asian jet based on a reanalysis dataset and climate model simulations. *J. Meteor. Soc. Japan*, **87**, 561–580.
- Kushnir, Y., and Coauthors, 2002: Atmospheric GCM response to extratropical SST anomalies: Synthesis and evaluation. *J. Climate*, **15**, 2233–2256.
- Kusunoki, A., J. Yoshimura, H. Yoshimura, A. Noda, K. Oouchi, and R. Mizuta, 2006: Change of Baiu rain band in global warming projection by an atmospheric general circulation model with a 20-km grid size. *J. Meteor. Soc. Japan*, **84**, 581–611.
- Large, W., and S. Yeager, 2004: Diurnal to decadal global forcing for ocean and sea-ice models: The data sets and flux climatologies. NCAR Tech. Note NCAR/TN460+STR, 111 pp.
- L'Heureux, M. L., S. Lee, and B. Lyon, 2013: Recent multi-decadal strengthening of the Walker circulation across the tropical Pacific. *Nature Climate Change*, **3**, 571–576, doi:10.1038/nclimate1840.
- Li, H., A. Dai, T. Zhou, and J. Lu, 2010: Responses of East Asian summer monsoon to historical SST and atmospheric forcing during 1950–2000. *Climate Dyn.*, **34**, 501–514.
- Lin, N., K. A. Emanuel, M. Oppenheimer, and E. Vanmarcke, 2012: Physically based assessment of hurricane surge threat under climate change. *Nature Climate Change*, **2**, 462–467, doi:10.1038/NCLIMATE1389.
- Liu, H., T. Zhou, Y. Zhu, and Y. Lin, 2012: The strengthening East Asia summer monsoon since the early 1990s. *Chin. Sci. Bull.*, **57**, 1553–1558, doi:10.1007/s11434-012-4991-8.
- Lorenz, E., 1969: Atmospheric predictability as revealed by naturally occurring analogues. *J. Atmos. Sci.*, **26**, 636–646.

- Lott, F. C., N. Christidis, and P. A. Stott, 2013: Can the 2011 East African drought be attributed to human-induced climate change? *Geophys. Res. Lett.*, **40**, 117–1181, doi:10.1002/grl.50235.
- Lyon, B., and D. G. DeWitt, 2012: A recent and abrupt decline in the East African long rains. *Geophys. Res. Lett.*, **39**, L02702, doi:10.1029/2011GL050337.
- Madden, R. A., and J. Williams, 1978: The correlation between temperature and precipitation in the United States and Europe. *Mon. Wea. Rev.*, **106**, 142–147.
- Madec, G., and Coauthors, 2008: *NEMO ocean engine*. Note du pole de modélisation, No. 27, Institut Pierre-Simon Laplace, 357 pp.
- Massey, N., and Coauthors, 2006: Data access and analysis with distributed federated data servers in climateprediction.net. *Adv. Geosci.*, **8**, 49–56.
- , T. Aina, C. Rye, F. E. L. Otto, R. Wilson, R. G. Jones, and M. R. Allen, 2012: Have the odds of warm November temperatures and cold December temperatures in central England changed? *Bull. Amer. Meteor. Soc.*, **93**, 1057–1059.
- Massonnet, F., T. Fichefet, H. Goosse, C. M. Bitz, G. Philippon-Berthier, M. M. Holland, and P.-Y. Barriat, 2012: Constraining projections of summer Arctic sea ice. *Cryosphere*, **6**, 1383–1394.
- Mastrandrea, M. D., K. J. Mach, G.-K. Plattner, O. Edenhofer, T. F. Stocker, C. B. Field, K. L. Ebi, and P. R. Matschoss, 2011: The IPCC AR5 guidance note on consistent treatment of uncertainties: A common approach across the working groups. *Climate Change*, **108**, 675–691.
- McBride, J. L., and N. Nicholls, 1983: Seasonal relationships between Australian rainfall and the Southern Oscillation. *Mon. Wea. Rev.*, **111**, 1998–2004.
- McCallum, B. E., and Coauthors, 2013: Monitoring storm tide and flooding from Hurricane Sandy along the Atlantic coast of the United States, October 2012. USGS Open-File Report 2013–1043, 42 pp. [Available online at <http://pubs.usgs.gov/of/2013/1043/>]
- McKee, T. B., N. J. Doesken, and J. Kleist, 1993: The relationship of drought frequency and duration to time scales. *Proc. Eighth Conf. on Appl. Climatol.*, Anaheim, CA, Amer. Meteor. Soc., 179–183.
- McRoberts, D. B., and J. W. Nielsen-Gammon, 2011: A new homogenized climate division precipitation dataset for analysis of climate variability and climate change. *J. Appl. Meteor. Climatol.*, **50**, 1187–1199.
- Meehl, G. A., and C. Tebaldi, 2004: More intense, more frequent, and longer lasting heat waves in the 21st century. *Science*, **305**, 994–997.
- Menéndez, M., and P. L. Woodworth, 2010: Changes in extreme high water levels based on a quasi-global tide-gauge data set. *J. Geophys. Res.*, **115**, C10011, doi:10.1029/2009JC005997.
- Meng, Q., M. Latif, W. Park, N. S. Keenlyside, V. A. Semenov, and T. Martin, 2012: Twentieth century Walker Circulation change: Data analysis and model experiments. *Climate Dyn.*, **38**, 1757–1773.
- Menne, M. J., C. N. Williams, and R. S. Vose, 2009: The United States Historical Climatology Network monthly temperature data - version 2. *Bull. Amer. Meteor. Soc.*, **90**, 993–1107.
- Merrifield, M. A., and M. E. Maltrud, 2011: Regional sea level trends due to a Pacific trade wind intensification. *Geophys. Res. Lett.*, **38**, L21605, doi:10.1029/2011GL049576.
- Met Office, cited 2013: Annual 2012. [Available online at <http://www.metoffice.gov.uk/climate/uk/2012/annual.html>.]
- Morice, C. P., J. J. Kennedy, N. A. Rayner, and P. D. Jones, 2012: Quantifying uncertainties in global and regional temperature change using an ensemble of observation estimates: The HadCRUT5 data set. *J. Geophys. Res.*, **117**, D08101, doi:10.1029/2011JD017187.
- Mueller, B., and S. Seneviratne, 2012: Hot days induced by precipitation deficits at the global scale. *Proc. Natl. Acad. Sci. USA*, **109**, 12398–12403, doi:10.1073/pnas.1204330109.
- Namias, J., 1982: Anatomy of Great Plains protracted heat waves (especially the 1980 US summer drought). *Mon. Wea. Rev.*, **110**, 824–838.
- Nicholls, N., 1984: Seasonal relationships between Australian rainfall and North Australian sea surface temperatures. *Extended Abstracts, Conf. on Australian Rainfall Variability*, Part 2, Arkaroola, South Australia, Australian Academy of Science & Bureau of Meteorology, 71–73.
- , 2004: The changing nature of Australian droughts. *Climatic Change*, **63**, 323–336.
- , W. Drosowsky, and B. Lavery, 1997: Australian rainfall variability and change. *Weather*, **52**, 66–71.
- Nitta, T., 1987: Convective activities in the tropical western Pacific and their impact on the Northern Hemisphere summer circulation. *J. Meteor. Soc. Japan*, **65**, 373–390.
- NOAA, cited 2013a: Climate change and Hurricane Sandy. [Available online at <http://www.esrl.noaa.gov/psd/repository/entry/show/PSD+Climate+Data+Repository/Public/Interpreting+Climate+Conditions+-+Case+Studies/Climate+Change+and+Hurricane+Sandy?entryid=98c8065f-d639-496a-a684-fe4762e1d1be>.]
- , cited 2013b: National Climate Data Center state of the climate. National overview—Annual 2012. [Available online at <http://www.ncdc.noaa.gov/sotc/national/2012/13/>.]
- , cited 2013c: NOAA National Climate Data Center. Billion-Dollar Weather/Climate Disasters. [Available online at <http://www.ncdc.noaa.gov/billions/events>.]
- Obeysekera, J., and J. Park, 2013: Scenario-based projection of extreme sea levels. *J. Coastal Res.*, **29**, 1–7.

- Ogallo, L. J., 1988: Relationships between seasonal rainfall in East Africa and the Southern Oscillation. *Int. J. Climatol.*, **8**, 31–43.
- O’Gorman, P. A., and T. Schneider, 2009: The physical basis for increases in precipitation extremes in simulations of 21st-century climate change. *Proc. Natl. Acad. Sci. USA*, **106**, 14773–14777.
- Otto, F. E. L., N. Massey, G. J. van Oldenborgh, R. G. Jones, and M. R. Allen, 2012: Reconciling two approaches to attribution of the 2010 Russian heat wave. *Geophys. Res. Lett.*, **39**, L04702, doi:10.1029/2011GL050422.
- Overland, J. E., and M. Wang, 2013: When will the summer Arctic be nearly sea ice free? *Geophys. Res. Lett.*, **40**, doi:10.1002/grl.50316.
- , J. A. Francis, E. Hanna, and M. Wang, 2012: The recent shift in early summer Arctic atmospheric circulation. *Geophys. Res. Lett.*, **39**, L19804, doi:10.1029/2012GL053268.
- Pal, J. S., F. Giorgi, and X. Bi, 2004: Consistency of recent European summer precipitation trends and extremes with future regional climate projections. *Geophys. Res. Lett.*, **31**, L13202, doi:10.1029/2004GL019836.
- Pall, P., M. R. Allen, and D. A. Stone, 2007: Testing the Clausius-Clapeyron constraint on changes in extreme precipitation under CO₂ warming. *Climate Dyn.*, **28**, 351–363.
- , T. Aina, D. A. Stone, P. A. Stott, T. Nozawa, A. G. J. Hilberts, D. Lohmann, and M. R. Allen, 2011: Anthropogenic greenhouse gas contribution to flood risk in England and Wales in autumn 2000. *Nature*, **470**, 382–385, doi:10.1038/nature09762.
- Parkinson, C. L., and J. C. Comiso, 2013: On the 2012 record low Arctic sea ice cover: Combined impact of preconditioning and an August storm. *Geophys. Res. Lett.*, **40**, 1356–1361, doi:10.1002/GRL.50349.
- Parris, A., and Coauthors, 2012: Global sea level rise scenarios for the US National Climate Assessment. NOAA Tech Memo OAR CPO-1, 37 pp.
- PCMDI, cited 2013: CMIP5 - Data Access - Availability. [Available online at <http://cmip-pcmdi.llnl.gov/cmip5/availability.html>.]
- Peterson, T. C., and R. S. Vose, 1997: An overview of the Global Historical Climatology Network temperature database. *Bull. Amer. Meteor. Soc.*, **78**, 2837–2849.
- , P. A. Stott and S. Herring, Eds., 2012: Explaining extreme events of 2011 from a climate perspective. *Bull. Amer. Meteor. Soc.*, **93**, 1041–1067.
- Pierce, D. W., T. P. Barnett, K. M. AchutaRao, P. J. Gleckler, J. M. Gregory, and W. M. Washington, 2006: Anthropogenic warming of the oceans: Observations and model results. *J. Climate*, **19**, 1873–1900.
- Pope, V., M. Gallani, P. Rowntree, and R. Stratton, 2000: The impact of new physical parameterizations in the Hadley Centre climate model: HadAM3. *Climate Dyn.*, **16**, 123–146.
- Portmann, R. W., S. Solomon, and G. C. Hegerl, 2009: Spatial and seasonal patterns in climate change, temperature, and precipitation across the United States. *Proc. Natl. Acad. Sci. USA*, **106**, 7324–7329.
- Power, S., T. Casey, C. Folland, A. Colman, and V. Mehta, 1999: Inter-decadal modulation of the impact of ENSO on Australia. *Climate Dyn.*, **15**, 319–324.
- , M. Haylock, R. Colman, and X. Wang, 2006: The predictability of interdecadal changes in ENSO activity and ENSO teleconnections. *J. Climate*, **19**, 4755–4771.
- Quesada, B., R. Vautard, P. Yiou, M. Hirschi, and S. I. Seneviratne, 2012: Asymmetric European summer heat predictability from wet and dry southern winters and springs. *Nature Climate Change*, **2**, 736–741, doi:10.1038/nclimate1536.
- Ralph, F. M., and M. D. Dettinger, 2012: Historical and national perspectives on extreme west coast precipitation associated with atmospheric rivers during December 2010. *Bull. Amer. Meteor. Soc.*, **93**, 783–790.
- Rayner, N. A., D. E. Parker, E. B. Horton, C. K. Folland, L. V. Alexander, D. P. Rowell, E. C. Kent, and A. Kaplan, 2003: Global analyses of sea surface temperature, sea ice, and night marine air temperature since the late nineteenth century. *J. Geophys. Res.*, **108** (D14), 4407, doi:10.1029/2002JD002670.
- Redmond, K. T., 2002: The depiction of drought: A commentary. *Bull. Amer. Meteor. Soc.*, **83**, 1143–1147.
- Rowell, D. P., 2005: A scenario of European climate change for the late twenty-first century: seasonal means and interannual variability. *Climate Dyn.*, **25**, 837–849.
- Rudolf, B., and U. Schneider, 2005: Calculation of gridded precipitation data for the global land-surface using in-situ gauge observations. *Proc., 2nd Workshop of the International Precipitation Working Group (IPWG)*, Monterey CA, World Meteorological Organization, 231–247.
- Rupp, D. E., P. W. Mote, N. Massey, C. J. Rye, R. Jones, and M. R. Allen, 2012: Did human influence on climate make the 2011 Texas drought more probable? [in “Explaining extreme events of 2011 from a climate perspective”]. *Bull. Amer. Meteor. Soc.*, **93**, 1052–1054.
- Sallenger, A., K. Doran, and P. Howd, 2012: Hotspot of accelerated sea-level rise on the Atlantic coast of North America. *Nature Climate Change*, **2**, 884–888, doi:10.1038/NCLIMATE1597.
- Scaife, A. A., and Coauthors, 2012: Climate change and stratosphere-troposphere interaction. *Climate Dyn.*, **38**, 2089–2097, doi:10.1007/s00382-011-1080-7.

- Scheff, J., and D. M. W. Frierson, 2012: Robust future precipitation declines in CMIP5 largely reflect the poleward expansion of model subtropical dry zones. *Geophys. Res. Lett.*, **39**, L18704, doi:10.1029/2012GL052910.
- Schiermeier, Q., 2011: Extreme measures. *Nature*, **477**, 148–149.
- Schneider, U., A. Becker, A. Meyer-Christoffer, M. Ziese, and B. Rudolf, 2011: Global Precipitation Analysis Products of the GPCC. Global Precipitation Climatology Centre (GPCC) Deutscher Wetterdienst, Offenbach a. M., Germany. [Available from ftp://ftp-anon.dwd.de/pub/data/gpcc/PDF/GPCC_intro_products_2008.pdf.]
- Schubert, S. D., M. J. Suarez, P. J. Pegion, R. D. Koster, and J. T. Bacmeister, 2004: On the cause of the 1930s Dust Bowl. *Science*, **303**, 1855–1859.
- Scofield, E., and J. P. Donnelly, 2007: Sedimentary evidence of hurricane strikes in western Long Island, New York. *Geochem. Geophys. Geosyst.*, **8**, Q06011, doi:10.1029/2006GC001463.
- Screen, J. A., 2011: Sudden increase in Antarctic sea ice: Fact or artifact? *Geophys. Res. Lett.*, **38**, L13702, doi:10.1029/2011GL047553.
- , and I. Simmonds, 2012: Declining summer snowfall in the Arctic: Causes, impacts and feedbacks. *Climate Dyn.*, **38**, 2243–2256.
- , —, C. Deser, and R. Tomas, 2013: The atmospheric response to three decades of observed Arctic sea ice loss. *J. Climate*, **26**, 1230–1248.
- Seneviratne, S. I., T. Corti, E. L. Davin, M. Hirschi, E. G. Jaeger, I. Lehner, B. Orlowsky, and A. J. Teuling, 2010: Investigating soil moisture–climate interactions in a changing climate: A review. *Earth-Sci. Rev.*, **99**, 125–161.
- , and Coauthors, 2012: Changes in climate extremes and their impacts on the natural physical environment. *Managing the Risks of Extreme Events and Disasters to Advance Climate Change Adaptation*, C. B. Field, et al., Eds., Cambridge University Press, 109–230.
- Sheffield, J., and E. F. Wood, 2008: Projected changes in drought occurrence under future warming from multi-model, multi-scenario, IPCC AR simulations. *Climate Dyn.*, **31**, 79–105, doi:10.1007/s00382-007-0340-z.
- Shiogama, H., M. Watanabe, Y. Imada, M. Mori, M. Ishii, and M. Kimoto, 2013: An event attribution of the 2010 drought in the South Amazon region using the MIROC5 model. *Atmos. Sci. Lett.*, in press, doi:10.1002/asl2.435.
- Sillmann, J., V. V. Kharin, F. W. Zwiers, X. Zhang, and D. Bronaugh, 2013: Climate extremes indices in the CMIP5 multi-model ensemble. Part 1: Model evaluation in the present climate. *J. Geophys. Res.*, **118**, doi:10.1002/jgrd.50203.
- Silverman, B. W., 1986: *Density Estimation for Statistics and Data Analysis*. Chapman and Hall, 175 pp.
- Simmonds, I., and I. Rudeva, 2012: The great Arctic cyclone of August 2012. *Geophys. Res. Lett.*, **39**, L23709, doi:10.1029/2012GL054259.
- Solomon, A., and M. Newman, 2012: Reconciling disparate twentieth-century Indo-Pacific ocean temperature trends in the instrumental record. *Nature Climate Change*, **2**, 691–699.
- Sousa, P., R. M. Trigo, P. Aizpurua, R. Nieto, L. Gimeno, and R. Garcia-Herrera, 2011: Trends and extremes of drought indices throughout the 20th century in the Mediterranean. *Nat. Haz. Earth System Sci.*, **11**, 33–51, doi:10.5194/nhess-11-33-2011.
- Stark, J. D., C. J. Donlon, M. J. Martin, and M. E. McCulloch, 2007: OSTIA: An operational, high resolution, real time, global sea surface temperature analysis system. *Proc., Oceans 2007 - Europe*, Aberdeen, Scotland, IEEE, 331–334.
- State Department, 2012: Increase in U.S. funding to drought relief in the Horn of Africa. U. S. State Department Press Release, 5 April 2012.
- Stott, P. A., and Coauthors, 2013: Attribution of weather and climate-related extreme events. *Climate Science for Serving Society: Research, Modelling and Prediction Priorities*, G. R. Asrar and J. W. Hurrell, Eds., Springer, 307–337.
- Stroeve, C. J., V. Kattsov, A. Barrett, M. Serreze, T. Pavlova, M. Holland, and W. N. Meier, 2012: Trends in Arctic sea ice extent from CMIP5, CMIP3 and observations. *Geophys. Res. Lett.*, **39**, L16502, doi:10.1029/2012GL052676.
- Sutton, R. T., and P. P. Mathieu, 2002: Response of the atmosphere–ocean mixed-layer system to anomalous ocean heat–flux convergence. *Quart. J. Roy. Meteor. Soc.*, **128**, 1259–1275.
- , and D. L. Hodson, 2005: Atlantic Ocean forcing of North American and European summer climate. *Science*, **309**, 115–118.
- , and B.-W. Dong, 2012: Atlantic Ocean influence on a shift in European climate in the 1990s. *Nature Geosci.*, **5**, 788–792, doi:10.1038/ngo1595.
- Sweet, W. V., and C. Zervas, 2011: Cool-season sea level anomalies and storm surges along the U.S. East Coast: Climatology and comparison with the 2009/10 El Niño. *Mon. Wea. Rev.*, **139**, 2290–2299.
- , —, and S. Gill, 2009: Elevated East Coast sea level anomaly: June–July 2009. NOAA Tech. Rep. NOS CO-OPS 051, 30 pp.
- Taylor, K. E., R. J. Stouffer, and G. A. Meehl, 2012: An overview of CMIP5 and the experiment design. *Bull. Amer. Meteor. Soc.*, **93**, 485–498.
- Tebaldi, C., B. H. Strauss, and C. E. Zervas, 2012: Modeling sea level rise impacts on storm surges along US coasts. *Environ. Res. Lett.*, **7**, 014032, doi:10.1088/1748-9326/7/1/014032.

- Tett, S. F. B., and Coauthors, 2007: The impact of natural and anthropogenic forcings on climate and hydrology since 1550. *Climate Dyn.*, **28**, 3–34, doi:10.1007/s00382-006-0165-1.
- Tierney, J., J. Smerdon, K. Anchukaitis, and R. Seager, 2013: Multidecadal variability in East African hydroclimate controlled by the Indian Ocean Peer reviewed article. *Nature*, **493**, 389–392.
- Trenberth, K. E., A. Dai, R. M. Rasmussen, and D. B. Parsons, 2003: The changing character of precipitation. *Bull. Amer. Meteor. Soc.*, **84**, 1205–1217.
- , and Coauthors, 2007: Observations: Surface and Atmospheric Climate Change. *Climate Change 2007: The Physical Science Basis*. S. Solomon, et al., Eds., Cambridge University Press, 235–336.
- Trigo, R. M., D. Pozo-Vazquez, T. J. Osborn, Y. Castro-Diez, S. Gámis-Fortis, and M. J. Esteban-Parra, 2004: North Atlantic oscillation influence on precipitation, river flow and water resources in the Iberian Peninsula. *Int. J. Climatol.*, **24**, 925–944.
- , M. A. Valente, I. F. Trigo, M. Miranda, A. M. Ramos, D. Paredes, and R. García-Herrera, 2008: North Atlantic wind and cyclone trends and their impact in the European precipitation and Atlantic significant wave height. *Ann. N. Y. Acad. Sci.*, **1146**, 212–234, doi:10.1196/annals.1446.014
- , C. Gouveia, and D. Barriopedro, 2010: The intense 2007–2009 drought in the Fertile Crescent: Impacts and associated atmospheric circulation. *Agric. Forest Meteorol.*, **150**, 1245–1257.
- UCAR, 2012: Doping the atmosphere. *AtmosNews*, February 6, 2012. [Available online at <http://www2.ucar.edu/atmosnews/attribution/doping-atmosphere>.]
- USACE, 2011: Sea-level change considerations in civil works programs. U.S. Army Corps of Engineers Circular 1165-2-212, various paging. [Available online at http://publications.usace.army.mil/publications/eng-circulars/EC_1165-2-212.pdf.]
- USDA, cited 2013a: Crop production 2012 summary. [Available online at <http://usda.mannlib.cornell.edu/MannUsda/viewDocumentInfo.do?documentID=1047>.]
- , cited 2013b: Livestock, dairy, and poultry outlook, February 2013. [Available online at <http://usda.mannlib.cornell.edu/MannUsda/viewDocumentInfo.do?documentID=1350>.]
- , cited 2013c: National Agricultural Statistics Service Agricultural prices database. [Available online at http://www.nass.usda.gov/Charts_and_Maps/Agricultural_Prices/Index.asp.]
- van Aalst, M. K., T. Cannon, and I. Burton, 2008: Community level adaptation to climate change: The potential role of participatory community risk assessment. *Global Environ. Change*, **18**, 165–179.
- van der Schrier, G., A. P. van Ulden, and G. J. van Oldenborgh, 2011: The construction of a Central Netherlands temperature. *Climate of the Past*, **7**, 527–542.
- van Ulden, A. P., and G. J. van Oldenborgh, 2006: Large-scale atmospheric circulation biases and changes in global climate model simulations and their importance for climate change in Central Europe. *Atmos. Chem. Phys.*, **6**, 863–881, doi:10.5194/acp-6-863-2006.
- Vautard, R., and P. Yiou, 2009: Control of recent European surface climate change by atmospheric flow. *Geophys. Res. Lett.*, **36**, L22702, doi:10.1029/2009GL040480.
- , and Coauthors, 2007: Summertime European heat and drought waves induced by wintertime Mediterranean rainfall deficit. *Geophys. Res. Lett.*, **34**, L07711, doi:10.1029/2006GL028001.
- Vicente Serrano, S. M., 2006: Spatial and temporal analysis of droughts in the Iberian Peninsula (1910–2000). *Hydrol. Sci. J.*, **51**, 83–97.
- Visser, H., and A. C. Petersen, 2009: The likelihood of holding outdoor skating marathons in the Netherlands as a policy-relevant indicator of climate change. *Climatic Change*, **93**, 39–54, doi:10.1007/s10584-008-9498-6.
- Viste, E., D. Korecha, and A. Sorteberg, 2012: Recent drought and precipitation tendencies in Ethiopia. *Theor. Appl. Climatol.*, **112**, 535–551, doi:10.1007/s00704-012-0746-3.
- Watanabe, M., and Coauthors, 2010: Improved climate simulation by MIROC5: Mean states, variability, and climate sensitivity. *J. Climate*, **23**, 6312–6335.
- WCRP, cited 2013: WCRP grand challenges. Accessed July 18. [Available online at <http://www.wcrp-climate.org/grandcha.shtml>.]
- Williams, A. P., and C. Funk, 2011: A westward extension of the warm pool leads to a westward extension of the Walker circulation, drying eastern Africa. *Climate Dyn.*, **37**, 2417–2435.
- Winton, M., 2011: Do climate models underestimate the sensitivity of northern hemisphere sea ice cover? *J. Climate*, **24**, 3924–3934.
- WMO, 2012: Building country-wide support for the Global Framework for Climate Services (GFCS). World Meteorological Organization, 10 pp. [Available online at http://www.wmo.int/pages/gfcs/documents/GFCS_general_2012_web_en.pdf.]
- , cited 2013: WMO Commission for Climatology Structure. [Available online at <http://www.wmo.int/pages/prog/wcp/ccl/cclstructure.php>.]
- Woollings, T., J. M. Gregory, J. G. Pinto, M. Reyers, and D. J. Brayshaw, 2012: Response of the North Atlantic storm track to climate change shaped by ocean–atmosphere coupling. *Nature Geosci.*, **5**, 313–317, doi:10.1038/NNGEO1438.

- Xoplaki, E., and Coauthors, 2012: Large-scale atmospheric circulation driving extreme climate events in the Mediterranean and its related impacts. *The Climate of the Mediterranean Region: From the Past to the Future*, P. Lionello, Ed., Elsevier, 347–417.
- Yasui, S., and M. Watanabe, 2010: Forcing processes of the summertime circumglobal teleconnection pattern in a dry AGCM. *J. Climate*, **23**, 2093–2114.
- Yin, J., M. E. Schlesinger, and R. J. Stouffer, 2009: Model projections of rapid sea-level rise on the northeast coast of the United States. *Nature Geosci.*, **2**, 262–266.
- Yiou, P., R. Vautard, P. Naveau, and C. Cassou, 2007: Inconsistency between atmospheric dynamics and temperatures during the exceptional 2006/2007 fall/winter and recent warming in Europe. *Geophys. Res. Lett.*, **34**, L21808, doi:10.1029/2007GL031981.
- , K. Goubanova, Z. X. Li, and M. Nogaj, 2008: Weather regime dependence of extreme value statistics for summer temperature and precipitation. *Nonlin. Processes Geophys.*, **15**, 365–378.
- Yu, R., and T. Zhou, 2007: Seasonality and three-dimensional structure of the interdecadal change in East Asian monsoon. *J. Climate*, **20**, 5344–5355.
- , B. Wang, and T. Zhou, 2004: Tropospheric cooling and summer monsoon weakening trend over East Asia. *Geophys. Res. Lett.*, **31**, L22212, doi:10.1029/2004GL021270.
- , J. Li, W. Yuan, and H. Chen, 2010: Changes in characteristics of late-summer precipitation over eastern China in the past 40 years revealed by hourly precipitation data. *J. Climate*, **23**, 3390–3396.
- Zervas, C. E., 2003: Long term changes in tidal response associated with the deepening of navigational channels. Proc., *Coastal Zone 03: Coastal Zone Management Through Time*, Baltimore, MD, NOAA Coastal Services Center.
- , S. Gill, and W. V. Sweet, 2013: Estimating vertical land motion from long-term tide gauge records. NOAA Tech. Rep. NOS CO-OPS 65, 22 pp.
- Zhang, J., R. Lindsay, A. Schweiger, and M. Steele, 2013: The impact of an intense summer cyclone on 2012 Arctic sea ice retreat. *Geophys. Res. Lett.*, **40**, 720–726, doi:10.1002/grl.50190.
- Zhang, X., L. Alexander, G. C. Hegerl, P. Jones, A. Klein Tank, T. C. Peterson, B. Trewin, and F. W. Zwiers, 2011: Indices for monitoring changes in extremes based on daily temperature and precipitation data. *Wiley Interdiscip. Rev. Climate Change*, **2**, 851–870.
- Zhou, T., D. Gong, J. Li, and B. Li, 2009: Detecting and understanding the multi-decadal variability of the East Asian Summer Monsoon - Recent progress and state of affairs. *Meteor. Z.*, **18**, 455–467.
- Zhu, Y., H. Wang, W. Zhou, and J. Ma, 2011: Recent changes in the summer precipitation pattern in East China and the background circulation. *Climate Dyn.*, **36**, 1463–1473.



 SUPPLEMENT

EXPLAINING EXTREME EVENTS OF 2012 FROM A CLIMATE PERSPECTIVE

Editors

Thomas C. Peterson, Martin P. Hoerling, Peter A. Stott, and Stephanie C. Herring

Special Supplement to the
Bulletin of the American Meteorological Society
Vol. 94, No. 9, September 2013

AMERICAN METEOROLOGICAL SOCIETY

S3. LIKELIHOOD OF JULY 2012 U.S. TEMPERATURES IN PREINDUSTRIAL AND CURRENT FORCING REGIMES

NOAH S. DIFFENBAUGH AND MARTIN SCHERER

Supplemental methods. We compare the frequency of occurrence of July 2012 surface air temperature, 500-hPa geopotential height, and 0 cm–200 cm soil moisture between global reanalysis and general circulation model simulations forced with preindustrial and current atmospheric constituent concentrations.

We focus our analysis on the National Centers for Environmental Prediction (NCEP) global reanalysis (Kalnay et al. 1996), but also compare those results with the ERA-Interim reanalysis and the HadCRUT4 station-based dataset (Figs. S3.3, S3.4). While these observationally based datasets allow us to quantify how rare July 2012 was within the context of recent history, they sample only a single realization of the climate system within the current forcing regime. We, therefore, call upon the Coupled Model Inter-

comparison Project phase 5 (CMIP5) global climate model experiments (Taylor et al. 2012), which include multiple realizations of the climate system within the current and preindustrial forcings (Table S3.1). These multiple realizations enable our quantification of the likelihood of a 2012-magnitude event to reflect both climate system variability within a forcing regime and the response of the climate system to changes in forcing. Because a far larger archive currently exists for monthly fields than for daily fields (PCMDI 2013), we focus our analysis on the monthly-mean July fields.

Prior to our quantification, we correct the biases in the mean and variability of the CMIP5 simulations to the mean and variability of the reanalysis. We perform this bias correction on the full time series of July temperatures in each of the CMIP5 preindustrial

Table S3.1.

Model	piControl (rli pl) length (yrs) tas, zg, mrso	piControl (rli pl) # of 33-yr periods tas, zg, mrso	Historical/RCP8.5 realizations analyzed tas	Historical/RCP8.5 realizations analyzed zg	Historical/RCP8.5 realizations analyzed mrso
CCSM4	501	15	1-6	1-5	1-5
CNRM-CM5	850	25	1,2,4,6,10	1,2,4,6,10	1,2,4,6,10
CSIRO-Mk3-6-0	500	15	1-10	1-10	1-10
GISS-E2-R	850	25			
IPSL-CM5A-MR	300	9			
MPI-ESM-MR	1000	30			
Nor-ESM1-M	501	15			

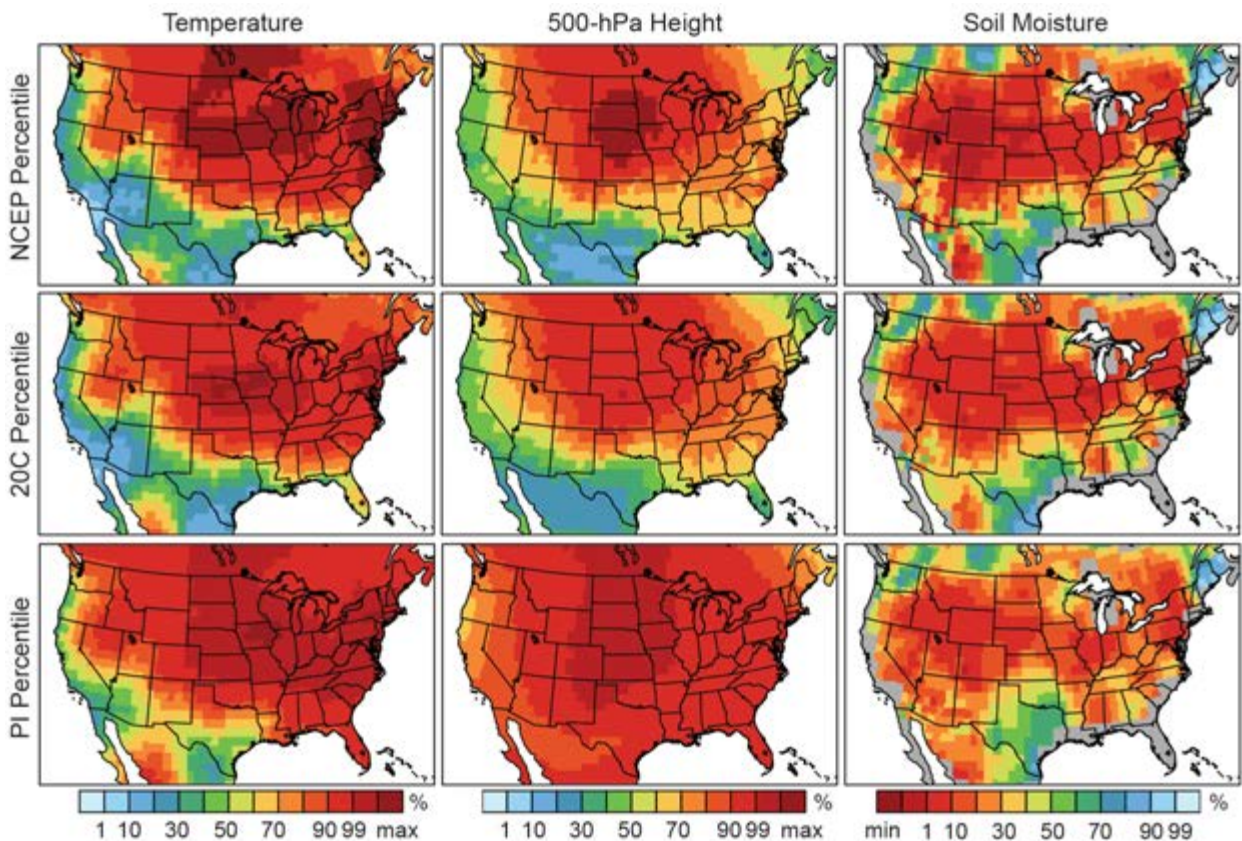


FIG. S3.1. The percentile of the Jul 2012 mean in the 1979–2011 period of NCEP (top row), the 1979–2011 period of CMIP5 (middle row), and the preindustrial period of CMIP5 (bottom row). The “max” (“min”) contour indicates areas where the 2012 value is greater than (less than) the maximum (minimum) value found in the population. See Supplemental methods for details of the ensemble analysis.

(“PI”) simulations and on the 1979–2011 time series of July temperatures in each of the CMIP5 20th century historical forcing (“20C”) simulations. We extend the CMIP5 20C experiment to 2011 by appending the 2006–11 period from the CMIP5 Representative Concentration Pathway (RCP) 8.5 experiment, which is the RCP that is most consistent with recent global emissions (Peters et al. 2013). For each model, we first subtract the respective means from the CMIP5 20C and PI simulations. We then multiply those resulting 20C and PI anomaly time series by the ratio of the standard deviations of the 1979–2011 NCEP reanalysis and the 1979–2011 period of the CMIP5 20C simulation. (Correcting the variability of both the 20C and PI simulations by the 1979–2011 variability-bias corrects the bias in present variability while also allowing for changes in variability between the preindustrial and present forcing.) We then add the 1979–2011 NCEP mean to the variability-corrected CMIP5 20C anomaly time series, thereby correcting the bias in the CMIP5 20C mean. We add the sum of the PI mean and the difference between the NCEP and CMIP5 1979–2011 means to the variability-

corrected PI anomaly time series, thereby correcting the bias in the CMIP5 PI mean while preserving the difference between the PI and 20C means.

In order to normalize across CMIP5 realizations of different lengths (Table S3.1) when calculating our likelihood metrics, we divide the 20C and PI simulations into subperiods of equal length. For the CMIP5 20C simulations, we select the 33-year period from 1979 (the start of the satellite era) to 2011 (the year prior to the 2012 event) in each realization, yielding 24 total 20C periods. For the CMIP5 PI simulations, we divide each realization into 33-year periods, yielding 134 total PI periods. We then calculate the likelihood metrics for each 33-year period in each realization and then take the mean across the respective populations of all 33-year periods in the multi-GCM 20C and preindustrial ensembles. For example, for calculating the number of years per event shown in Fig. 3.1 (in the original paper), we first calculate the number of 2012-magnitude events per year at each grid point for each 33-year period in each GCM realization. We then calculate the mean of the individual events-per-year values across the population of all

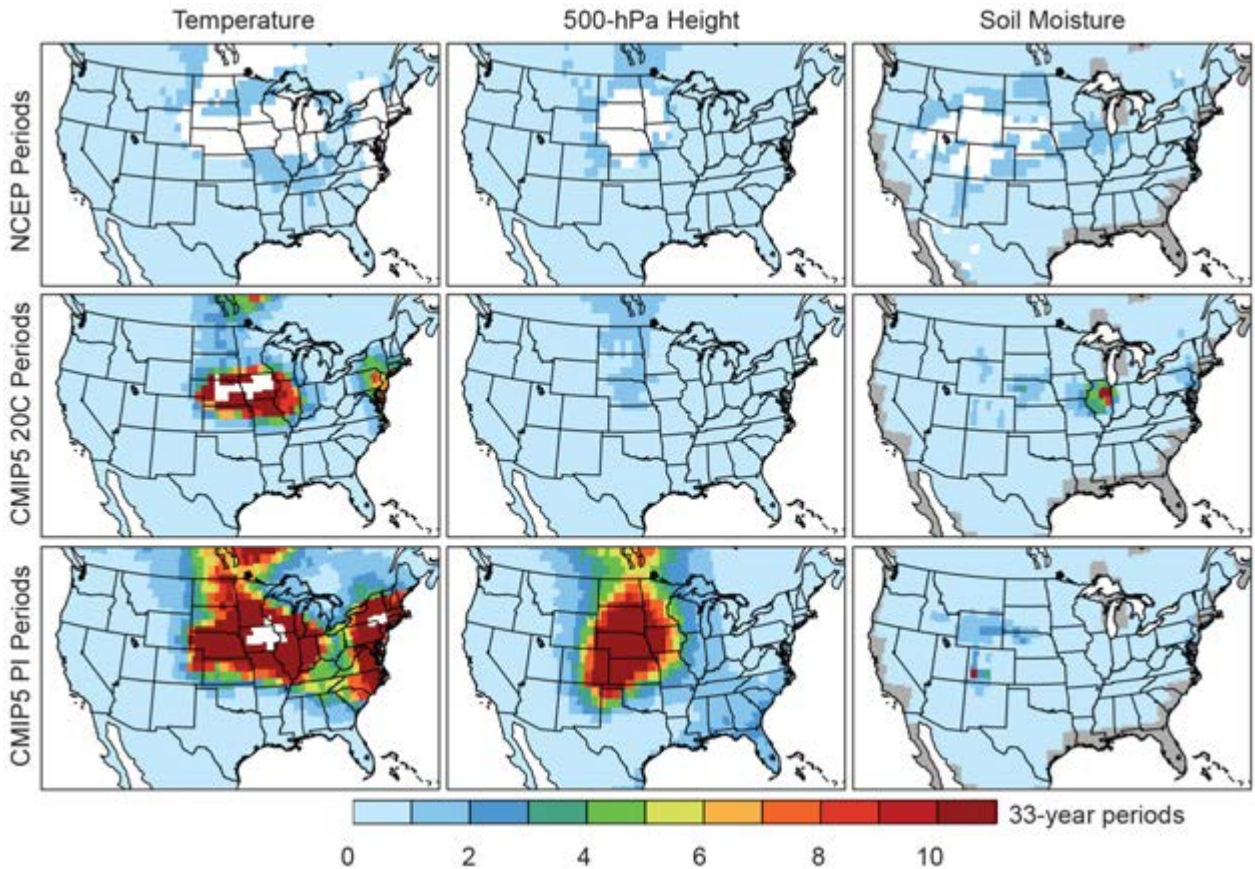


Fig. S3.2. The number of 33-year periods required to achieve an event of the Jul 2012 magnitude in the 1979–2011 period of NCEP (top row), the 1979–2011 period of CMIP5 (middle row), and the preindustrial period of CMIP5 (bottom row). White areas show where no event occurred in any realization. See Supplemental methods for details of the ensemble analysis.

33-year periods in the ensemble. Finally, we take the inverse of the ensemble-mean events-per-year value, yielding the ensemble-mean years-per-event value at each grid point.

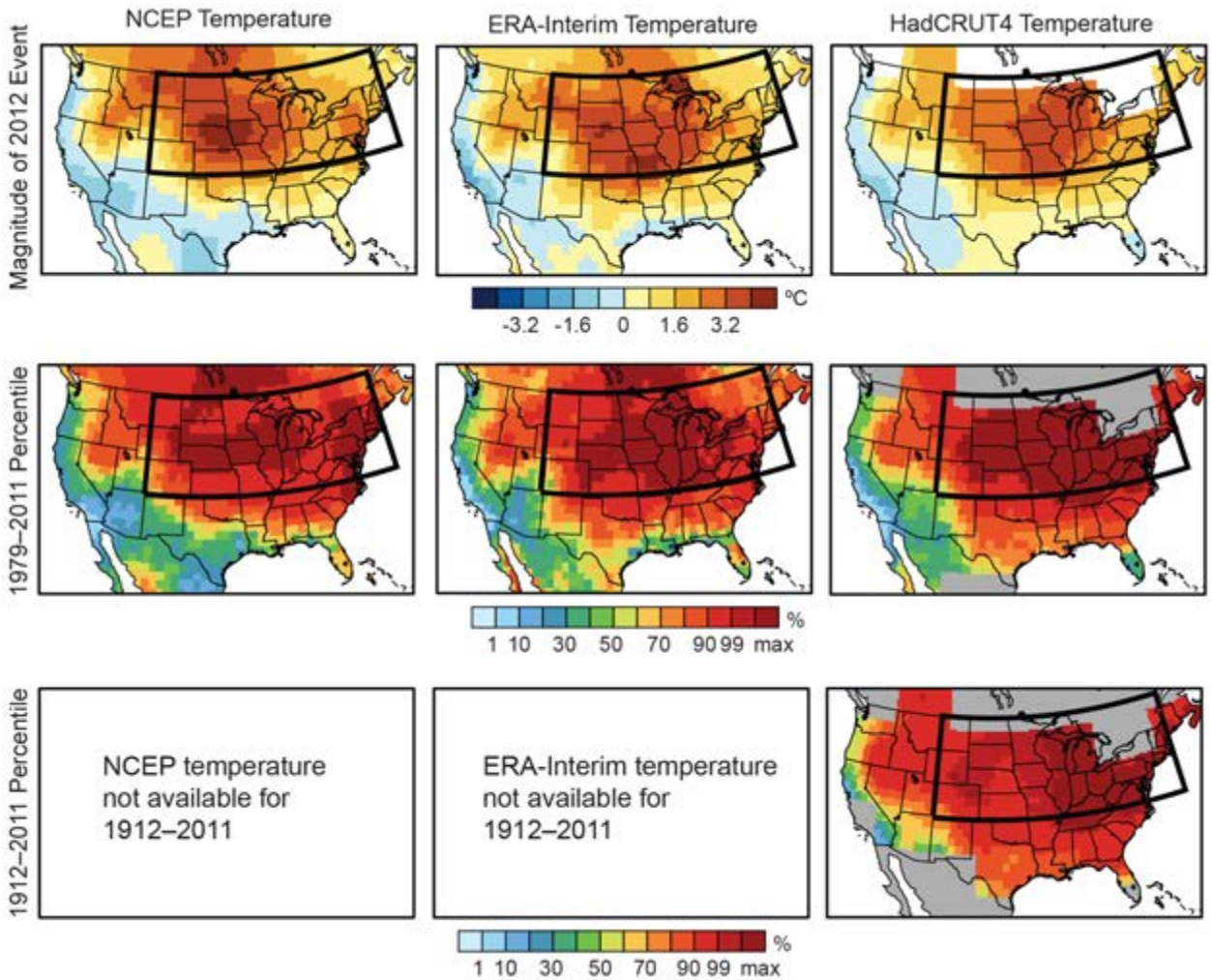


FIG. S3.3. Comparison of the July 2012 temperature in the NCEP reanalysis, the ERA-Interim reanalysis, and the HadCRUT4 station-based dataset. The top row shows the magnitude of the Jul 2012 event as an anomaly from the 1979–2011 mean. The middle row shows the percentile of the Jul 2012 mean in the 1979–2011 period. The bottom row shows the percentile of the Jul 2012 mean in the 1912–2011 period. The “max” contour indicates areas where the 2012 value is greater than the maximum value found in the population. The NCEP reanalysis panels are reproduced from Fig. 3.1 (in the original paper) and Fig. S3.1, respectively. All three datasets are first linearly interpolated to the common one-degree grid (see text). The box shows the region that is used in Figs. 3.1 and 3.2 (in the original paper).

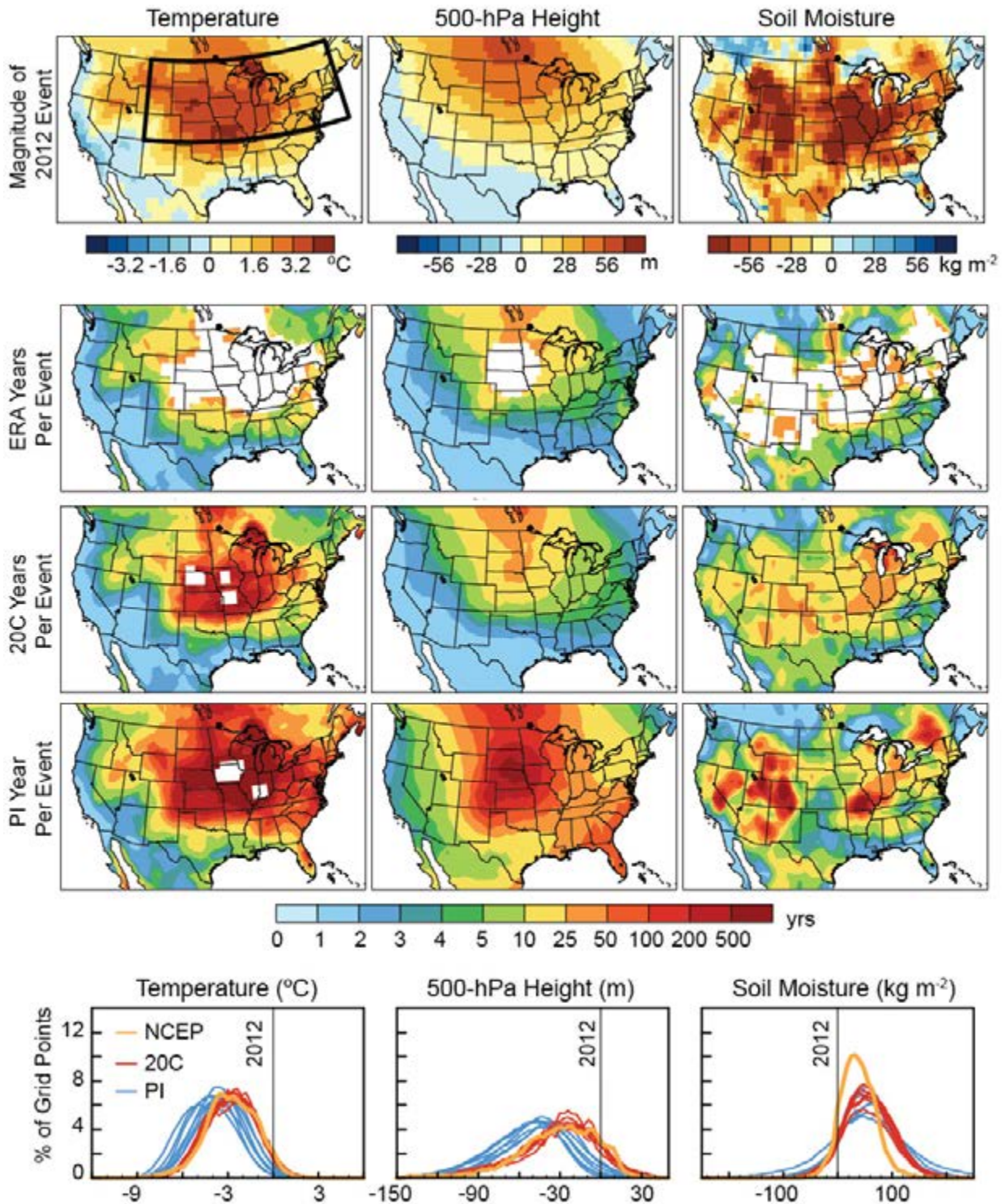


FIG. S3.4. (Top four rows) As in Fig. 3.1 (in original paper), but using the ERA-Interim reanalysis. (Bottom row) As in Fig. 3.2 (in original paper), but using the ERA-Interim reanalysis.

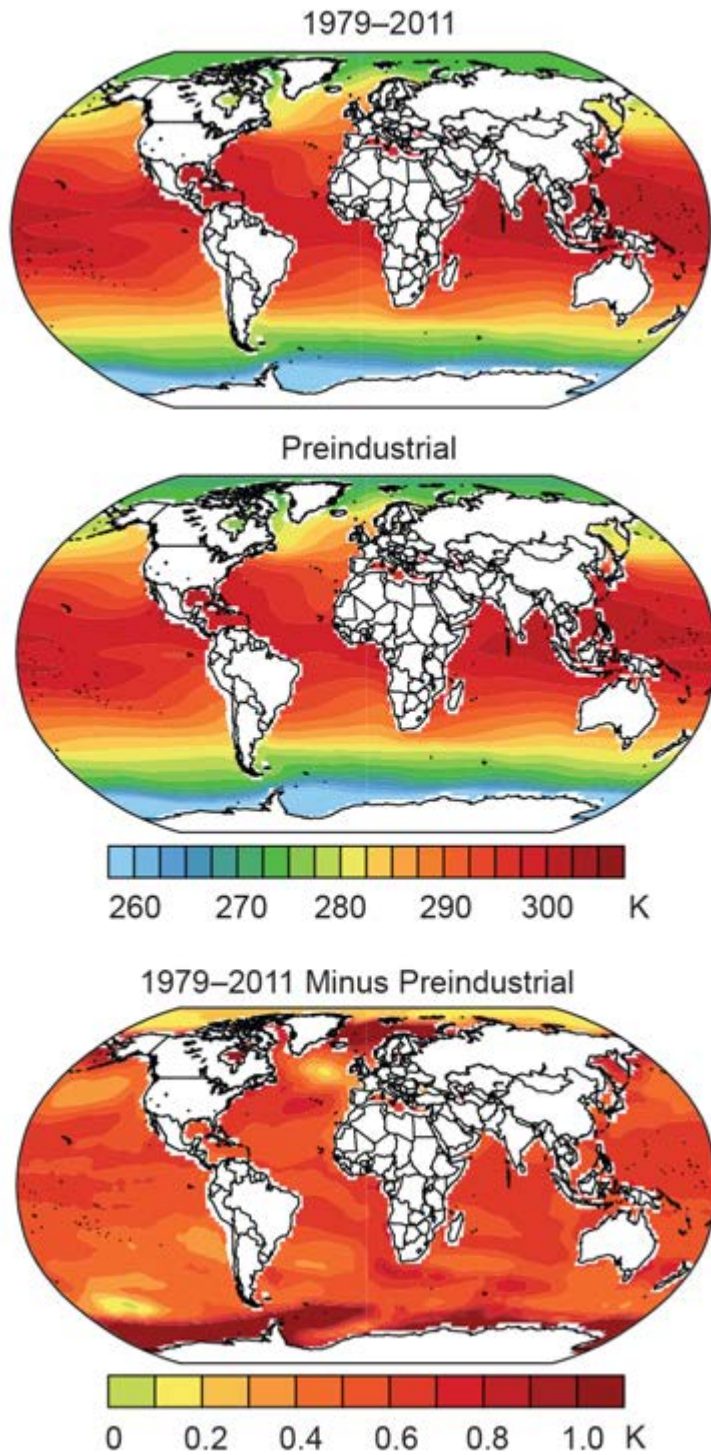


FIG. S3.5. (Top) The Jul mean surface air temperature in the CMIP5 1979–2011 period. (Middle) The Jul mean surface air temperature in the CMIP5 preindustrial control. (Bottom) The difference in Jul mean surface air temperature between the CMIP5 1979–2011 period and the CMIP5 preindustrial control, calculated as 1979–2011 minus preindustrial.

S5. THE EXTREME MARCH–MAY 2012 WARM ANOMALY OVER THE EASTERN UNITED STATES: GLOBAL CONTEXT AND MULTIMODEL TREND ANALYSIS

THOMAS R. KNUTSON, FANRONG ZENG, AND ANDREW T. WITTENBERG

The analysis in Fig. 5.2 of the main paper shows how observed and simulated trends from model All-Forcing runs, control runs, and observations can be compared quantitatively, using control-run variability to estimate confidence intervals on the modeled trends. This same methodology (which is described in greater detail in Knutson et al. 2013) can be applied in a similar manner to time series at individual grid points around the globe. Locations where warming trends are inconsistent with the control runs (detectable) and either consistent with or greater than the All-Forcing runs according to the methodology described in the main text are assessed as having a detectable anthropogenic contribution to the long-term trend.

The red-orange or dark red areas on the maps in Fig S5.1 (right column) depict grid points in the HadCRUT4 dataset that have some detectable warming due to anthropogenic forcing according to this criterion. We find that about 80% of the analyzed global area for March–May (MAM) seasonal means meets these criteria, with similar percentages for other seasons or the annual means.

The white regions in the maps (right column) show where the observed trend is classified as not detectable compared with model control run variability. Interestingly, the region of the eastern United

States that had such anomalously warm (record) MAM anomalies in 2012 is also a region that does not have a detectable warming trend during MAM for a number of the individual grid points in this region over 1901–2012 according to this analysis (Fig. S5.1i). However, after spatial averaging over the entire region of record MAM warmth, the trend since 1901 assessed as significant (Fig. 5.2 in the report). In addition, parts of the eastern tropical and subtropical Pacific and much of the extratropical North Atlantic also do not exhibit detectable (distinguishable from natural variability) long-term warming trends in any season at the gridpoint scale (Fig. S5.1f,i,l,o). We conclude that there is only marginal significance for an anthropogenic contribution to the extreme seasonal warmth during MAM 2012 over the eastern United States at the gridpoint scale based on this assessment.

Most of the other larger features in the seasonal extremes maps shown in the middle column of Fig. S5.1—e.g., June–August (JJA) warm anomalies in the Mediterranean region, in the Somali Current region off the east coast of Africa in JJA and September–November (SON), and the warming off the northeast coast of the United States and Canadian maritime provinces in JJA and SON—tend to occur in regions that have some detectable anthropogenic contribution to the 1901–2012 trends, according to our assessment.

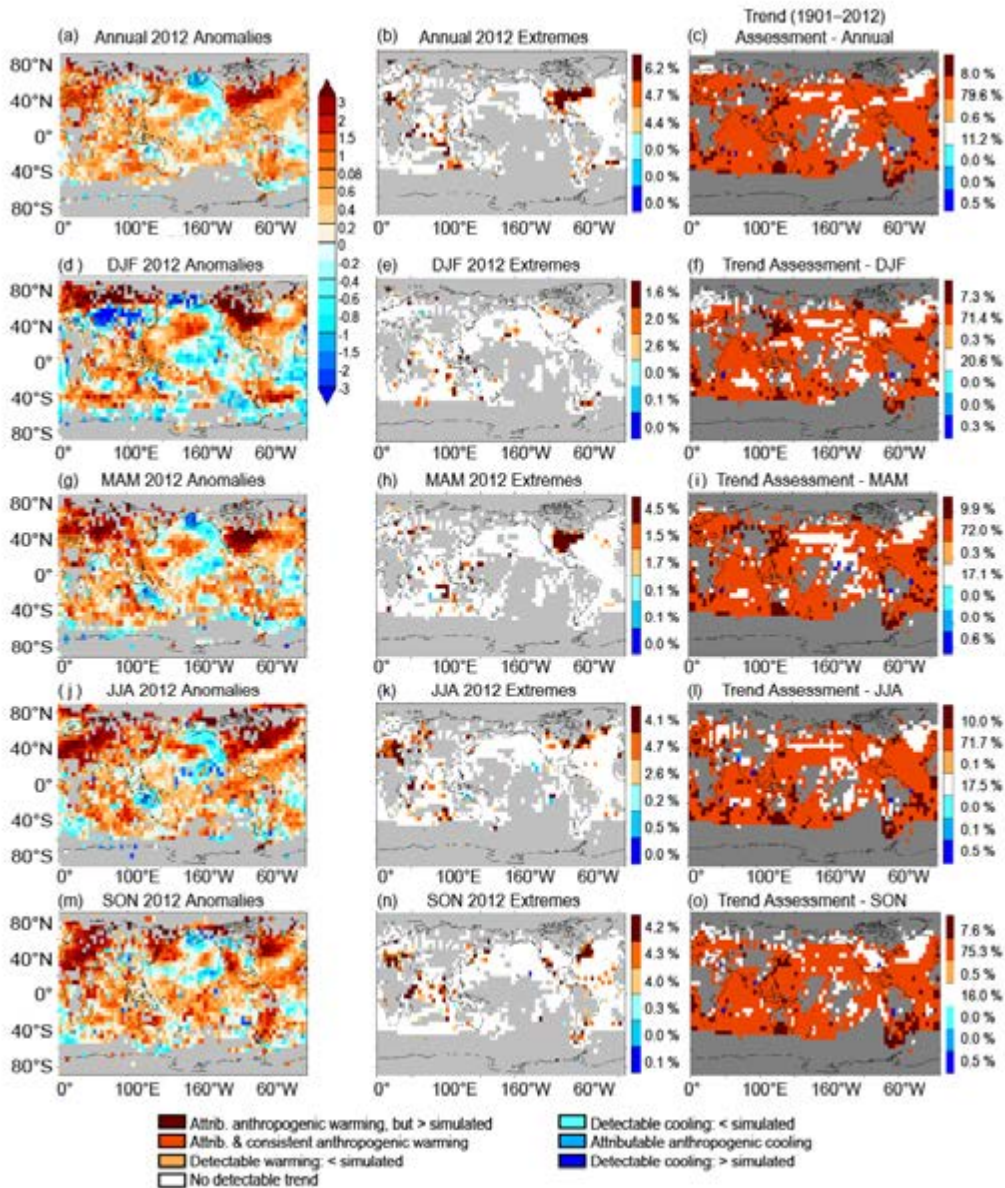


FIG. S5.1. (Left column) Annual- (a) or seasonal- (d,g,j,m) mean surface air temperature anomalies for 2012 (1961–90 base period) from the HadCRUT4 dataset (unit: °C). The seasons are DJF (Dec 2011–Feb 2012), MAM (Mar–May), JJA (Jun–Aug), and SON (Sep–Nov). (Middle column) Colors identify grid boxes with annual- (b) or seasonal- (e,h,k,n) mean anomalies that rank first (dark red), second (red-orange), or third (yellow-orange) warmest or first (dark blue), second (medium blue), or third (light blue) coolest in the available record. Gray areas did not have sufficiently long records, defined here as containing at least 100 available annual or seasonal means, with an annual mean requiring at least four available months and a seasonal mean requiring at least two of three months to be available. Left and middle columns are repeated from Fig. 5.1 in the report for ease of comparison. (Right column) Colors identify categories of trend assessment results for annual means (c) and various seasons (f,i,l,o), which were assessed by comparing the observed trends over the period 1901–2012 with modeled trends in either the All-Forcing (anthropogenic and natural combined) or the Control runs. Locations where no detectable observed trend was found are white (i.e., consistent with Control-run variability). Locations where observed trends are detectable and consistent with All Forcing runs are red-orange. Locations where observed trends are detectable and significantly greater than the All-Forcing run trends are dark red. Locations where observed trends are detectable but significantly less than the All-Forcing runs trends are yellow-orange. Consistent here means that the observed trend lies within the multimodel distribution (5th–95th percentiles) for a given forcing scenario (i.e., All-Forcing scenario or Control run with no external forcing), where the All-Forcing model distribution incorporates the uncertainty from the models due to both differences in response to forcing between the different models and the spread due to internal variability in the model control runs. See Knutson et al. (2013) for further details.

S7. SEPTEMBER 2012 ARCTIC SEA ICE MINIMUM: DISCRIMINATING BETWEEN SEA ICE MEMORY, THE AUGUST 2012 EXTREME STORM, AND PREVAILING WARM CONDITIONS

VIRGINIE GUEMAS, FRANCISCO DOBLAS-REYES, AGATHE GERME, DAVID SALAS Y MÉLIA,
MATTHIEU CHEVALLIER, AND MERCATOR-OCEAN

Supplemental Methods. The sea ice reconstruction that provided our sea ice initial conditions is briefly described here. A more extensive description and validation can be found in Guemas et al. (2013). This sea ice reconstruction is run with the Louvain-la-Neuve (LIM2; Fichet and Maqueda 1997; Goosse and Fichet 1999) sea ice model embedded into version 3.2 of the NEMO ocean model (Madec et al. 2008) and forced with ERA-interim (Dee et al. 2011) atmospheric surface fields through Large and Yeager's (2004) bulk formulae. The ocean temperature and salinity are nudged towards their monthly counterpart from the ORAS4 ocean reanalysis (Mogensen et al. 2011; Balmaseda et al. 2012). This nudging exerts a strong constraint on the sea ice extent as ice melts when transported towards an area where the (SST) is above the seawater freezing point. The timescale for the nudging is set to 360 days below 800 m and 10 days above, except in the mixed layer, but the SST and sea surface salinity (SSS) are also restored (-40 W m^{-2} and $-150 \text{ mm day}^{-1} \text{ psu}^{-1}$). The nudging is not applied in the 1°S – 1°N band to avoid disrupting the strong equatorial currents but is applied anywhere

else. Each member of the sea ice reconstruction is nudged toward a different member of the ORAS4 ocean reanalysis. Wind stress perturbations are added to the ERA-interim atmospheric surface fields for four of the five members. To obtain the wind stress perturbations, we compute the differences between the monthly 10-m wind speed of DFS4.3 (Brodeau et al. 2010) and ERA-interim over the 1979–2006 period. Those differences provide an estimate of the observational error in the wind field. We obtain 28 differences for each month of the year. January perturbations are then picked up randomly from the set of January differences, February perturbations from the set of February differences, etc. After drawing the perturbations for a complete year, i.e., 12 monthly perturbations, they are interpolated linearly to obtain daily perturbations. Finally, our five initial conditions are taken from a previous five-member sea ice reconstruction, which follows the exact same methodology but uses the DFS4.3 forcings.

S10. THE EXTREME EUROPEAN SUMMER 2012

BUWEN DONG, ROWAN SUTTON, AND TIM WOOLLINGS

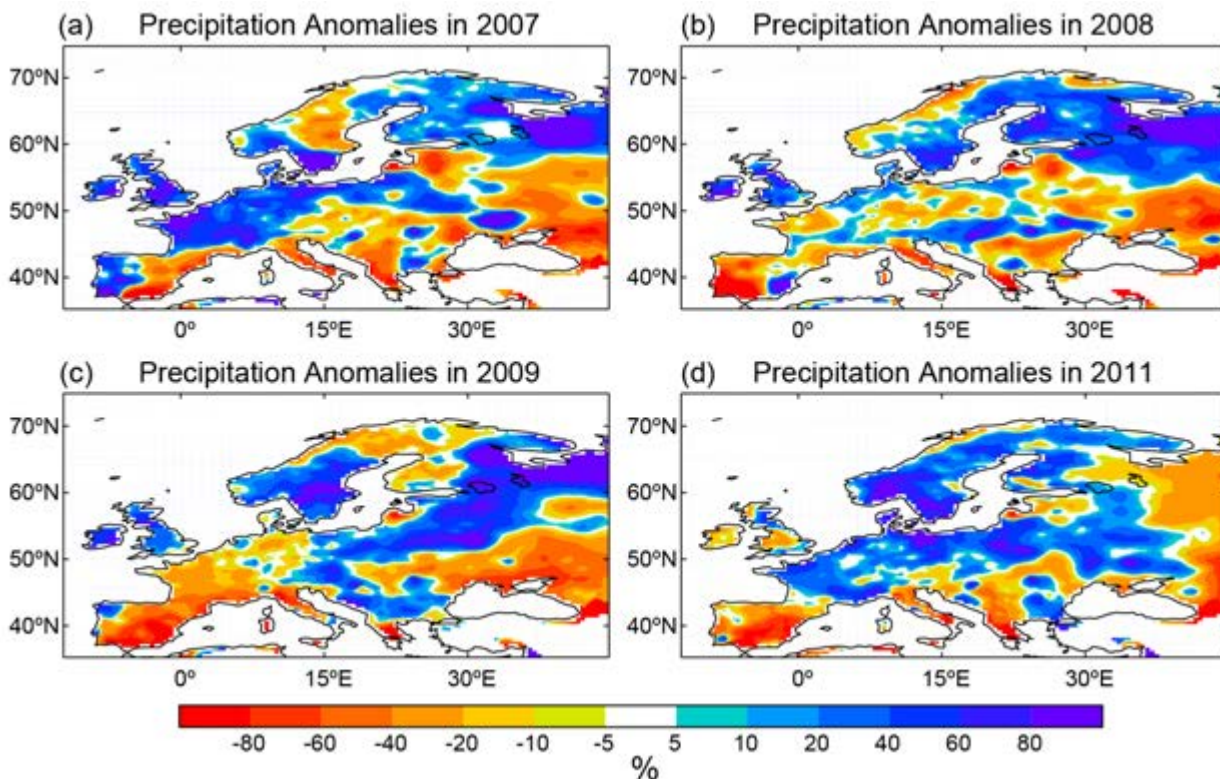


FIG. S10.1. Anomalies in precipitation for Jun–Aug (JJA) during recent years relative to the 1964–93 mean from the daily gridded E-OBS precipitation (version 7.0) over Europe (Haylock et al. 2008). Seasonal mean precipitation anomalies expressed as a percentage of the climatological mean value for 1950–2012. (a) For 2007, (b) for 2008, (c) for 2009, and (d) for 2011.

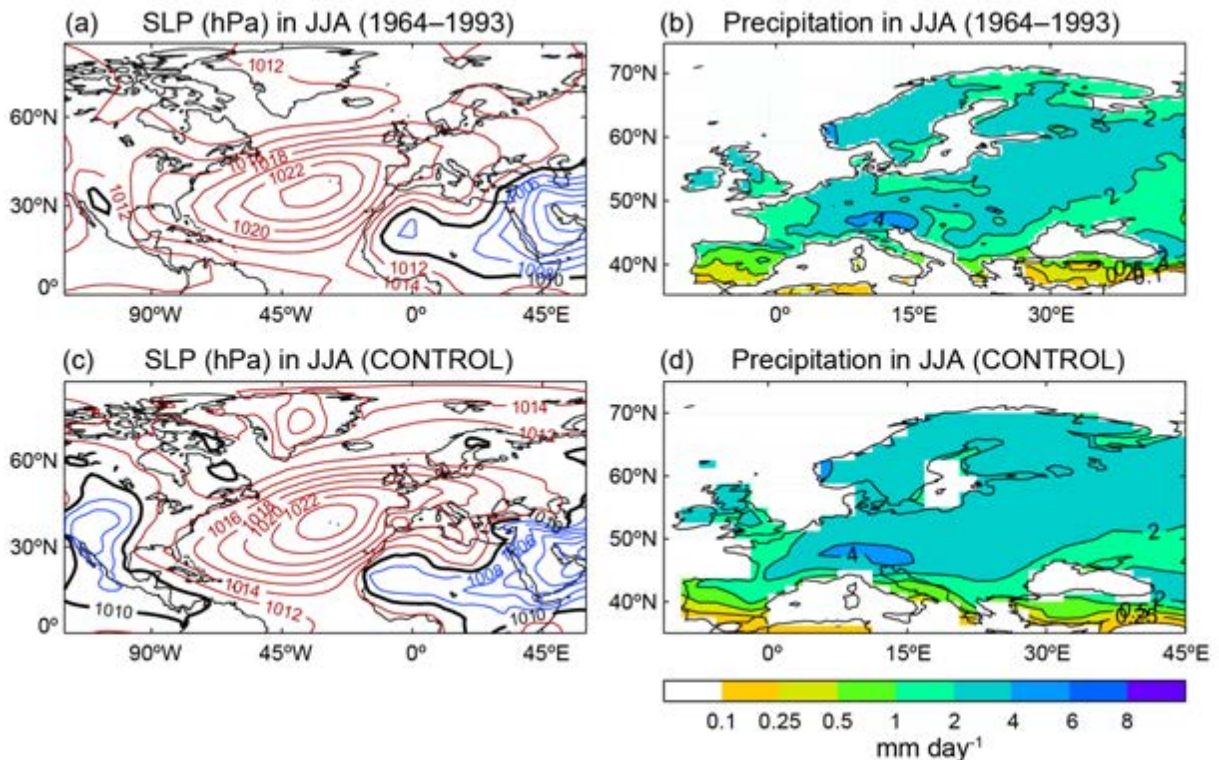


FIG. S10.2. Climatological seasonal mean (JJA) SLP (hPa) and precipitation (mm day⁻¹) in observations and in the CONTROL experiment. Observations are the mean value for 1964–93 of (a) SLP from HadSLP2 and (b) precipitation from the daily gridded E-OBS precipitation (version 7.0) over Europe (Haylock et al. 2008). Model climatology of (c) SLP and (d) precipitation are the last 25 year mean values.

S13. CONTRIBUTION OF ATMOSPHERIC CIRCULATION TO WET NORTH EUROPEAN SUMMER PRECIPITATION OF 2012

PASCAL YIOU AND JULIEN CATTIAUX

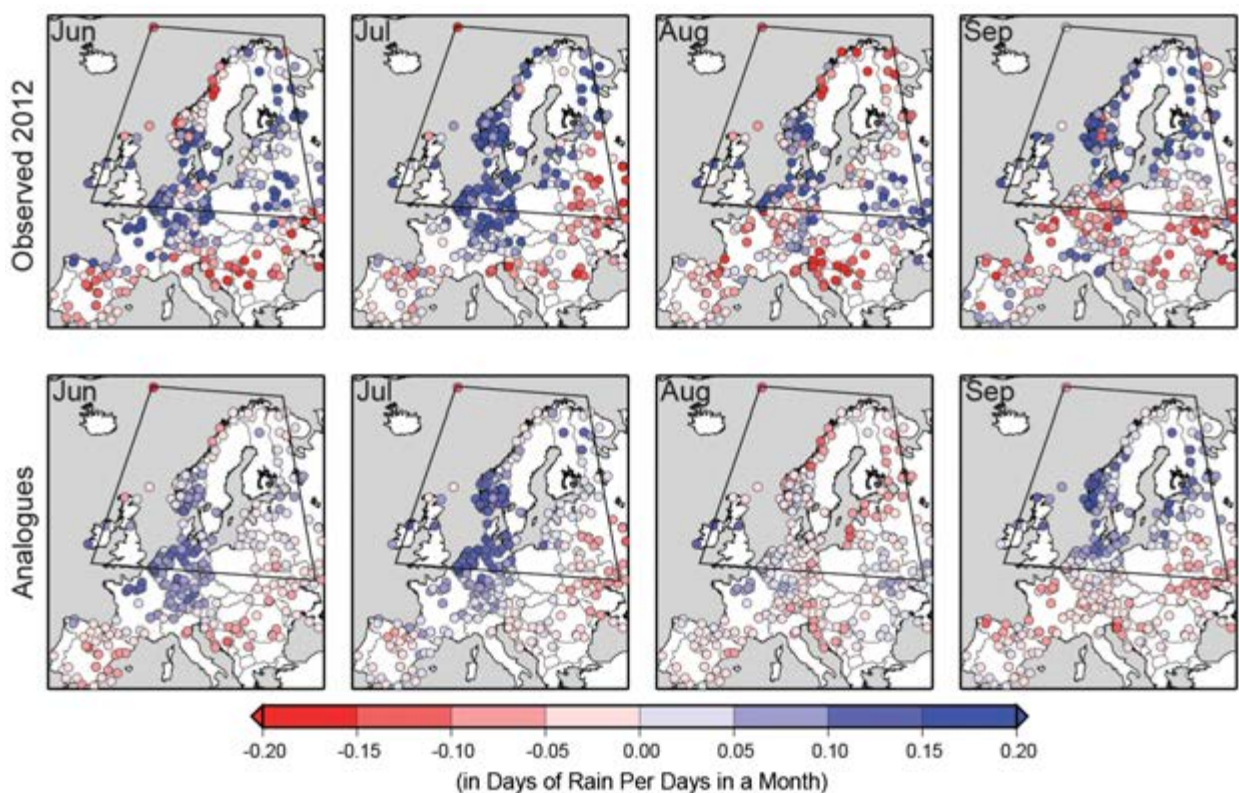


FIG. S13.1. Anomalies of precipitation frequencies over Europe (in fractions of seasons) for four summer months in 2012 (Jun–Sep). The colored points represent the 351 ECA&D stations we retained. The polygon outlines the region over which the averages were computed (50°N – 70°N , 8°W – 35°E). The upper panels represent observed precipitation frequency anomalies; the lower panels represent the median precipitation frequency anomalies obtained from 20 analogues of circulation.

S15. ATTRIBUTION OF 2012 AND 2003–12 RAINFALL DEFICITS IN EASTERN KENYA AND SOUTHERN SOMALIA

CHRIS FUNK, GREG HUSAK, JOEL MICHAELSEN, SHRADDHANAND SHUKLA, ANDREW HOELL, BRADFIELD LYON, MARTIN P. HOERLING, BRANT LIEBMANN, TAO ZHANG, JAMES VERDIN, GIDEON GALU, GARY EILERTS, AND JAMES ROWLAND

East African (EA) dry event March sea surface temperature (SST) transects. We briefly discuss equatorial transects of standardized NOAA Optimal Interpolation (OI) SSTs for March seasons associated with dry EA SPI events (Fig. S15.1). March SSTs were used to emphasize the potential for short-term predictability—if a consistent March SST pattern emerges, this may indicate that we could anticipate low March–May EA SPI outcomes. The averaged transects do indicate a coherent structure, indicating that a warmer Indo-Pacific combined with a cooler eastern Pacific may be conducive to EA drying. Most (1984, 1996, 1999, 2000, 2007, 2008, 2009, 2011, 2012) but not all (1983, 1992), of the individual dry season transects tend to indicate strong western-to-central Pacific SST gradients.

EA precipitation and SPI time series. The precipitation time series shown here is a new FEWS NET precipitation monitoring product (the Climate Hazard Group InfraRed Precipitation with Stations; CHIRPS) dataset. CHIRPS is produced by blending 1981–present

cold cloud duration based precipitation estimates based on geostationary infrared satellite observations with in situ monthly precipitation gauge observations (Funk et al. 2013, unpublished manuscript). This rainfall dataset has been developed to support real time drought monitoring. The 1981–2012 EA March–May CHIRPS and Global Precipitation Climatology Centre precipitation averages were almost identical (Fig. S15.2). The GPCC time series data was not available when this work commenced, hence our use of CHIRPS.

The EA SPI (McKee et al. 1993) time series was created by (i) fitting a gamma distribution to the 1981–2012 three-month EA precipitation totals and then (ii) translating the associated rainfall percentiles into an equivalent standard normal distribution z-score.

GFS estimation procedure. This section describes in more detail the statistical estimation approach used in this analysis. Local GFS precipitation exhibited

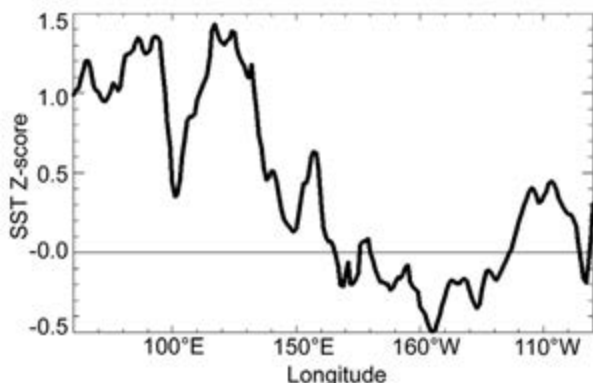


FIG. S15.1. Standardized equatorial (10°S–10°N) March NOAA OI SST transects for the 12 EA dry events shown with circles in Fig. 15.1b (in the original paper).

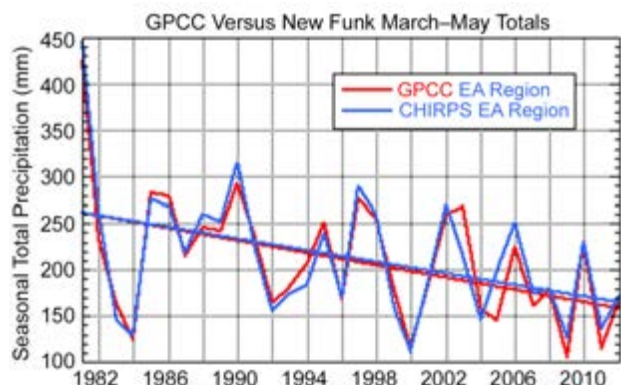


FIG. S15.2. EA March–May precipitation totals from CHIRPS and GPCC.

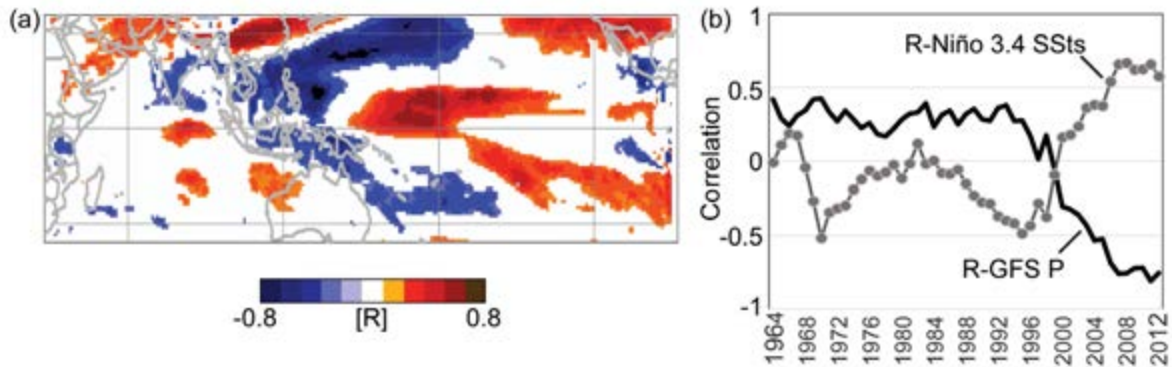


FIG. S15.3. (a) The 1993–2012 correlation between GFS March–May ensemble mean precipitation and the EA SPI time series. (b) Running 15-year correlations between EA SPI and Niño3.4 SSTs and GFS western Pacific SSTs.

low correlations with the EA precipitation ($r = 0.34$, 1982–2012), while rainfall in the Indo-Pacific exhibited (Fig. S15.3a) significant anti-correlations over the past 20 years (1993–2012), our estimates were based on a simple regression between western Pacific (0° – 20° N, 120° E– 160° E) GFS precipitation and EA SPI. Recent analyses have suggested that enhanced low-level convergence and precipitation in the western Pacific is associated with subsidence over and reduced moisture transports into the EA region (Lyon and DeWitt 2012; Williams and Funk 2011). Cross-validation (Michaelsen 1987) indicated a robust relationship with an r -squared value of 0.5, and slope coefficients that varied by $\pm 8\%$. Niño3.4 SST variations explained half of the 1993–2012 western Pacific GFS precipitation variance.

Interestingly, the relationship between EA SPI and Niño3.4 SSTs and western Pacific GFS precipitation exhibits substantial non-stationarity. Fifteen-running-year correlations with March–May GFS western Pacific (120° E– 160° E, 0° – 20° N) precipitation exhibit strong (< -0.7) anti-correlations over the 1993–2012 era (Fig. S15.3b), but this relationship turns slightly positive over the 1950–92 period. A similar, but slightly weaker, relationship to Niño 3.4 SSTs may also be observed, with recent (older) La Niña events correlated to droughts (pluvials). The drought impacts of recent La Niña events have apparently become more substantial (Williams and Funk 2011).

SI6. THE 2012 NORTH CHINA FLOODS: EXPLAINING AN EXTREME RAINFALL EVENT IN THE CONTEXT OF A LONGER-TERM DRYING TENDENCY

TIANJUN ZHOU, FENGFEI SONG, RENPING LIN, XIAOLONG CHEN, AND XIANYAN CHEN

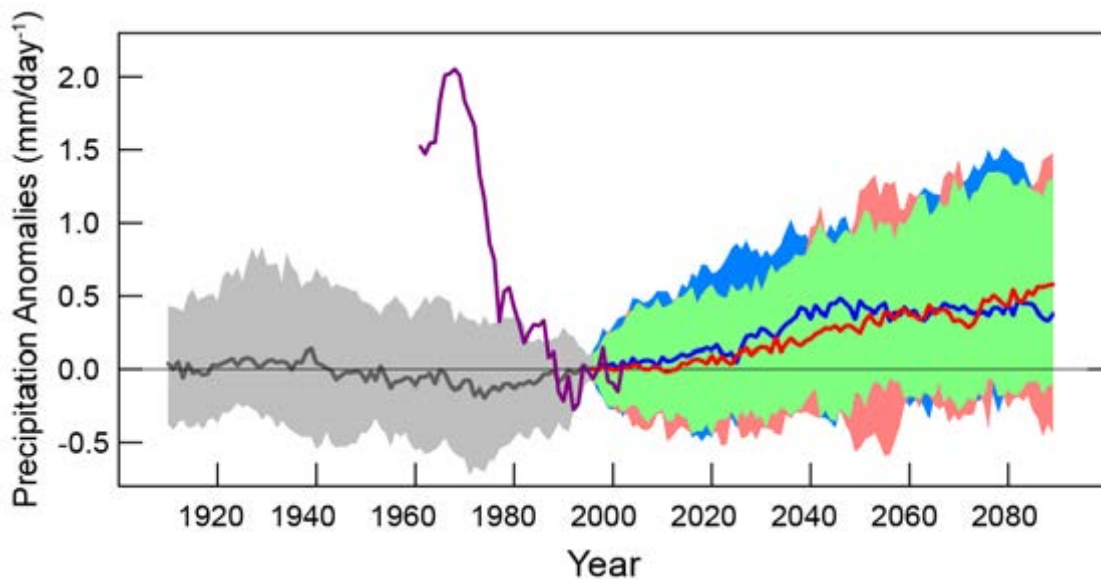


FIG. S16.1. Time series of Jul precipitation (21-year running mean) in North China (35°N – 43°N , 110°E – 122°E) relative to the base period average (1986–2005). Historical (gray), RCP4.5 (blue), and RCP8.5 (red) simulations by 39 CMIP5 model ensembles are shown in 10th, 90th (shading), and 50th (thick line) percentiles. Observations from 23 stations within the domain (purple) are overlaid.

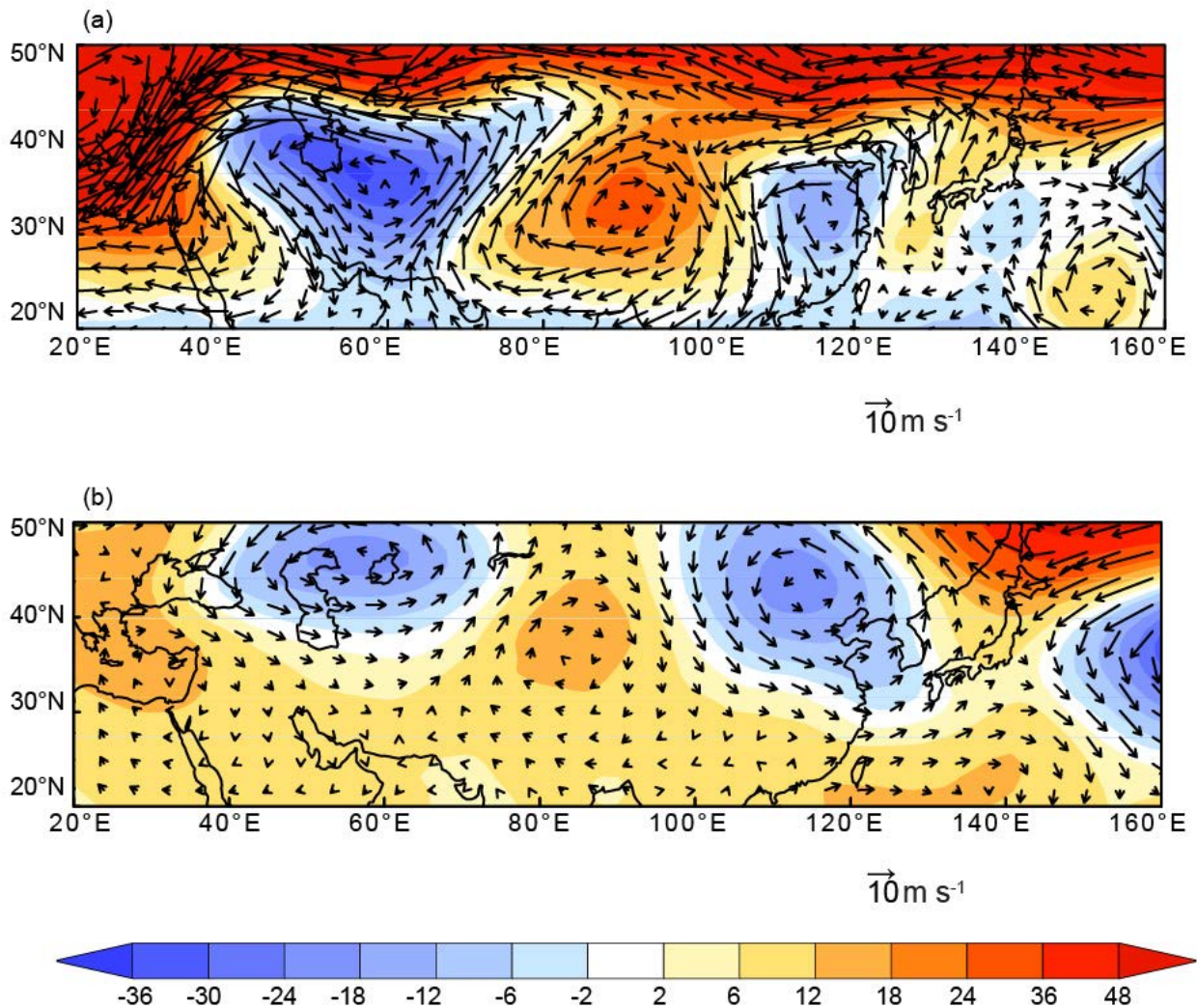


FIG. S17.2: (a) Anomalies in the 2012 rainy season (15 Jun–15 Jul) from the JRA-25 reanalysis: geopotential height [(m), shaded] and wind [(m s⁻¹), arrow] at 200 hPa. A wave train corresponding to the circumglobal teleconnection pattern is evident along the Asian jet and enhances the PASH. (b) Same as (a) but for a composite of the top 15 cases from the ALL-LNG run diagnosed by the PJ index.

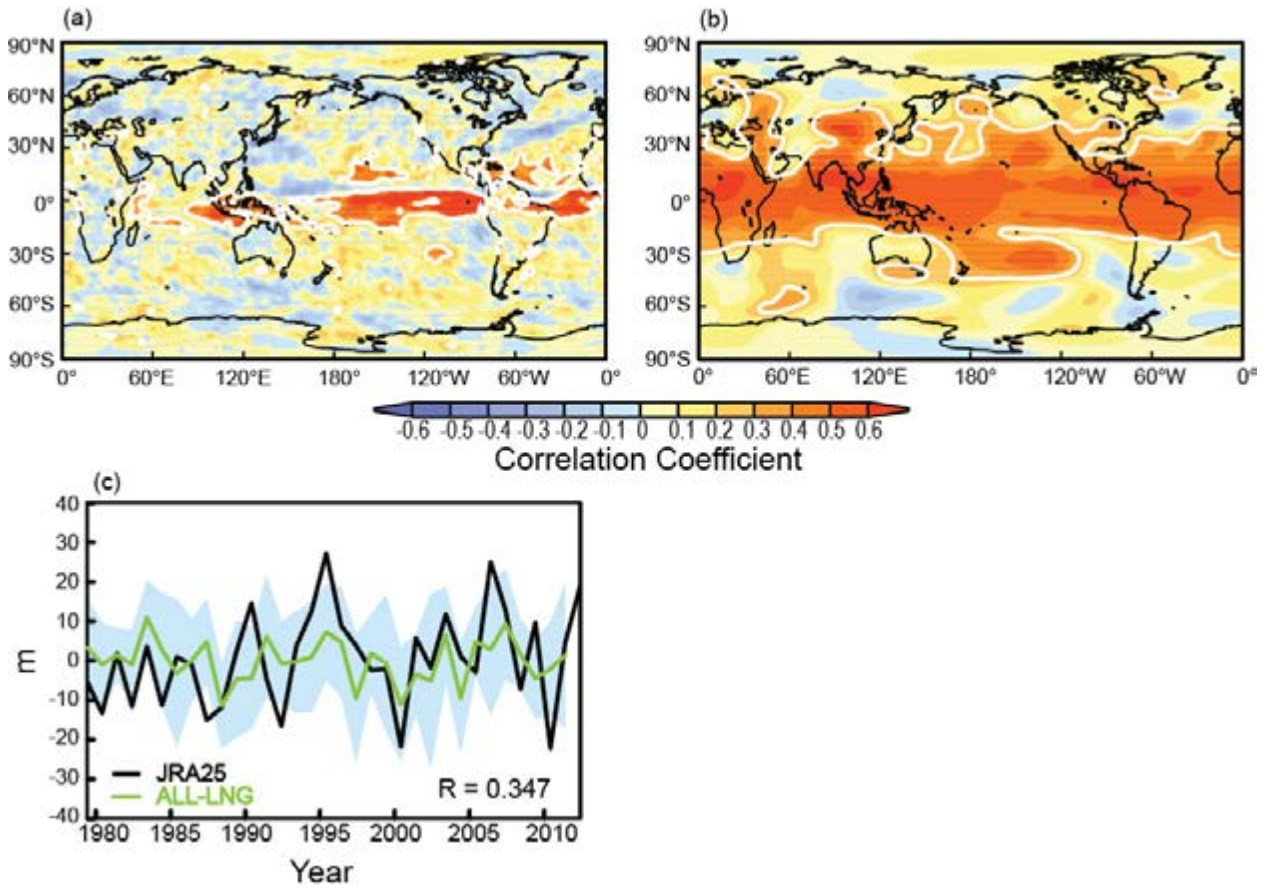


FIG. S17.3: (a) Correlation map of precipitation anomalies between GPCP and the ALL-LNG experiment for 1979–2011. White contours denote a 90% significance level. (b) Same as (a) but for 500-hPa geopotential height anomalies. (c) The PJ indices based on JRA25 (black) and the ALL-LNG run (green). Shading denotes the ensemble spread.

S18. LIMITED EVIDENCE OF ANTHROPOGENIC INFLUENCE ON THE 2011–12 EXTREME RAINFALL OVER SOUTHEAST AUSTRALIA

ANDREW D. KING, SOPHIE C. LEWIS, SARAH E. PERKINS, LISA V. ALEXANDER, MARKUS G. DONAT, DAVID J. KAROLY, AND MITCHELL T. BLACK

Table S18.1. CMIP5 models used in this study. This set of models simulates more realistic variability in the Niño-3.4 region. Bold font indicates models selected for further study as they show a nonlinear ENSO-extreme rainfall relationship in the same direction as observed.

Model	Run Identification numbers	Number of runs
bcc-csm1-l	rlilpl,r2ilpl,r3ilpl	3
CanESM2	rlilpl,r2ilpl,r3ilpl,r4ilpl,r5ilpl	5
CCSM4	rlilpl,r2ilpl	2
CNRM-CM5	rlilpl,r2ilpl,r3ilpl,r4ilpl,r5ilpl	5
CSIRO-Mk3-6-0	rlilpl,r2ilpl,r3ilpl,r4ilpl,r5ilpl	5
GFDL-CM3	rlilpl,r2ilpl,r3ilpl,r4ilpl,r5ilpl	5
GFDL-ESM2M	rlilpl	1
HadGEM2-ES	rlilpl,r2ilpl,r3ilpl,r4ilpl	4
MRI-CGCM3	rlilpl,r2ilpl,r3ilpl	3
NorESM1-M	rlilpl,r2ilpl,r3ilpl	3

S20. THE ROLE OF CLIMATE CHANGE IN THE TWO-DAY EXTREME RAINFALL IN GOLDEN BAY, NEW ZEALAND, DECEMBER 2011

SAM M. DEAN, SUZANNE ROSIER, TREVOR CAREY-SMITH, AND PETER A. STOTT

In addition to the two figures below, this analysis of a heavy rain event in New Zealand includes an animation of the vertical integral of specific humidity that is available here: <http://dx.doi.org/BAMS-D-13-00085.3>



FIG. S20.1. Aerial photo of slips on the hillsides of Golden Bay taken shortly after the event. Reproduced here with permission. Image copyright Gerry Draper.

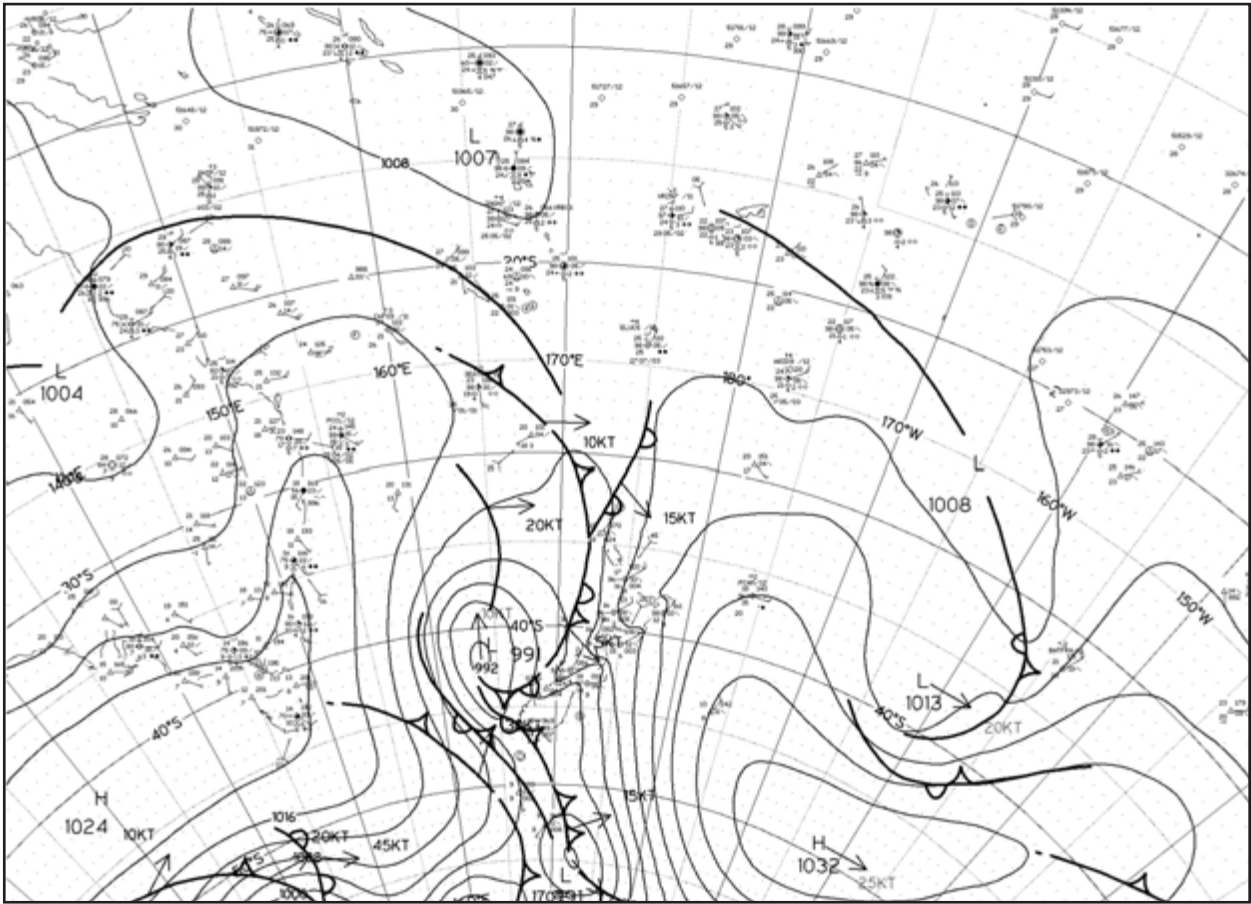
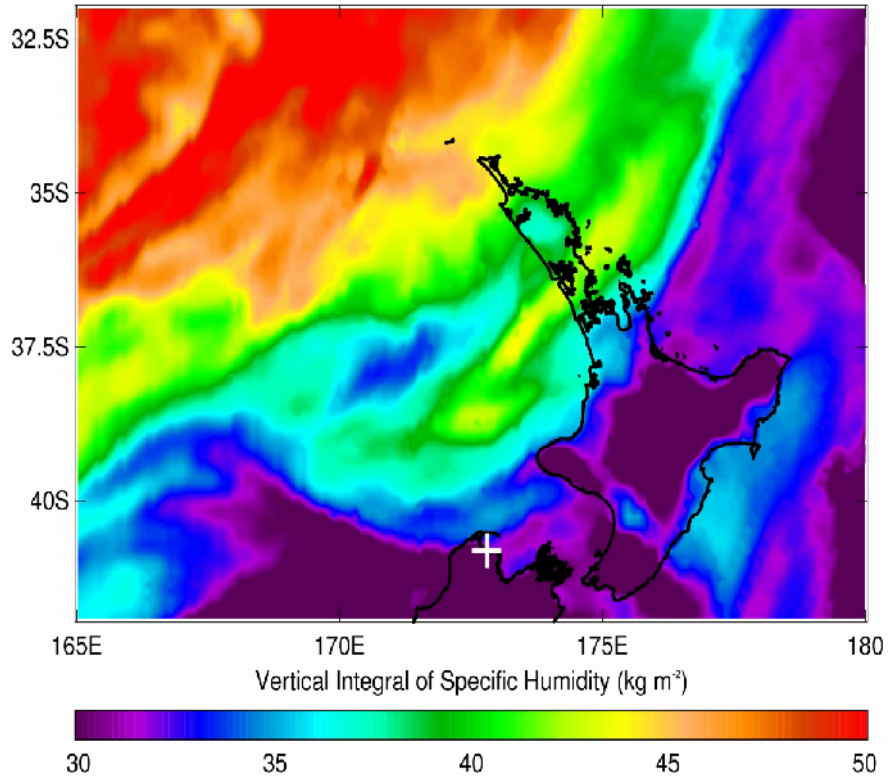


Fig. S20.2. Meteorological analysis chart showing the synoptic situation at 0600 UTC 14 Dec 2011.

NZLAM 12 km Operational Model at 07:00 13th December 2011 (UTC)



REFERENCES FOR SUPPLEMENTAL MATERIAL

- Balmaseda, M. A., K. Mogensen, and A. T. Weaver, 2012: Evaluation of the ECMWF ocean reanalysis system ORAS4. *Quart. J. Roy. Meteor. Soc.*, in press, doi:10.1002/qj.2063.
- Brodeau, L., B. Barnier, A. M. Treguier, T. Penduff, and S. Gulev, 2010: An ERA40-based atmospheric forcing for global ocean circulation models. *Ocean Modell.*, **31**, 88–104.
- Dee, D. P., and Coauthors, 2011: The ERA-interim reanalysis: Configuration and performance of the data assimilation system. *Quart. J. Roy. Meteor. Soc.*, **137**, 553–597.
- Fichefet, T., and M. A. M. Maqueda, 1997: Sensitivity of a global sea ice model to the treatment of ice thermodynamics and dynamics. *J. Geophys. Res.*, **102** (C6), 12 609–12 646.
- Goosse, H., and T. Fichefet, 1999: Importance of ice-ocean interactions for the global ocean circulation: A model study. *J. Geophys. Res.*, **104** (C10), 23 337–23 355.
- Guemas, V., F. J. Doblas-Reyes, K. Mogensen, Y. Tang, and S. Keeley, 2013: Ensemble of sea ice initial conditions for interannual climate predictions. *Climate Dyn.*, submitted, CLIDY-D-13-00147.
- Haylock, M. R., and Coauthors, 2008: A European daily high-resolution gridded dataset of surface temperature and precipitation. *J. Geophys. Res.*, **113**, D20119, doi:10.1029/2008JD10201.
- Kalnay, E., and Coauthors, 1996: The NCEP/NCAR 40-year reanalysis project. *Bull. Amer. Meteor. Soc.*, **77**, 437–471.
- Knutson, T. R., F. Zeng, and A. T. Wittenberg, 2013: Multi-model assessment of regional surface temperature trends: CMIP3 and CMIP5 20th century simulations. *J. Climate*, in press, doi:10.1175/JCLI-D-12-00567.1.
- Large, W., and S. Yeager, 2004: Diurnal to decadal global forcing for ocean and sea-ice models: The data sets and flux climatologies. NCAR Tech. Note NCAR/TN460+STR, 111 pp.
- Lyon, B., and D. G. DeWitt, 2012: A recent and abrupt decline in the East African long rains. *Geophys. Res. Lett.*, **39**, L02702, doi:10.1029/2011GL050337.
- Madec, G., and Coauthors, 2008: *NEMO ocean engine*. Note du pole de modélisation, No. 27, Institut Pierre-Simon Laplace, 357 pp.
- McKee, T. B., N. J. Doesken, and J. Kleist, 1993: The relationship of drought frequency and duration to time scales. *Proc. Eighth Conf. on Appl. Climatol.*, Anaheim, CA, Amer. Meteor. Soc., 179–183.
- Michaelson, J., 1987: Cross-validation in statistical climate forecast models. *J. Climate Appl. Meteor.*, **26**, 1589–1600.
- Mogensen, K., M. A. Balmaseda, and A. Weaver, 2011: The NEMOVAR ocean data assimilation as implemented in the ECMWF ocean analysis for system 4. ECMWF Tech. Memo. 668, 59 pp. [Available on line at <http://www.ecmwf.int/publications/library/do/references/show?id=90389>.]
- PCMDI, cited 2013: Earth System Grid CMIP5 database. [Available online at <http://pcmdi9.llnl.gov/esgf-web-fe/>.]
- Peters, G. P., and Coauthors, 2013: Commentary: The challenge to keep global warming below 2°C. *Nature Climate Change*, **3**, 4–6.
- Taylor, K. E., R. J. Stouffer, and G. A. Meehl, 2012: An overview of CMIP5 and the experiment design. *Bull. Amer. Meteor. Soc.*, **93**, 485–498.
- Williams, A. P., and C. Funk, 2011: A westward extension of the warm pool leads to a westward extension of the Walker circulation, drying eastern Africa. *Climate Dyn.*, **37**, 2417–2435.